Pile Tunnel Interaction

Paal-tunnelinteractie

Tiago Gerheim Souza Dias

Promotor: prof. dr. ir. A. Bezuijen
Proefschrift ingediend tot het behalen van de graad van
Doctor in de ingenieurswetenschappen: bouwkunde

UNIVERSITEIT
GENT

Vakgroep Civiele Techniek
Voorzitter: prof. dr. ir. P. Troch
Faculteit Ingenieurswetenschappen en Architectuur
Academiejaar 2016 - 2017

ISBN 978-90-8578-969-7
NUR 956
Wettelijk depot: D/2017/10.500/4

Members of the examination committee

Chair

Prof. Luc Taerwe, Ghent University

Reading Committee

Prof. Hans de Backer, Ghent University
Prof. Frits van Tol, Delft University of Technology
Prof. Robert Mair, University of Cambridge

Other members

Prof. Adam Bezuijen, Ghent University
Prof. Markus Thewes, Ruhr University Bochum
Prof. Wim Haegeman, Ghent University

"*For a successful technology, reality must take precedence over public relations, for Nature cannot be fooled.*"

Richard Feynman

Acknowledgments

I would like to thank my friends, wherever they may be, for their incessant support during these four years. Whenever I had a chance to go to Brasília, I was welcomed by my old friends and family as if I had never left, and that familiar feeling is something I will always cherish. Being away from my family is one of the things that certainly did not get any easier during these years. My mother is truly the best gift of my life, and I wouldn't be here without her endless love and dedication. I was lucky that I also had several reasons to come back. I met some great people in Ghent, and they have been amazing friends as we travelled together and enjoyed lazy Sunday afternoons. But most of all, I had Nathalia, and my home is where we are together, thank you for everything.

Professionally, I got to where I am through the thoughtful assistance of 3 A's: André Assis, Arsênio Negro, and Adam Bezuijen. The first was my mentor, a great teacher and friend, and the main reason I became a geotechnical engineer. He also introduced me to Arsênio, who hired me just after graduation. We worked together in Sao Paulo for a couple of months, and I had the chance to witness his remarkable attitude towards engineering, continuously learning and improving. He knew that I was looking for a PhD, so he referred me to Adam, who accepted my application as soon as I finished my masters. I am truly grateful to have been his student. He gave me the freedom to search for my own path, and the respect to discuss everything as equals. His scientific approach to engineering is something that I really admire, and hope to have learned for the rest of my career. I am deeply thankful to three of you.

Finally, I would like to thank the students, staff and professors of the Laboratory of Geotechnics for their assistance during this project, and acknowledge the financial support from the Brazilian Research Agency – CNPq.

Table of contents

List of symbols

A	Area of the flow domain in front of a TBM
Ap	Area of the pile toe
dh	Vertical distance
dl	Length of pile segments
Dp	Pile diameter
dr	Incremental radius at the tunnel face
dR	Radial contraction of the tunnel boundary
Dt	Tunnel diameter, also used to define the excavation diameter
du/dy	Velocity gradient perpendicularly to the grout flow
dx	Incremental thickness of the filtered grout
$d\theta$	Incremental angle at the tunnel face
E	Young's modulus
E_{50}^{ref}	Reference stiffness modulus for primary loading
Ei	Initial Young's modulus of the hyperbolic model
E_{oed}^{ref}	Reference tangent stiffness for primary oedometric loading
E_p	Young's modulus of the pile body.
E_{ur}^{ref}	Reference Young's modulus for unloading and reloading
Fd	Face distance: horizontal distance between the tunnel face and the projection of the pile alignment
FER	Foam expansion ratio
FIR	Foam injection ratio
F_{shaft}	Maximum total shaft force
F_{toe}	Maximum toe force
FWR	Foam water replacement ratio
fy	Body forces

G	Elastic shear modulus
G_0^{ref}	Reference shear modulus at very small strains
gap	Gap between the ground and the lining, or the ground and the shield, where the grout is flowing.
GP	Grout pressure
h_0	Initial thickness of the slurry grout
k	Ground hydraulic conductivity to the penetration fluid
K	Elastic bulk modulus
k_0	Coefficient of earth pressure at rest
k_c	Scaling factor to calculate the toe capacity based on the cone resistance
K_e	Bulk modulus to calculate the effective stress
K_{int}	Ratio between the horizontal effective stress at the interface and the in-situ vertical effective stress.
K_w	Bulk modulus of the water in the ground
Ld	Pile-tunnel lateral distance: horizontal distance between the centres of the pile and the tunnel
m	Power for stress-level dependency of stiffness
n	Ground porosity
n_1	Initial porosity of the supporting mixture
n_2	Final porosity of the supporting mixture
N_c	Scaling factor to calculate the toe capacity based on the undrained shear strength
nf	Porosity of the filtered grout
ni	Porosity of the liquid grout
N_q	Scaling factor to calculate the toe capacity based on the vertical effective in-situ stress
Nu	Derivative boundary condition along the horizontal direction
Nv	Derivative boundary condition along the vertical direction
OCR	Overconsolidation ratio
p	Isotropic stress
P_p	Perimeter of the pile shaft, assumed constant.
p_x	Grout pressure at point x
q	Deviatoric stress
q_b	Normal stress at the pile toe
$q_{b\,max}$	Maximum vertical normal stress to cause confined failure under the pile toe.
q_b^*	Toe mobilization state from where unloading started
q_c	CPT cone resistance

Q_F	Volume of foam
Q_L	Volume of the surfactant solution
Q_S	Volume of excavated ground
q_w	Discharge from the point source at the tunnel face, or from the liquid grout
r	Radial coordinate at the tunnel face
R	Initial Tunnel radius
Rb	Rebound factor of the toe mobilization model
R_{exc}	Excavation radius
Rf	Failure ratio of the hyperbolic model
$Rlin$	External radius of the lining
S	Slope of the tri-linear shaft mobilization model, defined through the ratios of shear mobilization to relative displacement – $(\tau/\tau_{max})/\Delta\delta$
s	Distance from a point at the tunnel face to a point along the tunnel centreline.
S^0	Initial in-situ stress
$S1$	First slope (elastic) of the tri-linear shaft mobilization model
$S2$	Second slope (elasto-plastic) of the tri-linear shaft mobilization model
$S3$	Third slope (unloading) of the tri-linear shaft mobilization model
$Si\,j$	Stress acting along the plane perpendicular to the direction i, but aligned with the direction j
S_u	Soil undrained shear strength
t	time
$tan(\varphi)$	Pile-soil interface friction coefficient
t_{max}	Time to achieve the maximum thickness of the filtered grout at constant pressure
u	Horizontal displacement
UBC	Pile ultimate bearing capacity
UCL	Ultimate compressive load
UTL	Ultimate tensile load
u_w	Water pressure
v	Vertical displacement
V_0	Initial grout volume
VL	Tunnel volume loss, ratio between the area of the surface settlement or boundary convergence and the original area of the excavation
vp	Penetration velocity in front of a TBM
WL	Pile working load, defined at the pile head.
W_p	Weight of the pile body

x	Thickness of filtered grout layer
x_{face}	Horizontal distance from the tunnel face to a point along the tunnel centreline.
x_{max}	Maximum thickness of the filtered grout at constant pressure
Xt	Horizontal coordinates of the tunnel centre
Zp	Pile length
Zt	Depth of the tunnel centre
α	Scaling factor to calculate the shaft capacity based on the undrained shear strength
β	Scaling factor of an effective stress analysis ($\beta=\tan\phi.K$).
γ	Volumetric weight
$\gamma_{0.7}$	Threshold shear strain at which $G = 0.722G_0$
γ_g	Volumetric weight of the grout
γ_p	Volumetric weight of the pile body
γ_{sat}	Volumetric weight for saturated ground
γ_{unsat}	Volumetric weight for unsaturated ground
δ	Settlement, vertical displacement
δ_{max}	Maximum surface settlement
δp	Pile settlement
δs	Ground settlement
Δl	Distance along the flow direction
Δp	Grout pressure dissipation due to shear
ΔR	Radial convergence
$\Delta\delta$	Relative displacement between the pile and the ground
$\Delta\delta^T$	Relative toe displacement for full mobilization
$\Delta\delta^*$	Relative displacement at the mobilization state from where unloading started.
$\Delta\sigma$	increment of axial stress
$\Delta\sigma_T$	Axisymmetric stress release around the tunnel
$\Delta\phi$	Difference in piezometric head
εxx	Normal strain in the x direction
εxy	Engineering shear strain along the XY plane
η	Grout dynamic viscosity
θ	Angle along the tunnel perimeter
λ	Tunnel, stress release factor /
I/μ	Scaling factor to calculate the shaft capacity based on the cone resistance

v	Poisson ratio
ve	Poisson ratio for drained conditions
vu	Poisson ratio for undrained conditions
σ	Normal axial stress in the pile section
σ_1	Major principal stress.
σ_3	Minor principal stress.
σ'_3	Effective minor principal stress
σ'_v	Vertical effective in-situ stress
σ^{ref}	Reference stress
τ	Shear stress at the pile-soil interface
τ_{ep}	Shear mobilization where there is a transition from the slope S1 to the slope S2 in the tri-linear shaft mobilization model
τ_g	Grout shear stress
τ_{max}	Maximum shear stress at the pile-soil interface
τ_y	Grout yield resistance
ϕ	Friction angle
$\phi\ (x_{face})$	Incremental piezometric head at a certain horizontal distance from the tunnel face
ϕ_0	Incremental piezometric head at the tunnel face
χ	Exponent of the toe mobilization model
ψ	Dilatancy angle

Summary

Pile tunnel interaction is a relatively new problem, most commonly found in urban areas. Deep foundations are used to support buildings and other elements of the urban infrastructure, while tunnels offer an alternative pathway for the flow of people and resources in and out of cities, without interfering with the densely constructed urban surface. These two structures have co-existed for decades. Most piles were installed along ground layers far from the deep-level bored tunnels, scarcely placed through the city. However, technological innovations have changed this: piles are now installed in deeper layers to support the ever rising buildings and shallower tunnels, much more widespread through the cities, can be built. This thesis analyses how the construction of a new tunnel might affect an existing pile foundation, explains the mechanism through which this happens and recommends a methodology to calculate the consequences for design.

The first step was to examine the current state of knowledge on **pile tunnel interaction** through an extensive literature review. Quantitative measurements collected from case studies, full-scale tests and scaled models. The results were set-up in a framework where they could be compared and contrasted, revealing patterns that were not distinguishable in individual studies. Most reported structures were not affected by a tunnel construction, but under certain conditions, interventions were necessary. Two mechanisms are described, one at the pile toe and one along the pile shaft. (1) The tunnel degrades the toe capacity, which mobilizes the shaft resistance for equilibrium. (2) Negative friction is induced along the pile shaft, which increases the loading at the pile toe. In both cases, once the shaft is fully mobilized, significant settlements occur to re-mobilize the pile toe.

The quantitative data reveals that the measured pile settlements are always inversely proportional to its lateral distance from the tunnel alignment. In loaded-piles, the average axial force along the pile reduces when the piles are right above the tunnel, but increases when the piles were farther away ($Ld > Rt$). The mathematical models used to compute the consequences of pile tunnel interaction have also been studied. A pilot methodology is proposed and the promising results set the course for the developments in this project. At that stage the model imposed the pile settlements and calculated the resultant axial forces. It did not consider the possibility of pile failure, or a constant load boundary condition.

For the analysis of **piles**, a new and accessible framework was created, where it is possible to calculate the pile settlements and load transfer for any loading condition, and to consider the effects of ground displacements. This last point connects the pile response with the tunnel excavation, and it was achieved by linking the load mobilization with the relative movements between the pile and the soil. The framework is based on an adapted version of the load transfer method, and implemented within a regular spreadsheet.

The functions defining the reactions from the shaft and toe have, for the most part, only been calibrated for pile loading. However, there are important mechanisms taking place during the unloading stage. These unloading functions are also very important to model the effects of ground displacements. While normally understood as the consequence of a load reduction, unloading can also be the consequence of ground settlements. The related literature and the details of the methodology were discussed. The results were then validated for an instrumented pile load test. The method is able to reproduce the field measurements of the load-settlement curve and axial loads along the pile body.

For the analysis of **tunnels**, specifically on the matter of predicting the induced ground movements, a new take on the problem has been proposed with a focus on pressurized tunnel boring machines (TBMs). The study tried to answer the following question: What are the forces acting on the excavation perimeter of a tunnel? This led to a general review of the processes around a TBM, the physical mechanisms involved, and the numerical techniques used to model them. The literature review shows how the mathematical models used to simulate a TBM tunnel have evolved from a basic stress release to direct accounts of the boundary pressures connected to different elements of a TBM.

An intrinsic feature of mechanized tunnelling is that every step of the excavation cycle is performed through mechanical or hydraulic systems. The interaction mechanisms between the TBM and the surrounding ground result from the

operation of these systems to excavate and support the ground around the tunnel. It is self-evident that for each of these actions there will be a reaction from the ground to achieve equilibrium. However, these mechanisms are often interpreted within idealized frameworks that do not account for important features of the ground reaction that have been observed in the field. Therefore, these frameworks need to be adapted to better represent the interaction between the TBM and the ground. Two methodologies were proposed to evaluate the stages of grout injection and grout consolidation around the tunnel lining at the back of a TBM. The methodology was then validated for an instrumented case study of a tunnel in The Netherlands. The model was able to reproduce the grout pressures around the excavation perimeter, and estimate the surface settlements better than the traditional stress-release method.

Finally, these two separate studies are combined into a design tool to compute the consequences of **pile tunnel interaction**. The pilot methodology is enhanced with more realistic models for the pile reaction. At this point, the load mobilization functions can account for pile failure and have distinct paths for loading and unloading. The pile settlements can be directly obtained through a root search for equilibrium, and don't have to be imposed anymore. Unfortunately, there are no instrumented field tests to this day where the pile settlements and axial forces were recorded concurrently to the grout pressures around a tunnel boring machine. However, the methodology can simulate the fundamental mechanisms of pile tunnel interaction identified in the literature review.

Samenvatting

Paal-tunnelinteractie is een relatief nieuw probleem, vooral in stedelijke gebieden. Paalfunderingen worden gebruikt als fundering voor gebouwen en andere elementen van de stedelijke infrastructuur, terwijl de tunnels een alternatieve route bieden voor de stroom van mensen en middelen in en uit de steden, zonder extra congestie in de dichtbevolkte stedelijke bebouwde omgeving. Deze twee bouwlagen bestaan al tientallen jaren, maar de meeste palen waren geïnstalleerd in de bovenste grondlagen ver van de in de diepere lagen aangebrachte geboorde tunnels. Dit is veranderd door technologische innovaties: palen zijn nu geïnstalleerd in diepere grondlagen en voor een steeds stijgend aantal gebouwen en het aantal ondiepe tunnels is toegenomen. Dit proefschrift analyseert hoe de bouw van een nieuwe tunnel een bestaande funderingspaal kan beïnvloeden, verklaart het mechanisme waarmee dit gebeurt en beveelt een methodologie aan om de gevolgen hiervan te berekenen voor het ontwerp.

De eerste stap was om de huidige stand van de kennis op het gebied van paal-tunnelinteractie te onderzoeken door middel van een uitgebreid literatuuronderzoek. Kwantitatieve metingen van case studies, full-scale tests en geschaalde modellen zijn verzameld. De resultaten van de metingen zijn zodanig verwerkt dat ze konden worden vergeleken en gecontrasteerd. Hieruit volgden patronen die niet te onderscheiden waren in de individuele studies. Het bleek dat de meeste paalfunderingen nauwelijks beïnvloed werden door de constructie van een tunnel, maar dat onder bepaalde voorwaarden, de beïnvloeding zodanig was dat een interventie nodig was. Twee mechanismen zijn beschreven, één voor de paalpunt en één voor de paalschacht. (1) De tunnel vermindert het draagvermogen van de paalpunt. (2) Negatieve kleef langs de paalschacht leidt tot

een toename van de belasting op de paalpunt. In beide gevallen leidt een volledige mobilisatie van de paalpunt tot een aanzienlijke toename van de zettingen.

Uit kwantitatieve gegevens bleek dat de gemeten paalzakkingen altijd omgekeerd evenredig zijn met de afstand van de paal tot de zijkant van de tunnel. Bij belaste palen vermindert de gemiddelde axiale kracht in de paal wanneer de palen recht boven de tunnel staan, maar deze neemt toe bij een grotere afstand tot de tunnel (Ld > Rt). Ook zijn de bestaande rekenmodellen om de gevolgen van paal-tunnelinteractie te berekenen onderzocht. Er werd een eerste eenvoudige methodiek ontwikkeld en de veelbelovende resultaten van deze methodiek hebben de verdere koers voor dit project bepaald. In dit eerste model wordt de paal zakking opgelegd en daaruit de resulterende axiale krachten berekend. Het houdt geen rekening met de mogelijkheid van bezwijken van de paal, of een constante belasting randvoorwaarde.

Voor de analyse van palen, werd een nieuwe en toegankelijk kader ontwikkeld, waarin het mogelijk is om paalzakking en lastenoverdracht te berekenen voor elke belastingtoestand en de effecten van passieve grondverplaatsingen in rekening te brengen. Hierdoor is een relatie mogelijk tussen de paal respons als gevolg van de gronddeformatie ten gevolge van aanleg van de tunnel. Dit werd bereikt door het koppelen van de belastingmobilisatie en de relatieve bewegingen tussen paal en grond. De berekening is gebaseerd op een aangepaste versie van de interactiemethode (load transfer method), en binnen een reguliere spreadsheet geïmplementeerd.

De functies die de reactie van de schacht en de paalpunt definiëren zijn vaak alleen gekalibreerd met paalbelastingen. Echter, in dit geval is ook ontlasten van de paal van belang. De ontlastingsfuncties zijn belangrijk om de effecten van passieve verplaatsingen te modelleren. Hoewel gewoonlijk opgevat als het gevolg van een belastingreductie kan ontlasten ook het gevolg zijn van zettingen. De literatuur en de bijzonderheden van de methode worden besproken. De resultaten zijn vervolgens gevalideerd aan de hand van een geïnstrumenteerde proefbelasting. De ontwikkelde methode is in staat om de gemeten last-zakkingscurve en de axiale belastingen langs de paal te reproduceren.

Voor het voorspellen van de door de tunnel geïnduceerde grondbewegingen is, een nieuwe methode ontwikkeld met de nadruk op tunnelboormachines (TBMs). Er is gezocht naar een antwoord op de volgende vraag: Wat zijn de krachten in het ontgravingsgebied van een tunnel? Dit heeft geleid tot een algemeen overzicht van de processen rond een TBM, de fysische mechanismen die betrokken zijn en de numerieke technieken die gebruikt worden om ze te modelleren. Een literatuurstudie laat zien hoe de rekenmodellen die worden

gebruikt om een TBM tunnel te simuleren zijn geëvolueerd van een eenvoudige grondontspanning berekening tot berekeningen van de drukken bij verschillende elementen van een TBM.

Een specifiek kenmerk van TBM tunneling is dat elke stap in de opgravingscyclus wordt uitgevoerd door middel van mechanische of hydraulische systemen. De interactie tussen de boormachines en de omringende grond volgt uit het gebruik van deze systemen voor graven en ondersteuning van de grond rond de tunnel. Het is vanzelfsprekend dat voor elk van deze acties een reactie van de grond nodig is om evenwicht te bereiken. Echter, deze mechanismen zijn vaak beschreven binnen geïdealiseerde kaders die niet goed de belangrijke kenmerken van de grondreacties weergeven zoals die in het veld zijn waargenomen. Daarom zijn deze kaders aangepast om tot een betere beschrijving te komen. Twee methoden zijn voorgesteld om de fase van groutinjectie en de fase van specieconsolidatie rond de tunnelringen achter een TBM te evalueren. De methodologie is vervolgens gevalideerd voor een geïnstrumenteerde case study van een tunnel in Nederland. Het model kon de grout-druk rond de uitgraving reproduceren, en beschrijft de maaiveldzakkingen beter dan de traditionele ´stress release' methode.

Ten slotte zijn deze twee afzonderlijke studies gecombineerd tot een ontwerpgereedschap om de gevolgen van paal tunnel interactie te berekenen. De eenvoudige methodiek werd uitgebreid met een meer realistisch model voor de paalreactie. De belasting mobilisatiefuncties kunnen nu het bezwijken van een paal goed beschrijven en hebben verschillende paden voor belasting en ontlasting. De paalzakkingen kunnen direct worden verkregen door te berekenen wanneer evenwicht wordt bereikt, en hoeven dus niet meer te worden opgelegd. Op dit moment zijn er echter geen geïnstrumenteerde proefbelastingen, waar de paalzakkingen en de axiale krachten tegelijkertijd zijn gemeten met de grout drukken rond een tunnelboormachine. Wel blijkt de methodologie de fundamentele mechanismen van paal tunnel interactie zoals beschreven in het eerste literatuuronderzoek te kunnen simuleren.

1. Introduction

Pile tunnel interaction is a relatively new problem. Tunnels have been a part of our physical infrastructure since 2200 BC, when an underground passage was built between a palace and a temple in the ancient city of Babylon, in what is today Iraq. Most ancient tunnels were used for religious ceremonies, water supply and drainage. In Roman times (753 BC to 476 AD) tunnels were also built for mining operations, hydraulic systems, and roads. Despite this early start, tunnel construction was laborious and critically limited to ground conditions where hand tools were applicable. These limitations were only surpassed in 1679, when engineers started to use gun powder to break through the ground of the Malpas tunnel, a navigation channel in France (ITA, 2016).

The 19th century saw the birth of the first public steam-powered railway lines in England, and in a few decades, a boost in railway lines between the major urban centres across Europe. In 1863, the first underground railway was inaugurated in London, a city whose population had exploded from 550 thousand in 1700 to 5.5 million by 1891, being the world largest city by then (Bairoch and Goertz, 1986). By the end of the century four other cities had metro systems: Budapest, Glasgow, Chicago and Paris. In 2014 there were metro systems in operation in 157 cities of 56 countries worldwide (UITP, 2015).

These new inner-city tunnels forced the technologies of inter-city railways into an urban environment, where there was a dense layout of houses and factories, and any disturbance could affect thousands of residents. Cut-and-cover tunnels, built through an open pit, would cause major disruptions along the whole tunnel alignment, so bored tunnels became a preferable choice, but had to place at considerable depths in order to limit the ground movements at the surface. These features kept most metro systems along the main transportation arteries

of the cities, limiting the extent to which they could really permeate the urban space.

The foundation technologies that supported these urban buildings had also been evolving for thousands of years. In any place where the shallow ground layers could not bear the construction loads, piles were used to mobilize deeper and more resistant layers. There are archaeological sites around the Alps with piled dwellings dating back to 5000 BC (UNESCO, 2011). One of the first written references to piles comes from the book *De architectura* written by the roman engineer Marcus Vitruvius around 30 BC: "*If solid ground is not found ... the place must be excavated … and piles … must be driven with a machine, as close to each other as possible*". These roman recommendations were applied throughout Europe, and piles can still be found in relatively good conditions 16 centuries after construction (Ulitskii, 1995). However, most piles were just a couple of meters long. In the Netherlands, 12.5 m long piles were used to build Amsterdam's city hall in the middle of the 17th century (Cultural Heritage Agency of the Netherlands, 2016).

In this former set-up, most piles were a few meters long, resting along ground layers that were far from deep-level bored tunnels, which were scarcely distributed along the city. But since then, technological advancements have brought these two elements of infrastructures closer together. Construction technology incorporated materials such as cast iron, steel and reinforced concrete, significantly increasing the average size of buildings and the required pile depths. Steel frame structures could now reach hundreds of meters, requiring piles up to 100 m long (Wang et al., 2013).

The 1960's saw the development of new concepts of tunnel support, incorporating shotcrete technology (Rabcewicz, 1964), which would unfold the sequential excavation method of tunnelling. Also in this decade, the first pressurized tunnel boring machine was used at the Paris RER Metro using compressed air. The idea was eventually discontinued, but it inspired the future slurry machines (Robbins, 2013). These breakthroughs boosted the construction of urban tunnels worldwide.

So the overall set-up had changed, piles were now resting on deeper layers to support the ever rising buildings, while tunnels became feasible in a much wider range of conditions, allowing metro systems to expand through the city and be excavated in shallower ground layers. The zones of influence of these systems would eventually intersect, raising concerns about possible detrimental consequences of their interaction. There are relatively few studies on the matter. By the year 2000 there were just about a dozen published papers. Since then the

topic has gained recognition as an important geotechnical and structural problem to be solved.

The objective of this thesis is to analyse how a new tunnel might affect an existing pile, to explain the mechanism through which it happens and to recommend a methodology to calculate the consequences for engineering design.

1.1. Thesis outline

Chapter 2 lays down the current state of knowledge on pile tunnel interaction through an extensive literature review. The first two sections expose the findings of case studies, full-scale tests and scaled models. The results from these physical models are then set-up in a framework where they can be compared and contrasted, revealing patterns that were not distinguishable among individual studies. Section 2.5 presents the different calculation methods that have been employed to compute the consequences of pile tunnel interaction, and their main results. Based on this accumulated knowledge, Section 2.6 presents the first attempt of this study to propose a methodology to calculate the consequences of pile tunnel interaction. This simplified methodology, and its promising results, gave the direction for the analysis of piles and tunnels proposed in the next chapters.

Chapter 3 proposes a new and accessible framework for pile analysis, where the model to calculate the pile settlements and load transfer mechanism for any loading condition can also cope with an arbitrary profile of ground settlements. The subject of deep foundations is reviewed briefly, leading to a decision to propose an adapted version of the load transfer method, and to implement it within a regular spreadsheet software. The details of the method and proposed load mobilization functions are discussed, followed by a validation of the method for an instrumented pile load test and the discussion of some conceptual results.

Chapter 4 presents a new take on the problem of estimating the ground displacements around a tunnel, with a specific focus on pressurized tunnel boring machines (TBMs). The chapter tries to approach the problem through a basic question: What are the forces acting on the excavation perimeter of a tunnel? This led to a general review of the processes around a TBM, the physical mechanisms involved, and the numerical techniques used to model them. Two new methodologies are then proposed to evaluate the stages of grout injection and grout consolidation around the tunnel lining at the back of a TBM. The methodology is then validated for an instrumented case study of a tunnel in The Netherlands.

Chapter 5 combines the methods from the previous two chapters into a design tool to compute the consequences of pile tunnel interaction. Some examples are discussed with a partial validation of the methodology. It will be shown that the methodology is able to reproduce the fundamental mechanisms identified in the literature.

Chapter 6 presents the conclusion and recommendations for future research projects.

2. Investigating Pile Tunnel Interaction

Chapter 2 until Section 2.4, is based on the Technical Paper: Dias, T.G.S., Bezuijen, A., 2015. Data Analysis of Pile Tunnel Interaction. ***Journal of Geotechnical and Geoenvironmental Engineering*** *141.*

The growth of the world's urban population and mobility needs in recent decades has triggered a demand for infrastructure within the context of a valuable and densely constructed urban space. The use of underground space can reduce surface congestion, notably through transportation infrastructure, such as subway lines and underground roads. These systems normally become necessary in cities with more than one million residents. The latest United Nations (UN) census reported almost 300 cities worldwide with such a population (UN, 2012). Because most of these cities are still developing their infrastructure, it is expected that the demand for underground structures will continue to increase throughout the world.

However, the context that generates this demand is also a limitation for several solutions. To be technically and socially accepted, an underground construction cannot disrupt traffic routes for too long or jeopardize the structural integrity or serviceability of surface structures. This has prompted the reduction in the number of cut-and-cover tunnels, the development of new methods to reduce the outline of deep excavations (Dias et al. 2015), and efforts to quantify the response of buildings to ground movements induced by excavations (Mair, 2011).

When a structure is supported by shallow foundations, the relative soil-building stiffness and the soil-foundation interface affect the magnitude of surface

settlements induced by tunnels (Farrell and Mair, 2011) and deep excavations (Elshafie et al., 2013) and how they are transferred to the structure. These effects are normally translated into adjusted values of distortion and lateral strain, which are used in design charts to estimate building damage (Son and Cording, 2005).

In the case of deep foundations, the interaction is more complex. The load transfer mechanism, ultimate bearing capacity, and load-settlement response of a pile can be affected by an excavation. To investigate this condition, a series of previously published tests and case studies is presented that focus on the effects of new tunnels on existing piles, herein referred to as PTI (pile-tunnel interaction). Their results are evaluated quantitatively to explore the reproducibility of different variables and postulate possible interaction mechanisms. For an analysis of piles in interaction with deep excavations the reader is referred to Korff (2012).

A related issue is to understand the consequences of constructing new piles over existing tunnels. It would be illuminating to present a concise review of this parallel condition, even though it is not the focus of this thesis. A known case study is the 1987 redevelopment of the Lee House in London over two small cast-iron tunnels that underwent minor and non-detrimental changes on their diameter and horizontal alignment due to the construction and loading of several under-reamed piles (Benton and Phillips, 1991). This issue has also been analysed using numerical methods (Schroeder, 2002) and physical tests. Photoelastic tests showed the locations at which driven piles were likely to have less effect on a tunnel (Standing and Leung, 2005). Centrifuge tests on sand revealed a localized increase in the lining bending moments when the piles were loaded (Chung et al., 2006), while on clay it was shown that the tunnel moved downward and away from the pile, in inverse proportion to the pile-tunnel lateral distance (*Ld*) (Yao et al., 2008).

Among the possible tools for PTI investigation, case studies can provide data that are not affected by scale effects or simplifications of layout and geology. However, operating structures are normally involved, and the risks of failure, structural damage, or just a delayed construction schedule will limit the possible tests in a case study. Even if the construction is instrumented, different layouts or construction conditions will normally not be adjusted to reach limit conditions, which in turn cannot be verified. An alternative is to create a full-scale pile test over the alignment of a tunnel construction, most likely outside the urban perimeter. The limitations for the tunnel remain, but the pile can be tested with any desirable layout and working load (*WL*) that complies with the tunnel depth and diameter.

Reduced-scale physical models can provide a consistent framework of soil constituents, drainage conditions, and construction procedures to test different layouts. However, soil stiffness and resistance have a nonlinear dependence on the stress level (Mayne et al., 2009), which hinders the possibility of adjusting the model results to prototype scale. The stress level on the model can be increased in a centrifuge test, retaining some scaling issues for the soil dilatancy but providing scalable results. In both cases, all the different aspects of conventional and mechanized tunnels are often replaced by the convergence of a model tunnel, which normally is already in the soil when the model is assembled.

For all these methods, a collective analysis depends on a common method to characterize the results and test conditions. Therefore, the geometric layouts of all PTI problems are reported according to the parameters described in Figure 2.1, considering all depths in reference to the ground surface. Pile settlement is presented as a positive displacement, and the bending moments, when reported, are described by the direction of bending. The axial forces along the pile are assumed positive for compression, and, unless stated otherwise, the pile working load (*WL*) is constant and positive. It is worth noting that any redistribution of forces, through changes of shaft friction or end bearing, must be counterbalanced to remain in equilibrium with the external load, even though just one of these changes may be reported.

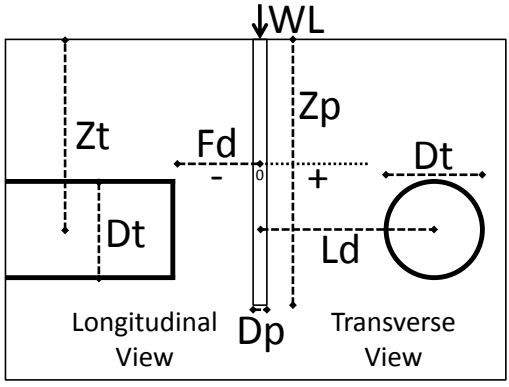

Figure 2.1. Parameters that define the geometric layout of a PTI problem

2.1. Case studies and full-scale tests

In 1989 an escalator tunnel (*Dt* = 8.25 m) was built to connect Islington High Street to the Angel Underground Station in London, U.K., between under-reamed piles Figure 2.2a supporting the Angel Square development: a seven-story building with two basement levels that was also under construction (Lee et al., 1994). The piles pass through 28 m of London Clay, but are founded in the

underlying Lambeth group. Tests on prototype piles (Dp = 0.75 m, Zp = 12.1 m) revealed that the use of a bitumen slip coating could reduce the shaft friction by 75%, diminishing the possible negative friction (Whitworth et al., 1993). The solution was implemented, and field measurements indicated that the piles followed horizontal ground movements, acting as slender elements, and that the preliminary design predictions were conservative.

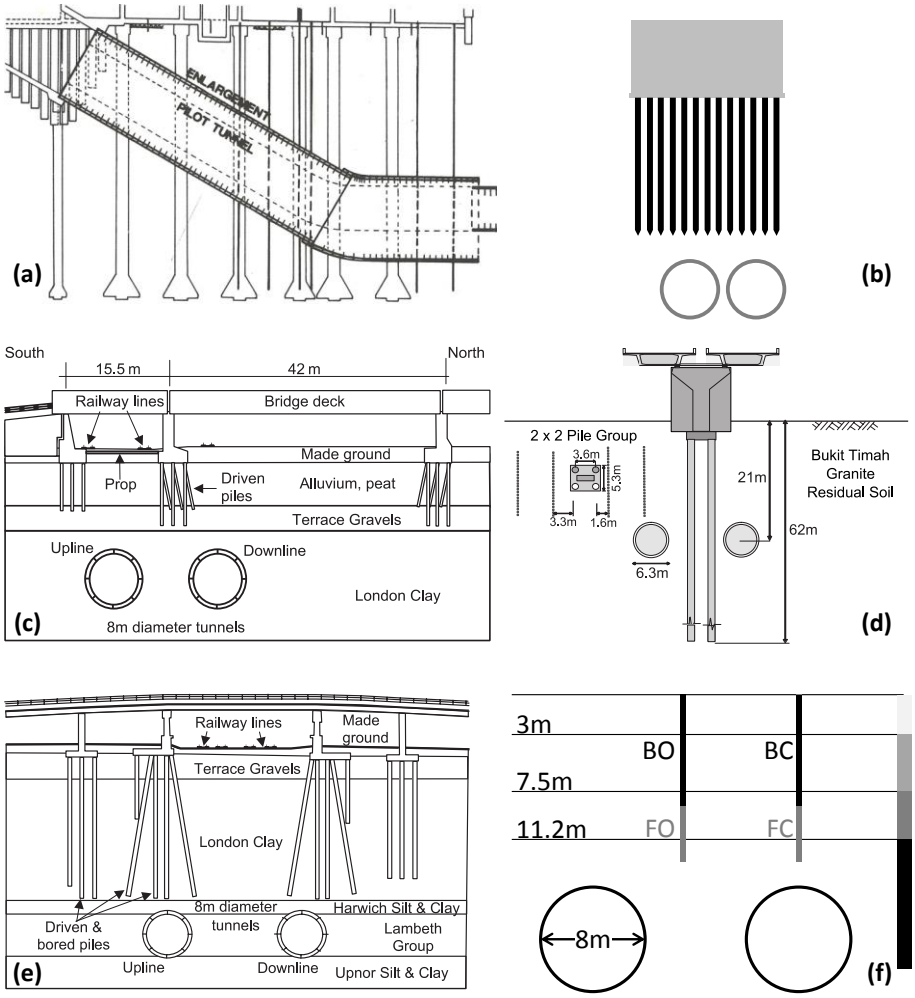

Figure 2.2. Examples of case studies and full-scale tests: (a) Angel Station escalator tunnel, U.K.; (b) Higashi-Shinagawa roadway bridge, Japan; (c) Renwick Road Bridge, UK; (d) MRT North East Line viaduct bridge, Singapore; (e) Ripple road flyover, U.K.; (f) full-scale test on the Channel Tunnel Rail Link, UK.

On the Island Line of the Mass Transit Railway in Hong Kong, China, the construction of deep excavations and tunnels through mixed ground induced settlements of variable magnitude that, however, caused little or no damage to several monitored pile-supported buildings (Forth and Thorley, 1996).

The Jubilee Line Extension project planned three parallel tunnels, excavated mostly in London clay (Dt = 8.7 to 11.7 m), close to the Bridge House in London, U.K. The structure was supported by bored and under-reamed piles, and there was concern that a lift shaft, added to the main building after its construction, could part from the building as a result of relative settlements (Selemetas et al., 2002). A jacking system was installed on the shaft basement and operated in response to a precise levelling system. The construction of the pilot tunnel and consolidation induced minimal settlements, but the enlargement of the station tunnel demanded jacking operations, compensating the induced movements.

Both tunnels (Dt = 7.25 m; Zt = 29 m) of the Rinkai Line railway in Tokyo, Japan, were excavated just 3 m below the piles of the Higashi-Shinagawa Bridge (Takahashi et al., 2004). The piles were founded on a gravel layer, while the tunnels were being excavated in an underlying dilluvial stiff sand layer. The slurry pressure tunnel boring machines (TBMs) were in a clearance of 2-0.5 m (Figure 2.2b), with the first tunnel excavated 100 m ahead of the second tunnel. Monitoring systems for surface and subsurface ground movements, shield chamber pressures, lining forces, and deformations were implemented because the contract limited the bridge settlement to 9 mm and the distortion to 1:15000. In a span of 80 m along the bridge section, grout was injected from the first tunnel to compensate the ground loss, which resulted in a maximum settlement of 4 mm on the bridge and 4.3 mm on the surface.

Three piled bridges of the Channel Tunnel Rail Link in London, U.K., were analysed based on the mechanism proposed by Selemetas et al. (2005), namely, that the tunnel causes a stress relief around the pile tip, mobilizing shaft friction and causing settlements (Jacobsz et al., 2005). The Renwick Road Bridge (Figure 2.2c) was supported by end-bearing piles on the Terrace gravel overlaying the London Clay where the tunnels were excavated. The piles were at different distances to the tunnel; thus, differential settlements were the main concern. The pile settlements were assumed to follow the predicted greenfield soil settlements at the pile tip level, and this was later confirmed by measurements. The calculated pier rotation could be supported by the concrete props between the two foundation blocks; thus, no intervention was necessary. This was not the case for the Ripple Road flyover (Figure 2.2e), which was supported by friction piles. Because the pile depths were unknown, the Terrace gravel layer was grouted to enhance the shaft friction and create a more rigid

zone underneath the pile cap, which could act as a raft. On the A406 viaduct, a different approach was tested. The axial and bending strains in the pile body of the friction pile were calculated considering a compatibility with the ground movements along the pile shaft. The structural stability of the viaduct was analysed making various assumptions about the foundation settlements (Zanardo et al., 2004), but the measurements ultimately indicated that the structure settled similarly to the surface.

One of the few case studies with in-pile instrumentation, and possibly the one most referred to, is the piled viaduct bridge on the North East Mass Rapid Transit (MRT) Line in Singapore (Figure 2.2d). The structure was planned together with the twin tunnels (Dt=6.3 m), which led to an unusual construction pattern where the piles were built before but loaded after the tunnels' excavation (Coutts and Wang, 2000). The axial forces along the piles of three piers along the viaduct increased owing to the tunnel excavation. The maximum axial force occurred when the tunnel was beside the pile section and decreased as the excavation proceeded. This phenomenon was more pronounced in the pile closer to the tunnel being excavated. The same project was analysed again, focusing on Pier 20 of the bridge, where the piles were significantly deeper than the tunnels: Zp = 62 m, while Zt = 21 m (Pang et al., 2005b; Pang, 2006). The ground was composed mostly of residual soils from granite. The first tunnel [volume loss (VL) = 1.38%] was built 300 m ahead of the second one (VL = 1.67%). For the first tunnel the axial force in the piles started to increase when the TBM was still at four diameters behind the pile section ($Fd = -4 \cdot Dt$). For the second tunnel the axial force reached almost 50% of the structural pile capacity. The transversal bending moments were toward the tunnel. The longitudinal moments were away from the drilling direction and always with a magnitude smaller than the transversal ones. Both moments reduced for Fd>0. When the piles were loaded, minimal changes took place in both bending moments but a significant increase, although with the same profile, occurred in the axial force. In general, all tunnelling-induced effects increased with VL and decreased with Ld.

Full-scale tests will be described in what follows. Their geometric layout parameters are listed in Table 2.1. Each test is identified by the study reference, identification code, geometric parameters, and ratio of working load to ultimate bearing capacity (WL/UBC). A full-scale test was prepared along the alignment of the second Heinenoord Tunnel in Heinenoord, Netherlands. A set of wooden and concrete piles was installed in clay columns created on site to reproduce the typical conditions of Amsterdam, where a layer of 10-12 m of clay overlies dense sand. On the test site, the clay layer was just 4-5 m thick (Kaalberg et al., 2005). The twin tunnels (Dt = 8.3 m; VL = 1-2%) had a clearance of 8 m. The pile

settlements defined three zones around the tunnel (Figure 2.3): where they were slightly larger than (Zone A), equal to (Zone B), or smaller than (Zone C) the surface settlements. Figure 2.4 presents the results of CPT (a) and pile load tests (b), whose locations were not reported. It is possible to notice small differences before and after the tunnel excavation. Based on those tests, it was concluded that for *Ld* > *Dt*, no significant stress relief on the pile toe or change in pile capacity should be expected.

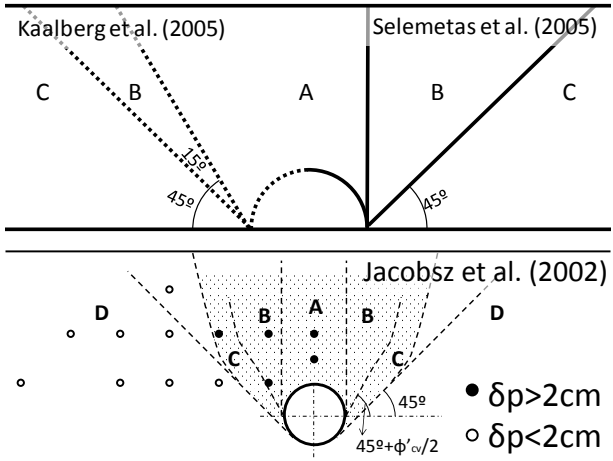

Figure 2.3. Zones of relative pile/soil surface settlements in different studies

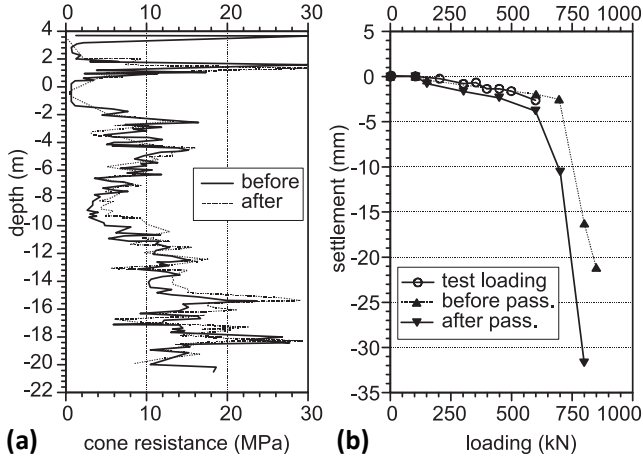

Figure 2.4. (a) CPT; (b) pile load test results on a full-scale test

Table 2.1. Geometric layout of centrifuge and full-scale physical tests

Reference	I.D.	*Dt* (m)	*Zt* (m)	*Dp* (cm)	*Zp* (m)	*Ld* (m)	*WL/UBC* (-)
(Bezuijen and Van der Schrier 1994) (Hergarden et al. 1996)	BH1	7.00	18.00	40	18.00	5.10	0.70
	BH2	7.00	18.00	40	18.00	6.70	0.70
	BH3	7.00	18.00	40	18.00	9.90	0.70
	BH4	7.00	18.00	40	18.00	16.30	0.70
	BH5	7.00	23.00	40	18.00	5.10	0.70
	BH6	7.00	23.00	40	18.00	6.70	0.70
	BH7	7.00	23.00	40	18.00	9.90	0.70
	BH8	7.00	23.00	40	18.00	16.30	0.70
(Hergarden et al. 1996)	HE1	7.00	14.50	40	18.00	5.10	0.75
	HE2	7.00	14.50	40	18.00	6.70	0.75
	HE3	7.00	14.50	40	18.00	9.90	0.75
	HE4	7.00	14.50	40	18.00	16.30	0.75
(Loganathan et al. 2000)	LO1	6.00	15.00	80	18.00	5.50	0.50
	LO2	6.00	18.00	80	18.00	5.50	0.50
	LO3	6.00	21.00	80	18.00	5.50	0.50
(Ran 2004)	RA1	6.00	15.00	*126	23.50	6.00	0.00
	RA2	6.00	15.00	*126	23.50	9.00	0.00
	RA3	6.00	15.00	*126	23.50	12.00	0.00
	RA4	6.00	15.00	*126	15.00	6.00	0.00
	RA5	6.00	15.00	*126	10.00	0.00	0.00
	RA6	6.00	15.00	*126	10.00	5.00	0.00
	RA7	6.00	15.00	*126	23.50	17.00	0.00
(Ong et al. 2005)	ON1	6.00	15.00	*126	20.50	6.00	0.00
(Ong et al. 2006)	ON2	6.00	15.00	*126	23.50	6.00	0.00
(Hartono et al. 2014)	HA1	6.00	21.00	130	15.00	0.00	0.00
	HA2	6.00	21.00	130	15.00	3.00	0.00
	HA3	6.00	21.00	130	15.00	12.00	0.00
(Jacobsz 2002)	JA1	4.50	21.45	90	15.00	0.00	0.65
	JA2	4.50	21.45	90	15.00	3.75	0.82
	JA3	4.50	21.45	90	15.00	7.50	0.50
	JA4	4.50	21.45	90	15.00	11.25	0.42
	JA5	4.50	21.45	90	15.00	15.00	0.60
	JA6	4.50	21.45	90	15.00	18.75	0.50
	JA7	4.50	21.45	90	18.75	3.75	0.53
	JA8	4.50	21.45	90	18.75	7.50	0.50
	JA9	4.50	21.45	90	18.75	11.25	0.47
	JA10	4.50	21.45	90	18.75	15.00	0.50
	JA11	4.50	21.45	90	18.75	22.50	0.63
	JA12	4.50	21.45	90	16.88	0.00	0.50
(Feng et al. 2002)	FE1	6.00	16.00	*100	24.00	5.00	0.00
	FE2	6.00	16.00	*100	24.00	5.00	0.00
	FE3	6.00	16.00	*100	24.00	5.00	0.00
	FE4	6.00	16.00	*100	24.00	9.00	0.00
	FE5	6.00	16.00	*100	24.00	9.00	0.00
	FE6	6.00	16.00	*100	24.00	7.00	0.00
	FE7	6.00	16.00	*100	16.00	5.00	0.00
	FE8	6.00	16.00	*100	13.00	5.00	0.00
(Lee et al. 2003)	LE1	6.00	9.00	106	27.00	4.50	0.00

(Lee and Chiang 2007)	LE2	6.00	9.00	106	27.00	4.50	0.25
	LE3	6.00	15.00	106	27.00	4.50	0.00
	LE4	6.00	15.00	106	27.00	4.50	0.25
	LE5	6.00	15.00	106	27.00	4.50	0.50
	LE6	6.00	21.00	106	27.00	4.50	0.00
	LE7	6.00	21.00	106	27.00	4.50	0.25
	LE8	6.00	27.00	106	27.00	4.50	0.00
	LE9	6.00	27.00	106	27.00	4.50	0.25
	LE10	6.00	27.00	106	27.00	4.50	0.50
(Marshall 2009)	MA1	4.65	13.65	90	7.20	0.00	0.63
	MA2	4.65	13.65	90	6.83	9.75	0.63
	MA3	4.65	13.65	90	6.90	4.58	0.63
	MA4	4.65	13.65	90	6.30	4.88	0.63
(Ng et al. 2013)	NG1	6.08	19.60	80	19.60	4.56	0.67
	NG2	6.08	19.60	80	19.60	4.56	0.67
	NG3	6.08	12.00	80	19.60	4.56	0.67
(Boonsiri and Takemura 2014) (Boonsiri and Takemura 2015)	BO1	7.00	21.00	100	14.00	7.00	N.A.>0
	BO2	7.00	21.00	100	14.00	10.50	N.A.>0
	BO3	7.00	14.00	100	14.00	7.00	N.A.>0
	BO4	7.00	21.00	100	21.00	7.00	N.A.>0
	BO5	7.00	21.00	100	21.00	10.50	N.A.>0
	BO6	7.00	14.00	100	21.00	7.00	N.A.>0
(Kaalberg et al. 2005)	KA1	8.30	19.75	N.A.	19.75	12.50	± 0.5
	KA2	8.30	19.75	N.A.	19.75	8.25	± 0.5
	KA3	8.30	19.75	N.A.	7.00	4.00	± 0.5
	KA4	8.30	19.75	N.A.	7.00	8.25	± 0.5
	KA5	8.30	19.75	N.A.	7.00	16.50	± 0.5
	KA6	8.30	19.75	N.A.	19.75	29.00	± 0.5
	KA7	8.30	19.75	N.A.	19.75	25.00	± 0.5
	KA8	8.30	19.75	N.A.	7.00	21.00	± 0.5
	KA9	8.30	19.75	N.A.	7.00	8.00	± 0.5
	KA10	8.30	19.75	N.A.	7.00	0.00	± 0.5
	KA11	8.30	19.75	N.A.	15.00	4.00	± 0.5
(Selemetas 2005) (Selemetas et al. 2005)	SE1-T1	8.00	18.90	48	13.00	0.00	0.50
	SE2-T1	8.00	18.90	48	13.00	9.00	0.50
	SE3-T1	8.00	18.90	48	8.50	0.00	0.50
	SE4-T1	8.00	18.90	48	8.50	9.00	0.50
	SE1-T2	8.00	18.90	48	13.00	16.00	0.50
	SE2-T2	8.00	18.90	48	13.00	7.00	0.50
	SE3-T2	8.00	18.90	48	8.50	16.00	0.50
	SE4-T2	8.00	18.90	48	8.50	7.00	0.50

Note: N.A. is inserted whenever the data was not available on the reference;
* These are squared piles and their *Dp* values represent the sizes of squared piles

Another full-scale test was conducted along the new Channel Tunnel Rail Link in Essex, U.K., during the construction of twin tunnels with an earth pressure balance shield (*Dt* = 8 m, *Zt* = 18.9 m, *VL* = 0.2-0.5%) on a location with 3 m of fill, alluvium to 7.5 m, Terrace gravel to 11.2 m, and London Clay underneath it,

with the groundwater level at 4 m depth (Selemetas 2005; Selemetas et al. 2005). Four driven cast-in-situ piles (Dp = 48 cm) were installed and loaded to 50% of their capacity: two end-bearing piles (Zp = 8.5 m) in the Terrace gravel and two friction piles (Zp = 13 m) in the London Clay, all instrumented with tip load cells (Figure 2.2f). The recorded settlements were also used to define three zones of relative pile/soil settlement around the tunnel, but with a different angle compared to Kaalberg et al. (2005), between Zones A and B (Figure 2.3). This might indicate that these angles are a function of the soil shearing resistance and the tunnel *VL*. The analysis of pile forces was hindered owing to head load variations, but general patterns could be captured. The base load decreased until Fd = 0 and increased with tail grout injection. The piles' axial force profile decreased in Zone A but increased for Zones B and C, whereas the bending moments were negligible. The deflection measurements were hindered by the effect of temperature fluctuations on the instruments.

These case studies and full-scale tests outlined the demand for a proper analysis of PTI. Some cases reported negligible and non-detrimental effects, but preventive measures were also necessary at times. Instrumented cases showed that not only settlements but also structural forces were induced in the piles, normally related to the tunnel *VL* and its relative position. It was also shown that the sequential process of a tunnel excavation may have stages that are more critical than the final plane-strain condition. More recent tests indicated that tunnels could induce a reduction in the pile base capacity, which should be compensated by a mobilization of shaft friction. If the ultimate shaft capacity is reached, significant settlements may occur until the end-bearing capacity is remobilized. This can differentiate the response of end-bearing and friction piles by their initial mobilization of shaft friction.

2.2. Small-scale physical models

The small-scale physical models will be described in this section on the basis of their qualitative results. The specific test conditions of each model are listed in Table 2.2. Among these conditions is the type of model tunnel used in each test, which is a determining factor for the induced stress/displacement field owing to the imposed contracted shape. In most cases, the applied *VL* in the models is much larger than what is normally achieved during a TBM tunnelling operation in the field. It should also be noted that some tests used a frame to load more than one pile simultaneously, which might have caused a redistribution of pile loads during tunnelling. Schemes and photos of the different model tunnels can be found in Figure 2.5.

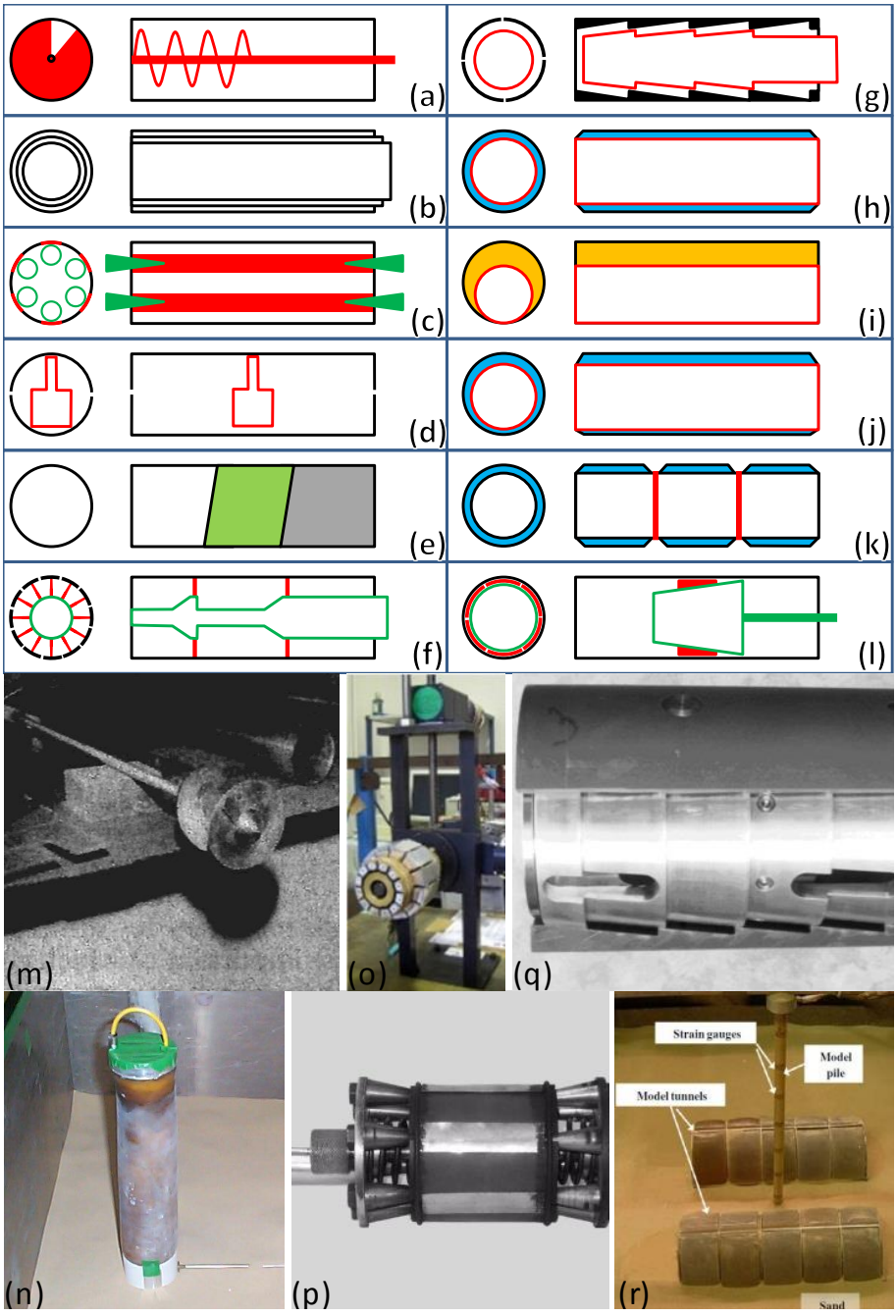

Figure 2.5. Schemes and photos of different model tunnels

Table 2.2. General test conditions of the small-scale tests

Type	Reference	Test conditions following the sequence: **I.** Materials and conditions; **II.** Model tunnel; **III.** Model pile; **IV.** Test routine.
1g test	(Morton and King 1979)	**I.** 1g test with dry coarse silt and fine sand. **II.** Hollow tube jacked in the soil from where a screw was rotated to excavate the model tunnel (Figure 2.5a, m). **III.** Wooden piles. **IV.** The piles were pushed in the soil and a constant load of around 1/3 of the ultimate load was maintained while the tunnel was excavated. A flow of soil through the screw was detected.
	(Ghahremannejad et al. 2006)	**I.** 1g test with rigid surface plate for surcharge and dry dense Sydney sand. **II.** Four concentric aluminium cylinders that are retracted simulating *VL* = 2, 4 and 6% (Figure 2.5b). **III.** Aluminium tube piles. **IV.** Piles and model tunnel were placed during sand pouring, the piles were then loaded and the cylinders were retracted.
	(Lee and Yoo 2006) (Lee and Bassett 2007) (Lee and Yoo 2008)	**I.** 1g plane strain test with a multi-size mixture of synthetic aluminium rods. **II.** A cylinder with six moveable segments supported by a shim that could move inducing *VL* = 4 to 20% (Figure 2.5c, p). **III.** Aluminium pile rows. **IV.** The piles were loaded and the volume loss was progressively increased while the displacements were captured by close range photogrammetry on reflective markers.
	(Broere and Dijkstra 2008)	**I.** Photoelastic test with crushed glass at medium compaction and a surcharge steel beam. **II.** Two half cylinders with a small motor inside to retract inducing *VL* = 0.6% (Figure 2.5d). **III.** Stainless steel pile rows with two piles each. **IV.** The piles were pushed, the surcharge was applied and the tunnel was retracted.
	(Meguid and Mattar 2009)	**I.** 1g test with a mix of sand, clay and cement. **II.** Aluminium lining (Figure 2.5e). **III.** Steel bars. **IV.** A casing was pushed in the model, the soil was removed and the aluminium lining was

		installed. The casing was then removed and the gap was allowed to close on the lining.
	(Shahin et al. 2009) (Shahin et al. 2011)	**I.** 1g plane strain test with multi-size mixture of aluminium rods. **II.** 12 segments around a shim that could simulate excavations with fixed centre or fixed invert and *VL* = 0.20 - 15.36% (Figure 2.5f, o). **III.** N.A. **IV.** N.A.
n-g tests, piles in clay	(Bezuijen and van der Schrier 1994) (Hergarden et al., 1996)	**I.** 40 g test with 2 layers of overconsolidated Speswhite kaolin clay, a thin layer of Eastern Scheldt sand, 2 layers of normally consolidated clay and sand. **II.** 4 segments of a cylinder around a core that could be moved through an indentation in their contact, simulating a volume loss up to 8% (Figure 2.5g, q). **III.** Closed aluminium tubes. The piles were connected by springs to a loading frame **IV.** Piles were placed 60 cm (prototype scale) above their final level and at 40g the piles were driven to their final depth. A load of 70% the driving load was sustained through a system of springs while the volume loss was induced. After spin-up of the centrifuge the excess pore pressure was dissipated before the volume loss increments.
	(Loganathan et al. 2000)	**I.** 100 g test with Kaolin clay pre-consolidated to 600 kPa. **II.** Rigid cylinder concentrically enveloped by a rubber membrane and oil filling the gap (Figure 2.5h). **III.** Brass tubes with a plastic end cap and an epoxy resin coating. **IV.** Piles installed at 1g after the consolidation step. After spin-up of the centrifuge the excess pore pressure was dissipated before the volume loss increments. After a 1% volume loss increment the excess pore pressure was stabilized for 8 days (prototype scale) before the next increment.
	(McNamara et al. 2003)	**I.** 100g test with Speswhite Kaolin clay pre-consolidated to 500 kPa and swelled to 250 kPa. **II.** Latex membrane filled with compressed air (Figure 2.5e).

		III. Treated steel. **IV.** Piles were augered with thin walled stainless steel tubes and installed at 1g and the tunnel air pressure was reduced to atmospheric conditions is 2-3 min.
	(Ran 2004)	**I.** 100g test with normally consolidated Malaysian kaolin clay. **II.** High density polystyrene foam inside a brass foil. The foam is dissolved in flight by the injection of a solvent (Figure 2.5e). **III.** Hollow square aluminium tubes with a thin layer of epoxy resin to protect the instrumentation. **IV.** It was not possible to enforce a precise control of *VL* neither at short term nor long term, as the brass lining continued to deform during consolidation steps.
	(Ong et al. 2005)	**I.** 100g test with Malaysian kaolin clay. **II.** Foam over a rigid steel cylinder and inside a rubber membrane. The foam is dissolved in flight and the final volume loss (3.3%) is controlled by the steel cylinder (Figure 2.5i). **III.** Square aluminium tubes. **IV.** The piles were installed at 1g and after the model spin-up the foam was dissolved.
	(Ong et al. 2006)	The same conditions as Ong et al. (2005) but with *VL* = 6.6 %
	(Hartono et al. 2014)	**I.** 100g test with lightly over-consolidated kaolin clay. **II.** Stainless steel cylinder placed eccentrically to the exterior latex membrane with water filling the gap (Figure 2.5j). **III.** Aluminium pipes. **IV.** The piles were installed at 1g and after the model spin-up and consolidation the tunnel volume loss was induced.
n-g tests, piles in sand	(Jacobsz 2002)	**I.** 75g test with Leighton Buzzard (fraction E) silica sand poured at a constant drop height and flow rate achieving a uniform relative density of 75%. **II.** Brass mandrel enveloped by a rubber membrane with water filling the gap (Figure 2.5h). **III.** Machined out of aluminium alloy tubing with a 60° conical tip.

	IV. The piles were installed at 1g, 1.875 m above their final level. The rest of the pile penetration was achieved in-flight.
(Feng et al. 2002)	**I.** 100g test with dry Toyoura sand poured by air pluviation at a constant drop height achieving 80% relative density. **II.** The same as Ran (2004). **III.** Hollow square aluminium tubes, already in place during sand pouring. **IV.** N.A.
(Lee et al. 2003 (Lee and Chiang 2007)	**I.** 100g test with Quartz sand pluviated with constant height and flow rate achieving 65% relative density. **II.** Air pressure inside a rubber bag with a filament tape (Figure 2.5e). **III.** Machined out of hollow aluminium tubes with conical tips. **IV.** The piles were placed before sand pouring and after the model spin-up the tunnel air pressure was reduced.
(Marshall 2009)	**I.** 75g test with dry fraction E silica sand poured by air-pluviation to 90% relative density. **II.** Rigid bras cylinder placed eccentrically to an exterior flexible rubber membrane with water filling the gap (Figure 2.5j, n). **III.** Half cylinders machined with a conical tip out of cylindrical aluminium rods. **IV.** The piles were placed against the front Perspex wall of the strongbox with an embedment length of 5.25 m during sand pouring, and driven to their ultimate depths in-flight. Particle image velocimetry and close-range photogrammetry techniques measured the model displacements around the pile section.
(Ng et al. 2013)	**I.** 40g test with dry Toyoura sand pluviated to 60-65% relative density. **II.** 3 to 5 cylindrical rubber bags, filled with water, and isolated by a rigid aluminium divider. Each rubber bag simulated *VL* = 1% over half a tunnel diameter (Figure 2.5k, r). **III.** Aluminium tube. **IV.** The piles were placed before sand pouring and after the model spin-up the tunnel volume loss was induced.

(Boonsiri and Takemura 2014) (Boonsiri and Takemura 2015)	**I.** 100g test with dry Toyoura sand pluviated to 80% relative density. **II.** Rubber membrane over a steel ring supported by a wedge shaped shim that could be retracted (Figure 2.5l). **III.** Acrylic model piles assembled in groups of 2x2 with 5 m of centre to centre spacing. **IV.** The piles were placed before sand pouring and after the model spin-up the tunnel volume loss was induced.

The first model, and probably the first study, on PTI (Figure 2.6a) detected how the pile response depended on its relative position to the tunnel and on the subsurface ground deformations, even though the modelling technique had an ineffective face control system, which caused failure up to the surface in most tests (Morton and King, 1979). Another test reported that pile effects increased with *Ld*. This was probably due to a stiff surcharge plate on the surface that could not comply with the settlements, resulting in an uneven load distribution (Ghahremannejad et al., 2006).

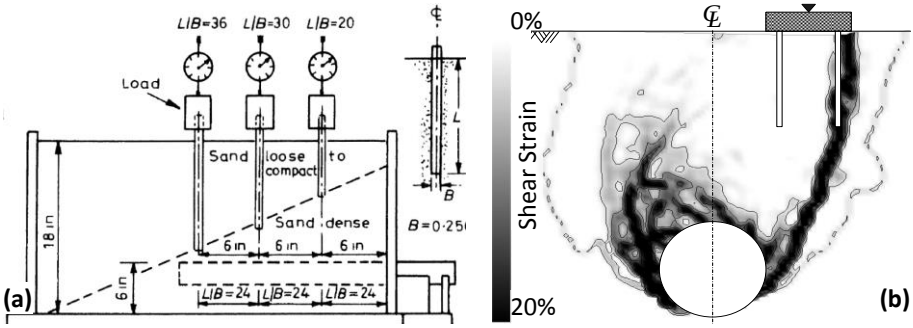

Figure 2.6. Examples of 1 g tests: (a) test setup; (b) shear strain profile on a test

In one plane-strain test, the displacements of the tunnel centre were related to PTI as the *VL* increased. For $Ld = 0$, the tunnel just settled, while for $Ld > 0$ horizontal movements away from the pile row were also induced, markedly from $Ld = 1$ to $2 \cdot Dt$ and $Zp < Zt$ (Lee and Yoo, 2006). The axial force increased for $Zp > Zt$ and decreased otherwise, in inverse proportion to *Ld*. The array of tested PTI layouts was divided by two criteria: where large settlements did or did not occur, with a distinction that the division was extended below the tunnel centreline (Lee and Bassett, 2007), and where the shear bands around the tunnel and the pile tip did or did not form a connection (Lee and Yoo, 2008). A photoelastic test, with special techniques to measure the stresses, could also

capture an increase in shear stress around the pile tips that decreased with *Ld* (Broere and Dijkstra, 2008).

In a 1 g test (Meguid and Mattar, 2009) measured lining bending moments proportional to the pile Ld, which was implicated to have occurred owing to the load transfer from the lining to the piles. However, this entails a representation of load as a scalar variable and does not explain the mechanism. When a pile raft was tested, the settlement trough was not Gaussian shaped and the position of the maximum settlement moved closer to the building loads. This asymmetry was also present on the shear strain profile (Figure 2.6b), and on the increments of axial force, because of tunnel *VL*, both of which were dependent on the pile position (Shahin et al. 2009; 2011).

The qualitative aspects and mechanisms of these small-scale studies can guide the understanding of PTI. However, the tested *VL*s normally exceeded considerably the modern tunnelling state of practice, and the quantitative data cannot be adapted to the scale of a real project.

The centrifuge tests will be described hereafter. The layout details are listed in Table 2.1 by the same parameters of the full-scale tests. The specific test conditions of each model are listed in Table 2.2. A typical layout for centrifuge tests and a real setup on a strongbox can be found in Figure 2.7.

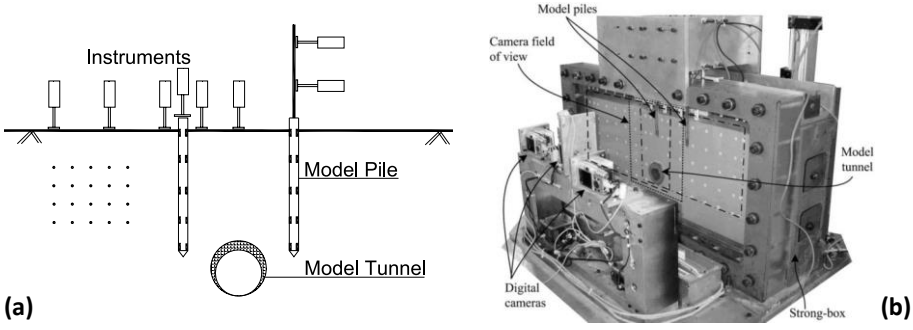

(a) **(b)**

Figure 2.7. (a) General test layout; (b) setup on a strongbox for centrifuge tests

Probably the first PTI centrifuge test was conducted in the Netherlands, where a sand layer, under saturated soft clay, typically bears both the tunnel construction and the tip of driven piles (Bezuijen & Van der Schrier, 1994; Hergarden et al., 1996). A group of four piles was loaded with a plunger, and every pile was loaded through a spring. The results indicated that the pile settlements were larger when $Zp = Zt$ but more spread when $Zt > Zp$. The piles were generally under negative friction after installation, but for very small *VL*s the pile already settled more than the soil around it, mobilizing positive friction.

When the pile settled to the maximum stroke of the loading spring, negative friction developed again. A preliminary test indicated that a higher *WL* would cause higher pile settlements. Based on these results a mechanism was proposed: the tunnel excavation causes a reduction in the high horizontal stresses generated in the sand layer during pile driving, leading to a reduction in the pile's base capacity. Following this first study, most tests were conducted with homogeneous profiles of either clay or sand, and so they will be divided accordingly.

The first study on clay tested a single pile and a 2×2 pile group with centre-to-centre spacing of 2.5 m (Loganathan et al., 2000). For the front row of the pile group an increase in the axial force was measured and associated with negative friction due to soil settlements down to the tunnel depth, which was followed by a decrease below it, only when $Zp > Zt$. The pile settlements were around 11 mm at 1% *VL* for all layouts, in contrast with the soil settlements, which decreased from 10.4 to 7.7 mm, at the equivalent pile locations, as the tunnel depth increased. In another study (Mcnamara et al., 2003), the presence of the piles induced an increase in the horizontal displacements around the tunnel when compared with greenfield conditions. In addition, the settlement trough shifted toward the piles, in inverse proportion to *Ld*.

The tests from Ran (2004), with non-loaded piles, indicated smaller pile settlements when $Zp > Zt$. As in other studies, all tunnelling-induced effects were inversely proportional to Ld and directly proportional to *VL*. An increase in the axial force was detected down to the tunnel depth for all piles, regardless of their *Ld*. However, these results were measured after just 2 days of pore pressure dissipation because the quarter bridge strain gauge circuits, which have a tendency to drift with time owing to temperature changes, hampered the analyses of the long-term pile responses. In this study, the deformed shape of the model tunnel tended to be elliptical, pushing the soil away around the tunnel springline.

For two later tests, with non-loaded piles, a new model tunnel, with a better control of the *VL*, was used together with instruments employing full-bridge strain gauge circuits. In one study, the magnitude of the axial force increased with consolidation retaining a uniform profile along the depth, with the maximum close to the tunnel depth (Ong et al., 2005). In another study, the axial force also increased with consolidation, but the maximum value shifted from the pile mid-depth in the short term to the tunnel depth in the long term. These observations were connected to the relation between soil and pile settlements, which was the depth of the maximum axial force where the soil settlement is the same as the pile settlement (Ong et al., 2006).

The most recent study on clay detected that non-loaded piles above the tunnel depth were submitted to a decrease in axial force associated with positive friction. The magnitude of the induced tension decreased as the pile got closer to the tunnel roof. For piles at a certain *Ld* from the tunnel, the axial force increased from the top until 2/3 of the pile length and decreased from there on. It was also noted that the pile settlements followed the surface trough for all *VL*s (Hartono et al., 2014).

The first study on sand may also have been the first to define zones around the tunnel in terms of the pile settlements in relation to the ground-surface settlements (Jacobsz et al. 2001; Jacobsz 2002; Jacobsz et al. 2002; 2004). In Zones A and C, the pile settlements were equal to the surface settlements (Figure 2.3), whereas in Zone B they were larger and in Zone D smaller. Inside Zone A, the vertical distance between the tunnel and the pile greatly influenced the pile response. Piles inside Zones A and B suffered a reduction in their base load associated with an increase in the shaft friction. On the other hand, piles in Zone D experienced a small increase in the base load owing to negative friction on the upper part of the pile and no base resistance degradation. Zone C represented a transitional response between Zones B and D.

Another study modelled an unloaded pile with the tip 1 m above the bottom of the strongbox, which might have been intended to represent an embedded pile. This study did not comment on pile settlements; however, the measurements of axial force indicated the development of negative friction until the tunnel depth regardless of the pile *Ld* but in direct relation to the *VL* (Feng et al., 2002; Feng, 2004).

Pile settlements have been reported to be higher than the surface settlements when $Zp = Zt$, but lower when $Zp > Zt$, and always directly proportional to the *WL* and inversely proportional to the *Ld* (Lee et al. 2003;.Lee and Chiang 2007). Non-loaded piles developed negative friction along depths above *Zt* and positive friction below it, possibility owing to soil heave from the tunnel invert and always in inverse proportion to *Ld*. This condition could even induce tension when the pile tip was much deeper than the tunnel. On loaded piles around *Zt*, a base-load reduction was induced with an increase in the mobilized friction, which caused significant settlements. When the pile was deeper than the tunnel, the base load increased and the mobilized friction decreased above the tunnel centreline and increased below it, inducing smaller pile settlements.

An interesting approach was presented by Marshall & Mair (2011), who combined data from Jacobsz (2002) and Marshall (2009) to analyse the relation between the *VL* that induced pile failure, and the distance from the tunnel centre

to the pile tip, normalized by the tunnel radius. The adopted definition of pile failure was a distinct increase in the rate of pile displacements.

A model tunnel, which could model the face advancements, was used to analyse PTI owing to twin tunnels (Ng et al., 2013). When the tunnels were at pile mid-depth, an almost linear relation could be traced between the pile settlements and the face distance, starting at $Fd = -0.75 \cdot Dt$ and developing half the final settlements between $-0.25 \cdot Dt$ and $+0.25 \cdot Dt$. Above the tunnel depth, a reduction in the shaft friction was induced, which was compensated by an increase at deeper levels. This progressed with the second tunnel to a stage of practically null shaft capacity above the tunnel depth. When the tunnels were close to the pile tip, a reduction in the tip and lower shaft capacities occurred between $Fd = -0.25 \cdot Dt$ and $+0.25 \cdot Dt$, which was compensated by the mobilization of shaft capacity at smaller depths. However, for $Fd > 0.25 \cdot Dt$ the capacities increased again, demobilizing the upper shaft friction. The settlements for the first case ($Zt \approx 0.5 \cdot Zp$) were 1.5 and 2.2 times larger, for the first and the second tunnel respectively, than for the second case ($Zt \approx Zp$). For both cases the settlements were related, based on the pile load-settlement curve, to an equivalent increase in the *WL* between 15 and 36%.

For pile groups that were shallower than the tunnel, Boonsiri and Takemura (2015, 2014) reported an increase in the axial force in the piles closer to the tunnel and a decrease in the piles farther away. When piles and tunnel were at the same depth, there was an increase in the axial force in both piles.

The results of these centrifuge tests bring to attention two points of analysis. The first is how the pile position around the tunnel can be used to assess the ratio between pile and ground-surface settlements. This should be handled with care because these ratios were normally measured in one setup, and therefore not in greenfield conditions, but can be used with estimated tunnel greenfield settlements. The settlement trough, in the presence of piles, has been reported to be either narrower and deeper (Lee et al., 2003) or practically the same as the greenfield (Boonsiri and Takemura, 2015, 2014), or even that the pile settlements were out of the greenfield range, both at the surface and at the pile tip level (Marshall, 2009). The second point is the unfolding of more complex changes of the load-transfer mechanism. The pattern described for the full-scale tests was also measured in these studies. However, among the centrifuge tests, there were cases where an increase in the base load was measured, which implies that the pile base resistance was not degraded and that negative friction developed on the pile shaft.

2.3. Data analysis on physical tests

A comparison of results from PTI should rely on a framework where different layouts can be easily distinguished or associated. A two-dimensional (2D) diagram, where one point locates a PTI layout, was conceived (Figure 2.8) with the tunnel centre as the origin of the vertical and horizontal axes, where distances were normalized by the tunnel diameter. This neutralizes the tunnel depth on behalf of its relative distance to the pile tip. Based on this diagram, the pile settlements and axial force distributions were analysed.

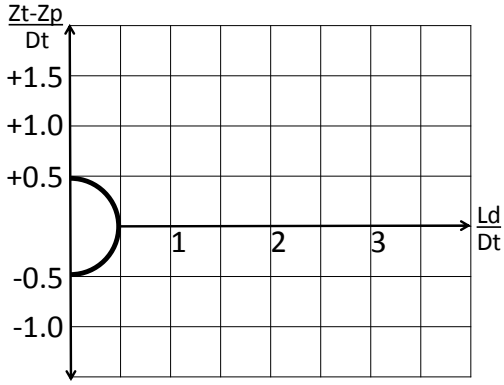

Figure 2.8. 2D diagram to locate different PTI layouts

The pile settlements, normalized by their diameter, are reported as a function of the tunnel *VL* for 20 layouts based on the centrifuge tests of Hergarden (HE), Jacobsz (JA), and Marshall (MA) and are presented in Figure 2.9. The piles in which the final normalized settlement was less than 0.5% were omitted from the graph.

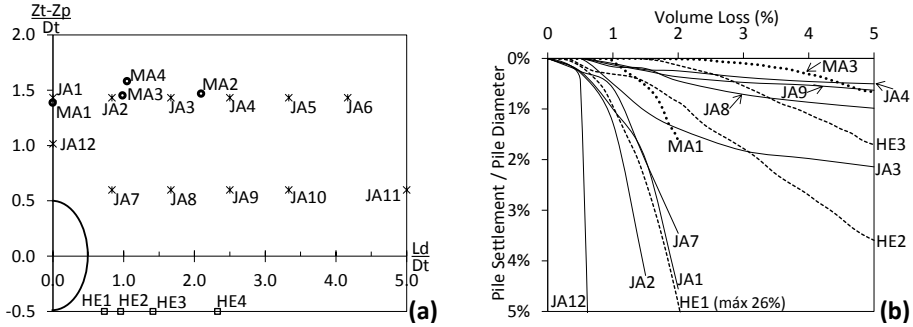

Figure 2.9. (a) Diagram with different PTI layouts; (b) the pile settlements normalized by their diameter as a function of *VL*

The first study used a spring loading system that progressively decreased the pile load after 1% *VL*, which probably reduced the steepness of the settlement curve. With the exception of HE1 and JA12, the piles did not reach what is normally considered a failure displacement (10%·*Dp*) owing to their interaction with the tunnels. In any case, their magnitude should be evaluated by the serviceability limits of the supported structures.

Leaving the magnitude aside, one can focus on the susceptibility of the pile settlements to the tunnel *VL*. The piles just above the tunnel (JA1, JA12, MA1) and within a *Ld* of 0.9·*Dt* (JA2, JA7, HE1) presented settlement curves with significant inflexion points before 1% *VL* for all cases except MA1. Within this region (*Ld* ≤ 0.9·*Dt*) the settlements were very sensitive to the pile depth, relative to the tunnel roof. Just above the tunnel, the *VL* on the settlement curve inflexion point was two to three times higher for piles that were at +1.5·*Dt* (JA1, MA1) than for piles at +1.0·*Dt* (JA12). The data also indicated that at a certain Ld, the pile settlements grew progressively smaller as the pile got deeper, from +1.5·*Dt* (JA2, JA3) to +0.5·*Dt* (JA7, JA8) and to −0.5·*Dt* (HE1, HE2, HE 3, HE 4), and that at a constant relative pile depth, the pile settlements decreased as the *Ld* increased.

The results from those studies that only reported settlements at a certain *VL* were evaluated in two ways: the pile settlement as a percentage of its diameter (Figure 2.10a) and the ratio between pile settlement and ground-surface settlement at the same position (Figure 2.10b), which was normally taken from the best-fit settlement trough. These values were evaluated on the PTI diagram in three classes of results.

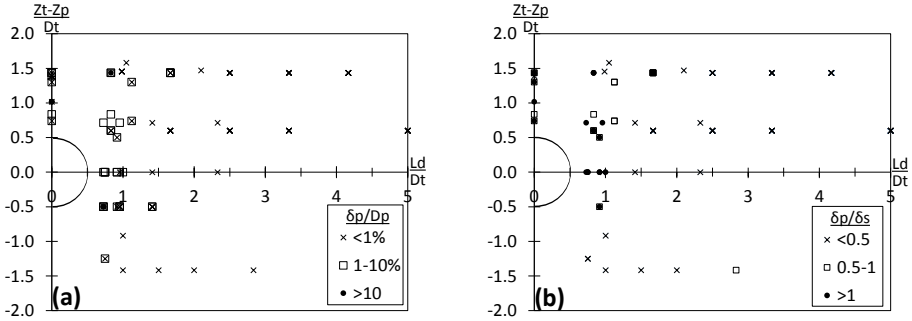

Figure 2.10. (a) Maximum settlements as a percentage of their diameter; (b) maximum settlements as a ratio of the ground surface settlements

It became evident that the pile location was insufficient to determine its response because different classes occur at the same points around the tunnel. However, it was possible to verify that for *Ld* > 2·*Dt* the pile settlements were generally

smaller than 1% of their diameters and 50% of the surface settlements. Closer to the tunnel, settlements in excess of 10%·*Dp* were only reported in three cases. It is, in principle, possible to trace a boundary for the relative pile/surface settlements. However, on the basis of the combined test results, such a boundary would not start at the tunnel springline, nor would it be just upward, as was suggested in the studies from Figure 2.3.

An attempt was made to correlate these two settlement results to four independent variables of each study: (*Zt*−*Zp*)/*Dt*, *Ld*/*Dt*, *WL*/*UBC*, and *VL*. The multivariate regression could not reproduce the settlements considering these four parameters. However, it revealed that the lateral distance (*Ld*/*Dt*) had the best correlation with both settlement results. Therefore, a practical approach was to trace the limit boundary for all recorded measurements in relation to the *Ld* (Figure 2.11). As in the previous results, the region close to the tunnel hosts a wide range of settlements that depend on factors other than the *Ld*. However, from a Ld greater than 1-1.5·*Dt*, the values can be bound with a higher reliability. This allows preliminary estimations of pile settlements owing to PTI based solely on their *Ld* to the tunnels and supported by an extensive set of measurements.

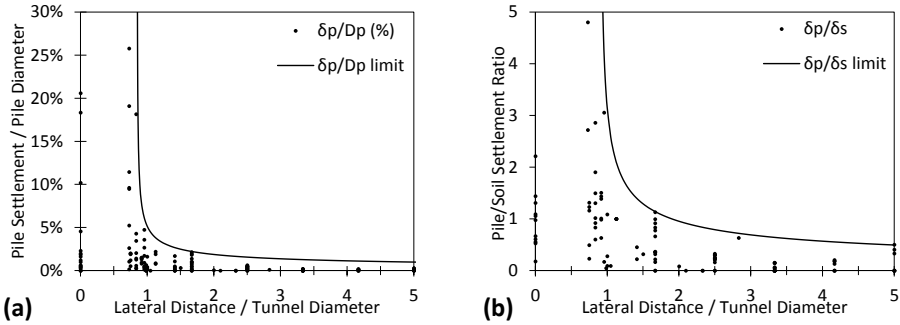

Figure 2.11. (a) Limit values for all measured settlements, as a percentage of their diameter; (b) as a ratio of the ground surface settlements, at different lateral distances normalized by the tunnel diameters

The analysis of induced increments of axial stress was divided into non-loaded and loaded piles. The layouts for the non-loaded piles from the centrifuge tests of Feng (FE), Ran (RA), Lee (LE), Hartono (HA), and Ong (ON) can be found in Figure 2.12a. For the loaded piles from the centrifuge tests of Lee (LE), Loganathan (LO), Boonsiri (BO), and Ng (NG) and the physical test from Selemetas (SE), the layouts can be found in Figure 2.12b. The results were divided into different graphs to allow for a better differentiation of the results.

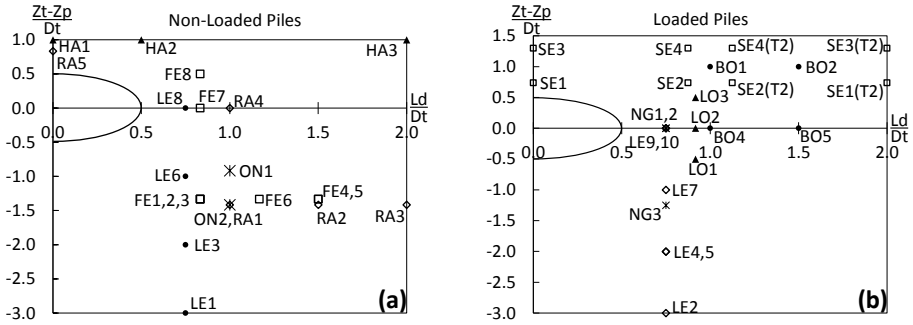

Figure 2.12. Diagrams for layouts of (a) non-loaded piles; (b) loaded piles

For the non-loaded piles, the tunnel interaction induced positive axial stress (compression) in most piles (Figure 2.13). When the piles were deeper than the tunnel, the stress in the piles increased from the surface to the tunnel springline, then decreased up to the pile tip. In those cases, where the pile was more than 2·*Dt* deeper than the tunnel (LE1, LE3) the decrease reached a state of negative axial stress (tension), and in the same way, the magnitude decreased after a certain depth. When the piles were above or at the tunnel springline, the stress just increased from the surface until the pile tip.

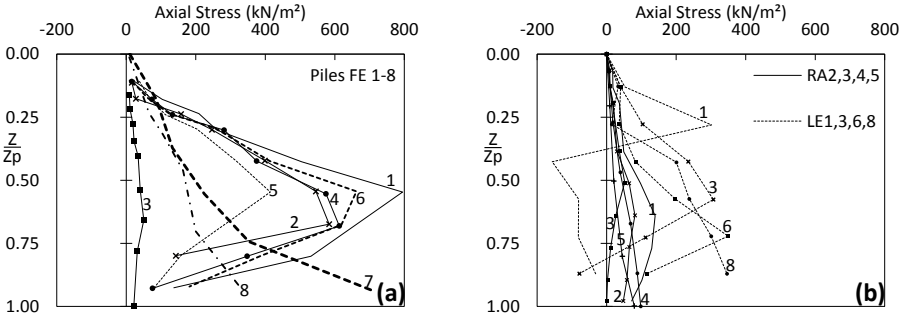

Figure 2.13. Axial stress profiles for (a) Piles FE1 to 8; (b) Piles RA2 to 5 and piles LE1, 3, 6, and 8

The results from Hartono (Figure 2.14a) were against these trends: the piles were subjected to a stress profile that decreased in magnitude close to the pile tip, even though the tunnel was deeper than the piles, and two piles above the tunnel (HA1, HA2) were subjected to tension along their entire lengths. At a certain depth, the maximum axial stress decreases with an increase in the *Ld*, as can be seen with piles FE1, FE6, FE4, RA1, RA2, and RA3. On the other hand, at a certain *Ld*, the results differ: while some show an increase in the maximum axial stress as the pile gets deeper (FE8, FE7, FE1, RA4, RA1; ON1, ON2), others show the opposite trend (LE8, LE6, LE3, LE1). In six cases where the *VL* was the

only variable (FE1, FE2, FE3; FE4, FE5, HA1, HA2, HA3), it is possible to infer that the magnitude of the induced axial stress is directly proportional to the tunnel *VL*. When low-permeability soils were tested, undrained loading conditions were probably induced, conditioning the results to the dissipation time. Two tests (ON1 and ON2) revealed that the magnitude of the axial stress profile increased with time (Figure 2.14b).

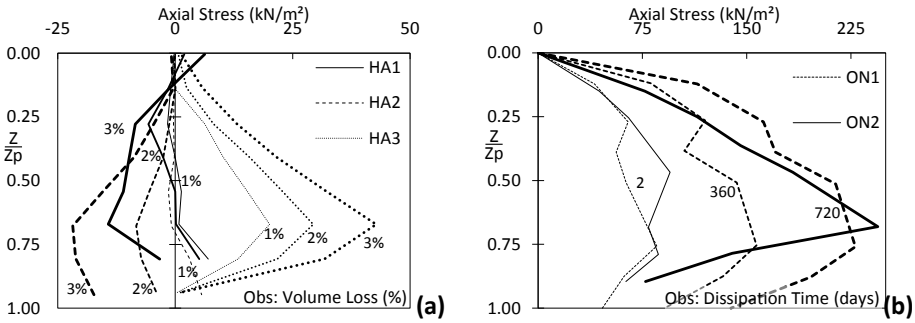

Figure 2.14. Axial stress profiles for (a) Piles HA1 to 3; (b) Piles ON1 and ON2

For the loaded piles, the profiles of axial stress are presented as increments over the values due to the *WL* (Figure 2.15). In cases where two tunnels were excavated, the axial stress due to the second tunnel was subtracted from the stress caused by the first tunnel. In some cases (NG2, NG3), both tunnels are at the same relative position to the piles, whereas in other cases (SE1, SE2, SE3, SE4), they represent different layouts.

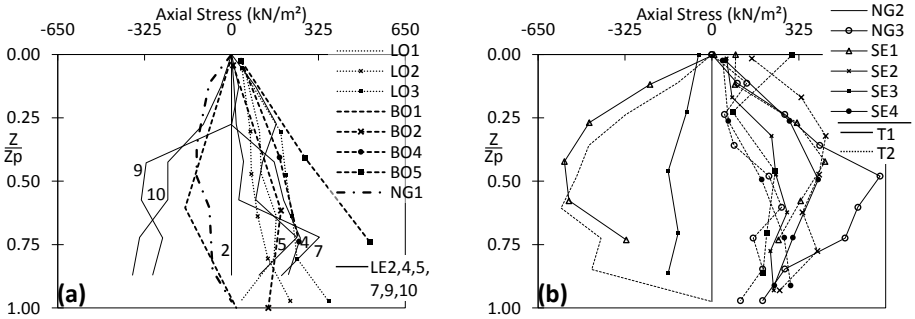

Figure 2.15. Profiles of increments of axial stress for piles in interaction with (a) single tunnel; (b) two tunnels

Above the tunnel (SE1, SE3-T1) and on the springline until a *Ld* of 0.75·*Dt* (NG1, NG2; LE9, LE10), the tunnel induced a reduction in the pile axial stress. The same happened on Pile BO1, although all other piles at similar positions presented an opposite response. Just above the tunnel the stress decrease was larger for

deeper piles (SE1-T1). The effect of the different WLs on the same layout could not be revealed because of the variable shapes of the profiles of stress increments (LE9, LE10; LE4, LE5). Above the tunnel springline, a comparable deeper pile has been reported to induce both larger (SE4-T2, SE2-T2; SE3-T2, SE1-T2; BO2, BO5) and smaller (SE4, SE2; LO3, LO2) increments of axial stress. No increments of axial stress were detected for a very deep pile (LE2) and under the first tunnel excavation around pile NG2.

2.4. Overview of physical tests

Tunnel construction in interaction with deep foundations is a matter of increasing concern in major urban areas that will certainly spread to other cities, as their underground infrastructures develop. However, a great deal of uncertainty is still evident in regulations for minimum tunnel clearance and in the design of preventive measures against PTI effects. To face this problem, more than 50 tests, through a wide range of layouts and soils, were analysed, and compared (Dias and Bezuijen, 2015a, 2014a).

The case studies revealed that most structures were not affected by a tunnel construction, but under certain conditions, preventive and active interventions were necessary. Overall two mechanisms were described for the tunnel effects on piles: (1) The tunnel degrades the pile base capacity, which requires a mobilization of shaft friction with limited settlements, and once the shaft is fully mobilized, higher settlements are necessary to recompress and mobilize the base. (2) The base capacity is not degraded and the relative pile-soil settlements induce negative friction on the pile shaft, which increases the base load. Several studies reported that the ratio between pile and ground-surface settlements depended on the pile position in relation to the tunnel; however, it is still debatable whether and how greenfield displacements are related to displacements in the presence of piles.

The quantitative data revealed that, in terms of pile settlements, most piles did not reach failure (10%·Dp) and that for Lds larger than two tunnel diameters (Ld > 2·Dt) the pile settlements were generally smaller than 1% of their diameter and 50% of the equivalent surface settlements. When considering the axial force in piles, it was established that the tunnel induced compressive forces in non-loaded piles that increased to the tunnel depth and decreased at deeper levels. For loaded piles the results indicated a reduction of axial force in the piles closer to the tunnel and an increase in piles farther away. The increments of axial force were generally inversely proportional to the Ld. Overall, the analysis of the assembly of data from the different sources enabled the results from each study to be compared and contrasted and the global mechanism of PTI to be clarified.

2.5. Mathematical models

A mathematical model translates a certain interpretation of a physical system, conceived from experimental evidence and reasoning, into mathematical expressions. If these expressions can be solved, and the results agree with experiments, the model is assumed to represent the system accurately, even though a causality implication between the variables may be linked to an external factor or biased through assumptions in the model.

In geomechanical problems there are normally two dimensions of mathematical models. The first are the material models, normally based on continuum mechanics and elastoplastic theory, that represent the relation between stresses and strains through constitutive relations. The second is the analysis of a physical setup with a certain geometry, where the partial differential equations (PDEs) governing static or dynamic equilibrium have to be solved for certain boundary conditions, with implicit assumptions for water drainage or coupled with the PDEs for the mass flow of water. In practice, most problems involve an equation system that cannot be solved analytically, so numerical methods are employed to solve the PDEs, most commonly the finite element method.

In this framework, every aspect of the physical system to be considered in the analysis must be related or adapted to one of its variables: geometry, constitutive relations or boundary conditions. If, for example, an intrinsically discontinuous problem, as a tunnel excavation, needs to be considered within a continuous framework, it has to be adapted. The excavated region can be removed from the calculation domain (geometry), taken to be extremely deformable as to create minimum reaction forces (constitutive relations), or replaced by an equivalent set of forces or displacements along its perimeter (boundary conditions).

Overall it is fair to say that each geomechanical mathematical model will carry with it a considerable list of assumptions and adaptations, all of which influence the computed results. This is even more significant in complex problems such as pile tunnel interaction, where considerations of interface between geotechnical and structural elements are also involved.

So a literature review of mathematical models for pile tunnel interaction cannot follow the structure from the review of physical tests. While some of the reviewed studies presented validation steps, the bulk of results comes from parametric analyses, which can easily assume unrealistic parameters and calculate meaningless results. Another problem is that in most cases far too many details are omitted from the published records, so that not even the logic and consistency of the modelling procedures can be verified. Therefore, it was considered that any effort to quantitatively correlate the results of these models

would be devoid of significance. Accordingly, the literature review will be focused on the mechanisms and qualitative results reported on each study.

The studies were divided by the way in which they considered the pile-tunnel system, in a single model where the aspect of both the pile and the tunnel were represented, or in two separate models where pile and tunnel are treated separately and interact through a specific variable.

The first one-step numerical analysis of pile tunnel interaction reported that the pile settled, as a rigid body, in a magnitude similar to the soil settlements at the depth of the pile toe (Figure 2.16). Consequently, the lateral distance from the tunnel significantly reduced the pile settlements (Vermeer and Bonnier, 1991). This rigid body response was also reported by Cheng et al. (2007), but depending on the relation between the tunnelling induced displacements and the pile axial rigidity, the pile settlement could also decrease along the pile body (Pang, 2006).

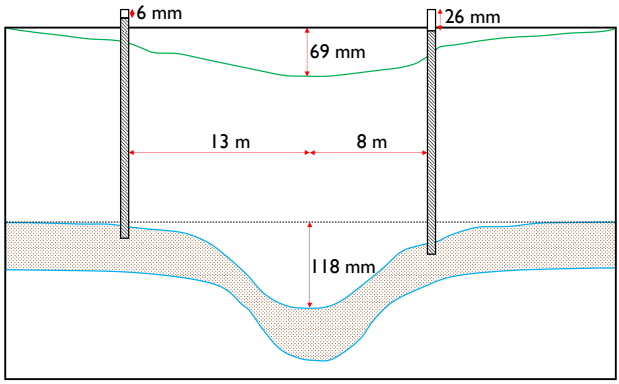

Figure 2.16. Diagram from Vermeer and Bonnier (1991), where the pile settlements followed the ground settlements at the toe level

This inverse proportionality between pile settlements and the lateral distance was also reported in practically all studies. However, the relative magnitude between pile settlements and surface soil settlements was highly inconsistent. One study proposed that the piles settled more than the soil (Lee and Ng, 2005a) in a constant ratio (Lee and Ng, 2005b). Other studies had this ratio as a function of the pile relative depth to the tunnel. Pile settlements increased with toe depth (Yang et al., 2011), and were smaller than the soil for piles above the tunnel depth, but higher for piles deeper than the tunnel (Cheng, 2003; Cheng et al., 2004). This direct relation can be questioned by studies that reported that the pile presence can reduce (Lee et al., 2009; Mroueh and Shahrour, 2002; Pang, 2006; Pang et al., 2005a) or increase (Lee, 2012a) the greenfield soil settlements.

Regarding the longitudinal distance between the excavation face and the pile projection (*Fd*), the pile settlements were reported to change in one case from -3·*Dt* to +0.5·*Dt* (Lee and Ng, 2005b), and in a different case to start from -2.*Dt* and reach 50% the final value when the face was aligned with the pile (*Fd*=0) (Yoo and Wu, 2011) and in yet another one to have their highest gradients from -1·*Dt* to +1·*Dt* (Lee, 2012a). In a series of parametric analyses, Pang (2006) concluded that for a TBM excavation an increase in the excavation rate and face pressure can decrease the pile settlements, while the grout and lining stiffness's have a minor effect. A different study assessed that for embedded piles, the deformability of the bearing layer is directly proportional to the pile settlements (Mahmood et al., 2011). For settlements and other tunnelling induced effects, all studies reported a direct proportionality with the tunnel volume loss. When the piles are in a group there were normally less settlements (Lee, 2012a) and also smaller increments of axial force (Pang, 2006).

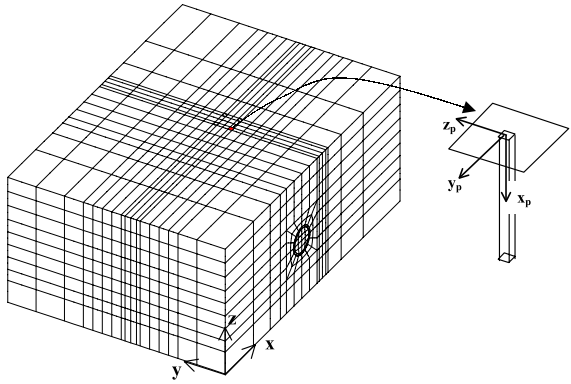

Figure 2.17. Three dimensional finite element mesh from Mroueh and Shahrour (2002), where both the tunnel and the pile are explicitly modelled.

The effects of tunnel excavation on the pile load transfer mechanism were consistently reported, emphasizing the effects of the relative pile tunnel position. The maximum axial force was stated inversely proportional to the lateral distance (Pang, 2006) and directly proportional to the pile depth (Yang et al., 2011; Lee, 2012a). A conceptual model was presented by Cheng (2003), where the relative pile tunnel position was determined by a triangular zone from the tunnel springline to the surface. Inside this zone there was sharp reduction in the stresses on the pile toe (Yang et al., 2009), associated with plastic yielding (Lee and Ng, 2005b) and softening, and a consequent increase in the positive shaft friction to preserve equilibrium (Lee and Jacobsz, 2006; Lee et al., 2007). The softening of the pile toe caused a reduction in the profile of axial force (Yoo and Wu, 2011), which could even lead to tensile forces (Yang et al., 2011).

Outside this zone, the relative tunnel induced settlements create negative friction on the pile shaft from the surface until the depth of the tunnel centreline (Mroueh and Shahrour, 2002), causing an increase in the profile of axial force (Yoo and Wu, 2011). It is interesting to notice that for a shallow pile, an increase in the lateral distance can increase the axial forces, as the pile toe moves out of the defined zone (Cheng et al., 2004). The changes in the axial force have been reported with higher rates from Fd=-0.25·Dt to +0.25·Dt (Lee and Jacobsz, 2006; Lee et al., 2007), or from -2.Dt to +1.Dt (Yoo and Wu, 2011), or just to increase until Fd=0 (Pang, 2006). The maximum axial force has also been reported to increase with the soil shear stiffness (Cheng, 2003; Cheng et al., 2004; Pang, 2006).

The analyses of Pang (2006) resulted in similar increments of axial force for piles with and without a head load. However, when the non-loaded pile was loaded after the tunnel excavation, the settlements and the maximum axial force were higher than when it was loaded before, probably due to stiffness degradation in the ground due to tunnelling induced strains. Lee (2012a) suggested that the axial force profile could be calculated by the β-method of pile design, with different β coefficients above and below the tunnel depth.

In real cases, the piles should be connected with and loaded by a superstructure, such as a building or a bridge. The presence of the building in the analysis has been reported to reduce the pile settlements by 20% and generate a soil settlement profile that was more uniform with depth (Yoo and Kim, 2008). As the building connects piles at different positions relative to the tunnel, it may be the case that when a pile closer to the tunnel is settling, the building pulls other piles up (Ninić et al., 2011).

Certain studies discussed secondary effects of pile tunnel interaction, for example: the effects of pile construction and loading on an existing tunnel (Higgins et al., 2000; Namazi et al., 2011a); the effect of isolating the pile shaft from the ground displacements (Zou, 2003; Zou et al., 2003); how a contiguous pile wall can reduce the minimum face pressure for tunnel stability (Namazi et al., 2011b); how an extreme case where the pile toe was cut during tunnelling can be managed with grouting (Lee et al., 2011); and how parallelization techniques can optimize these calculations (Meschke et al., 2013; Ninić, 2015).

Whenever two separate models were used to represent the pile and the tunnel, the first step was to determine the ground displacements induced by the tunnel excavation assuming greenfield conditions through empirical, analytical or numerical methods. These displacements were then used as input of a separate analysis to assess how the pile responded to these displacements, assuming an

initial working load. The equations to represent the pile response were solved analytically or with numerical methods.

The boundary element method (BEM) was the first numerical tool employed to calculate the pile response in this type of analysis (Chen et al., 1999). The ground movements were assessed with the analytical solution of Loganathan and Poulos (1998) (hereafter referred to as L&P) for tunnels in homogeneous undrained clay, a widely employed method for this type of analysis. The lateral and axial responses of a non-loaded pile were assessed in two independent formulations. The pile was formulated as an elastic beam in the code PALLAS to calculate the pile lateral response, and as an elastic column in the code PIES to calculate the axial response. In both cases the soil was modelled as an elastic continuum and limit values for the pile-soil lateral stress, skin friction and end bearing pressure were used to simulate soil failure and interface slippage.

Through a series of parametric analyses, the authors assembled a set of design charts to predict the maximum values of bending moment, lateral deflection, settlement and both compressive and tensile axial forces in the pile. The charts required the input of the tunnel ground loss and radius, the undrained shear strength of the clay, the ratio between pile and tunnel depth and the pile diameter. A good prediction of the lateral deflection of a pile from the case study described by Lee et al. (1994) was achieved, but the other parameters were not evaluated. This methodology was later adapted to examine the settlements and tilt of pile groups via the superposition method (Poulos, 2002).

The software PALLAS was also used with the soil displacements from a 3D finite element model. The simulation prescribed boundary displacements to model the tunnel volume loss in a linear elastic soil (Surjadinata et al., 2006). The method provided conservative predictions when compared to Chen et al. (1999) but it's ability to account for different modelling techniques for the tunnel was a significant advantage (Surjadinata et al., 2005). A series of these analyses were combined in design charts based on the ground loss, tunnel depth and diameter, pile length and pile soil relative stiffness. The readings of a base chart were corrected by the pile slenderness and lateral distance to the tunnel and provided estimates of the pile maximum displacements, bending moments and axial forces. The case studies of Lee et al. (1994) and Pang (2006) were analysed with satisfactory agreement (Surjadinata et al., 2011).

A three dimensional BEM formulation, able to incorporate externally imposed ground movements, was implemented in the software GEPAN described by Xu and Poulos (2000). The closed-form solutions for the ground movements from Sagaseta (1987), Verruijt and Booker (1996) and L&P were included in the code

(Xu and Poulos, 2001). The method was validated against the measurements of lateral deflection from Lee et al. (1994) and compared with results of a 3D finite difference analysis with reasonable agreement (Loganathan et al., 2001). The GEPAN calculation was about 300 times faster than the finite difference analysis.

Basile (2012) presents another BEM software called PGROUPN, used for the analysis of pile groups. The deformability of the pile soil interface was set to depend on the interface stress through a hyperbolic law while interface slippage was accounted by a limit stress. The pile was formulated as a Bernoulli-Euler beam and the group interactions were simultaneously accounted for through Mindlin's solutions. Based on the soil displacements from L&P, the software achieved results comparable to Kitiyodom et al. (2005) and Xu and Poulos (2001) for single piles and pile groups. The effect of the limit skin friction was perceived in a reduction of the induced axial force and was in agreement with the results from Chen et al. (1999). When the interface stress dependency was accounted, the reduction of axial force was even higher. Basile (2014) included a validation with the case study from Pang (2006) with a fairly good agreement.

The finite element method (FEM) was also used to assess the pile response. Ghazavi (2001) presented this type of formulation for a single pile using the vertical displacements of L&P and assuming a linear elastic and stress free pile. The differential equation for the pile vertical equilibrium was solved incrementally in a FEM framework. The soil displacements were connected to independent load-settlement formulations for the shaft and the toe. The results of the method were comparable to Chen et al. (1999), but in a more straightforward formulation.

Piled raft foundations were analysed with a hybrid FEM code named PRAB, where the raft was represented as a thin plate connected to piles that were modelled as elastic beams. The soil was simulated with sets of three orthogonal springs on the raft, the pile shaft and the pile toe. The interaction among all structural elements through the soil continuum was approximated by Mindlin's solutions. The basic formulation for homogeneous soil (Kitiyodom and Matsumoto, 2002) was also adapted to layered soils with a modified form of Mindlin's solutions (Kitiyodom and Matsumoto, 2003).

Based on the soil displacements from L&P the results from PRAB were validated against the BEM analyses of Xu and Poulos (2001) and Loganathan et al. (2001) with a very good match (Kitiyodom et al., 2005b). When the ground displacements were estimated from a finite difference simulation, the results were in agreement with a one-step finite difference model of pile tunnel interaction (Kitiyodom et al., 2006; Masumoto et al., 2006).

The third method applied to solve the equations of pile response was the finite difference method (FDM). Huang et al. (2009) presented the first FDM framework using the tunnel displacements from L&P. The formulation divided the vertical and lateral responses of the pile and assumed displacement compatibility with the ground movements. The soil was modelled by Winkler springs with a constant lateral shaft rigidity, and vertical shaft and toe rigidities derived from Randolph and Wroth (1979). The group effect was accounted by a reduction in the ground displacements around the pile. This shielding effect was calculated in the vertical direction by the logarithmic attenuation function proposed by Randolph and Wroth (1979) and in the horizontal direction by Mindlin's solutions. The FDM was used to iteratively solve the vertical and lateral equilibrium equations accounting for the group interactions. The method was verified against other studies and predicted the induced bending moments quite well. On the other hand, the predictions of axial force were smaller than from the GEPAN analyses of Xu and Poulos (2001) and Loganathan et al. (2001), and the centrifuge results of Loganathan et al. (2000); but higher than the centrifuge results of Ong et al. (2006); and in good agreement with the case study of Coutts and Wang (2000).

A similar method was developed with a unified load and unload transfer model for the pile-soil interaction. This model had the advantage that all the spring's rigidities could be directly estimated from ground parameters. A hyperbolic vertical shaft spring was considered (Zhang et al., 2011). These features resulted in a better agreement with the method from Chen et al. (1999), and the centrifuge results of Loganathan et al. (2000) and Lee and Chiang (2007).

Another approach combined an analytical soil model based on the response of multi-layered elastic materials with Mindlin's solutions to form the pile equilibrium equations. This method was implemented for the analysis of piled rafts in the PPRL software for their vertical response (Huang and Mu, 2012) and in the LPPR software for their lateral response (Mu et al., 2012). No slip or gap was assumed between the pile and the soil. And the pile presence was set to reduce the free-field tunnelling displacements, calculated by the L&P method, around a single pile and around adjacent piles in a pile group. Interactions between the raft, the piles, and the ground were also simulated. The PPRL software corrected the excessive axial forces predicted by Huang et al. (2009). The results from both codes were in good agreement with the methods of Xu and Poulos (2001) and Kitiyodom et al. (2005) for single piles and the centrifuge model of Ong et al., (2006). When compared to the piled group analysis of Kitiyodom et al. (2005), the software achieved more accurate results and both agreed that soil raft interaction was insignificant for passive loads.

Devriendt and Williamson (2011) compared another method based on Mindlin's solutions for an elastic ground mass (Poulos and Davis, 1968) with the empirical assumptions that the pile head settles similarly to the greenfield displacements at a depth equivalent to 2/3 the pile length or at the depth of the pile neutral axis. All methods produced roughly the same results. A back analysis of one pile from Selemetas (2005), fitted to the pile load-settlement curve, slightly over-predicted the induced settlements and axial forces.

One study performed a Euler numerical integration of the pile vertical equilibrium equations, considering axial compression and interface shear stress (Yang and Wang, 2002). The ground settlements were estimated from the empirical method of Mair et al. (1993). The interface shear stress increased linearly with the relative displacements normalized by a maximum value of 2.5 mm and the boundary conditions were null top load and toe displacement.

A few studies were able to solve the equations for a pile subjected to external ground displacements analytically. To cope with the several possible profiles of ground settlements along depth, Klar and Soga (2005) presented solutions for profiles described by polynomial, cosine and exponential functions. Assuming a linear superposition principle, the authors were able to devise closed form solutions for the pile settlements along depth.

One of the more recent studies, in a very singular approach to problem, used cavity contraction solutions to calculate the stress increments caused by the tunnel volume loss. These increments were then used to estimate the variation in the toe bearing capacity of a pile, calculated through a cavity expansion analysis (Marshall, 2012; Marshall and Haji, 2015). In this way the authors identified the critical volume loss to cause failure for a certain distance between the pile toe and the tunnel.

This literature review of mathematical models for pile tunnel interaction shows the different ways engineers have tried to represent this problem. Several models can be considered accurate, as they were validated with case studies or physical tests. However, most models were calibrated for limited ranges of ground displacements and pile loads.

One of the mechanisms identified in Section 2.4 depends on the shaft resistance and the pile response at partial and full shaft mobilization. However, most models do not consider a limit on pile resistance, as they are either based on elastic solutions or unable to solve the large deformations involved in pile failure, as most one-step continuum numerical models. Among the models that do account for failure, most consider the pile-soil interaction through some version of Mindlin's solutions, which was originally formulated for point forces inside

homogeneous, elastic and isotropic semi-infinite bodies. So the range of applicability, even with a limit on the interface stress, is questionable.

Another prevalent problem is reproducibility. Most one-step numerical analyses omitted important details on the constitutive models, modelling steps, and boundary conditions, so that the methodology is not adaptable to a new study. Among the different formulations used to solve the equations of pile response, most required a specific solution algorithm for the numerical analysis, which was normally recorded in a software (e.g. PALLAS, PIES, GEPAN, PGROUPN, PRAB, PPRL, LPPR, etc.). However, these codes have either been discontinued or are practically inaccessible for the large majority of the engineering public.

Considering these observations, the outline of a methodology to calculate the consequences of pile tunnel interaction was planned. The first layer of reasoning, which will be expanded in Chapter 3, considered that numerical analyses where the pile is modelled within a continuum ground domain are still not a reliable option for engineering practice. Therefore, the initial outline did not include one-step numerical analyses, but adopted the widely accepted assumption that the ground settlements are a suitable variable to link the independent models used to represent the pile and the tunnel. This decision severed the methodology in two parts:

1. Design a system for pile analysis that can cope with tunnelling induced ground settlements and can be implemented in an accessible framework.
2. Develop a model to predict the ground movements during tunnelling.

The outline would then be closed by combining both points into a general two-stage mathematical model. The next section presents how a simple version of this outline was tested, and how the results supported the continuation of the project in this direction. The model imposes the pile settlements and calculates the resultant axial forces. It does not consider the interaction with the pile toe, or the possibility of pile failure, and the load boundary conditions are not constant. All these limitations have been solved in the next chapters. Hereafter, tunnelling induced ground settlements/displacements will simply be referred to as “ground settlements/displacements”.

2.6. Tentative simplified methodology

Section 2.6 is based on the Conference Paper: Dias, T.G.S., Bezuijen, A., 2014. Pile-Tunnel Interaction: A conceptual analysis. ***8th International Symposium on Geotechnical Aspects of Underground Construction in Soft Ground****, Seoul, South Korea.*

This section presents a very simple model to evaluate the pile settlement and increment of axial force due to a tunnel excavation. The displacement field around the tunnel can be used both to estimate the pile settlement and calculate the differential displacements around the pile-soil interface. Assuming that no pile failure occurs, an elastic model relates these differential displacements to increments of axial force on the pile. The parameters to define the pile-tunnel relative position were discussed in Figure 2.1.

Assuming a certain displacement field around a tunnel, the settlements on a vertical section along the imaginary pile position, for example above the tunnel, can be determined (δs on Figure 2.18). Assuming that the pile settlements (δp) are equal to the soil settlements at some level along the pile depth. Three possibilities are presented: at the surface, at 2/3 of the pile depth and at the pile toe.

The pile is assumed to settle as a rigid body and does not follow the same settlement profile as the soil. At a certain depth, if the soil settlements are higher than the pile settlement, negative friction develops, increasing the axial force on the pile. If the soil settlements are smaller than the pile settlement, positive friction develops, reducing the axial force on the pile. This mechanism has been assumed for piles subjected to ground displacements, and has been confirmed by the centrifuge tests of Williamson (2014) (Mair and Williamson, 2014). Considering that in this example the pile settlement is derived from the soil settlements, at a certain depth the pile and the soil settlement will be equal. This position is normally referred as neutral plane and it is an imposition in this methodology.

These incremental stresses can be added to the axial load distribution to verify that the ultimate pile capacity is not reached. This will, of course, depend on the maximum shear force that can develop on the pile-soil interface. This study assumes an elastic interface, but in reality once the shear resistance is achieved slippage will occur with no further increments.

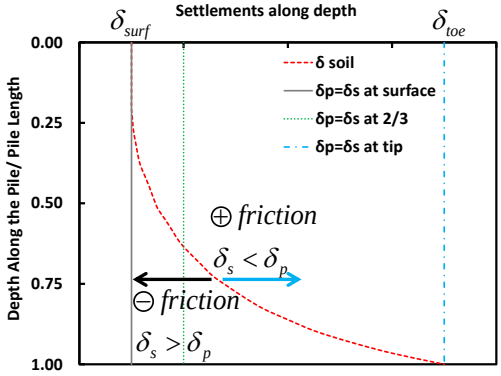

Figure 2.18. Example for pile-tunnel interaction analysis.

Take for example the profile of Figure 2.18 and the assumption that the pile and soil settlements are equal at the level of the pile toe. In this case the soil settlements are smaller than the pile's along all its length and therefore only positive friction develops. On the other hand, in the case where the pile and soil settlements are equal at the surface, soil settlements are higher than the pile's along all its length and only negative friction develops. For the intermediate case, where the pile and soil settlements are equal at the level of 2/3 the pile depth, both positive and negative friction develop. On the top 2/3 of the pile the soil settles less than the pile inducing positive friction. On rest of the pile the soil settles more, inducing negative friction.

Even from numerical methods, the soil settlements are normally known in a discrete number of points along the section. The increment of axial stress ($\Delta\sigma$) between two points (n, $n+1$) can be determined by the average difference between the soil and the pile settlement (δ). This average is then divided by the pile length between the two points, which is equivalent to the average interface shear strain. Considering a certain shear modulus (G) for the interface, the shear stress can be directly determined. If the stress is then integrated along the interface surface and divided by the cross-section area of the pile, the increment of axial stress can be determined as:

$$\Delta\sigma = \left[\left(\delta_s^n - \delta_p\right) + \left(\delta_s^{n+1} - \delta_p\right)\right]\frac{2.G}{D_p} \qquad (1)$$

This equation calculates the increment of axial force caused by the imposed boundary condition of pile settlement. The tunnel induced displacements were obtained from a drained plane-strain finite element analysis of an unlined tunnel with a stress release factor λ = 0.50, which corresponded, for the soil conditions

mentioned below, to a volume loss of 0.42% at the tunnel and 0.91% at the surface. The tunnel springline was at a depth of 30 m and the tunnel diameter was 8 m. The soil was modelled by the Hardening Soil with small-strain stiffness model. The parameters were estimated from the empirical correlations of Brinkgreve et al. (2010) for sand at a relative density of 0.75 and are namely: ϕ = 37°; ψ = 7°; ν = 0.2; m = 0.466; E_{50}^{ref} = 45 MPa; E_{oed}^{ref} = 45 MPa; E_{ur}^{ref} = 135 MPa; G_0^{ref} = 111 MPa; $\gamma_{0.7}$ = 1.25.10^{-4}. The parameters k_0 = 0.50 and γ = 20 kN/m³ were adopted. For the complete formulation of the model the reader is referred to Brinkgreve et al. (2013).

The vertical displacements were assessed on sections positioned at lateral distances (*Ld*/*Dt*) of 0, 0.35, 0.50, 1.00 and 2.00 tunnel diameters from the tunnel centreline, and are shown in Figure 2.19. Three pile lengths were analysed: 22 (A); 30 (B) and 34 m (C). Pile A was analysed at *Ld*/*Dt* of 0, 0.35, 0.50 and 1.00. Pile B at *Ld*/*Dt* 0.50, 1.00 and 2.00 and Pile C at *Ld*/*Dt* 1.00.

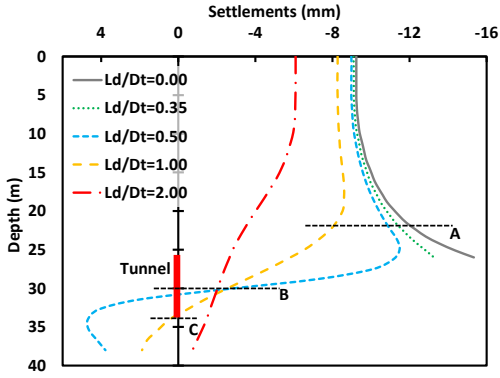

Figure 2.19. Settlement profile around the tunnel

In all analyses the piles were assumed to settle the same as the soil at their toe level, as marked on Figure 2.19. The interface shear modulus was assumed *G*=20 MPa and the piles were all 1 m in diameter. Following the layout of Figure 2.8, the piles can be positioned according to Figure 2.20. Point A0.35, for example, refers to a 22 m long pile, whose toe is one tunnel diameter above the tunnel springline and 0.35 tunnel diameters to the side of the tunnel centre.

The results of this conceptual model were compared to six other studies discussed in Section 2.3 (Bezuijen and van der Schrier, 1994; Feng et al., 2002; Jacobsz et al., 2004; Kaalberg et al., 2005; Lee and Chiang, 2007; Selemetas et al., 2005).

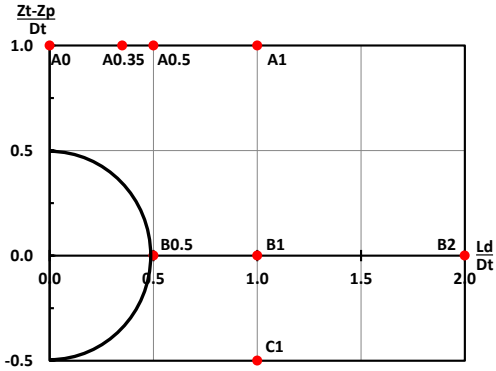

Figure 2.20. Pile's tip positions around the tunnel

According to the methodology exposed, the pile settlements (equal the soil settlement at the pile toe level) were calculated and compared to the soil surface settlements for the different lengths and positions. Figure 2.21 presents the results of pile and surface settlements and their ratio.

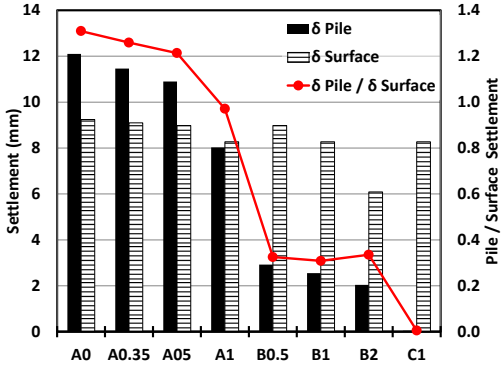

Figure 2.21. Pile / Surface settlement ratio for the different piles of the analysis.

All the A piles settle more than the surface, with the exception of Pile A1, where the pile/surface settlement ratio is slightly smaller than 1. Piles B and C settle less than the soil at the surface. As the lateral distance increases for Piles B, the magnitude of settlements decrease but the settlement ratio remains roughly constant. Pile C1 presents no settlements, as its toe level matches the depth where the soil displacements at that lateral position changed from negative to positive.

Figure 2.22 presents the ratio of pile and surface settlement together with the results of four studies that reported these values. The points are marked on the layout of Figure 2.8 together with the ratio value. The calculated values are in red to be distinguished from the measured values.

Where *Ld*/*Dt* is higher than 1, all the literature data agrees with the model, as the settlement ratios are smaller or equal to 1. For *Ld*/*Dt* between 0.5 and 1.0 the model implied that the settlement ratios would be higher than unity for piles toes above the tunnel and smaller than unity close to the tunnel springline. Most results agree with that, but there are two points in disagreement. The point with the ratio of 0.85 was probably under a different profile of soil displacement due to different soil conditions. The other point is likely to have failed as it was very close to the tunnel and under a load equivalent to 70% its capacity. Directly above the tunnel, the data from Selemetas et al. (2005) agrees with the model prediction of higher pile settlements, but the results from Jacobsz et al. (2004) present a settlement ratio below 1. All the points in disagreement with the predictions are circled in Figure 2.22.

Based on the settlement profiles (Figure 2.19) the increment of axial stress on the piles (Figure 2.20) was calculated according to Equation 1, the results are shown in Figure 2.23. In this methodology, the increment of axial stress is a direct consequence of interface shear modulus and the relation between the soil settlement profile and the imposed pile settlement. The piles that settled more than the surface soil settlements (A0, A0.35 and A0.5) developed positive friction along most of their sections, which resulted in a decrease in their axial force. The stress increments decrease with depth as the soil settlements approach the value of the pile settlement. The gradient of axial stress is directly connected to the gradient of the soil settlements along the pile depth.

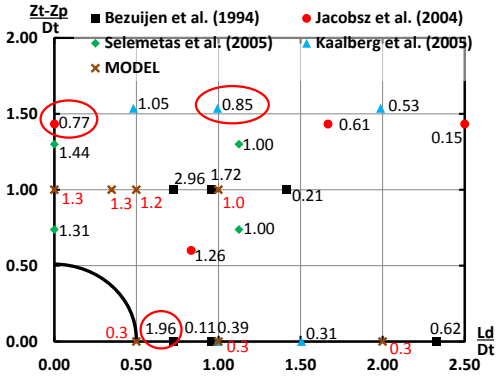

Figure 2.22. Pile / Surface settlement ratio calculated and reported on literature.

On the other hand, piles that presented settlement ratios below unity developed negative increments of axial stress over most of their depth. All piles that were 30 m deep (B) presented similar stress profiles, with an inflexion at the depth when the difference between the pile and the soil settlements start to decrease.

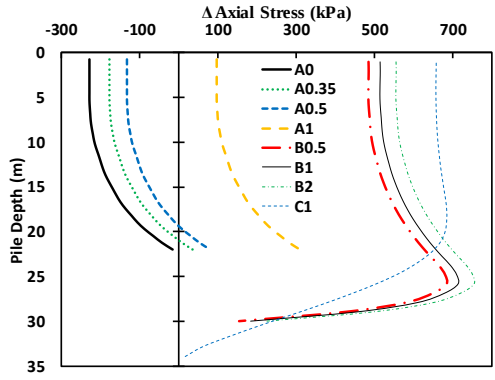

Figure 2.23. Increment of axial stress on the different piles of the analysis.

The results of three studies that reported increments of axial force due to tunnel construction are presented in Figure 2.24. Those values are not to be compared quantitatively with the results of our calculations, which assumed an arbitrary interface shear modulus and are not bounded by load boundary conditions. However, the general response of increase of decrease in axial stress can be compared.

On the top of the tunnel, the piles also presented a decrease in the axial stress. The gradient however, was quite different. The results of the calculation model indicate a steady decrease in the axial force increment, which was not at all present for Pile S2 and just evident on the last 1/3 of Pile S1. Pile S3 agreed roughly with Pile A1 from the model. Pile S4 presented a decrease in the axial stress that was not evident in the model. Piles L1 and F1 had positive axial stress increments along all their depths. Pile L2 presented the expected inflexion, but on a deeper level than Pile C1 from the model.

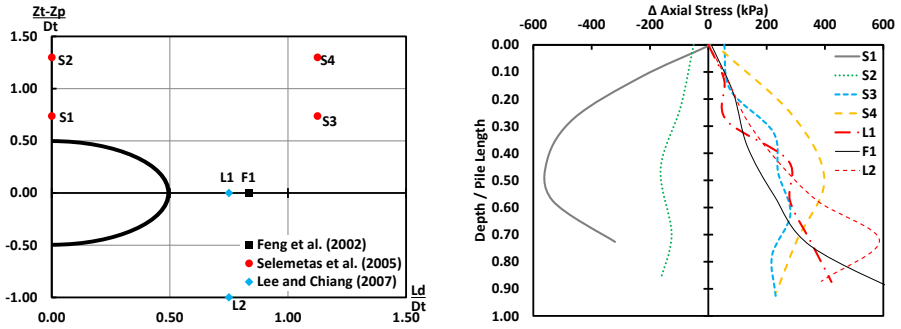

Figure 2.24. Increment of axial stress from literature.

A simple model for the analysis of tunnelling induced pile settlements and the consequent increment of axial stress was presented. The model is a first step to

understand how a pile can interact with the displacement field around a tunnel (Dias and Bezuijen, 2014b).

Based on an example plane strain calculation of an unlined tunnel, different possible pile locations were evaluated. The results were compared to six studies from the literature and considerable agreement was obtained for the trends of ratios of pile to surface settlement and increment of axial stress.

Some features of the pile response that were normally associated with complex changes on the pile load-transfer mechanism could be captured with a simple relation between pile and soil settlements.

3. Deep Foundations

This chapter presents the first part of the methodology outlined in the end of Section 2.5, namely that an accessible system for pile analysis, able to cope with ground settlements, must be designed. The subject of deep foundations is reviewed briefly, leading to the decision to base the system on an adapted version of the load transfer method, and to implement it within a regular spreadsheet. The details of the method and proposed load mobilization functions are discussed, followed by a validation of the method for an instrumented pile load test and the discussion of some conceptual results.

3.1. Literature review

Piles are slender foundation elements intended to support structural loads by mobilizing soil resistance along their depth. A pile is set up by either replacing or displacing the original ground. Bored piles replace the ground causing minimal disturbance in the surrounding soil (Example shown in Figure 3.1). The conditions at the pile-soil interface depend on the type of auger, the time between drilling and concreting, the power of the drilling equipment, the use and characteristics of a support fluid or casing and the concrete pressure. Piles that displace the original soil, disturbing the surrounding soil and the interface, can be screwed in the soil or driven by vibration, hammering or jacking (Example shown in Figure 3.2). These piles densify the soil resulting in a relatively larger bearing capacity. In the case of cast in-situ piles, the displacing element is a plugged casing (Franki) or a drilling tool (Drilled Displacement Piles, e.g. Omega Piles).

The pile-soil interaction is dictated by these construction methods and the ground characteristics. However, these construction processes cannot be directly modelled by standard numerical methods and are particularly challenging

for analytical formulations. Advanced numerical methods, able to cope with these mechanisms, are being developed (Dijkstra et al., 2011; Engin et al., 2011; Fischer et al., 2007; Henke, 2010; Lobo-Guerrero and Vallejo, 2005), but are still not applicable to routine calculations, which forces the state of practice towards more straightforward methods for pile design.

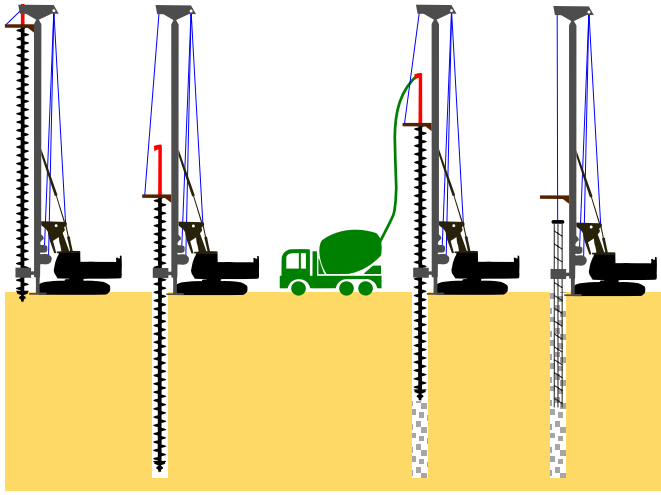

Figure 3.1. CFA Pile - A continuous flight auger drill is used to excavate a hole in the ground. Concrete is then injected through the drill as the auger is extracted. The cage of reinforcement bars is then inserted in the hole.

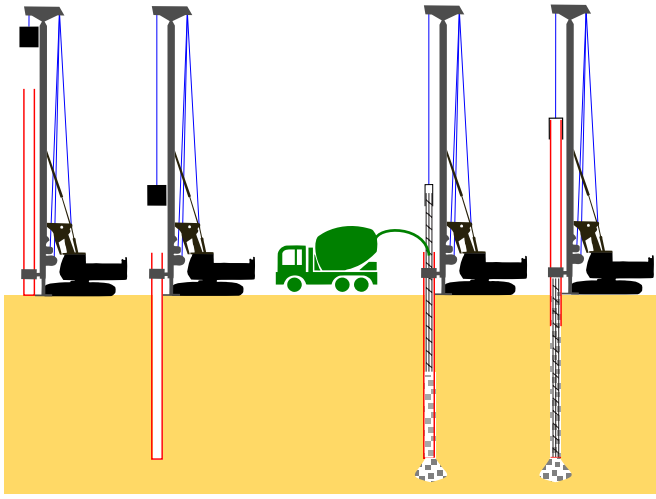

Figure 3.2. Franki Pile – A steel tube, with an expendable shoe, is driven in the ground using a hammer. Concrete and the cage of reinforcement bars are placed inside the tube. The tube is then removed while the concrete is compacted due to vibration.

Methods to estimate the pile ultimate bearing capacity under axial loading (UBC), normally consider the ultimate compressive load (UCL), but can also assess the ultimate tensile load (UTL). Shaft and toe capacity are normally analysed independently, with a few exceptions (Borghi et al., 2001). The toe capacity is defined as the average vertical normal stress ($q_{b\ max}$) to cause confined failure of the soil under the toe area (A_b). It can be calculated through the soil's undrained shear strength ($N_c.S_u$), cone resistance ($k_c.q_c$), or vertical effective in-situ stress ($Nq.\sigma'_v$) through their respective scaling factors: N_c, k_c, N_q (Fleming et al., 2008).

The shaft capacity is the integration along the pile depth and perimeter of the maximum shear stress (τ_{max}) at the pile-soil interface. This is normally calculated through an effective stress analysis ($\beta.\sigma'_v$), where the scaling factor represents both the interface friction coefficient and the ratio (K_{int}) of horizontal effective stress at the interface to in-situ vertical effective stress ($\beta=tan\varphi.K_{int}$). On top of that, it can also be related to the undrained shear strength ($\alpha.Su$) or cone resistance (q_c/μ) along the pile depth.

Design manuals and local practice recommend different values for these scaling factors based on pile type and ground conditions. Despite significant developments in experimental methods and analytical formulations (Randolph, 2003), recent assessments of current design methods show that there still is a considerable dispersion on the estimates of the capacity of driven piles (Jardine et al., 2005) and shaft friction for piles in clay (Karlsrud, 2014). Another issue is the definition of an ultimate toe capacity. It has been advocated that an ultimate toe capacity does not exist (Fellenius, 1999), or that for non-displacement piles it is only achieved at impractical displacements (Hirayama, 1990). In any case, a limit state of force and displacement for the toe response can be assumed for practical purposes, even if it doesn't represent physical failure.

To face these uncertainties, pile load tests are normally recommended and even required by law in some countries (ABNT, 2010), to confirm/calibrate the design predictions. The test defines the load settlement curve for a single pile, which can be analysed to determine the pile capacity (Chin, 1970) or to model the overall load-settlement response (Fleming, 1992; Massad, 1995). These methods tend to be very practical, but they consider the whole pile system through only the pile head response, disregarding the relation between the compressibility of the pile and the progressive shaft mobilization along depth. On top of that, it has been pointed out that with the commonly used pile spacing, test and reaction piles can interact, causing the obtained load-settlement response to be somewhat different from a single pile response (Comodromos et al., 2003).

Wood (2004) points out that a proper factor of safety for the ultimate limit state is intended to define a working load that indirectly guarantees the functionality of the structure without the need for direct calculations. However, for onshore structures this indirect approach tends to be insufficient, as rigorous limits of admissible settlements may call upon direct methods for settlement analysis. Pile settlements can be estimated through elastic-based methods (Randolph and Wroth, 1978), where the head load is resolved in profiles of settlements and axial load by imposing compatibility of displacements between the pile body and the soil (Poulos and Davis, 1968). The soil displacements are obtained through Mindlin's equations for a point load within an elastic semi-infinite mass (Mindlin, 1936). However, it should be noted that the pile loads in these methods are not directly bound by any account of axial capacity (Poulos, 1989).

These solutions assume the ground profile through averaged values or specific types of variation, such as a linear increasing shear modulus. Without a more detailed ground characterization, it is suitable to adopt these models, as they are easy to calibrate and the relation between parameters and results is normally straightforward. However, with the progress of continuous profiling in-situ tests, such as the CPT, other methods that can explicitly consider the different ground characteristics along the pile can be used.

The load-transfer method, first proposed by Coyle & Reese (1966), calculates the load and settlement profiles along the pile through mobilization functions for the pile toe and at several points along the shaft. By imposing a toe displacement, the equilibrium of the pile segments can be iteratively calculated upwards until the pile head. The capacities of both the toe and the shaft have to be described as functions of the local pile settlement and can be bound by the pile capacity (Poulos and Davis, 1980). Heterogeneous ground profiles can be directly modelled by assigning different functions along the pile.

These mobilization functions have, for the most part, only been calibrated for pile loading. However, there are important mechanisms taking place through the unloading stage. Irreversible deformations and residual loads are important examples related to the plasticity of the pile-soil interface and the rebound of the pile toe. Moreover, by ignoring the unloading path the models predispose the range of possible solutions for equilibrium. Therefore, two modifications are proposed for the general load transfer method:

1. Include a distinct unloading path in the load transfer functions.
2. Change the variable of pile settlement for a relative pile-soil settlement, enabling the framework to consider the effects of ground displacements.

The first point was adapted from the mathematical model of Massad (1995), which has been successfully applied to the analysis of bored and driven piles (Massad, 2014; Viana da Fonseca et al., 2007). The model considered a uniform shaft friction along the whole pile and the shaft mobilization depended on the head settlement. The second point has been proposed for the analysis of piles in interaction with deep excavations (Korff, 2012), where a hyperbolic tangent mobilization function was combined with linear profiles of ground settlement to derive analytical solutions of the interaction consequences.

In this thesis the transfer functions, with loading and unloading paths, are defined along the whole pile and their mobilization depends on the local relative pile-soil settlement. The modified method is implemented in a spreadsheet software with subroutines programmed in Visual Basic for Applications (VBA). This framework is considered an accessible option for educational purposes and for any user to update the method if they wish to do so. A field load test is used to calibrate the model and some examples are discussed to illustrate the benefits of including the unloading path and the relative displacement variable.

A proposal to use this framework as part of a teaching methodology for axially loaded piles is presented in Dias and Bezuijen (2015b). This was not included in this thesis, as it was deemed irrelative to the main problem of pile tunnel interaction.

3.2. Load transfer method

For this calculation routine the pile body is defined by its cross section area (A_p) and perimeter (P_p), volumetric weight (γ_p), length (Zp) and elastic modulus (E_p). The pile is divided in elements of equal length (dl), defining nodes from the head (i = 1) to the toe ($i = n$). At each node, the parameters for the shaft mobilization are specified so that variations with depth can be modelled. The ultimate head loads are calculated in compression (UCL = F_{toe} + F_{shaft} - W_p) and in tension (UTL = F_{shaft} - W_p) considering the weight of the pile body (W_p). If this is not considered, it can lead to misleading assessments of the direction of shear forces along the pile shaft. For example, an increase in normal stress with depth can be interpreted as a downward shear force, but it can also be the result of an upward shear force with a magnitude smaller than the weight of the pile body ($\tau.Pp < \gamma_p.Ap$). The normal axial stress (σ) is calculated downwards for all nodes through the expression:

$$\sigma^{i+1} = \sigma^{i} + \gamma_p.dl + \frac{P_p.dl}{2.A_p}\left(\tau^{i} + \tau^{i+1}\right) \qquad (2)$$

where τ^i is the shear stress acting at node i, determined through the load transfer models.

The pile settlement (δp) is calculated upwards through the expression:

$$\delta_p^i = \delta_p^{i+1} + \frac{\sigma^i + \sigma^{i+1}}{2.E_p}.dl \qquad (3)$$

These equations form an implicit system to be solved iteratively along the pile nodes for an imposed relative settlement at the pile toe, which can be easily achieved in a spreadsheet with iterative calculations. In a standard load-transfer formulation, without unloading paths, the system forms a bijective relation between loads and settlements. A procedure that explores the domain of toe displacements will automatically obtain the domain of head loads, tracing a unique load-settlement curve. However, in the present formulation, the relation between loads and displacements depends on the previous states that defined the limits of toe and shaft mobilization.

In this case the load at the pile head defines a boundary condition and the toe relative displacement has to be determined so that there is a balance between the normal stress at the pile toe and the mobilized toe reaction. This can be achieved with root finding schemes such as the false position method (Figure 3.3) or Ridders' method (Press et al., 2007).

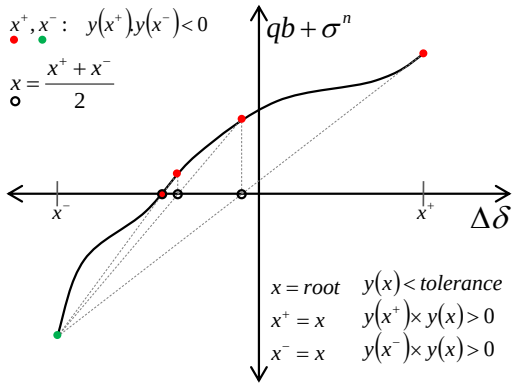

Figure 3.3. Example of a root search routine with the false position method

Both methods have been tested, and the false position method was more efficient for this system. This calculation routine is implemented in a Microsoft Excel (2016) spreadsheet with subroutines in VBA. In order to change the variable of pile settlement for a relative pile-soil settlement, it is important to properly define the displacement variables. Vertical displacements, also called settlements,

(δ) are assumed positive downwards, and relative displacements ($\Delta\delta$) are defined as the difference between the pile settlement (δp) and the soil settlement (δs) at any point along the pile (Figure 3.4). So a negative $\Delta\delta$ means that the soil settles more than the pile in that point, developing a downward shear stress at the interface, also known as negative friction. At the pile toe, $\Delta\delta < 0$ indicates that there are no reaction forces from the toe, as the soil is not in contact with it. On the other hand, a positive $\Delta\delta$ is associated with upward shear, also called positive shaft friction, and an upward toe reaction. The displacements are always measured from the reference position of each point, calculated considering the pile head at the ground surface and uniform segments along the unstrained pile body.

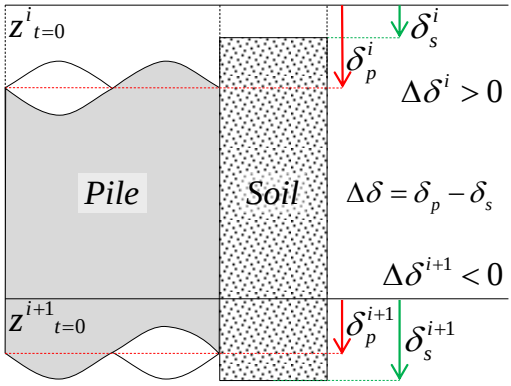

Figure 3.4. Scheme defining the soil settlement (δs), pile settlement (δp) and relative displacement ($\Delta\delta$).

The foundations of the load transfer method are the models defining the reactions from the shaft and toe as functions of the relative displacements. Since the method was proposed it has been recognized that the shape of these functions varies considerably, so that particular curves have to be used at different depths (Coyle and Reese, 1966). Based on a field test and laboratory experiments on steel friction piles in clay, three curves were proposed to represent different depths (Figure 3.5a), where the shaft friction was normalized by the shear strength near the piles, which was estimated from the unconfined compression tests. Kraft et al. (1981) modelled these curves with a theoretical elastic model for the pre-peak section, and the results of direct shear tests for the post-peak section.

Briaud and Tucker (1984) calibrated 2-parameter hyperbolic curves to model both shaft and toe mobilization of piles driven in sand and proposed correlations to SPT values. They also made one of the few references to an unloading path

for a load-transfer analysis, although it was used indirectly to propose an offset in the mobilization curves to correct for residual stresses. In a general analysis of bored cast-in-place piles, Hirayama (1990) also used hyperbolic curves (Figure 3.5b) with specific values for the toe and shaft mobilization. To estimate the ultimate shaft and toe capacities, a few correlations with CPT and SPT values were discussed for tests in Japan.

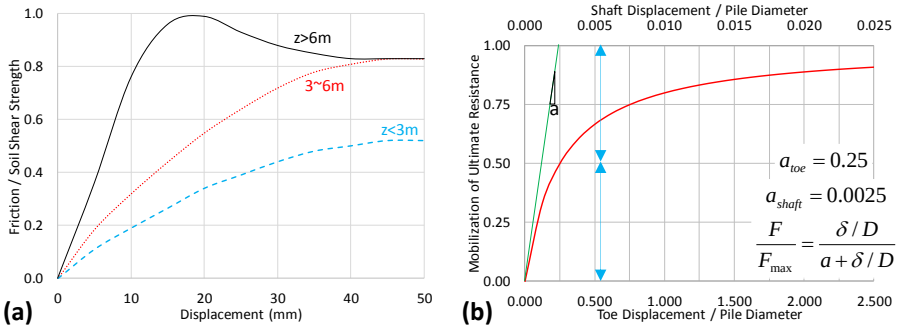

Figure 3.5. Load transfer functions for shaft mobilization from (a) Coyle and Reese (1966) and (b) Hirayama (1990)

Two load tests on concrete bored piles have been used by Frank et al. (1991) to calibrated tri-linear mobilization models based on pressuremeter tests and French design methods (Figure 3.6a). Developing analytical solutions for homogeneous and Gilson ground profiles, Guo and Randolph (1998, 1997) proposed elastic-perfectly plastic load transfer models based on elastic soil properties. For the shaft friction, full mobilization was achieved at a displacement of 1 to 2% of the pile radius. Other studies developed this multi-linear approach further, considering the possibility of softening along the shaft (Figure 3.6b), in an explicit mathematical formulation (Liu et al., 2004; Zhao et al., 2005).

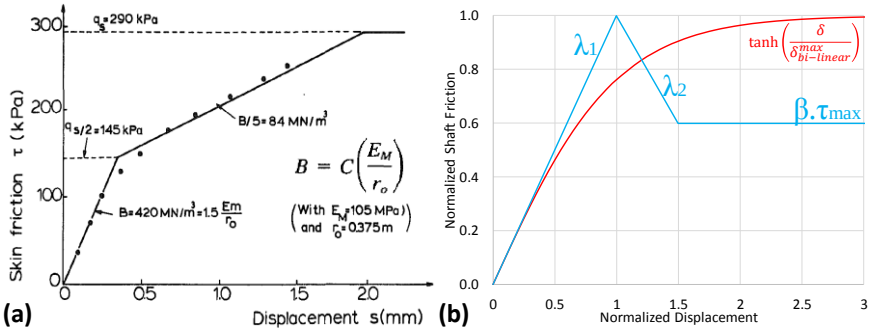

Figure 3.6. Load transfer curves for shaft friction from Frank et al., 1991 (a), Korff, 2012 and Liu et al., 2004 (b)

A recent study also proposed the use of a hyperbolic tangent function (Korff et al., 2016). The function is asymptotic, as the hyperbolic models, and it depends on the displacement used to normalize the variable, which was recommended as the displacement for maximum shaft mobilization in a bi-linear model (Figure 3.6b). There have also been proposals to determine these curves with direct field tests, through the incremental loading of a CPTU cone followed by a dissipation test, where both the sleeve friction and the displacements are recorded (Ali et al., 2010).

Through a parametric numerical analysis with a nonlinear elastoplastic constitutive model, Lee and Salgado (1999) determined the load-settlement curves for the toe of axially loaded non-displacement piles in sand, depending on the stress level and relative density. The curves could be fitted with exponential functions (Figure 3.7a). Multi-linear models have also been proposed by Liu et al. (2004), but the softening feature was never mentioned for the toe (Figure 3.7b).

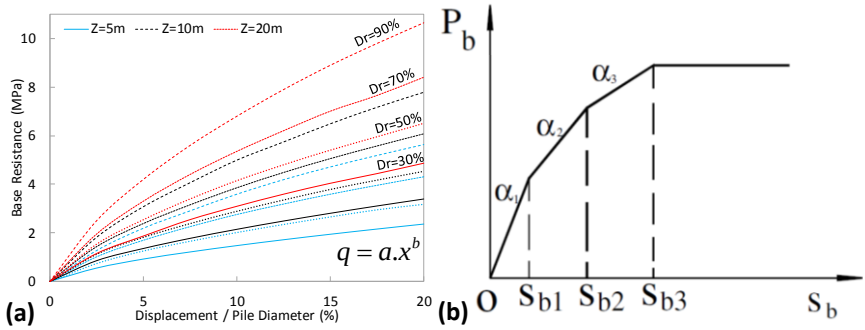

Figure 3.7. Load transfer curves for toe mobilization from Lee and Salgado, 1999 (a) and Liu et al., 2004 (b)

This brief literature analysis reveals that, despite the long history of the load-transfer method, there is still considerable divergence regarding the appropriate models and how their parameters relate to the different ground conditions and pile types. In the light of these, proper analysis still rely on full scale instrumented pile load tests (Zhang et al., 2011) or centrifuge studies (Fioravante, 2002). However, a few points came about in most studies. The displacements to mobilize the shaft in shear are much smaller than to mobilize the toe in compression. While the former is normally achieved with a few millimetres, the latter can reach 10-20% of the pile diameter, or more. The interaction of these two scales in a foundation system leads to displacements at the shaft that significantly surpass the limit for interface slippage. This is a fundamental aspect to be considered to formulate the mobilization models.

3.3. Shaft mobilization model

This study adopted a tri-linear model for the shaft friction. The interface shear stress can be mobilized both upwards and downwards, and it was assumed that in both directions the same absolute value is achieved at full mobilization (τ_{max}). Once full mobilization is reached both models are perfectly plastic, in the sense that the displacements can continue to develop without changes in the mobilized shear stress. The model defines a transition level of mobilization (τ_{ep}) from the elastic (*S1*) to the elastoplastic (*S2*) slopes, which are defined directly through the ratios of shear mobilization to relative displacement ($\tau/\Delta\delta$). If unloading develops after the transition level has been reached, it develops through a distinct unloading slope (*S3*). An example diagram for this model is traced in Figure 3.8.

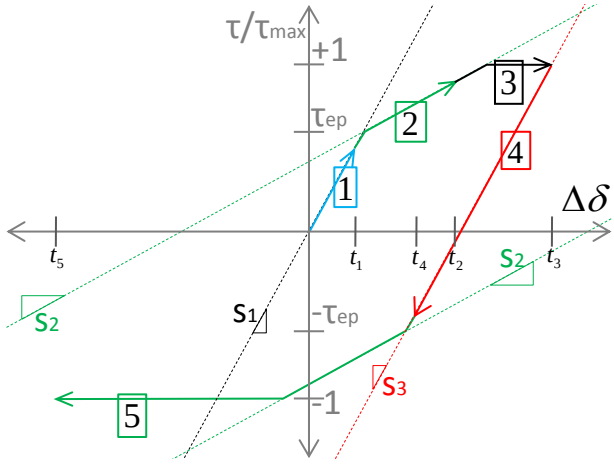

Figure 3.8. Scheme for the tri-linear mobilization model.

From the initial condition (t = 0) of zero mobilization, shear starts to develop through the elastic slope, as in Step 1. During Step 2, the transition level is reached and from there on the elastoplastic slope is used to determine the resultant shear. Step 3 reaches the point of full mobilization, from where the displacements can develop further with no change in the mobilized shear. Step 4 presents an increment in the opposite direction, which immediately results in demobilization along the unloading slope. These same patterns are used for negative mobilization, where there is a change in slope once the transition mobilization is reached, which continues until full mobilization, as can be seen in Step 5.

For a more flexible implementation it is useful to define these functions so that from any equilibrium condition, a solution can be found regardless of the size of the increment, for either loading or unloading. This is possible if the mobilization

functions are formulated so that they only need to be updated once equilibrium is reached again, but not during iterations. At each step the values of shear mobilization (τ/τ_{max}) and relative displacement ($\Delta\delta$) have to be recorded for the next step. Based on those values, the resultant shear for any increment of relative displacement can be calculated as described in Figure 3.9.

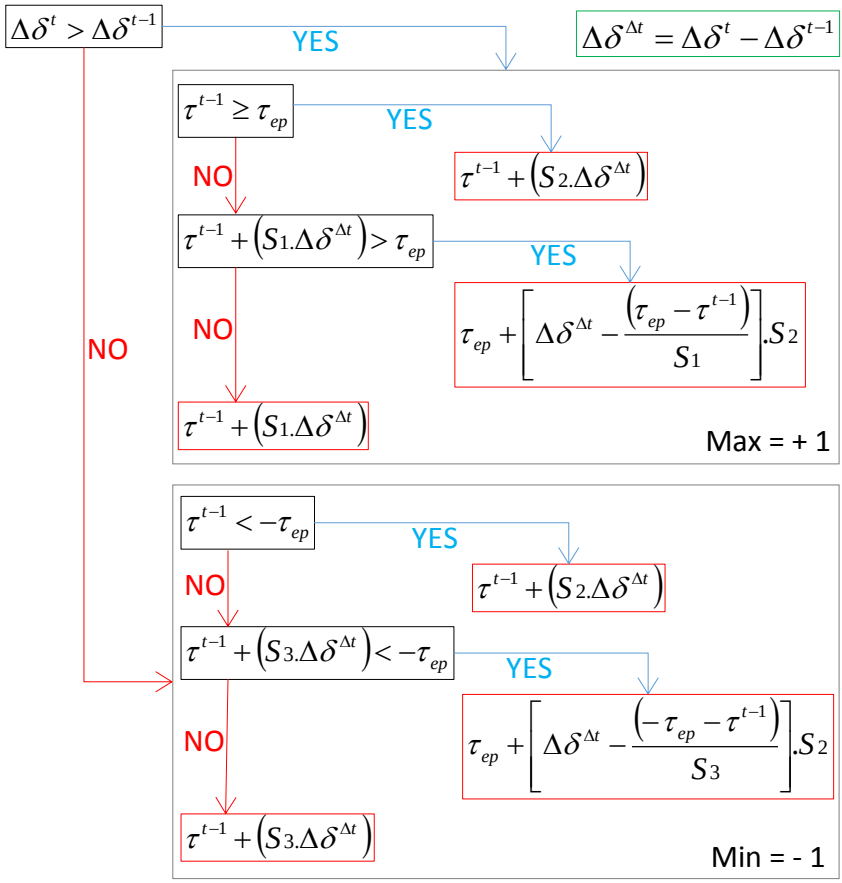

Figure 3.9. Calculation algorithm

3.4. Toe mobilization model

An exponential model was proposed for the pile toe, where mobilization only occurs for positive relative displacements, as, by definition, negative values represent a condition where the soil is not in contact with the pile toe. For the loading branch a monotonic function has to be defined, starting at the origin ($\Delta\delta$=0, q_b=0) and reaching full mobilization ($q_{b\,max}$) at a certain relative displacement, defined as $\Delta\delta^T$. An efficient way to model this mobilization is to use a power function in the form:

$$\frac{q_b}{q_{b\max}} = \left(\frac{\Delta\delta}{\Delta\delta^T}\right)^{\chi} \quad (4)$$

Figure 3.10a presents the resultant curves where 10 to 60% of the toe resistance is mobilized at 10% of $\Delta\delta^T$. This index is normally used in the state of practice to define the toe reaction. The unloading branch has to be defined in a way that does not violate the restrictions of the domain, that is to say that it shouldn't calculate toe mobilization for $\Delta\delta < 0$. Considering this limitation and the large range of displacements for toe mobilization, as discussed in Section 3.1, a fixed set of slopes, such as defined in the shaft model, is not an appropriate solution. Instead, a variable slope model can easily be implemented through a rebound factor (*Rb*). From a certain state of mobilization ($\Delta\delta^*$; q_b^*), the rebound factor defines the relative displacement necessary to reach a state of zero toe reaction ($Rb.\Delta\delta^*$) through a linear path. This is equivalent to define a surrogate linear model where full mobilization, set at q_b^*, is reached at $\Delta\delta^*$, and null mobilization at $(1 - Rb).\Delta\delta^*$. Mobilization will remain null for any new step where $\Delta\delta < (1 - Rb).\Delta\delta^*$. The linear unloading slope will be followed in case of $(1 - Rb).\Delta\delta^* < \Delta\delta < \Delta\delta^*$, and the original loading model shall be used again when $\Delta\delta > \Delta\delta^*$ occurs.

An example for this model for $\chi = 1$ and $Rb = 0.1$ is on Figure 3.10b. The steps with primary loading (Steps 1 and 4) follow the line between (0 ; 0) and ($\Delta\delta^T$; 1). At each unloading step (Steps 2, 3 and 5), the stress is mobilized/demobilized considering the stresses at $\Delta\delta^*$ as the maximum through the range defined by *Rb*. For relative displacements smaller than this range, the toe reaction is zero and only re-mobilized again inside the range.

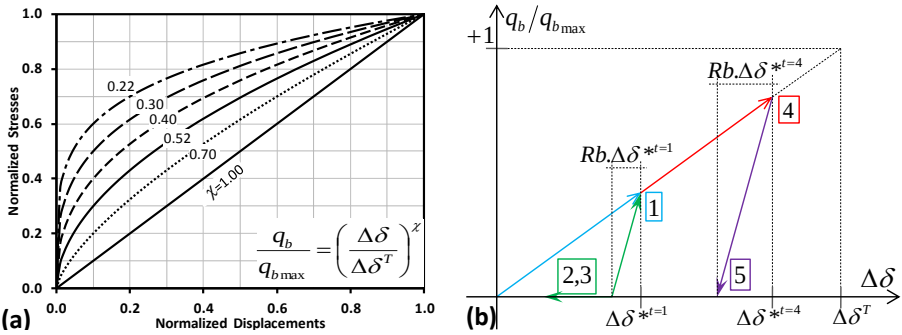

Figure 3.10. Monotonic functions for the loading branch of the toe model (a) and toe mobilization model (b)

3.5. Validation

To calibrate the models discussed hitherto, an adequate axial load test is required with some form of strain measurements along the pile body. For recommendations on well documented test procedures see Bica et al. (2014). However, a systematic methodological issue challenges the validation of the models proposed in this study, namely that the instrumentation data is normally not recorded during unloading. The authors identified one study that defies this trend (Glisic et al., 2002), so that it could be used to validate the pile response during both loading and unloading.

The tests were conducted in Taiwan with 35 m long, 1.2 m diameter cast-in-situ piles, bored by means of reverse circulation. These piles were designed for 365 tons of compressive capacity and 220 tons of uplift capacity. The test loads were applied through hydraulic jacks at the pile head. The poured concrete was designed for a compressive resistance of 24.5 MPa at 3 weeks. The steel reinforcement was composed of 24D10 longitudinal with D4@15 cm shear bars along the top cage (0 to 12 m), and 16D10 longitudinal with D4@25 cm shear bars along the middle (12 to 24 m) and bottom (24 to 32 m) cages.

The axial strains were obtained with eight long-gauge (4 m) fibre optics sensors placed in series along the main rebar, starting at 1 m depth. The sensor consists of two optical fibres, the measurement fibre and the reference fibre, contained in the same protection tube. The measurement fibre is coupled with the host structure and is prestressed to 0.5% to measure both shortening and elongation. The reference fibre is loose and independent from the structure in order to compensate thermal influences to the sensor. The optical signal is sent from the reading unit through a coupler to the sensor, where it reflects off mirrors placed at the end of each fibre and returns back to the reading unit where it is demodulated by a matching pair of fibres. The returned light contains information concerning the deformations of the structure. The resolution of the system is 2 μm. The eight sensors were installed in a single chain, placed along the main rebar, one sensor in each cell. On top of that, the settlements at the pile head were monitored with linear variable differential transformers (LVDTs). The ground was composed of intercalated layers of low plasticity clay (CL) and silty sand (SM), according to the unified soil classification system.

The measured distributions of axial load along the pile depth for the full load-cycle are in Figure 3.11. Between the depths of 20 and 24 m the axial load is practically constant, indicating a soil layer with poor mechanical properties, as described by Glisic et al. (2002). However, the load profile presents a very distinctive slope for the last three loading stages, showing an increase with depth

that was not evident before. A possible explanation for that local response would be that in the first stages the weight of the pile is balanced by the shaft friction, but that this friction degraded in the last loading stages. However, this interpretation is not part of the proposed methodology and cannot be verified at this moment.

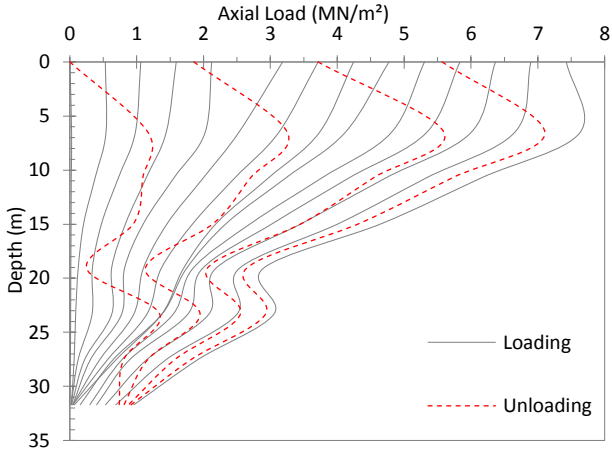

Figure 3.11. Distributions of axial load recorded in the pile load test.

Apart from that, the shaft friction varied significantly along the depth, as can be noted in the changes in the slope of the axial load profiles. It is noticeable how the unloading steps do not match any loading profile. It should be noted that these profiles were traced from the average strains along seven sections of the pile. The pile head settlements were significantly higher for loads above 4 MPa, as it can be seen in Figure 3.12a. After unloading, significant axial loads and a residual settlement of 41 mm remained locked in the pile.

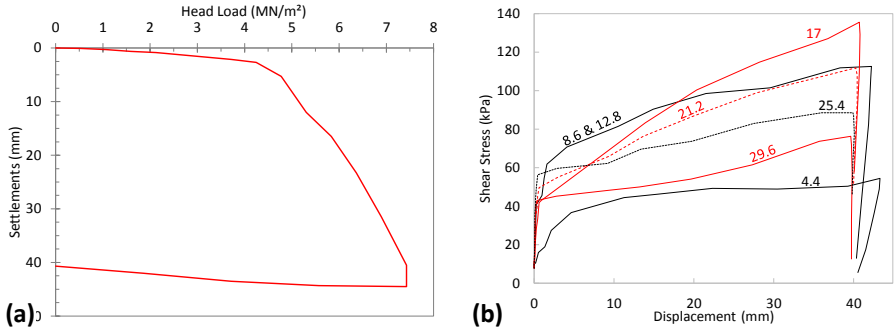

Figure 3.12. Head settlements recorded (a) and shaft mobilization curves (b) recorded in the pile load test

The first attempt to calibrate the load transfer models was to calculate, using Equation 2, the average shear between each of the seven segments. These values were then related to the displacements along the pile, calculated from the head settlement and the accumulated strains until the section of analysis. These calculated curves can be seen in Figure 3.12b, which could be fitted well with the tri-linear model discussed in Section 3.3. The highest friction was attained at the depth of 17 m and in all models the elastic slope (*S1*) was significantly higher than the elastoplastic (S2) and similar to the unloading slope (*S3*) in some cases.

Five phases of the calibration process (M1 to M5) are discussed. The first one used the curves from Figure 3.12b, assuming *S1* = *S3*, through the entire length of each section, which resulted in a very stiff pile response, as it can be seen in Figure 3.13.

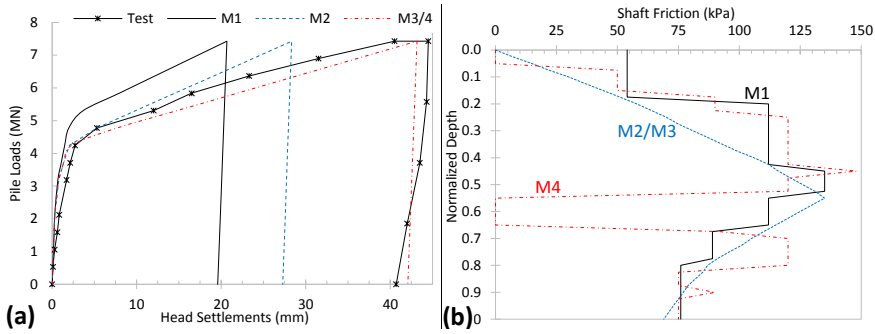

Figure 3.13. Calibration phases in terms of load-settlement curve (a) and maximum shaft friction along depth (b).

The second model (M2) interpolated linear segments between the measured values of maximum friction. The result was less stiff, in good agreement along the first segment of the load-settlement curve, but still far from the test results in the second segment. The third model (M3) used the same maximum friction profile, but reduced the elastoplastic slope (*S2*) by 45%, which resulted in a fair agreement through the whole load-settlement curve.

However, another point of validation for the model are the profiles of axial load. Figure 3.14 presents the model results against the measurements for two stages of loading and two of unloading. The agreement for M3 is rather poor, which highlights how a load-settlement calibration doesn't guarantee correspondence of axial loads. In light of this, the fourth calibration strategy was attempted (M4). For each head load, the load transfer method was used to match the profile of axial loads through local variations of mobilized shaft friction, which was set independent of pile settlements at this point. Once the axial loads matched, the toe displacement was changed so that the head settlement matched the

measured value. At this stage, the shear force and the local settlement, which included the pile compressibility, were recorded for each point along the shaft. These values were then used to calibrate the tri-linear model. The results during loading improved significantly, but they were still far off during unloading, which invalidated the initial assumption that *S1* was equal *S3*. The final step was to calibrate the unloading slopes separately (*S3* ≠ *S1*). This resulted in a very good agreement with the test, as can be seen in Figure 3.15.

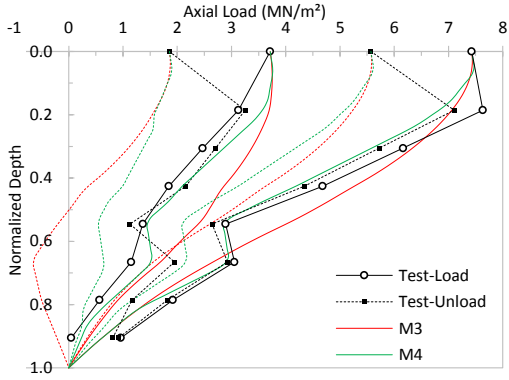

Figure 3.14. Calibration phases in terms of axial load profile.

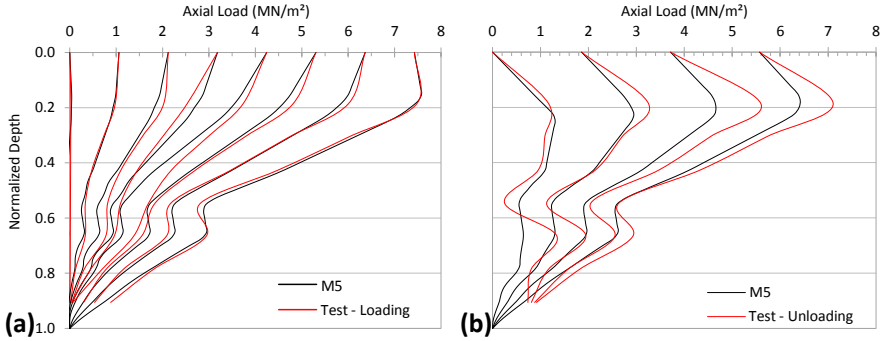

Figure 3.15. Axial load profile along depth for the calibration model M5 during loading (a) and unloading(b).

3.6. Conceptual results

A few conceptual examples will be presented in this section to illustrate some features of the load transfer model with the characteristics discussed in this chapter. The first examples consider a 20 m long, 1 m in diameter pile. The shaft resistance is based on a geostatic stress distribution, with a soil volumetric weight of 20 kN/m³, and a scaling parameter $\beta = 0.3$. The resultant shaft capacity is F_{shaft} =3.63 MN. The shaft model is set perfectly-plastic, with *S1* = *S3* = 0.2 mm^{-1}

and $S2$ = 0. The toe model is set with a maximum displacement $\Delta\delta^T$ = 100 mm, rebound factor Rb = 0.1, and mobilization exponent χ = 0.3. The toe capacity is set to 4.1 MPa, which corresponds to 50% the ultimate compressive load. The pile body had a volumetric weight of 25 kN/m³ and a compressibility of Ep = 10 GPa. A full load-unload cycle was simulated.

The load settlement curve is presented with the toe reaction and the global shaft force (Figure 3.16a). The maximum settlement was 114 mm, which is the results of $\Delta\delta^T$ and the compressibility of the pile body. During loading, the shaft was fully mobilized at about 4 MPa, when the pile had undergone about 15 mm of settlements. This is 3 times the settlement necessary to locally mobilize the shaft ($1/S1$) and highlights the effect of the pile compressibility on the shaft mobilization. During unloading, the toe rebounded to about 55% of its capacity, requiring a downward shaft force to be in equilibrium. The residual settlement was around 100 mm.

The profile of axial load with depth exposes more details of this mechanism (Figure 3.16b). The progressive increase in slope along the load profiles indicates a distinct shaft mobilization along depth, especially for the first loading steps. During unloading, negative slopes of the load profiles indicate a reversal in the friction direction, creating what is referred to as residual loads locked in the pile. Looking directly at the levels of shaft mobilization along depth (Figure 3.16c), this evolution can be better understood.

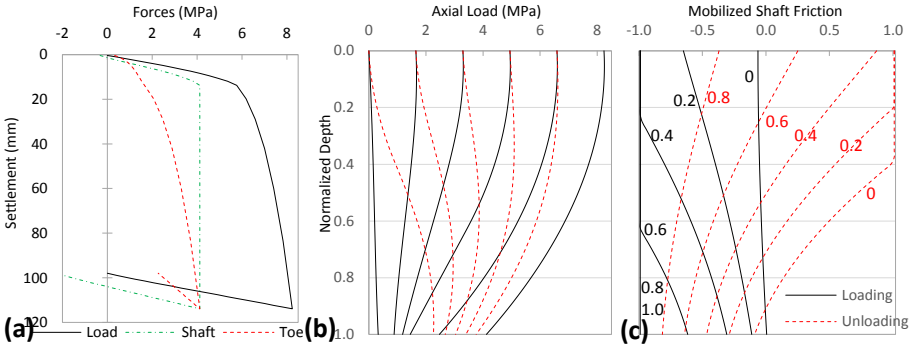

Figure 3.16. Conceptual simulation - full load-unload cycle: load settlement curve for the forces at the pile head, pile toe, and the total shaft force (a); profiles of axial load with depth (b); mobilized shaft friction for different loads, normalized by the maximum load (c).

During loading, mobilization advances from the top down, as the higher loads on top squeeze the pile increasing the relative displacement. At about 80% the maximum load, the shaft is fully mobilized. During unloading, as the load around

the pile head decreases, the elastic rebound of the pile body and the non-elastic rebound of the pile toe, progressively demobilize the shaft from the top down. Already at 60% the maximum load, the shaft friction at the top started to act downwards.

Residual loads are not routinely measured in load tests, which normally disregard the strains before the loading steps. This has been associated with erroneous estimations of pile resistance and misleading models, as the critical depth for shaft capacity (Fellenius, 2002a, 2002b). These residual loads depend on the process of pile construction and long term set-up effects, and to compute them without explicitly modelling these factors will always depend on arbitrary modelling procedures. However, the sequence followed in this example, to load the pile to failure and completely unload it, is a procedure that has been suggested to model pile installation and compute residual loads in a finite element analysis (Altaee et al., 1992).

To explore this possibility, different residual loads (final load profile after a full load-unload cycle) were calculated to explore the parameters controlling its magnitude. The same parameters were considered along the shaft, the pile body was considered weightless, but with the same compressibility, and the toe response was changed in terms of rebound factor (*Rb*) and capacity. To focus the analysis on the mechanism, the profiles were normalized by the maximum head load and presented with the profile for the maximum load and the profile for maximum negative friction and zero head load.

From the results shown in Figure 3.17, one can readily observe that from the pile head until a certain depth, the residual load profile follows the curve of full downward shaft mobilization.

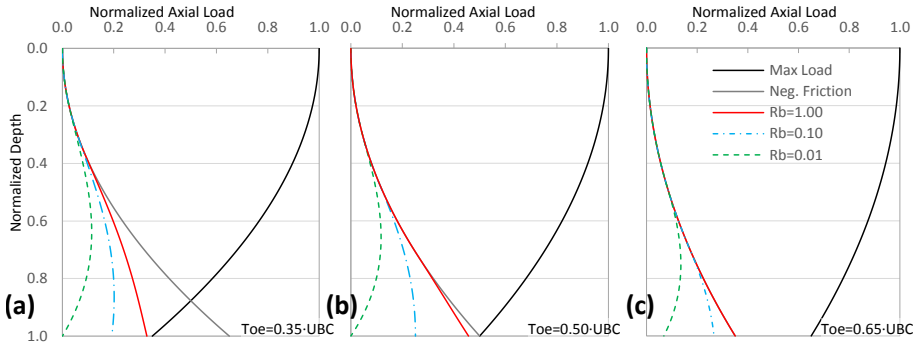

Figure 3.17. Residual loads after a full load-unload cycle considering toe resistance of 25 (a), 50 (b) and 75% (c) of the UCL. The legend depicts the different toe rebound factors.

For these conditions, the normalized depth at which the profiles start to shift is roughly the same as the ratio between the toe capacity and the ultimate compressive load. A consequence of equilibrium is that the residual toe load cannot be higher than the toe capacity or the downward shaft capacity. From this upper bound the residual toe load will be roughly proportional to the toe rebound. When the unloading range of the toe ($Rb\ \ \Delta\delta^T$) is smaller than the one of the shaft, and the toe capacity is less than 50% UTC, the residual toe load will be zero.

3.7. Overview

The framework for pile analysis presented in this chapter fulfils the requirements for the first part of the methodology outlined in Section 2.5. It is an accessible system, able to cope with ground settlements. It can also be used with the different methods to predict pile capacity and directly accounts for the necessary displacements to mobilize it. The discrete formulation can model the different properties along the pile depth, as in the case of soil layering. Modelling distinct unloading functions enables loading cycles to be simulated as well as the analysis of residual loads.

These unloading functions are also very important to model the effects of ground displacements. While normally understood as the consequence of a working load reduction, in a framework based on relative displacements, unloading can also be the consequence of ground settlements. In other words, it can be the result of the pile body moving up or the ground moving down, it only depends on the resultant relative displacement.

This framework is flexible enough to simulate various pile conditions, but, as any mathematical model, it represents nothing without a proper input. At the moment, instrumented pile load tests are the most reliable source for this. However, most real cases don't have that level of information, so estimates of pile capacity and mobilization displacements from the state of practice can also be used. The mobilization functions can be calibrated within the framework, which in turn enables a link between load-displacement and pile compressibility along the pile.

At this point it is not possible to trace definitive relations between the parameters of the load mobilization functions and the ground properties or even its general composition (clay or sand). The same can be stated for the difference between bored and driven piles. Therefore, it is important to calibrate these functions with a properly instrumented pile load test. The concept of this framework would ideally reach the state of practice to the point where the

geotechnical characterization for a soil/pile system would aim at calibrating the parameters of the model. This would require a characterization of shaft and toe capacities, always associated with corresponding relative displacements and the mobilization functions, as they can be promptly used in this straightforward formulation.

4. Tunnelling

This chapter presents the second part of the methodology outlined in the end of Section 2.5, which required a method to predict the ground movements due to tunnelling. This is perhaps the most central and recurrent research topic in soft ground tunnelling, with a very extensive literature. Therefore, the option of analysing a comprehensive data compilation was not as attainable as for the problem of pile tunnel interaction (Section 2.3). Instead, this chapter tries to focus on a basic question: What are the forces acting on the excavation perimeter of a tunnel?

This is a very difficult question to answer for conventional tunnelling methods, where the construction advances through a cyclic process of excavation, spoil removal and support installation. These methods often rely on a partitioned excavation, where part of the face can still offer support while a structural element is applied (see Figure 4.1).

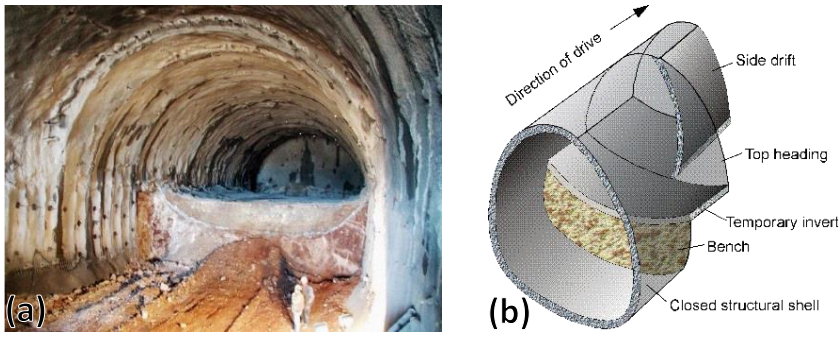

Figure 4.1. Partitioned excavation face, photo (Hoek et al., 2008) showing top-bench division with a temporary shotcrete invert (a) and scheme (Hoek, 2004) with other possible sections (b).

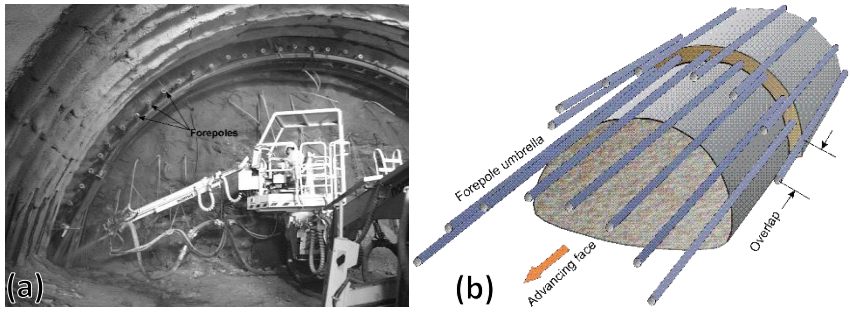

Figure 4.2. Supporting elements ahead of the face, photo (Kavvadas, 2005) with forepoles and fibreglass injections (a) and scheme (Hoek, 2004) showing how these systems overlap (b).

Support elements can also be driven ahead of the face, combined with different techniques of grout treatment (see Figure 4.2). More often than not, these elements are not modelled explicitly, but represented through an adaptation of the available variables (as explained in Section 2.5). Therefore, the internal support pressure used in most models isn't the *"force acting on the excavation perimeter of a tunnel"*, but an abstract adaptation of the combined effects of partial excavation, ground reinforcement, and different support elements.

Arguably, this question has a more manageable answer for mechanized tunnelling, specifically for closed-face tunnel boring machines (Figure 4.3). This construction technique offers a more direct control over the pressures acting on the excavation. A paste of ground mixed with additives is kept under pressure in front of the TBM, while pressurized grout is injected around the lining from the back. These processes can be actively controlled through the operation of mechanical and hydraulic systems composing the machine.

Figure 4.3. Illustration of a tunnel boring machine working under a city (ixtract GmbH, 2014).

Mechanized tunnels are constantly used in urban spaces, and have become a viable option for projects with strict limits of disturbance, where underground solutions were deemed unsuitable in the past. So it is fair to assume that a great deal of pile tunnel interaction cases will happen around tunnel excavated with TBMs. Therefore, this chapter will present an attempt to:

1. Study how the excavation fluids act around a TBM, setting up a comprehensive mathematical model to compute the forces.
2. Adapt a methodology to predict the ground movements due to tunnelling to take these forces as an input.

To tackle the second point one has to understand the frameworks used to evaluate ground displacements. For more than 30 years now, the traditional empirical methods (Peck, 1969) and analytical solutions (Sagaseta, 1987) are being replaced by numerical calculations (Rowe et al., 1983). However, most of these calculations are based on the stress release method, where a certain fraction of the in-situ ground stress is applied as internal forces around the tunnel. So the boundary stresses are not at all linked with the TBM operation, but are instead based on the in-situ stress.

This chapter will proceed to review these basic numerical techniques, and how they have been adapted so far to represent mechanized tunnels (Section 4.1). An overview is then presented explaining the main elements guiding the interaction between the tunnel boring machine and the ground (Section 4.2), based on a review of published sources. From there on, a new methodology is presented to predict the forces and consequent ground movements during the phases of grout injection (Section 4.3) and grout consolidation (Section 4.4). The methodology is then validated for an instrumented case study of a tunnel in The Netherlands (Section 4.5).

4.1. Numerical modelling of tunnel construction

Section 4.1 is based on the Conference Paper: Dias, T.G.S., Bezuijen, A., 2014. Tunnel modelling: Stress release and constitutive aspects. ***8th International Symposium on Geotechnical Aspects of Underground Construction in Soft Ground****, Seoul, South Korea.*

Tunnel construction in soft ground has evolved significantly over the last 20 years, especially on the matter of settlement control. The routine volume loss of mechanized tunnels decreased from 6% to less than 1%. This was achieved by guiding the TBM operation to control the main factors that induced soil displacements, like the face pressure and the soil-lining void closure. This

approach was effective but tended to analyse these factors individually with no account for their possible influence on the global mechanism of tunnel construction.

The same pattern emerged from tunnel design methods that are particularly focused on the surface settlements. Again, significant contributions came from this; the settlement trough has been thoroughly analysed since its effect on buildings was addressed by Burland and Wroth (1974). Its description and quantification was of utmost importance for the development of underground constructions in urban centres without jeopardizing the stability of surface structures.

Alongside of these trends, the use of the finite element method for the analysis of geotechnical problems has increased notably. However, the vastness of choices in modelling procedures, which include the constitutive model, mesh, parameters and boundary conditions, tend to produce results that are user-dependent and often limited in the aspects they can reproduce from real cases or physical models. Ergo a great deal of tunnel modelling aimed solely on predicting the settlement trough, and did so without accounting for the effect of the new construction techniques. To achieve a better prediction, boundary conditions, constitutive parameters or state variables were sometimes adapted without a clear physical meaning. This normally hindered the model's reliability and capacity to cope with the different tunnelling or soil conditions.

Considering these aspects, this section presents an analysis of the basic principles of plane strain numerical modelling of tunnel construction. The literature review presents how the basic stress release concept evolved to account for TBM tunnel construction. That is followed by two groups of analyses: a simple linear elastic model to remark on the effects of the soil compressibility and initial stress state and a comparative analysis on the effects of different constitutive models to represent the soil. The tunnelling convergence and settlement trough as well as the stress paths on soil elements at the crown and at springline will be presented.

4.1.1. Literature review

The underground opening of a tunnel can be evaluated mechanically as a simple process. For an unlined tunnel the stress state on the imaginary boundary surface of the excavation is taken from the initial in-situ stress to a condition of zero normal and shear stress. This path can be done in increments that are normally called stress release factors (λ) and represent a percentage of the full path. For the case of a lined tunnel it is normally assumed that part of the stress release will develop with a free boundary (λ), as in the unlined tunnels (Figure 4.47).

After the lining is installed the remaining stress (1-λ) will be released and reach equilibrium with the lining. The soil-lining interaction and the lining rigidity will then dictate the state of equilibrium.

A series of analyses on modelling procedures for TBM tunnels was initiated by Rowe et al. (1983), that also remarks the importance of modelling the soil's cross-anisotropic deformability to achieve better displacement predictions. Knowing the gap that exists between the excavated boundary and the lining, the partial stress release factor will be the one that induces a tunnel converge that closes that gap. From then on, soil-lining interaction develops. On subsequent studies, this gap parameter was revised to account for the quality of workmanship, face protrusion and other aspects. The bottom line is that a displacement criterion controlled the partial stress release factor.

In an attempt to simulate the three-dimensional aspect of a TBM tunnel, two plane-strain models were combined, for the transversal and longitudinal sections of a tunnel (Finno and Clough, 1985). Cohesive soils were represented by the modified cam clay model and cohesionless soils by a nonlinear pseudo-elastic law. The tunnel face in the longitudinal model was displaced until the horizontal forces matched the measured TBM jacking forces. The ratio between the vertical and the out-of-plane horizontal displacement was applied in the transversal model until the horizontal displacements matched the inclinometer measurements by the side of the tunnel. From this state the first stress release was applied until the tunnel convergence closed the gap to the lining. The subsequent steps were soil-lining interaction and consolidation of the excess pore water pressure.

Abu-Farsakh and Voyiadjis (1999) tried to model the same tunnel, with the same soil models, but relying less on measured parameters. The longitudinal model advanced until the specified face pressure was achieved. The outward displacement of the transversal model had an elliptical profile with a ratio between the major and minor axes of five. The profile was applied until the increment of pore water pressure on the tunnel springline was the same as the one calculated on the longitudinal section. After the correct displacement was determined, a new tunnel section was modelled with a smaller diameter so that after the displacements were imposed, the geometry of the boundary matched the excavated diameter. The stress release factors were applied along the tunnel boundary by an elliptical profile, this time with a major/minor axis ratio of 1.50 (Figure 4.47d). Again, the final phases were the soil-lining interaction and consolidation of excess pore water pressure.

Other studies only analysed the tunnel transversal section, but accounted for the pressure increase due to grout injection on the tail-void. Bernat et al. (1999)

modelled the TBM excavations of the Lyons-Vaise metro by calibrating the partial stress release factors of an unlined tunnel with the measured tunnel crown displacements. The soil was represented by the CJS model with kinematic strain-hardening. A single partial stress release was compared to a cycle of stress reduction, increase ($\lambda < 0$) and reduction to account for the grout injection.

The tunnel excavation can also be modelled by imposing displacements on the excavation boundary. However, there might be a case where the resultant boundary stresses are not representative of an excavation and the procedure only mimics the measured displacements. Dias et al. (1999) presented a 2D model where the tunnel invert was fixed and a ring plate element was set on the excavation boundary. The soil was modelled as a drained Mohr-Coulomb material. As the excavation advanced, the plate rigidity changed from TBM to grout properties. The passage of the cutter-head was simulated by a reduction of the soil-plate interface strength, to induce sliding, and by a reduction of the plate ring diameter. The TBM passage, grout injection and grout consolidation were simulated by a sequence of contraction, expansion and contraction of the ring diameter.

Ding et al. (2004) analysed the different TBM phases by combining stress release factors with special interface elements and a beam-joint discontinuous lining. A simple model and empirical relations were presented to calibrate the normal and tangential interface stiffness to represent the properties of fresh and consolidated grout. Two distributions of grout pressures were also tested against measurements of an Osaka subway line (Figure 4.47e). Konda et al. (2013) modelled the TBM phases by a set of normal forces on the tunnel boundary together with a full stress release ($\lambda = 1$). That allowed the internal tunnel pressures to be determined with no relation to the in-situ stress. The soil was assigned the t_{ij} constitutive model on an undrained analysis (Figure 4.47f).

Among these stress-based approaches for plane-strain modelling of TBM tunnels, a progression can be traced from basic stress release factors to direct representations of boundary pressure gradients related to the different TBM elements. As mentioned, when using stress release factors, the boundary stresses of the excavation are always connected to the gradients of the initial stress state. The gradient can be adjusted through an asymmetric distribution of λ, as in Abu-Farsakh's model, by a combination of partial stress release factors and internal pressures as in Ding's or by a total stress release and internal pressures as in Konda's model.

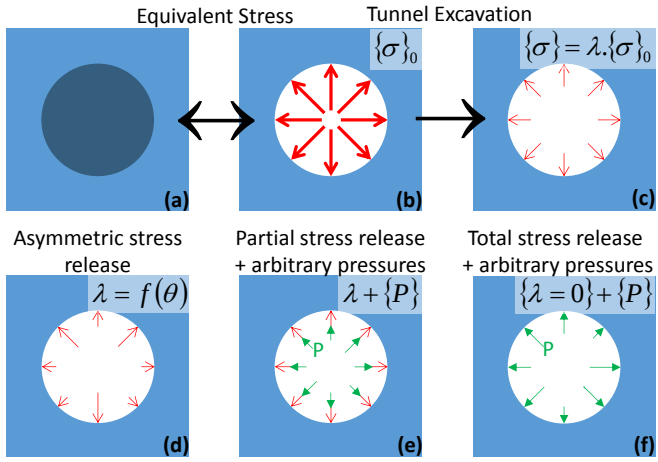

Figure 4.4. Original stress release method: The original ground (a) is replaced by an equivalent stress (b), which is scaled to represent a tunnel excavation (c). Different approaches to adjust the stress release method, asymmetric release (d), partial release combined with pressure (e), total release with pressure (f).

On top these different modelling strategies, there is also the choice of a constitutive model to represent ground behaviour. This is one of the most critical issues for geotechnical engineering in general, as a compromise is always necessary between the aspect to be modelled and the available soil tests to calibrate the required parameters. Another problem is that aside from the measurement induced bias and even within assumed homogeneous soil strata, natural soils are variable in their properties. Shirlaw (1999) presents how when tunnelling through the same geological strata, using the same tunnelling method and crew, the settlements over a tunnel can change over 2.5 times. Research around this issue is out of the scope of this thesis. However, as this is an underlying issue of all numerical calculations, a few fundamental aspects for the analysis of tunnel models will be highlighted hereafter.

4.1.2. Demonstrative calculations

A set of drained plane-strain finite element calculations were performed to analyse the patterns of boundary stress and the effects of the constitutive models on the response on an unlined tunnel modelled by increments of stress release. The calculations were performed on the software Plaxis 2D (2012), where the stress paths, tunnel convergence and surface settlements were assessed.

The first analysis considered a circular tunnel (8 m in diameter; centre at 30 m deep) and a dry linear elastic soil (Young's modulus E = 50 MPa; Poisson's ratio ν = 0.30; Volumetric weight γ = 20 kN/m³). The effects of variations in the

coefficient of earth pressure at rest (k_0) and the Poisson's ratio were assessed. A second group of models considered the same layout, with k_0=0.50. The soil was analysed with four constitutive models: Linear Elastic (LE); Linear elastic perfectly-plastic with a Mohr-Coulomb failure criterion (MC) and a non-associated flow rule (MC.C); Hardening Soil (HS) and Hardening Soil with small-strain stiffness (HS.s). The parameters were obtained from the empirical correlations of Brinkgreve et al. (2010) for sand at a relative density of 0.75, but with the same volumetric weight of the first analysis. All the parameters are listed in Table 4.1. For the complete formulations of the models, the reader is referred to Brinkgreve et al. (2013).

Table 4.1. Constitutive parameters

	LE	MC	MC.D	HS	HS.s
E (MPa)	45	45	45	-	-
ν	0.2	0.2	0.2	0.2	0.2
ϕ (°)	-	37	37	37	37
ψ (°)	-	-	7	7	7
E_{50}^{ref} (MPa)	-	-	-	45	45
E_{oed}^{ref} (MPa)	-	-	-	45	45
E_{ur}^{ref} (MPa)	-	-	-	135	135
m	-	-	-	0.466	0.466
G_0^{ref} (MPa)	-	-	-	-	111
$\gamma_{0.7}$	-	-	-	-	$1.25\ 10^{-4}$

There is a recurrent discussion on whether soil dilatancy should be considered when employing the Mohr-Coulomb model. The formulation implies that on drained analyses, shear strains can develop indefinitely without reaching the critical state. To evaluate this aspect for tunnel modelling, the Mohr-Coulomb model was employed considering dilatancy (MC.D) and disregarding dilatancy (MC). A triaxial test was simulated for each constitutive model through the Soil Test software and the results are on Figure 4.5.

The hyperbolic stress-strain relation of the Hardening Soil models (Hs and Hs.s) can be seen on the upper curves. All models, with the clear exception of the LE, converge to the Mohr-Coulomb failure criterion, corresponding to a deviatoric stress of 300 kPa. The dilatant response of the MC.D model can be seen in contrast with the MC. Both the Hardening soil models together with the MC.D present unrestrained dilatancy as no critical state is reached and no dilatancy cut-off was assigned.

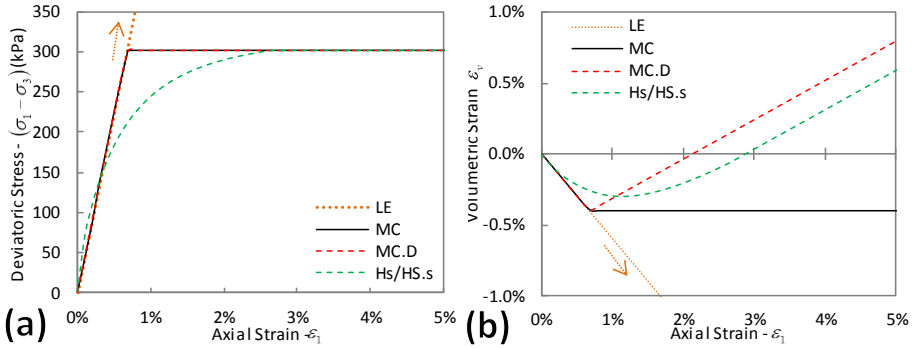

Figure 4.5. Results of triaxial test simulations, showing the mobilization of deviatoric stress (a) and the occurrence of volumetric strains (b).

4.1.3. Results and discussion

As the boundary stresses are set through stress release factors, they are always related to the original stress state, and do not vary with different constitutive models. It is important to note that when the in-situ stress state is not isotropic ($k_0 \neq 1$), both normal and shear stresses will be acting on the boundary (Figure 4.6).

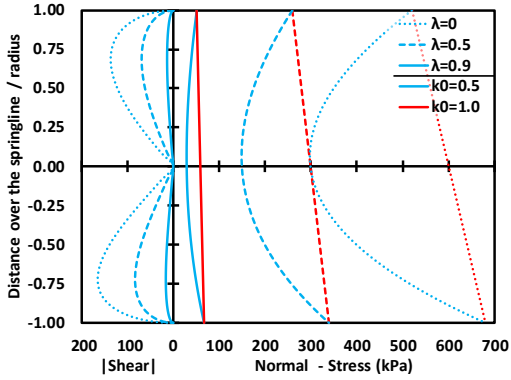

Figure 4.6. Boundary stresses. The type of line represents the stress release factors and the colour represents the coefficients of earth pressure at rest.

The results from the linear elastic analyses, considering k_0 equals 1, 0.5 and 2, were evaluated (Figure 4.7a) in terms of the increments of isotropic (p) and deviatoric (q) stress invariants on the tunnel crown and springline. For the isotropic state (k_0=1) the increment is predominantly of deviatoric stress. For the other states the response is distinguishable on whether the normal stress is the initial major (σ_1) or minor (σ_3) principal stress. The initial normal stress is the minor principal stress on the tunnel crown for k_0=2 and on the tunnel springline

for k_0=0.50. In those cases, the tunnel excavation, a reduction in the normal stress, represents a decrease in σ_3 and an increase in the hoop stress, which is σ_1. Therefore, a path of increase of deviatoric and mean stress is the result. On the opposite conditions, the decrease of σ_1 and the increase in σ_3 result in a reduction in the isotropic stress.

The difference on the initial stress state also affects the volume loss measured by the tunnel convergence and by the settlement trough (Figure 4.7b). The increase in the horizontal stress increases the tunnel convergence without significantly affecting the settlement trough. It is important to notice that the notion of equivalency between the tunnel convergence and the settlement trough can only be applied in undrained conditions, when the soil is practically incompressible (ν=0.5). However, it is common in practice to assume this equivalency even for compressible soils.

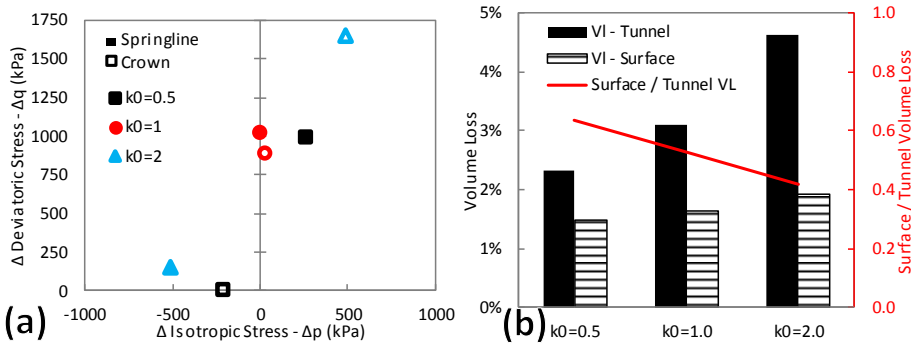

Figure 4.7. Increments of p and q (a) and volume loss measured at the surface and at the tunnel (b) for different k_0 values

For a linear elastic analysis, being all the other parameters fixed, a relation can be traced between the ratio of volume losses on the surface and at the tunnel and the Poisson's ratio, as it can be seen on Figure 4.8. Leca and New (2007) reported that the so called deformation dampening can also be a consequence of the presence of a stiffer or dilating soil over the tunnel.

The analyses with the different constitutive models were conducted in stress release increments of 10% the original state, until the solution did not reach convergence. The maximum λ for the different models was: MC = 0.7; MC.D = 0.8; HS = 0.9; HS.s = 0.8. The linear elastic analysis does not account for a failure criterion, so there is no limit for λ. For the sake of comparison, the surface settlements are presented for λ=0.7, with the parameters of the adjuster Gaussian curve (Figure 4.9). The volume losses (Figure 4.10) and the stress paths (Figure 4.11) are presented from λ = 0.1 to λ = 0.7.

A typical problem with the settlement trough of 2D models is most evident in the LE results: the trough is too shallow. However, the trough becomes deeper when plastic deformations are taken into account, and wider when hardening is considered. The consideration of small strain stiffness reduces the maximum settlements without affecting the extent of the settlement trough. The settlement troughs from the HS model were reported to be significantly deeper than the MC for higher overconsolidation ratios (Vermeer et al., 2003).

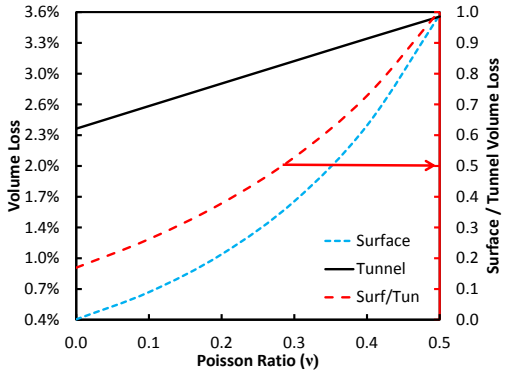

Figure 4.8. Volume losses as a function of the Poisson's ratio.

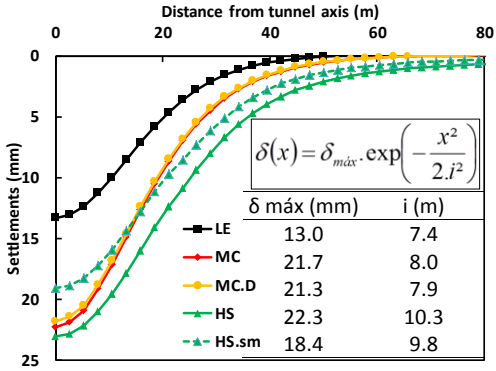

Figure 4.9. Surface settlements for different constitutive models.

As discussed, drained analyses do not hold the equivalency between the volume loss measured on the surface and the tunnel convergence. However, there is a direct correlation between stress release and the tunnel volume loss (Figure 4.10a). For the MC and MC.D models the relation deviates from the linear elastic from λ=0.5 on, as the model is actually linear elastic until plasticity is reached. On the other hand, the Hardening Soil models that present a hyperbolic stress-strain relation deviate from the linear elastic model from early stages and present a smaller volume loss at the tunnel level.

The ratios between surface and tunnel volume losses are on Figure 4.10b. Again there is a clear distinction between the LE, MC and MC.D models and the Hardening Soil models (HS and HS.s). As presented in Figure 4.8, for the LE model the ratio is constant and smaller than 1 for all values of λ. The MC models present an increase in the ratio from λ=0.5 on, when both volume losses increase, but on a higher pace on the surface. In contrast to that, both HS models present ratios above 2 for all values of λ, as the volume loss on the surface was higher than the tunnel contraction.

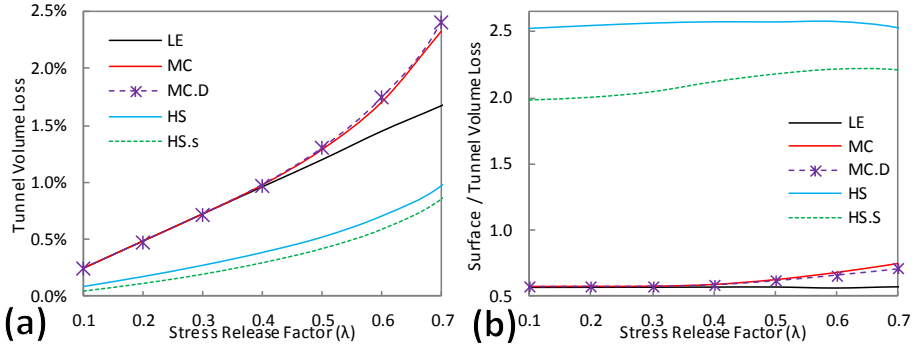

Figure 4.10. Tunnel convergence (a) and surface/tunnel volume loss ratio (ab) for different constitutive models.

From the linear elastic analyses, it is understood that for k_0=0.5, the final stress boundary is of zero vertical stress on the tunnel crown and zero horizontal stress on the tunnel springline, inducing deviatoric and positive isotropic stress increment on the springline and a reduction of the isotropic stress on the tunnel crown. The stress paths for the different constitutive models can be seen in Figure 4.11.

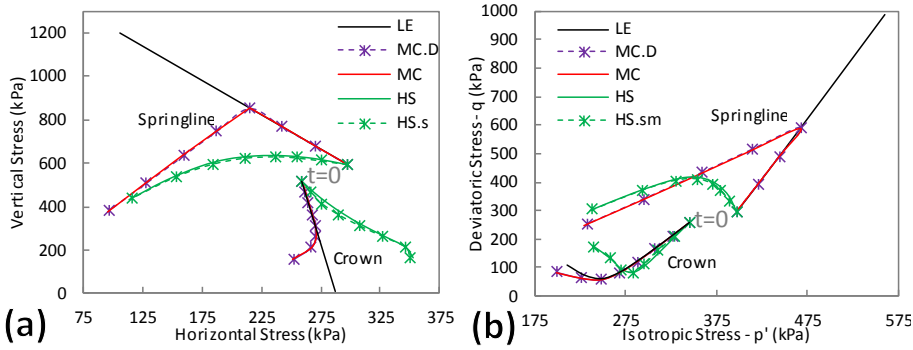

Figure 4.11. Stress paths for vertical x horizontal stress and isotropic x deviatoric stress for different constitutive models.

The stress path on the springline is of typical loading, leading to failure. For the MC and MC.D materials the path is the same until the Mohr-Coulomb failure line is reached. From there on there is a decrease in the vertical stress that reduced the deviatoric stress along the failure line. For the Hardening Soil models, the decrease in the horizontal stress is not followed by the increase in the vertical stress, therefore there is a negative increment on isotropic stress that leads more directly to the failure line.

4.1.4. Overview

From the literature review it was possible to demonstrate how the concept of plane-strain modelling of TBM tunnels is evolving. The boundary pressures when a stress release factor is used, holds a relation to the initial stress state and not to the TBM elements acting on that section (Dias and Bezuijen, 2014c). However, the basic linear elastic analysis presents how the initial stress state is important for the stress paths imposed in the soil elements due to the excavation. The effects of the soil's compressibility on the relation between the surface volume loss and the tunnel contraction were also assessed in the linear elastic analysis.

When different constitutive models were considered, and a maximum strength was assigned to the soil, the tunnels were not stable over the whole path of stress release. The surface settlements and their relation to the tunnel contraction were very different, especially between the models with linear and non-linear stress-strain relations. The recurrent discussion on where soil dilatancy should be considered when applying the Mohr-Coulomb model did not result in significant differences for the results.

This clear understanding of the modelling conditions and implications is very important for the practice of tunnel design, so that the analyses can reach reliable predictions with a consistent physical significance.

4.2. Mechanized tunnelling

> *Section 4.2 is based on the Conference Paper: Dias, T.G.S., Bezuijen, A., 2015. TBM Pressure Models - Observations, Theory and Practice.* ***15th Pan-American Conference on Soil Mechanics and Geotechnical Engineering - Invited Lectures****, Buenos Aires, Argentina.*

The section presents an overview of the main elements guiding the interaction between a tunnel boring machine and the ground. Figure 4.12 presents the main elements of a soft ground TBM. The internal structure is particular of an earth pressure balance machine (EPB), but the geometric details are similar for all

TBMs. The cutting tools, positioned at the cutterhead (A), loosen the soil at the tunnel face. As the soil flows through the openings at the cutterhead, into the excavation chamber (B), it blends in the supporting mixture, which is kept pressurized to support the face. The system that controls how the spoils are extracted from the chamber is also responsible for keeping the pressure stabilized between the tunnel face and the bulkhead. In EPB machines, the mixture is composed of the excavated soil and additives, and is removed from the chamber mechanically, through a screw conveyor. In slurry pressure balance (SPB) and mixshield machines, the mixture is mostly composed of a slurry suspension, and is removed through a hydraulic circuit. The chambers of mixshield machines are divided by a submerged wall, in a working chamber, completely filled with slurry, and a pressure chamber, partially filled with a pressurized air bubble that controls the pressure at the chamber.

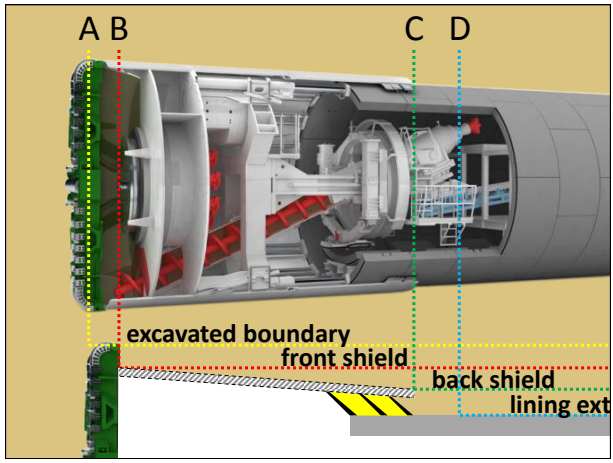

Figure 4.12. Basic structure of a TBM with highlight to the progressive diameter reduction from the cutterhead (A), to the front (B) and back (C) of the shield and the lining extrados (D).

The diameter of the cutterhead determines the size of the excavated boundary (A), which tends to be larger than the front of the TBM shield (B). The shield is always tapered, so the front diameter (B) is slightly larger than the diameter at the back (C). After the lining segments are combined in a ring inside the shield, the machine thrusts itself forward, leaving the lining in contact with the tail void grout (D). From the moment the cutterhead passes a cross-section, the structure from the TBM to the tunnel lining presents a progressively smaller diameter to support the excavation. To mitigate the convergence of the soil from A to D, grout is injected from the back of the shield. To prevent water or grout from

coming in the TBM, the contact between the shield and the lining is sealed with steel brushes filled with pressurized grease (Guglielmetti et al., 2007).

An intrinsic feature of mechanized tunnelling is that every step of the excavation cycle is performed through mechanical or hydraulic systems that compose the tunnel boring machine (TBM). The interaction mechanisms between the TBM and the surrounding ground result from the operation of these systems to excavate and support the ground around the tunnel. It is self-evident that for each of these actions there will be a reaction from the ground to achieve equilibrium. However, these mechanisms are often interpreted within idealized frameworks that do not account for important features of the ground reaction that have been observed in the field. Therefore, these frameworks need to be adapted to better represent the interaction between the TBM and the ground.

These should consider how the geotechnical aspects of the ground reaction and the rheological properties of the excavation fluids (foam, bentonite, and grout) affect the mechanisms around the TBM. To organize the discussion, the TBM-ground interaction will be divided in four elements: face pressure, flow around the TBM, tail void grouting and lining equilibrium (Bezuijen and Talmon, 2008). Each element is contrasted between the ideal mechanism and the observed ground responses. And, wherever possible, an alternative framework is presented.

A recent development for the analysis of face stability in permeable ground is presented in Dias and Bezuijen (2016). This was not included in this thesis, as it was deemed irrelevant to the main problem of pile tunnel interaction.

4.2.1. Face pressure

The face of a TBM is the most erratic zone to define conceptual boundaries for a theoretical model. The cutterhead rotates and the cutting tools scrape the ground from the tunnel face while additives are injected to condition the material. Water, polymers, bentonite and foam can be used under different conditions (Thewes et al., 2011). The loosened ground with additives, herein referred to as mixture, flows through the openings at the cutterhead and in the excavation chamber until it reaches the screw conveyor or the hydraulic circuit. The structure of the mixture is very important to understand how the face pressure is transferred to the tunnel face. Slurry suspensions on SPB and mixshield machines, which can be extracted through a hydraulic circuit, are normally more fluid than the paste consistency necessary to control the pressure gradient along the screw conveyor on EPB machines. However, in both cases, the mixture presents a very open matrix, where the solid particles are in a

suspension with negligible effective stresses. The rheology can then be considered equivalent to a fluid and, as the mixture flows slowly, viscous forces are not considered at this point.

These fluid mixtures can only support isotropic stress states, represented by an equivalent scalar pressure. Adversely, the undisturbed ground at the tunnel face will, in most cases; be standing under an anisotropic stress state, set by the coefficient of earth pressure at rest (k_0). Therefore, it is fundamentally unfeasible to transfer a face pressure that will match the in-situ stress of the ground in every direction, due to the basic fact that the supporting mixture cannot stand it (Figure 4.13). The fact that the supporting mixture has such a loose matrix that it acts as a fluid raises the question of whether the face pressure should be considered by its hydraulic head or just as a total stress boundary. Here, a parallel is normally traced with slurry walls, where the supporting fluid creates an impermeable layer on which the fluid pressure is applied and the hydraulic head is dissipated. In this way, the pressure can be transferred to the ground without changing the hydraulic boundary conditions.

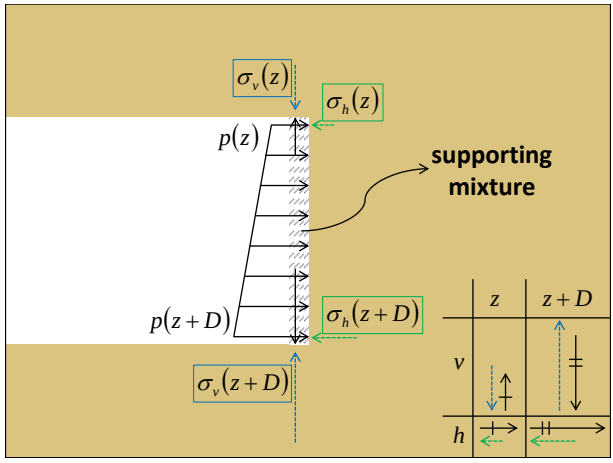

Figure 4.13. Differences between the stress states of the supporting mixture (fluid) and the ground (solid).

The same thing should occur at the TBM face, through the so-called filter cake. However, one should consider that the ground at the tunnel face is constantly being removed while the filter cake is being formed, which can affect the process. This problem was identified when excess pore pressures were measured in front of SPB (Bezuijen et al., 2001, 1999) and EPB machines (Bezuijen, 2002), revealing that the ideal process of cake formation is not always achieved and depends on the properties of the ground, the additives and the excavation speed (see Figure 4.14).

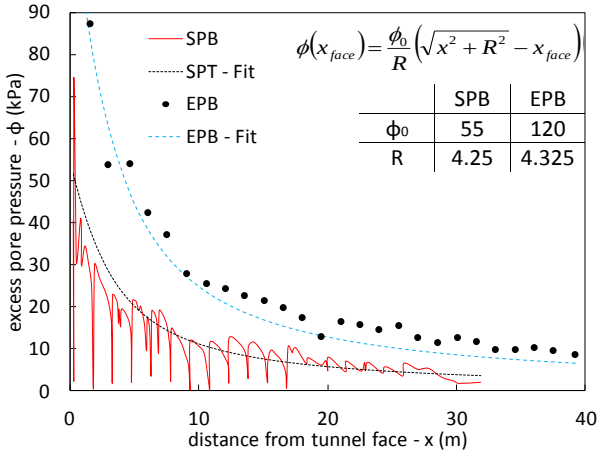

Figure 4.14. Measurements of excess pore water pressure in front of SPB and EPB tunnels

To quantify these effects, one must first understand how the supporting fluid creates an impermeable layer on the ground. The pressure in the supporting fluid must be higher than the water pressure in the ground, inducing the fluid to flow into the ground. The fluid carries suspended material that clogs the ground pores, reducing its permeability. As far as this process is concerned, the foam bubbles to condition permeable soils on EPB TBMs have the same purpose as the slurry particles on SPB and mixshield TBMs.

The second step is to quantify the gradient inducing the flow from the face. An analytical formulation can be derived (Bezuijen et al., 2001), based on the approximation that there is an infinitesimal constant hydraulic source all over the tunnel face. This distributed head is defined with reference to the in-situ water pressure. By equating the volumetric flow rate from the source ($A=dr.r.d\theta$) with the one at a certain radial distance (s) along a semi-spherical domain in front of the tunnel ($A=2.\pi.s^2$), one obtains:

$$q_w.r.d\theta.dr = k.\frac{d\phi}{ds}.\frac{4.\pi.s^2}{2} \qquad (5)$$

where q_w is the discharge from the point source, assumed constant all over the tunnel face.

By integrating Equation 5 along the following limits: $\phi = [\phi(S), \infty]$; $s = [S, \infty]$; $r = [0, R]$; $\theta = [0, 2\pi]$, and defining $s = (x_{face}^2 + r^2)^{0.5}$, one obtains:

$$\phi(x_{face}) = \frac{\phi_0}{R}\left(\sqrt{x^2 + R^2} - x_{face}\right) \quad (6)$$

where ϕ_0 is the incremental piezometric head at the tunnel face (x_{face}=0).

From Equation 6 it is possible to calculate the hydraulic gradient at the tunnel face as:

$$\left.\frac{d\phi}{dx_{face}}\right|_{x_{face}=0} = \frac{\phi_0}{R}\left(\frac{x_{face}}{\sqrt{x^2 + R^2}} - 1\right)\Bigg|_{x_{face}=0} = -\frac{\phi_0}{R} \quad (7)$$

The penetration velocity can then be defined as:

$$v_p = \frac{k.\phi_0}{n.R} \quad (8)$$

where n is the ground porosity and k is the ground hydraulic conductivity to the penetration fluid.

Therefore, the face pressure should be kept at a certain pressure so that the supporting fluid can penetrate the ground faster than the excavation velocity. Otherwise, the excavation tools will always be scraping deeper than the fluid penetration, cancelling the effect of an impermeable layer. In this case, the hydraulic head of the supporting fluid is not dissipated and groundwater flow is induced from the tunnel face to the ground. There are some recent attempts to model this process numerically with a separate model for the slurry penetration (Zizka et al., 2015).

The increments of pore water pressure in front of the tunnel can affect the face stability and the tunnel interaction with surrounding structures. On top of that, the water outflow has special consequences for foam conditioning, which depends heavily on the amount of water in the supporting mixture. The foam is formed by mixing a surfactant solution, which presents a certain liquid volume (Q_L), with compressed air. This forms a structure where pockets of gas are trapped in the foam bubbles. The volume of foam (Q_F) is used to calculate the foam expansion ratio ($FER=Q_F/Q_L$), diving it by the original liquid volume of the solution, and the foam injection ratio ($FIR=Q_F/Q_S$), dividing it by the volume of excavated ground (Q_S). Once the foam blends in the supporting mixture, its additional volume will increase the initial porosity of the mixture (n_1), described in Figure 4.15a, to a porosity that is suitable for the TBM operation (n_2). For an initially dry mixture, and no flow, the foam will occupy the air spaces

(Figure 4.15b), so the necessary volume of foam to increase the porosity from n_1 to n_2 can be calculated as:

$$V_F^{(dry)} = V_i \cdot \frac{n_2(1-n_1)}{1-n_2} \tag{9}$$

If the mixture is originally saturated, one must consider the possibility that the face pressure will induce groundwater flow from the face, in which case the initial amount of water will be reduced or even increased, depending on the flow conditions. Considering the hypothesis that there is no water flow (Figure 4.15c), the necessary volume of foam can be calculated as:

$$V_F^{(no-flow)} = V_i \cdot \frac{n_2 - n_1}{1-n_2} \tag{10}$$

For the case where water flows out of the mixture (Figure 4.15d), the necessary volume of foam can be calculated as (Bezuijen, 2013):

$$V_F^{(flow)} = V_i \cdot \frac{n_2(1-n_1)}{1-n_2} - V_{W2} = V_i \cdot \left(\frac{n_2 - n_1}{1-n_2} + n_1.FWR \right) \tag{11}$$

where the Foam Water Replacement Ratio (*FWR*) is defined as the volume of water that flows out of mixture over the initial volume of water.

Using Equations 9, 10 and 11, one can calculate the necessary foam injection ratio for any condition.

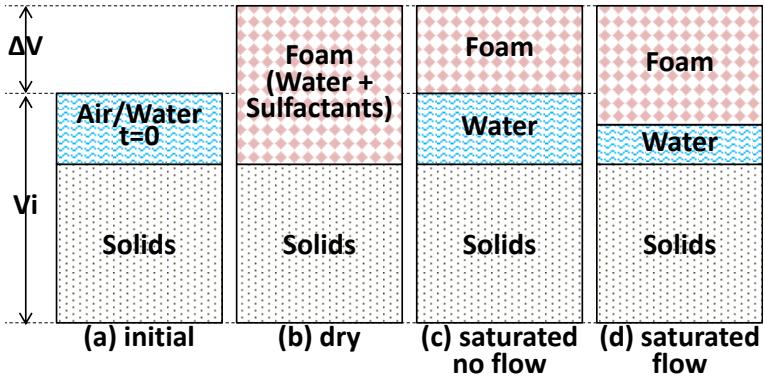

Figure 4.15. Representative volumetric elements for the solid, water and foam phases in a supporting mixture

4.2.2. Flow around the shield

While a certain cross-section is between the face and the tail, the general understanding is that structure of the TBM shield is what supports the excavation. Then, when the shield is propped forward, it leaves a fully assembled lining ring as permanent support. It was already discussed how the diameter of the shield is progressively smaller from the cutter head to the tail of the TBM (Figure 4.12). It is reasonable to consider, for current machines, that the cutterhead excavates a diameter 1 to 3 cm larger than the front of the shield (over-excavation) and that along the shield the diameter reduces about 0.4 % (Bezuijen, 2009, 2007). The volume loss due to the convergence of the excavation boundary can then be calculated as:

$$V_L = 1 - \left(1 - \frac{\Delta R}{R_{exc}}\right)^2 \tag{12}$$

where ΔR is the radial convergence and R_{exc} is the excavation radius.

Considering a tunnel of 10 m in diameter and an over-excavation of 3 cm, the radial convergence comes to 3.5 cm, which is equivalent to a volume loss of 1.4 %. This volume loss around the tunnel can be assumed equal to the volume of the settlement trough, provided that the excavation does not induce volumetric strains (Dias and Bezuijen, 2014c). In this case, if the mechanism is correct, the minimum volume loss due to a TBM excavation would be the one imposed by its geometric characteristics. However, it is not uncommon nowadays to achieve volume losses as low as 0.2 %. This observation led to the proposition of a different mechanism for the ground interaction around the shield.

For this process, both the grout, injected at the back of the TBM, and the mixture, supporting the tunnel face, are considered to act as fluids. As such, provided there is a longitudinal pressure gradient and a gap between the soil and the shield, these fluids will flow around the TBM. The resultant pressure distribution controls the tunnel convergence and prevents the complete closure of the soil-shield gap. To simulate this process, it is necessary to model the viscous flow of the excavation fluids and the relation between the boundary pressures and the excavation convergence.

The mechanical response of the grout and the supporting mixture can be modelled as Bingham plastic fluids. In this model, the material behaves as a rigid body until a limit shear stress is reached, from where it starts to flow as a viscous fluid. In this formulation the shear stress can be described as:

$$\tau_g = \tau_y + \eta \frac{du}{dy} \tag{13}$$

where τ_y is the yield resistance, η is the dynamic viscosity and du/dy is the velocity gradient perpendicularly to the flow.

There are several techniques available to characterize these parameters (Mohammed et al., 2014). If small velocities are considered, the second term of Equation 13 can be disregarded and the shear stress can be assumed equal to the yield resistance. This is a reasonable assumption for the flow around the TBM and it simplifies the calculation process. However, while it does not require the assumptions of the shear rate distribution in one hand, it turns the model unable to solve the velocity field in the other. In this way, if the flow between the soil-shield gap is considered equivalent to a flow between parallel plates, the pressure dissipation due to one interface can be calculated as:

$$\Delta p = \frac{\tau_y . \Delta l}{gap} \tag{14}$$

where Δl is the distance along the flow direction, defined in the same unit as the gap.

The other element of the simulation is the relation between the boundary pressures and the excavation convergence. In a homogeneous, isotropic and elastic medium, under isotropic stress conditions ($k_0=1$), a linear relation can be traced between the tunnel convergence (ΔR) and an axisymmetric stress release ($\Delta\sigma_T$) around the tunnel (Verruijt, 1993):

$$\Delta\sigma_T = 2\frac{\Delta R}{R}G \tag{15}$$

where G is the shear modulus and R is the initial radius of the tunnel.

Figure 4.16 presents the results of Equation 15 for a tunnel with an initial radius of 5 m, ground shear modulus of 13 MPa and an initial in-situ stress of 500 kPa.

These two models can be programmed in a spreadsheet to simulate 1D flow around the TBM and obtain the resultant pressures and convergences. The gravitational field can be disregarded at this stage. An example result is presented in Figure 4.17 considering the following parameters: excavated radius = 5 m; initial in-situ stress = 400 kPa; ground shear modulus = 50 MPa; face pressure = 300 kPa; grout pressure = 600 kPa; shield length = 5 m;

over-excavation = 1 cm; tapering = 1 cm; grout yield strength = 1.5 kPa; mixture yield strength = 80 Pa (equivalent to bentonite).

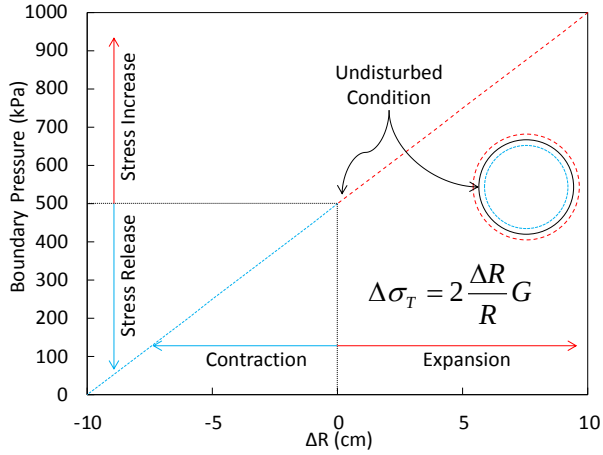

Figure 4.16. Relation between boundary pressures and excavation convergence.

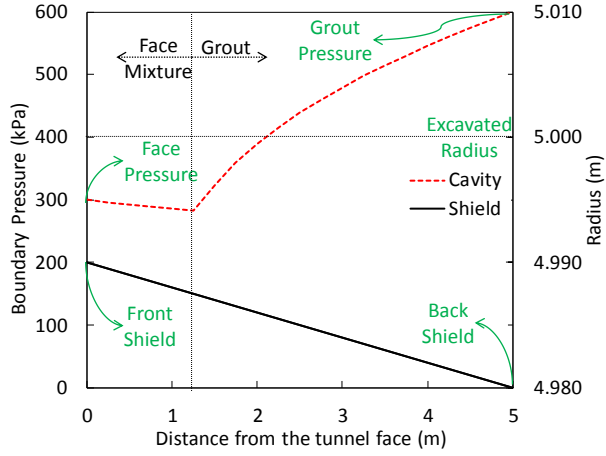

Figure 4.17. Example calculation for the flow around the TBM

The results indicate that the ground does not come in direct contact with the shield. As the face pressure is smaller than the in-situ stress, the excavation converges about 50 mm around the front of the shield. The bentonite then flows back 1.25 m along the soil-shield gap. On the other side, the grout pressure is higher than the in-situ stress, which causes the excavation to expand about 100 mm. The grout then flows back 3.75 m along the gap with a steep pressure drop. In this set-up, the volume loss just after the cutterhead is about 0.2 % while at the tail of the TBM is -0.4 %, which is a better estimate of measured values.

This model is a rather crude representation of reality. It assumes one pressure in the bentonite and one in the grout. In reality there is a pressure distribution around the tunnel perimeter and the shield is in contact with the ground in some places. However, it is a more accurate approximation than just assuming that the shield is completely embedded in soil.

4.2.3. Tail void grouting

The pressure of the grout that is injected at the TBM tail will determine the expansion/convergence of the excavated boundary and the flow pattern around the TBM shield. However, the main purpose of the grout injection is to fill the gap between the back of the shield and the lining ring (Figure 4.12). The diameter of the lining is normally 1.5 to 8 % smaller than the back of the TBM, which is equivalent to a tunnel volume loss between 3 and 15% for full gap closure (Shirlaw et al., 2004).

The process of tail grouting is, at times, understood as a volumetric problem. The logic goes as follows: Once the TBM is trusted forward, it leaves behind a gap between the soil, which was previously supported by the shield, and the lining ring that was left in place. So, by injecting a volume of grout equal to the volume of the gap, soil convergence can be avoided. However, this logic fails whenever the ground deforms faster than the process described, and/or the previously injected grout is still fluid, and/or grout volume is not constant but decreases due to consolidation. All these conditions can be assumed for most regular cases. Therefore, the focus has to change from controlling the injected volume to keeping the gap pressurized.

Field measurements were performed during the excavation of the Sophia Rail tunnel, a 4.2 km twin tunnel with an external diameter of 9.5 m and a 0.4 m thick concrete lining. The tunnel crown was located at a depth of 14.77 m where the overburden pressure was approximately 200 kPa. A single component grout was used in the tail void. In each tunnel, one full-ring of the lining was instrumented with 14 pressure sensors, monitored from the moment the rings were placed to about 11 hours after leaving the shield. A detailed analysis of the data can be found in Bezuijen et al. (2004). For the sake of objectiveness, the time series of all instruments is combined in two averages: grout pressure and vertical gradient, where most relevant aspects can be seen (Figure 4.18).

The origin of the time axis is set from the moment the lining comes in contact with the grout. When the TBM was excavating and advancing, grout was constantly being injected into the gap. This caused the pressures to increase

during drilling, with some oscillations in the first two cycles. During stand still, on the other hand, the pressure decreased.

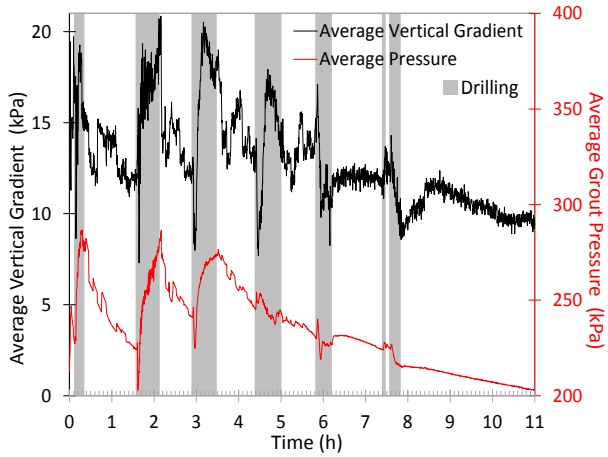

Figure 4.18. Measurements of average grout pressures and vertical gradients with time

Just before the first two drilling cycles, one can see a considerable decrease in the grout pressure. This happened because the TBM advanced a few seconds before the grout pumps were activated, illustrating the fallacy of understanding the process of tail void grouting as a volumetric problem. For the fourth cycle onwards, the grout injections on the TBM tail were not noticed anymore. The pressure decrease continued through the whole time, but with a smaller rate after the fifth cycle.

Focusing on the vertical gradients around the lining, there were also marked differences between the phases of drilling and stand-still. When the grout was injected, during the first cycles, the gradient was around 20 kPa which is equivalent to the grout volumetric weight. During stand-still there was a sharp decrease to about 15 kPa followed by a reduction with time to about 10 kPa.

Qualitatively, these results can be understood as follows: While the grout is being pumped, the flow direction is predominantly longitudinal so only the gravity field determines the vertical gradient. During stand-still, the grout flows along the tangential direction of the cross-section. As the grout pressure dissipates due to shear, the vertical gradient is reduced just after drilling stops. With time, as the grout pressures are higher than the local groundwater pressure, the grout loses water to the ground. This consolidation process progressively reduces the grout pressure, and forces the vertical gradient towards the gradient of the

groundwater. As the grout starts to harden and the consolidation advances, the pressure variations due to new injections are no longer noticeable.

To obtain quantitative results, each of these processes needs to be modelled. The pressure increase during the excavation is a direct consequence of the operation of the grout injection system. A pressure controlled operation can be calculated based on mechanical equilibrium. However, for a case of volume controlled operation, the pressure field can only be determined considering a compressible fluid, where the energy and the mass conservation/momentum equations can be linked. It should be noted that, in these arguments, the operational feasibility of the system, such as achievable discharge, frequency of maintenance and necessary backup utilities, are not directly assessed, but should always be verified with the mechanical design team.

The first aspect to be considered for the phase of stand-still is the tangential grout flow. Overall, this problem can be formulated in a way similar to the problem of flow around the shield, modelling the flow of a viscous plastic fluid in equilibrium with a deformable boundary (Talmon et al., 2001). The same rheological grout model (Bingham plastic fluid, with $\tau_g = \tau_y$) is assumed to calculate the pressure field around each injection nozzle, where the pressure boundary conditions of the problem are stated. Referring to Figure 4.19, the pressure at point B can be calculated from the injection pressure of the nozzle, at point A with:

$$p_B = p_A - \frac{\tau_g}{gap}.dl - \gamma_g.dh \tag{16}$$

where *dl* is the distance along the flow path, *dh* is the vertical distance and γ_g is the volumetric weight of the grout.

The pressure at point C is then calculated similarly as:

$$p_C = p_A - \frac{\tau_g}{gap}.dl + \gamma_g.dh \tag{17}$$

The simplest approach to deal with multiple nozzles (6 to 8 in a regular TBM) is to calculate the pressure field around the whole domain for each individual nozzle and assume that the maximum pressure at each point around the perimeter composes the resultant field. For a constant gap, these equations can be programmed in a spreadsheet to calculate the grout pressures in a discrete set of points along the tunnel perimeter. However, the ground deformation in

equilibrium with the grout pressures should also be considered. Again, the gap between the tunnel and the lining can be assessed through a relation between the boundary pressures and the excavation convergence/expansion. The isotropic model from Equation 15 can be used, observing its limitations. Together, these two models can be programmed in a spreadsheet to simulate the 2D flow around the lining and obtain the results of pressure and convergence.

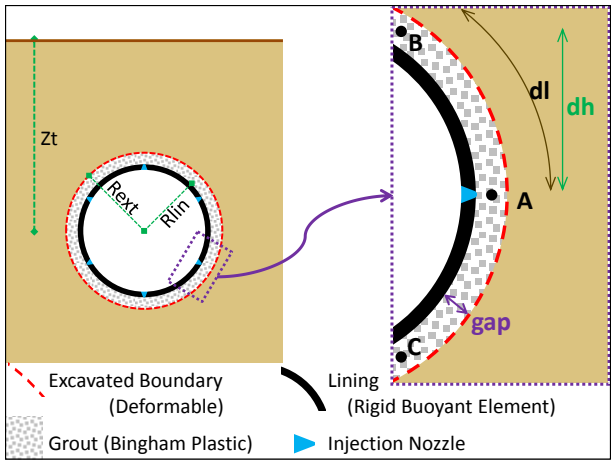

Figure 4.19. Elements to model the tangential grout flow

An example result is presented in Figure 4.20 considering the following parameters: excavated radius = 5 m; initial tunnel-lining gap = 15 cm; depth of the tunnel centre = 30 m; ground Young's modulus = 45 MPa, ground Poisson's ratio = 0.3 ; ground volumetric weight = 20 kN/m³; coefficient of earth pressure at rest = 0.5; groundwater level at the surface; grout yield strength = 0.5 kPa; grout volumetric weight = 20 kN/m³. A layout of six injection nozzles was considered, each one with an injection pressure of 400 kPa.

The results indicate a profile of grout pressures with an average vertical gradient of 14 kPa/m, and with a similar magnitude to the in-situ normal stress at the tunnel springline. As the grout pressure is smaller than the normal stress at the tunnel roof and invert, the excavation converges, in an average of 1 cm, which is equivalent to a volume loss of 0.4%. The grout pressures can also be used to assess the resultant vertical force acting on the lining ring. For this set up an upwards force of 1170 kN/m was calculated.

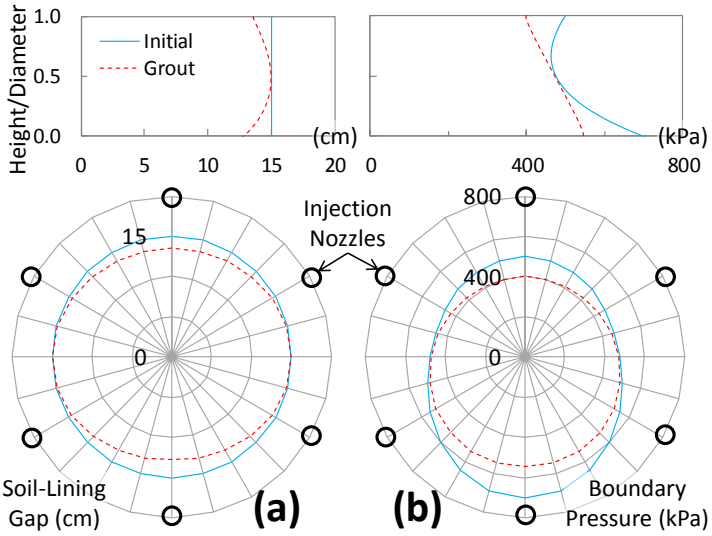

Figure 4.20. Example calculation for the tangential grout flow in terms of the soil-lining gap (a) and the boundary pressures (b).

The second aspect to be accounted for is the consolidation of the grout, which is responsible for the decrease of both the gradient and magnitude of grout pressures during stand-still (Bezuijen and Talmon, 2003). The geotechnical aspect of this process, which is sometimes called grout filtration, is analogous to the one described for the face pressure transfer. But here there is no reason to assume that a filter cake is formed in the ground, so only an external layer of filtered grout is considered. Therefore, the water flow from the grout to the ground will depend on the difference in water pressure between both regions, the permeability of the filtered grout and its thickness. A scheme of the process can be seen in Figure 4.21 for 1D conditions. The slurry grout is characterized by its initial volume (V_0) and porosity (n_i). The filtered grout is characterized by its porosity (n_f).

Considering incompressible fluids and a constant volume of solids, the continuity equation is:

$$q_w.dt = \frac{\left(n_i - n_f\right)}{\left(1 - n_i\right)} dx \tag{18}$$

where q_w is the water discharge, which can be calculated through Darcy's law, dt is the time increment, and dx is the incremental thickness of the filtered grout.

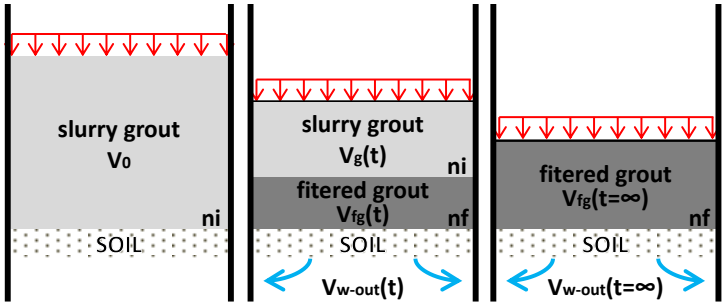

Figure 4.21. Volumetric scheme for the process of grout consolidation

The loss of hydraulic head within the slurry grout is negligible, so the pressure in the liquid slurry (see Figure 4.21) can be considered constant. When the permeability of the ground and the filtered grout are of the same order of magnitude, the hydraulic head will dissipate through both layers, increasing the groundwater pressure nearby (Masini et al., 2014). On the other hand, in fine sand or coarser grained soils it very likely that the permeability of the ground is significantly higher than the one of the filtered grout. In this case, the dissipation through the ground can be neglected, so that all the pressure difference between the groundwater and the grout is dissipated through the filtered grout layer (Bezuijen and Talmon, 2003). The following derivations assume the second case. By substituting the formula for the discharge (q_w=$k.\Delta\phi/x$) in Equation 18, assuming a constant difference in piezometric head ($\Delta\phi$), and integrating with $x(0) = 0$ as a boundary condition, one obtains:

$$x(t) = \sqrt{\frac{(1-n_i)}{(n_i-n_f)} 2.k.\Delta\phi.t} \tag{19}$$

where x is the thickness of the filtered grout layer, k is the permeability of the filtered grout, $\Delta\phi$ is the pressure difference between the groundwater and the grout, and t is the time.

The process will stop once all the slurry grout has been filtered. The time necessary to reach this stage can be calculated as:

$$t_{\max} = \frac{(1-n_i).(n_i-n_f)}{(1-n_f)^2.2.k.\Delta\phi}.h_0^{\,2} \tag{20}$$

where h_0 is the initial thickness of the slurry grout.

However, the difference in piezometric head isn't normally a constant. The pressure of the slurry grout has to be in equilibrium with the tunnel boundary, so the deformability of the ground needs to be considered. The isotropic model from Equation 15 can be used, observing its limitations. Assume that the consolidation process starts from an equilibrium condition, so that the grout pressure is equal to the tunnel boundary pressure. From this stage, the volume reduction due to the consolidation of the grout will lead to the convergence of the boundary and the related pressure reduction (see Figure 4.16). In other words, the grout pressure will reduce as the grout consolidates due to the stress release of the deformable ground. Assuming that all grout phases are fully saturated, the reduction of the initial grout volume is equal to the volume of water expelled from the slurry, which can be obtained through the direct integration of Equation 18. If this variable is set as ΔR from the convergence model, and the resulting $\Delta\sigma_T$ is discounted from the initial pressure difference $\Delta\phi$, one obtains a new incremental form for the thickness of the filtered grout:

$$x.dx = \left(\frac{(1-n_i)}{(n_i - n_f)} \Delta\phi - \frac{2.G}{R} x \right).k.dt \tag{21}$$

The solution of this equation is by no means trivial. However, if the first computation of *dx* is done with a very small *dt* with Equation 19, the calculation can proceed numerically, where each computation of *dx* is based on the previous value of *x*. Even in the incremental form it is possible to obtain the maximum thickness of the filtered grout as:

$$x_{\max}\Big|_{\frac{dx}{dt}=0} = \frac{\Delta\phi.R}{2G} \cdot \frac{(1-n_i)}{(n_i - n_f)} \tag{22}$$

An example calculation of these 1D models is presented in Figure 4.22 considering the following parameters: porosity of the slurry = 0.4; porosity of the filtered grout = 0.3; grout pressure = 500 kPa; ground water pressure = 400 kPa; initial grout thickness = 15 cm; permeability of the filtered grout = 10^{-8} m/s; ground shear modulus = 50 MPa; initial tunnel radius = 5 m.

The results show a remarkable difference between the calculations with constant and variable boundary pressures. The first aspect is that the constant pressure can build up a much thicker layer of filtered grout, as the grout will be completely dewatered. On the other hand, the case with a deformable boundary rapidly decreases the pressure, reaching equilibrium with the groundwater and stopping the process, while part of the grout is still in slurry form. The consolidation led

to 0.5 cm of convergence, which corresponds to 0.2 % volume loss. This can be calculated through the relation between the thickness of the filtered grout and the water outflow (Equation 18).

The main feature to be acknowledged here is that the grout pressures will converge to the groundwater pressures. One can apply this concept for the whole tunnel perimeter, which will result in a decreasing pressure magnitude and a vertical gradient converging to 10 kPa/m. Both conclusions are in direct agreement with the field observations.

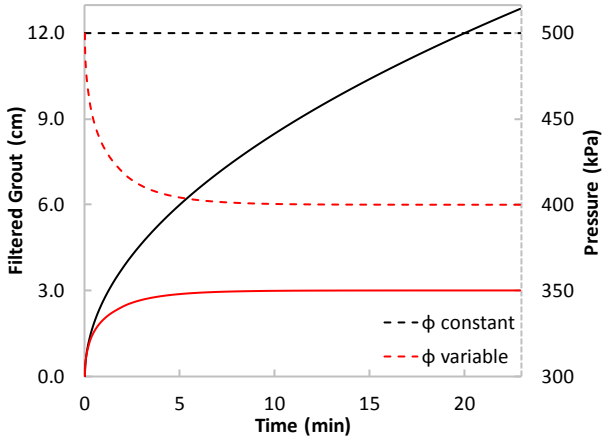

Figure 4.22. Example calculation of grout consolidation with constant a variable boundary pressure

4.2.4. Lining equilibrium

The lining equilibrium is directly dependent on the pressure gradients of the grout, as they are in direct contact after the ring leaves the tail of the TBM. Through the aforementioned mechanisms, the lining can be seen as a buoyant structure immersed in a pressurized viscous fluid that is flowing as it hardens and consolidates (Bezuijen et al., 2004). The first aspect to be considered is that the vertical gradient of the grout pressures results in an upwards force acting on the lining, which might not be in balance with the weight of the lining. The calculation example from Figure 4.20 reached a resultant upward force of 1170 kN/m. Considering an external radius of 4.85 m, a typical lining ring thickness of 50 cm, and a volumetric weight of 25 kN/m³, the full lining ring weighs about 360 kN/m. The net result of these two forces is 800 kN/m upwards.

If the forces are unbalanced in an individual lining section, the lining is forced to move upwards until either the resultant grout pressures match the lining weight or the lining comes in contact with the roof of the ground cavity, which will then

react until equilibrium is reached. One way to reduce the net force is to re-design the injection layout and/or the grout properties. Keeping all the other parameters constant, the same example results in a null net force for a grout with 1.8 kPa of yield strength instead of the original 0.5 kPa. However, as just discussed, the gradient of grout pressure is bound to change with time due to consolidation, so it is inexorable that in one stage or the other there will be a non-null net force acting on the lining.

Another way to look at this problem is to consider the rings to be interlocked in the longitudinal direction, so that all lining rings respond together. This process can be modelled through an equivalent 1D beam. One possibility is to represent the TBM jacking forces in one end and the hardened grout in the other. The time for the grout to harden will correspond to a certain number of installed rings that will set the length of the equivalent beam (Bezuijen et al., 2004). This approach has been successfully applied to reproduce measurements of vertical lining movements (Bezuijen and van der Zon, 2005). For fast settling grouts, where the length of the liquid phase is small when compared to the tunnel diameter, the 1D hypothesis will probably be unsuitable and more complex models are needed. Another possibility is to consider a semi-infinite beam set partially on the liquid grout and partially on an elastic foundation that represents the hardened grout (Figure 4.23). The analytical solution of this problem has been used to reproduce measurements of the lining bending moments and inclination (Talmon and Bezuijen, 2013).

If the resultant displacements are excessive, the relative movement between the rings can lead to steps in the tunnel and damage to the circumferential joints, movements along the radial joints and even structural damage to the lining.

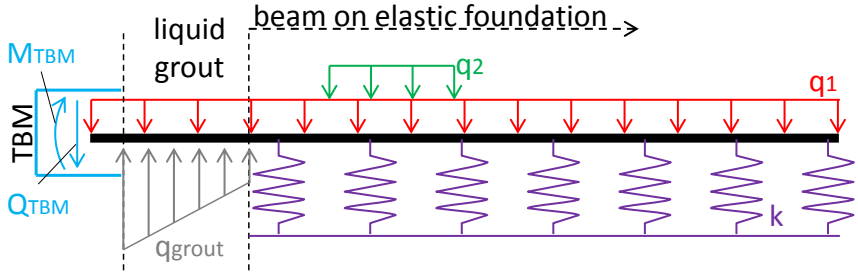

Figure 4.23. Lining model scheme as a 1D equivalent beam on a semi-infinite elastic foundation.

4.2.5. Overview

This section developed the idea that to understand the TBM mechanisms, which have been traditionally presented as simple mechanical processes, it is essential

to consider the geotechnical aspects of the TBM-ground interaction along the different excavation phases (Dias and Bezuijen, 2015c).

The observed consequences of this interaction have been presented together with theoretical frameworks that can model the mechanisms and reproduce some results. It is evident that these models do not cover every aspect of a tunnelling project. A TBM is a complex set of mechanical and hydraulic systems. Several operational/logistic processes are also not contemplated, such as: TBM steering, spoil removal, supply of lining elements, ring building, lining joints, among others. All these aspects need to be analysed and eventually modelled (Scheffer et al., 2014) for an adequate tunnel project.

A point of note is that all these interaction processes, from the face-pressure to the lining equilibrium, are interdependent. This is more evident for direct interactions: The face and grout pressures setting the gradient for the flow around the shield; The grout setting the forces acting on the lining. However, it might also take place indirectly, through the ground reaction and the pore-water pressures around the tunnel. It might be the case that, at a certain cross-section, an increment of pore-water pressure, induced through the face pressure transfer, is not fully dissipated when grout consolidation starts to develop. This conjecture is normally not considered because the grouting pressures tend to be much higher than the face pressures, dominating the process. However, mechanized tunnelling is constantly evolving. A certain scale that is now insignificant might be dominant for a larger diameter tunnel, faster excavation, different types of grout, more or less permeable soils, etc.

Even though these models are quite useful to represent what happens around the tunnel, they are based on a simplified relation between the boundary pressures and the excavation convergence, with no means to compute the settlement trough or the settlements along a pile section.

Therefore, a conceivable method to predict the ground movements due to tunnelling, is to use these models of TBM-ground interaction to substantiate the boundary conditions of a continuum numerical calculation, and to take its results back into the interaction model. In this way, the real forces acting on the excavation perimeter can be used in the numerical model, which should improve the prediction of settlements. The next two sections will develop this idea for the phases of grout injection and grout consolidation within two finite element packages: FlexPDE and Plaxis.

4.3. Iterative calculation of grout pressures

Section 4.3 is based on the Conference Paper: Dias, T.G.S., Bezuijen, A., 2015. TBM Pressure models: Calculation tools. ***ITA World Tunnel Congress 2015****, Dubrovnik, Croatia.*

The models from Section 4.2 enable a conceptual understanding of the mechanisms and main parameters that influence the process of the TBM interaction with the surrounding soil. However, they cannot be directly used with the numerical methods described in Section 4.1 to estimate the tunnel volume loss and settlement trough.

This section proposes a new solution for this issue during the phase of grout injection. A model for the grout flow is associated with a finite element model to calculate the induced soil displacements in a dynamic equilibrium between the boundary pressures and the soil-lining gap. These two elements are combined in a calculation tool with a user friendly input-output layout.

A spreadsheet is used to calculate the grout pressures, based on the rheological model for the grout behaviour discussed in Sections 4.2.2 and 4.2.3. A finite element code, where the grout pressures are used as boundary conditions, is then used to calculate the soil displacements. These displacements are imported back to the spreadsheet, where the results of the two models can interact until numerical equilibrium is achieved.

From here on this chapter will focus on the phase of tail void grouting, as it is considered the main source of ground settlements during normal excavation operations. However, other stages of the excavation might also contribute significantly to the final displacement field. It should also be noted that the tunnel lining is considered fixed and rigid, which might not be a reasonable assumption in some cases. Some ideas on how to consider the buoyancy of the lining and its structural properties are discussed in the next sections.

As discussed in Section 4.1, previous studies have already defined grout pressures in numerical simulations to disconnect the forces at the excavation boundary from the initial ground stresses. These pressures have been defined as uniform (Dias et al., 1999; Swoboda and Abu-Krisha, 1999), varying with the height (Dijk and Kaalberg, 1998; Kasper and Meschke, 2004; Melis et al., 2002) or angle (Ding et al., 2004) around the tunnel. These distinctive methodologies all adopted fixed distributions of grout pressure, while the mechanism discussed in Section 4.2 indicates that the distribution depends on the equilibrium between the injected pressure and the ground deformations, requiring an iterative calculation scheme.

4.3.1. Numerical model – FlexPDE

The software FlexPDE, a general partial differential equation solver, is used to solve the boundary value problem of the mechanical equilibrium associated with a tunnel excavation. The software uses the finite element and the finite difference methods for the solution of non-linear coupled systems and has accessible input and output features combined with automatic mesh generation, time-step control, and choice of non-linear approaches (PDE Solutions Inc., 2012). These general solvers tend to have a steep learning curve, and can potentially make the programming of stress-strain analyses a straightforward procedure. Most applications to geotechnical engineering have been over unsaturated soil mechanics, slope stability and coupled thermo-mechanical problems (Gitirana Jr and Fredlund, 2003). The software operates over an input script that defines the necessary elements for the calculation, namely the definition of variables, parameters, partial differential equations, domain, boundary conditions and post-processing options. The code resembles a programming language even though it cannot cope with recursive procedures. This poses some difficulties in implementing incremental constitutive relations but it can easily cope with explicit models, as the linear elastic. The whole code is described in Annex C.

As a plane strain equilibrium calculation, the variables to be solved are the displacements on two orthogonal directions, which are also used to define the domain. For this analysis a Cartesian XY system was chosen and the variables were named *u* for the X direction and *v* for the Y direction. The PDE's to be solved concern the equations in the X (horizontal) direction:

$$\frac{\partial Sxx}{\partial x} + \frac{\partial Sxy}{\partial y} = 0 \tag{23}$$

where S_{ij} is the stress acting along the plane perpendicular to the direction *i*, but aligned with the direction *j*. And in the Y (vertical) direction:

$$\frac{\partial Sxy}{\partial x} + \frac{\partial Syy}{\partial y} + fy = 0 \tag{24}$$

where *fy* represents the body forces.

The three variables (normal stresses S_{xx} and S_{yy} and the shear stress S_{xy}) cannot be solved with these two equations. The stresses can be related to the normal strain in the X direction:

$$\varepsilon_{xx} = -\frac{\partial u}{\partial x} \tag{25}$$

The normal strain in Y direction:

$$\varepsilon_{yy} = -\frac{\partial v}{\partial y} \tag{26}$$

And the engineering shear strain along the XY plane:

$$\varepsilon_{xy} = -\frac{\partial v}{\partial x} - \frac{\partial u}{\partial y} \tag{27}$$

A linear elastic model, formulated in terms of the elastic bulk modulus (*K*) and shear modulus (*G*), is used to define, as a function of the strains, the normal horizontal stress:

$$Sxx = Sxx^0 + \left(K + \frac{4.G}{3}\right).\varepsilon_{xx} + \left(K - \frac{2.G}{3}\right).\varepsilon_{yy} \tag{28}$$

The normal vertical stress:

$$Syy = Syy^0 + \left(K - \frac{2.G}{3}\right).\varepsilon_{xx} + .\left(K + \frac{4.G}{3}\right).\varepsilon_{yy} \tag{29}$$

And the shear stress:

$$Sxy = Sxy^0 + G.\varepsilon_{xy} \tag{30}$$

The index 0 corresponds to the initial in-situ stress. As all strain components depend on the two displacement variables (*u*, *v*) it is possible to solve them with the two equilibrium equations. These deformability parameters are assumed constant, setting a homogeneous isotropic linear elastic model.

To simulate undrained conditions, the elastic parameters can be manipulated similarly to what is implemented in PLAXIS (Brinkgreve et al., 2013). The method defines two Poisson's ratio for drained (νe) and undrained (νu) conditions. The shear modulus remains unaltered, while the bulk modulus is written in the form:

$$K = 2.G.\frac{(1+\nu_u)}{3.(1-2.\nu_u)} \tag{31}$$

The modulus is used to solve the equilibrium equations, but then separated into a so-called effective bulk modulus:

$$K_e = 2.G.\frac{(1+\nu_e)}{3.(1-2.\nu_e)} \tag{32}$$

And the remaining water bulk modulus:

$$K_w = K - K_e \tag{33}$$

The increments of water pressure are then calculated as:

$$u_w = u_{w0} + K_w.(\varepsilon_x + \varepsilon_y) \tag{34}$$

For drained conditions, one must only set the $\nu u = \nu e$, which turns $Ke = K$ and $Kw = 0$, resulting in no increments of water pressure. All calculations in this thesis consider only drained conditions.

What connects the grout model with the equilibrium calculation are the grout pressures used as boundary conditions and the resultant soil-lining gap, used to re-calculated the grout pressures. The gap can be calculated within FlexPDE through the expression:

$$gap = \sqrt{(x - Xt + u)^2 + (y + Zt + v)^2} - R_{lin} \tag{35}$$

where *Xt* and *Zt* are the horizontal and vertical coordinates of the tunnel centre, *x+u* and *y+v* are the coordinates of the deformed tunnel perimeter, and *Rlin* is the external radius of the lining.

For the purposes of the numerical calculation, the grout pressure is a stress boundary condition in the normal direction to the tunnel perimeter. In FlexPDE, all vectors have to be defined along the directions of the displacement variables, in this case X and Y. But as the grout pressure is considered isotropic, it has the same values in a radial direction. Nevertheless, it is defined in the software as a derivative boundary condition along the horizontal:

$$Nu = Sx.\cos(\theta) + Sxy.\sin(\theta) \tag{36}$$

And vertical direction:

$$Nv = Sxy.\cos(\theta) + Sy.\sin(\theta) \quad (37)$$

A Microsoft Excel (2016) spreadsheet is used to generate the input (boundary conditions) for, and take in the results (deformations) from, a FlexPDE calculation. Subroutines programmed in Visual Basic for Applications (VBA) are used to automatically generate the script, run the software and import the results. The FlexPDE script is created with a command for the generation of text files, reading parameters from the cells and saving the code as a *.PDE* file. The script includes the values for the constitutive parameters of the soil, geometric characteristics of the tunnel, and grout pressures, as well as instructions to generate output files in a standard format. The script is then processed in FlexPDE through a *ShellExecute* command. The output results are filtered, averaged for the domain used to calculate the grout pressures, and imported to the appropriate cells, which automatically re-calculates the grout pressures.

The grout pressures are calculated from the gap, initially assumed equal the geometric gap between the cutterhead and the lining radius, using the same rheological model described in Section 4.2.3. The calculation domain assumes vertical symmetry, so only half of the tunnel perimeter is simulated. A set of nodes is defined from the tunnel roof to the invert at a regular interval of 15°. An injection nozzle can be defined at each of the 13 nodes. Equations 16 and 17 are programmed to calculate the pressure field due to each injection nozzle. At each node, the resultant grout pressure will be the maximum value from all nozzles. The net force is calculated incrementally through the products between the average grout pressures, and the horizontal projection of the lining between each two nodes. The volume loss can be calculated considering the tunnel radius as the sum of the lining radius and the average tunnel-lining gap.

4.3.2. Examples

The example from Section 4.2.3, presented in Figure 4.20, can be re-calculated, with the same parameters, within this new framework considering the ground domain around the tunnel. As both models rely on linear elastic parameters, their results are quite similar (Figure 4.24). The calculated profiles of grout pressures are basically undiscernible, while the resultant tunnel-lining gap shows more clearly how this numerical method can take into account the in-situ anisotropic stress state ($k_0 \neq 1$). A much more pronounced expansion of the excavation around the tunnel springline was calculated in this new framework.

However, the most important output of this methodology is the displacement field around the tunnel. Figure 4.25 presents the calculated settlement trough for this example. With a maximum settlement of 7.5 mm, a total volume loss of 0.06 % was measured at the surface, a much smaller value than 0.37 % calculated in the numerical framework, and 0.34 % in the analytical one. Assuming the constitutive model is appropriate, an empirical estimation of the surface settlements based on the volume loss due to tunnel contraction would severely overestimate the settlements, as the volumetric strains of the ground wouldn't be taken in to account.

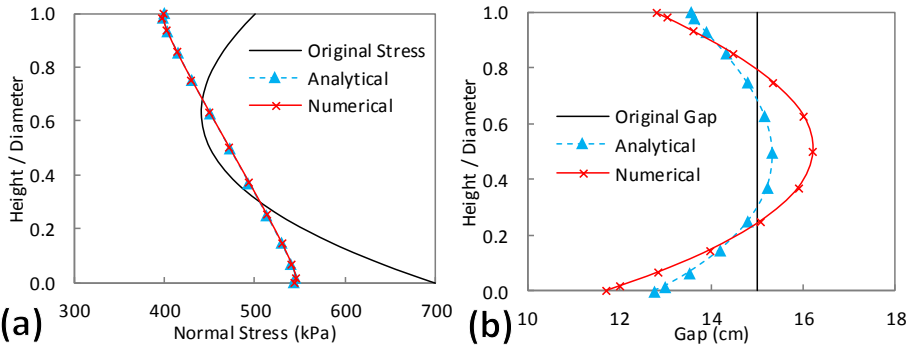

Figure 4.24. Calculation results from the analytical and numerical frameworks: grout pressures (a) and tunnel-lining gap (b).

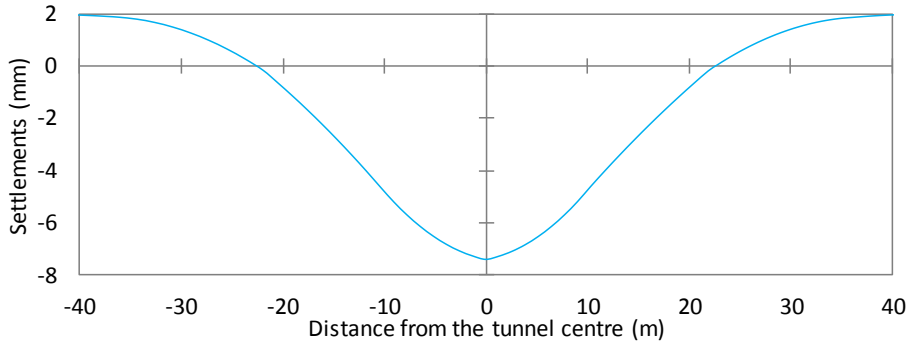

Figure 4.25. Surface settlements during the grout injection phase.

Continuing with these same parameters, namely: excavated radius = 5 m; initial tunnel-lining gap = 15 cm; depth of the tunnel centre = 30 m; ground Young's modulus = 45 MPa, ground Poisson's ratio = 0.3; ground volumetric weight = 20 kN/m³; coefficient of earth pressure at rest = 0.5; groundwater level at the surface; grout yield strength = 0.5 kPa; grout volumetric weight = 20 kN/m³, a few conceptual examples of different injection strategies were calculated.

The profile of grout pressures results from an intricate balance between the gap, the yield strength and unit weight of the grout and the injection strategy. Therefore, it is not an easy task to match the stress gradients of the soil and the grout. Another side of this balance is the net force over the lining, which is smaller when a more isotropic pressure distribution is created. On top of that, there is the resultant volume loss, which reflects a balance between expansion and contraction along the excavation perimeter, so a small resultant value does not mean that the displacement field around the tunnel is null. It is worth noting that this model does not consider the operational convenience of different injection systems Three injection layouts will be presented: one nozzle at the roof, two at springline and one at the invert. All layouts will be tested with an injection pressure of 500 kPa.

Figure 4.26a presents the results of the first layout with the nozzle at the tunnel roof, where the balance between the self-weight and the shearing dissipation of the grout pressure creates a relatively uniform loading around the lining. Placing another nozzle at 500 kPa anywhere around the lining will barely change this distribution, so it is not analysed. Extra nozzles can be needed for the appropriate discharge, but this model only considers how the nozzles affect the pressure distribution. The grout pressures are higher than the soil pressure from the top to about 20% the tunnel height. The effect of this can be seen at an expansion of the excavated perimeter (gap>initial gap) on the tunnel shoulders and a contraction on the tunnel invert. The difference is balanced quite well, resulting in a marginal volume loss of 0.03% on the tunnel boundary. This isotropic loading is also pronounced over a small net force of 42 kN acting upwards on the lining.

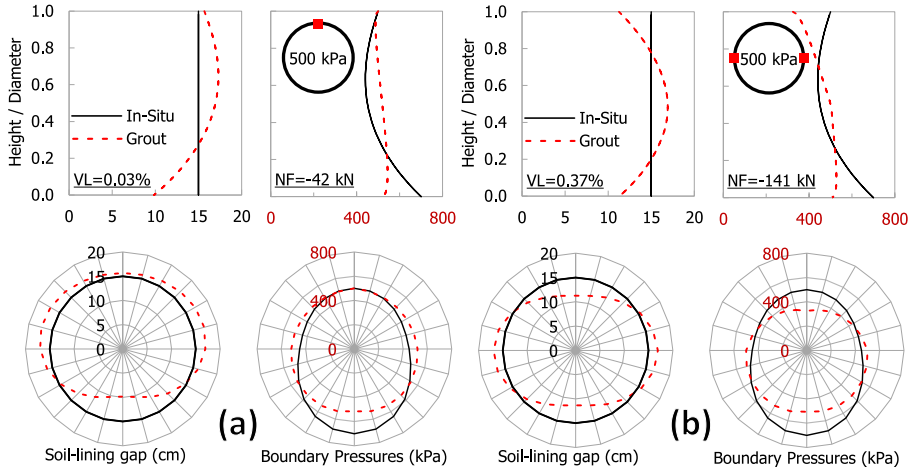

Figure 4.26. Example with injection nozzle at the tunnel roof (a) and Example with injection nozzle at the tunnel springline (b)

Another possible strategy would be to place the injection nozzle at the tunnel springline. The same shear/gravity balance occurs from the nozzle downwards. However, both dissipation forces are combined upwards, decreasing the grout pressure on the tunnel roof. The resultant profile is somewhat the mirror projection of the soil stresses. As it can be seen in Figure 4.26b, this becomes evident in the convergence profile with higher gaps along the springline and higher convergence on the roof and invert. The balance between convergence and expansion is not as good as in the previous example. The resultant volume loss is 0.37% and the net force on the lining is 141 kN acting upwards.

The last calculation places the injection nozzle at the tunnel invert (Figure 4.27a). As in the previous case, there is significant pressure dissipation towards the tunnel roof. This is pronounced in convergence around the tunnel roof and a much higher volume loss (1.16%). However, this injection strategy is the one that most resembles the stress gradient of the soil. If the pressure is calibrated, in this case to about 700 kPa, the same pattern can result is a null volume loss, as it can be seen in Figure 4.27b.

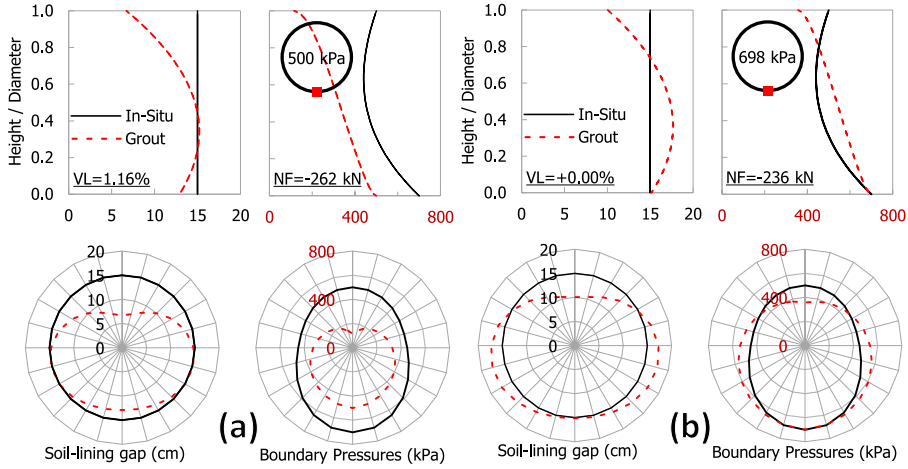

Figure 4.27. Example with injection nozzle at the tunnel invert / Example with injection nozzle at the tunnel invert and higher injection pressure

4.3.3. Overview

There have been significant advancements regarding how the processes around a TBM are understood and managed to achieve more reliable tunnel excavations. However, the quantitative models that represent these processes still feature as exceptional tools for the design of these tunnels, which includes the prediction of settlements (Dias and Bezuijen, 2015d). This section presented how a model for the grout flow can be associated with a finite element model to calculate the

induced soil displacements in a dynamic equilibrium between the boundary pressures and the soil-lining gap. These two elements were combined in a calculation tool with a user friendly input-output layout.

The model was used to compute different examples and their consequences in terms of volume loss and net force on the lining. For a 500 kPa injection pressure, the layout with an injection nozzle on the tunnel roof resulted in the smaller settlements and lower net force. The worst case for this layout was re-calculated with a different injection pressure and resulted in a null volume loss. In all the cases, different soil and grout properties can turn the patterns described in the example section in different directions. However, the point here is that with an objective and accessible framework, any condition can be processed and the results evaluated in a few minutes.

4.4. Iterative calculation of grout consolidation

In another step to adapt the TBM models (Section 4.2) to be used within a numerical calculation (Section 4.1), this section proposes a solution for the phase of grout consolidation. First, Section 4.4.1 discusses the basic problem of how to adapt the one-dimensional model of grout consolidation (Section 4.2.3) to the 2D tunnel domain. This conceptual model is formulated with the analytical relation between pressure and convergence from Equation 15. The calculation algorithm was programmed in a Python script, described in Annex D.

Once this framework is established, the concept is applied in a formulation where the finite element method is used to calculate the induced ground displacements. The models were processed with the software Plaxis (2016), which allowed other constitutive models to be used to represent the ground (Section 4.4.2). It is important to highlight how the methods discussed in this thesis can be applied to different software, as they only operate within the `I/O` lines. The Python scripts to manage the calculation and control Plaxis are described in Annex E.

4.4.1. Analytical model – Python

The variable pressure consolidation model assumes that the pressure of the liquid grout is always in equilibrium with the ground pressure at the tunnel boundary. When water flows from the grout into the ground, leaving a layer of consolidated (also called filtered) grout, the volume balance calls for a reduction in the total thickness of the grout layer. This contraction is followed by the tunnel boundary, and is associated with a reduction in the ground pressure (Figure 4.16). From the initial assumption, this will cause an equivalent reduction in the pressure of the liquid grout, reducing the driving force of consolidation.

The differential equation for this process assumes a Darcy flow where the gradient between the grout and water pressure is fully dissipated through the filtered grout layer. The water discharge (q_w.dt) is set equivalent to the boundary contraction (dR), as in:

$$k.\frac{(GP(dr)-Uw)}{x}.dt = dx\frac{(n_i - n_f)}{(1-n_i)} \tag{38}$$

where *k* is the permeability of the filtered grout, *GP(dR)* is the grout pressure, which depends on the boundary contraction (*dR*), *Uw* is the water pressure, *x* is the thickness of the filtered grout, *dt* is the time increment, *dx* is the incremental thickness of the filtered grout, *ni* is the porosity of the liquid grout and *nf* is the porosity of the filtered grout.

Equation 38 can be solved numerically from an initial non-null filtered grout layer, which can be calculated with the analytical formula from Equation 19. The numerical solution can reach convergence with larger time increments if an explicit formulation considering the mid-point values is used, as in:

$$dx_{t+dt} = k.\frac{\left(\frac{GP_t + GP_{t+dt}}{2} - Uw\right)}{x_t + \left(\frac{dx_{t+dt}}{2}\right)}.\frac{(1-n_i)}{(n_i - n_f)}.dt \tag{39}$$

The first idea to adapt this one-dimensional model to the domain of the tunnel perimeter is to simply apply it directly at each calculation node. From an initial state where the distributions of grout and water pressures are known, the gradient at each point would cause consolidation and the contraction of each point would be associated with a localized pressure dissipation. An example of this adaptation is presented in Figure 4.28, considering the same parameters from Section 4.3.2, with one injection nozzle at the tunnel roof setting a pressure of 375 kPa, and k_0 = 1, *ni* = 0.4, *nf* = 0.3, and *k* = 5.10^{-8} m/s.

The results are in agreement with the conceptual understanding of the process. The grout pressure decreases with time, while the vertical gradient progresses towards the gradient of water pressures. The derivative of the variables with time decreases, as the gradient inducing consolidation is dissipated.

However, there is a problem with this idea. During consolidation, the grout pressure at each point only depends on the gradient regarding the water pressure, it has no relation with the volumetric weight and yield stress of the

grout. So there is no guarantee that the calculated grout pressures are in equilibrium with the gravity field and the friction forces.

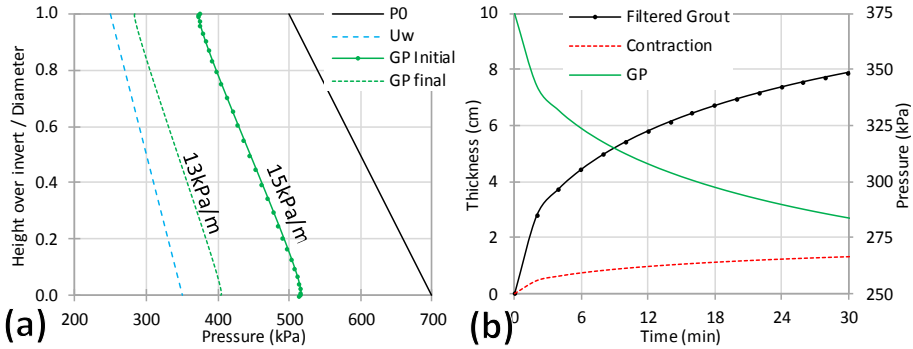

Figure 4.28. 1D Grout consolidation – Profiles of in-situ radial stress, water pressure and grout pressures at t=0 and t=30 min (a), and time evolution of grout pressure, filtered grout and contraction at the tunnel roof (b).

A better adaptation of the one-dimensional model is to consider the volume balance of the whole perimeter. The total water discharge at each time step has to match the total boundary convergence. The profile of grout pressure is calculated from the pressures at reference nodes, where the pressure is changed until the necessary convergence is achieved. For a set-up with equidistant nodes along the perimeter, the total values are equivalent to the arithmetic average of all nodes.

During consolidation, it is assumed that the injection nozzles can no longer be used for the reference pressures, as grout is not being injected. Therefore, in this pressure based framework, a new reference pressure must be established, from which all the other pressures can be calculated. A common issue in the distribution of grout pressure during injection is that it normally results in an upward force acting on the lining ring. This forces the lining to move up in the mixture, which is equivalent to the grout moving down along the soil-lining gap. In this way, it is possible to assume the grout pressure at the tunnel roof as a reference, from where the pressure in all the other nodes can be calculated, as the grout flows from the roof towards the invert.

A particular feature of the rheological grout model used in this thesis, the Bingham plastic model, is that for a null shear rate, the resultant shear stress can be any value between - τ_y and + τ_y. In other words, the shear stress can change directions, from the injection phase to the consolidation phase, in order to achieve equilibrium, without any relative movement, as long at the yield stress is not exceeded. Therefore, the lining doesn't actually have to move in relation to

the grout for the shear stress directions to change to the new boundary conditions.

Therefore, this analytical model for a 2D grout consolidation, can be implemented as follows:

1. Assume an initial grout pressure at the tunnel roof, from the phase of grout injection, and calculate the grout pressures around the tunnel, as in Section 4.2.3.
2. Calculate the equilibrium between the grout pressures and the soil-lining gap.
3. Calculate the average contraction associated with the water discharge due to consolidation.
4. Find a new grout pressure at the tunnel roof so that the calculated grout pressure distribution results in a soil-lining gap that is equivalent to the gap from Step 2 subtracted of the contraction from Step 3.

In this system, the grout pressures are always in equilibrium with both the gravity field and the friction forces, while continuity is guaranteed for the whole tunnel perimeter, as the contraction of the grout layer due to consolidation is matched by the convergence of the tunnel boundary, associated with a reduction in the grout pressures. Iterative calculations are required in two levels of this system. First, as in all others, to find equilibrium between the grout pressures and the soil-lining gap. And second, to find the grout pressure at the tunnel roof to cause an average contraction equal the total water discharge. This level can be implemented as a root finding scheme, such as the false position method described in Section 3.2. The previous example is re-calculated with this new concept, and the results are presented in Figure 4.29. The calculation algorithm is described in Annex D.

The results also agree with expectations, but here the profile of grout pressures is in equilibrium with the gravity field and the shear forces. The reduction in the vertical gradient is smaller than the previous example, as it is now only a consequence of higher shear forces acting along a thinner soil-lining gap.

At this point it is not clear how the mechanism develops once the water pressures are reached. One can assume that once the gradient at a certain point disappears, the mechanism stops locally and the grout shear forces change to accommodate this fixed pressure. Another possibility is that the shear forces remain fully mobilized, dictating the grout pressure distribution even for values smaller than the groundwater pressure. In these points the water would flow in the soil-lining gap, until there is a balance between the regions of inflow and outflow. Most likely, a more complex framework is needed to understand this

process. One where the velocity field can be computed considering how the grout properties change with time and the lining responds to the buoyant forces. However, this would also require a more extensive input, which is not available at the moment. More details on further research are discussed in Chapter 6.

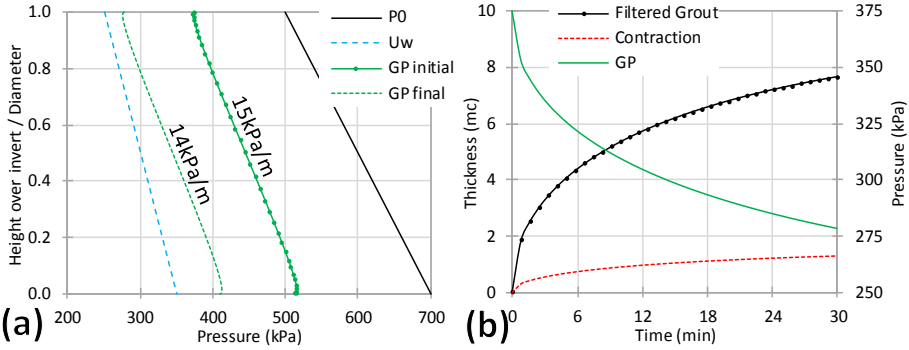

Figure 4.29. 2D Grout consolidation – Profiles of in-situ radial stress, water pressure and grout pressures at t=0 and t=30 min (a), and time evolution of grout pressure, filtered grout and contraction at the tunnel roof (b).

For now, this framework is considered suitable to represent grout consolidation around a tunnel. The next section explains how this framework can be used with a numerical calculation. Once the ground displacements are calculated with the finite element method, it is possible to estimate the tunnel volume loss and settlement trough.

4.4.2. Numerical model – Plaxis

Plaxis 2D is a finite element package for deformation and stability analyses in geotechnical engineering. In this section, it will be used to solve the boundary value problem of mechanical equilibrium during a tunnel excavation. The user does not interact with the definition of variables, equilibrium equations or constitutive equations, as with FlexPDE. The software requires an input of domain, constitutive parameters, and boundary conditions, which are normally established through a graphic user interface. This wouldn't be a suitable option for the iterative calculation cycles required in these TBM models.

However, since 2015, Plaxis can be operated through a remote script programmed in Python, a high-level interpreted programming language based on free and open-source software. This allows the user to control both the Input and Output programs via an external Python interpreter, to either directly write input commands on-the-fly or to run script files. The Python script can also be used to process the output, check for objective conditions, and run recursive

procedures to guide the calculation. This is a useful feature within this framework, where a few hundred calculation cycles are required.

The software provides a more representative calculation of the ground deformations through the use of advanced soil models. Some relevant aspects of tunnel analyses with different constitutive models have been discussed in Section 4.1, and the general idea of using a constitutive model within a mathematical representation of a physical system has been discussed in Section 2.5. However, there are deeper issues behind the development of constitutive models for multiphasic granular materials, such as the critical state condition (Gens and Potts, 1988; Wood, 1990), the combination of a deviatoric and a cap function to account for the yield surface (Schanz et al., 1999), small strain stiffness (Viggiani and Atkinson, 1995), the advantages of studying soil behaviour through the spatially mobilized plane (Nakai, 2004), and others. These discussions are out of the scope of this thesis, but should always be considered during a geotechnical numerical analysis.

The numerical integration and the different techniques of error control implemented in this package result in a much more robust calculation scheme, which comes at a cost of processing time. Therefore, the Python scripts devised in this section shouldn't rely on a full definition of the model at each calculation cycle, as with FlexPDE, but should only change the necessary parameters. Another issue that arises from the use of elasto-plastic constitutive models is that every new stage in time depends on the stress and strain paths from the previous stages. Therefore, each time step during grout consolidation has to be a new calculation stage (phase) in Plaxis. The whole script is divided into four modules, which are fully explained in Annex E, but can be schematically understood as:

1. Create Model: Defines dimensions of the domain, ground layers, constitutive models and parameters of each layer, tunnel position, dimensions and divisions for the grout pressures to be declared. Defines a fine mesh, which is automatically created (Figure 4.30). From the initial phase where the geostatic stresses are calculated through the body forces, the script defines the first phase, where the ground elements inside the tunnel are deactivated, while the polycurve elements with the tunnel boundary pressures are activated. This base file is then saved in a certain folder.
2. FEA Calculation: Creates a new calculation phase, if required, declares the new grout pressures and calculates the model. The coordinates, displacements and water pressures around the tunnel are imported

from the Output software. The results are averaged and interpolated for the position of the nodes in the grout pressure calculation.

3. Iterative Grout Pressure: For a certain grout pressure at the tunnel roof, and from an initial soil lining gap, the equilibrium between grout pressures and tunnel contraction is calculated using the 2nd routine. The calculation assumes convergence if the difference in soil-lining gap from two consecutive calculations is smaller than 5 mm for all nodes.
4. Grout Consolidation: At each time step, the average contraction due consolidation is calculated. A root finding scheme calculates the new grout pressure at the tunnel roof to cause an average reduction in the soil-lining gap that is equivalent to the consolidation contraction. At each iteration of the scheme, the profile of grout pressures at equilibrium is calculated using the 3rd routine. The calculation stops at the last time step, or if the thickness of the grout layer surpasses the soil-lining gap.

The whole calculation progresses faster if the output is only processed at the tunnel boundary. So, once the calculation is finished, another routine can be applied to retrieve the surface settlements at specific time steps. The total processing time of this algorithm can reach the scale of hours, so it is important to save the necessary data so if the calculation stops at any point, if the software crashes for example, it can be started again from the saved last iteration. A Microsoft Excel (2016) spreadsheet is used to write these scripts and import the end results for analysis.

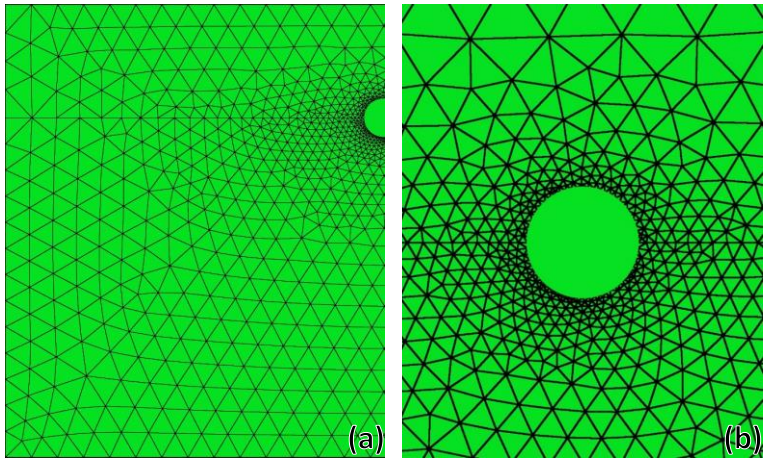

Figure 4.30. Example of an automatically generated fine mesh in Plaxis.

4.4.3. Examples

An example calculation is presented for a 10 m diameter tunnel, centred at a depth of 30 m (Figure 4.31).

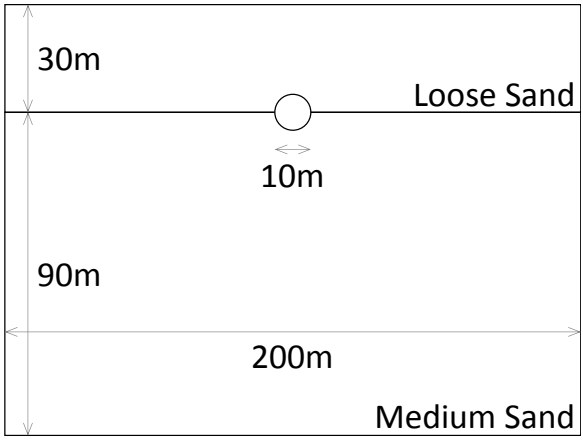

Figure 4.31. Sketch of the calculation domain.

The profile of grout pressures was calculated considering an initial soil-lining gap of 15 cm, grout yield stress of 0.5 kPa, volumetric weight of 20 kN/m³, permeability of filtered grout of 2.10^{-8} m/s, initial porosity of 0.4 and final porosity of 0.3. At the onset of consolidation, the grout pressure at the tunnel roof was set at 450 kPa. A total period of 30 min was simulated in steps of 50 s. The ground was simulated with two layers of sand.

The parameters were estimated from the empirical correlations proposed by Brinkgreve et al. (2010). The first layer was 30 m thick and represented loose sand at a relative density of 20%. The second layer, extended for the rest of the model, represented a sand at 50% relative density. The parameters for the Hardening-Soil model are in Table 4.2 and the results are in Figure 4.32.

Table 4.2. Parameters for the grout consolidation example in Plaxis

Parameters	Loose	Medium
γ_{unsat} (kN/m³)	15.8	17.0
γ_{sat} (kN/m³)	19.3	19.8
ϕ (°)	31	34
ψ (°)	0.5	4.0
Rf	0.975	0.937
E_{50}^{ref} (MPa)	12	30
E_{oed}^{ref} (MPa)	12	30
E_{ur}^{ref} (MPa)	36	90
m	0.6375	0.5437

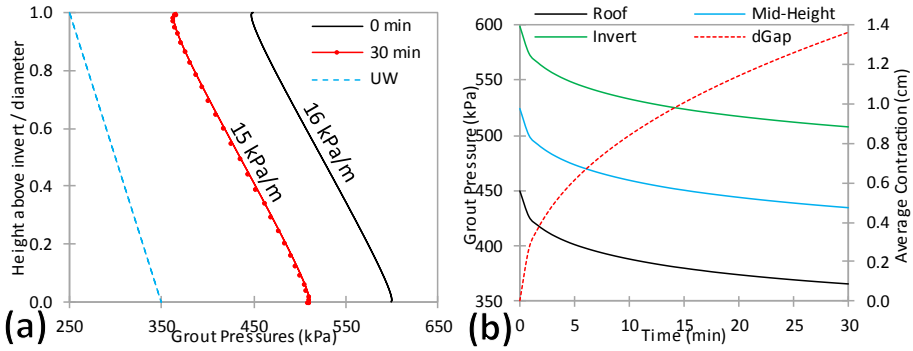

Figure 4.32. Numerical calculation of grout consolidation – Profiles of grout pressure and water pressures along the tunnel height (a), and as they evolved with time together with the average boundary contraction (b)

During these 30 min, the pressure at the tunnel roof dissipated from 450 kPa to about 365 kPa, while the vertical pressure gradient changed minimally, from 16 to 15 kPa/m (Figure 4.32a). This reduction caused an average contraction of the tunnel boundary of 1.36 cm. The progression of the pressures with time can be seen in Figure 4.32b, for three points around the tunnel. The total pressure difference along the tunnel invert and at mid-height was slightly larger than at the tunnel roof (90 vs 85 kPa).

At the onset of consolidation, the average deformation of the excavation boundary was practically null, with regions of contraction and expansion cancelling each other out, so that the resultant volume loss was -0.11%. After consolidation, the region around the tunnel roof had contracted significantly, causing a volume loss of +0.43% (Figure 4.33a). Comparing the dissipation of pressure with the resultant deformations, it is clear how the tunnel invert had a more rigid response than the tunnel roof, roughly by a factor of 10x. This anisotropy is not present in the linear elastic calculations, where the loading direction has no influence on the result. In terms of surface settlements, the results were even more pronounced. The net expansion of the boundary at the start of consolidation caused the surface to settle up 15 mm in a trough equivalent to 0.7 % volume loss. During the first 15 min the displacements had practically doubled (δ_{max} = 27 mm, *VL* = 1.32%), but as the pressure dissipation slowed down, the rate of the displacements also decreased, so that at 30 min, the maximum settlement was 32 mm and the volume loss was 1.57% (Figure 4.33b).

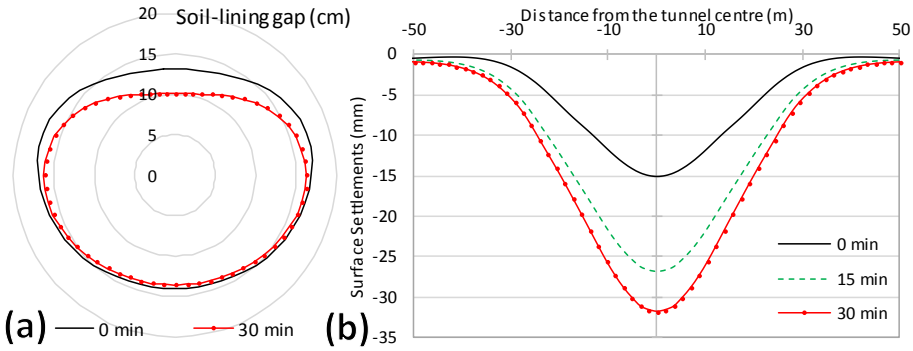

Figure 4.33. Numerical calculation of grout consolidation – Polar plot of soil-lining gap (a), and surface settlements at different times (b).

4.4.4. Overview

Following a series of developments in this chapter, this section presented how a model for the grout consolidation can adapted to a two-dimensional domain, and associated with a finite element model to calculate the induced soil displacements at each time step. A different finite element package was used so that other constitutive models could be used to model the ground, and to show that, as the methodology only operates on the input/output lines of software, it can be adapted to different packages. To manage the substantial number of calculations and results, the algorithms were implemented in Python, a programming language based on free and open-source software.

Two different ideas on how to adapt the 1D consolidation model were discussed theoretically and through examples based on an analytical model. The most suitable idea was then adapted to interact with Plaxis, a finite element software for geotechnical analysis. The model was then used to compute one example of a tunnel excavated between two layers of sand, modelled as elastoplastic materials. The results highlight how continuity must be guaranteed for the tunnel boundary as a whole. With the use of advanced constitutive models, the reaction of the tunnel invert is normally much stiffer than at the tunnel roof. If the pressure profile was assessed locally, this would cause a much faster dissipation around that region, causing a distribution of grout pressures violating equilibrium. Again, the most important output of this methodology is the displacement field around the tunnel. During consolidation, even though the tunnel boundary suffered minimal convergence, the settlements at the surface increased significantly, causing more than 30 mm of settlement above the tunnel centre. These results are a direct consequence of the input parameters, chosen at will for the example, as the point of these models is that within an objective and

accessible framework, any condition can be processed and the results evaluated in a few minutes.

4.5. Validation – Green Heart Tunnel

The HSL-Zuid is the 125 km-long Dutch section of the high-speed railway line connecting Amsterdam, Rotterdam and Antwerp. The line passes by the *Groene Hart* region in The Netherlands, a preserved natural area surrounded by the four largest Dutch cities. To minimize the impact on this typical landscape, the lines goes into a 7 km-long tunnel, named after the region, close to the city of Leiden, as it can be seen in Figure 4.34.

Figure 4.34. Location of the Green Heart Tunnel.

The tunnel was designed as a single tube with train lines in both directions, which required a circular tunnel with an internal diameter of 13.3 m, providing an internal area of 139 m². A slurry pressure balance tunnel boring machine was used to excavate the whole tunnel alignment. The TBM shield, named Aurora, was 12.395 m long and 14.85 m in diameter close to the cutterhead (Figure 4.35). It had six injection lines positioned every 60° from the tunnel roof. The TBM backup reached up to 120 m in length during construction, with systems to supply the lining segments and remove the spoils. The excavation started on 2 / Nov / 2001, direction South, and the TBM broke through on 17 / Jan / 2004, after 35870 segments had been installed and $1.3.10^6$ m³ of spoil had been removed (Tunnelbuilder.com, 2004). The tunnel lining was made out of precast reinforced concrete segments, 60 cm thick, combined in 2 m long rings (9 + 1) with an outer diameter of 14.5 m. The average depth of the tunnel centre was 26.9 m.

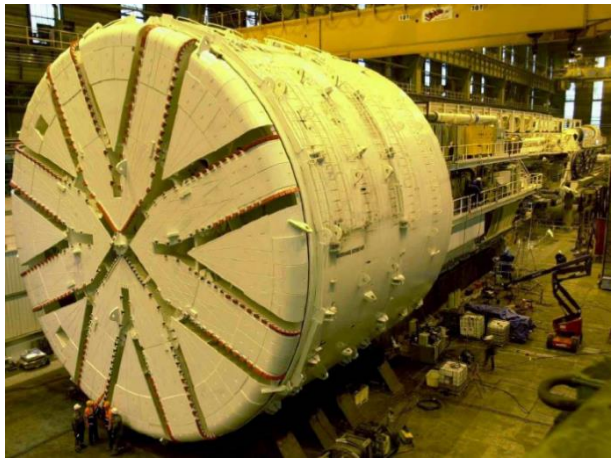

Figure 4.35. Slurry TBM used in the Green Heart Tunnel (TEC, 2014).

Most of the excavation took place within two sand layers below a thick mixed stratum of soft peats, clays, and sand. A simplified geological profile is presented in Figure 4.36.

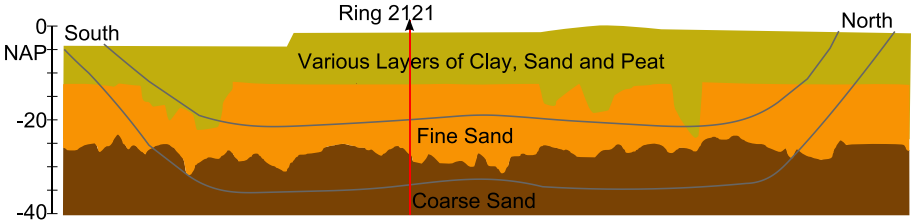

Figure 4.36. Geological profile along the Green Heart Tunnel (adapted from Talmon and Bezuijen, 2008).

The field measurements from one instrumented section of the tunnel are used here to validate the methods proposed in this chapter. The lining ring N° 2121, centred 4226.96 m away from the north portal, was instrumented with three pressure gauges. The sensors were placed on the lining extrados along a depression filled with tail void grease. The ring started to be erected on 3 / Jun / 2003 at 14:40, more than 4 m inside the shield. The segments got out of the shield between 19:27 and 21:24 the same day. Right above this ring, at the projection 4227.30 m away from the north portal, a line of 13 settlement sensors was installed at the surface. Figure 4.37 presents the details of this cross section. The pressure sensors captured the first grout injection around the ring at 21:33, which is set at time 0 for all the discussions hereafter.

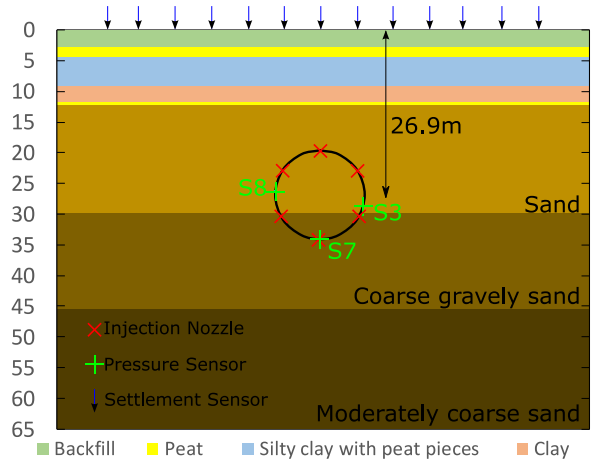

Figure 4.37. Cross section around ring N° 2121 with the geological layers, tunnel depth, location of the instruments and injection nozzles.

4.5.1. Field measurements

The displacements recorded by seven sensors at the surface are presented in Figure 4.38 together with the relative positions of the TBM.

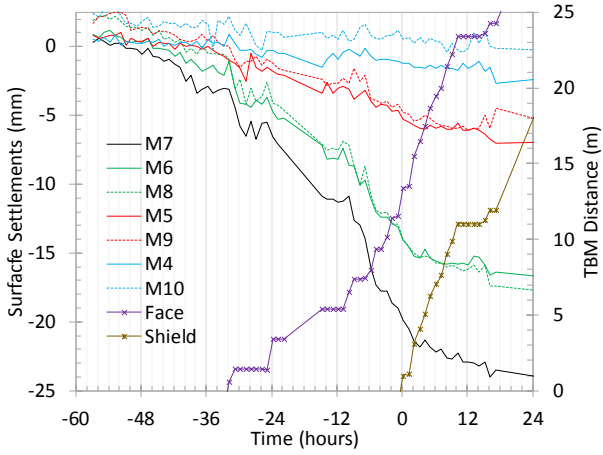

Figure 4.38. Surface settlements and TBM position with time.

The surface settlements started to progress around 48 h before grout was actually injected under the section. Unfortunately, the position of the TBM is not known until 16 h after that (-32 h), when face was just below the section and the maximum settlement was around 3 mm (M7). In the next 6 h (-24 h), the TBM face advanced 3.4 m pass the section, causing a maximum settlement of 7 mm. From there until about 12 h before injection, the excavation advanced one more

ring (2 m) at a rate that was slower than usual, which nonetheless caused the settlement at above the tunnel centre to reach 11 mm.

In the next 20 h (-10 to +10), the TBM advanced at an average rate of 86 cm/h, causing a steep settlement progression until about 2 h after the injection, when the settlement at M7 was about 21 mm. The settlement troughs at 10 different moments are presented in Figure 4.39.

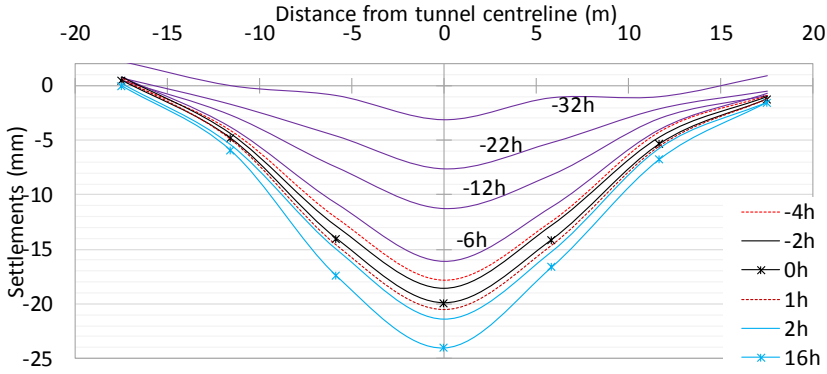

Figure 4.39. Settlement troughs with time.

While that was happening on the surface, grout was being injected underground. The three pressure sensors S7, S3 and S8 were positioned at 34.15, 28.71 and 26.32 m deep, respectively. The pressures recorded during the first 24 h after injection can be seen in Figure 4.40, with the reference water pressure at each depth. The small inversions in the settlements after injection roughly match the peaks of grout pressure around 4 and 7 h.

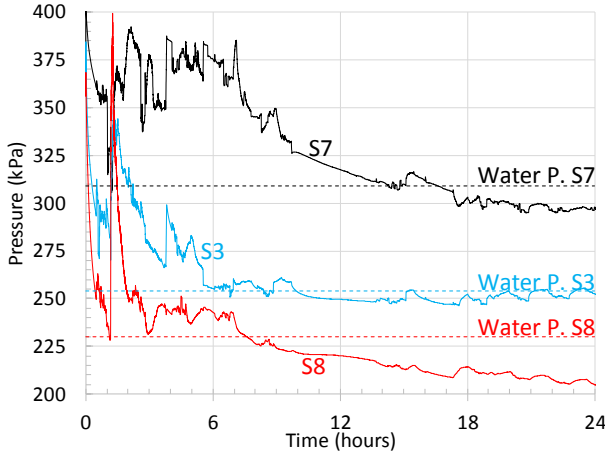

Figure 4.40. Grout pressures during the first 24 h after the first injection.

The first incidence of grout consolidation happened between the first and second peaks of pressure, during the first hour after injection. This period is explored in Figure 4.41, where the profiles of grout dissipation can be seen in more detail, together with the pressure distribution along the vertical direction.

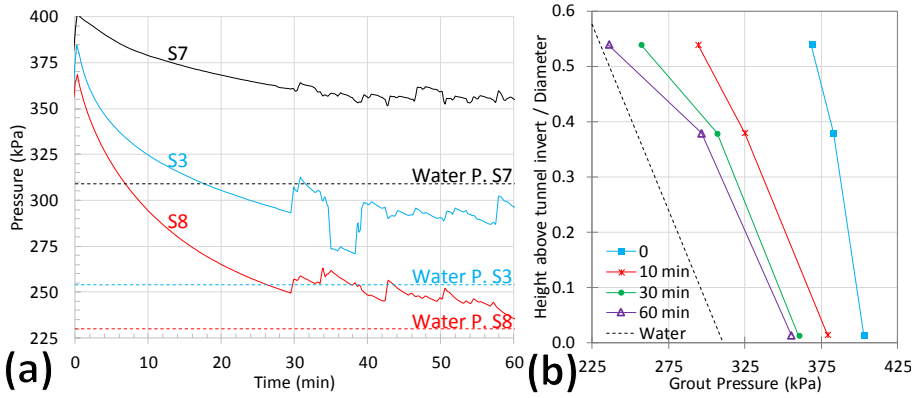

Figure 4.41. Grout pressures during the first consolidation period. Time progression (a) and distribution along the vertical direction (b).

As described in the theoretical section, the pressure dissipation slows down with time, towards the water pressure. At the injection phase, the pressure at S8, close to the tunnel springline, had the highest gradient to the water pressure at that time. After 60 min, that gradient was almost null, as the pressure in the grout approached the water pressure, more significantly than around the other two sensors.

The ground parameters were obtained from investigations conducted around a section roughly 500 m closer to the north portal than the section of analysis, where the geology was practically the same (Ring 1888). The profile is divided in four layers: soft ground (A), fine sand (B), dense coarse sand (C), and coarse gravely sand (D). The parameters to represent these layers with the Hardening Soil model are in Table 4.3.

The grout was composed of sand, fly ash, lime and chemical additives. Direct tests were only conducted on March 2002, more than a year before the TBM was around Ring 2121. A fresh sample was collected from a supply container in the TBM, with a density of 1850 kg/m³ and a water content of 0.201. A vane shear test indicated a yield stress between 0.5 and 1.5 kPa for the first 12 h after the grout had been mixed.

The next two sections will validate if the methods from Sections 4.3 and 4.4 can reproduce the results measured around the Green Heart Tunnel.

Table 4.3. Ground parameters around Ring 2121 of the Green Heart Tunnel

Layer	A	B	C	D
Depth (m)	0 - 12	12 – 30	30 – 45	>45
γ (kN/m³)	14	20	20	20
E_{50}^{ref} (MPa)	3	[29; 65]	[62; 124]	[44; 89]
E_{oed}^{ref} (MPa)	2	[17; 38]	[34; 69]	[25; 49]
E_{ur}^{ref} (MPa)	9	[116; 260]	[248; 496]	[177; 354]
m	0.9	0.9	0.5	0.5
c (kPa)	4	0	0	0
φ (°)	22	[32; 36]	[31; 33]	[29; 34]
Ψ (°)	0	[2; 6]	[1; 3]	[0; 3]
OCR	1.3	1.0	1.0	1.0
k_0	0.5	0.5	0.5	0.5

4.5.2. Grout injection

The analytical method is used as a first attempt to reproduce the profile of grout pressure presented in Figure 4.41b at the moment of injection. The model requires a single parameter to represent the ground, the shear modulus. The reference stiffness modulus for primary loading (E_{50}^{ref}) can be adapted to elastic parameters, for zero cohesion, through the expression (Brinkgreve et al., 2013):

$$E_i = \left(\frac{2}{2 - Rf}\right) . E_{50}^{ref} . \left(\frac{\sigma'_3}{\sigma^{ref}}\right)^m \tag{40}$$

where Rf is the failure ratio, σ'_3 is the effective minor principal stress, and m is the parameter that defines the level of stress dependency.

Considering the reference modulus from layer B (E_{50}^{ref} = 29 MPa, m = 0.9), at the depth of the tunnel centre (σ'_3 = 100 kPa), and the standard values Rf = 0.9 and σ^{ref} = 100 kPa, it is possible to obtain an equivalent Young's Modulus of E = 53 MPa. The shear modulus can then be calculated with the standard Poisson ratio of the Hardening soil model (ν = 0.2).

Considering the six injection points around the tunnel working with an injection pressure of 320 kPa, and a grout yield stress of 1.5 kPa, the analytical model can calculate a profile of grout pressures reasonably close to the measured values (Figure 4.42a). The figure also shoes the geostatic stress normal to the tunnel, which is quite similar to the grout pressures for the top 60% of the tunnel height. For an estimate of displacements, the traditional Gaussian curve can be used to

fit the settlement trough, which results in an equivalent volume loss of 0.19 % (Figure 4.42b). This is perfect agreement with the average tunnel contraction calculated in the model (7.2 mm). However, this is not a direct estimate of the surface settlements, it is an empirical curve fit considering that the contraction of the tunnel boundary is equivalent to the volume of the settlement trough.

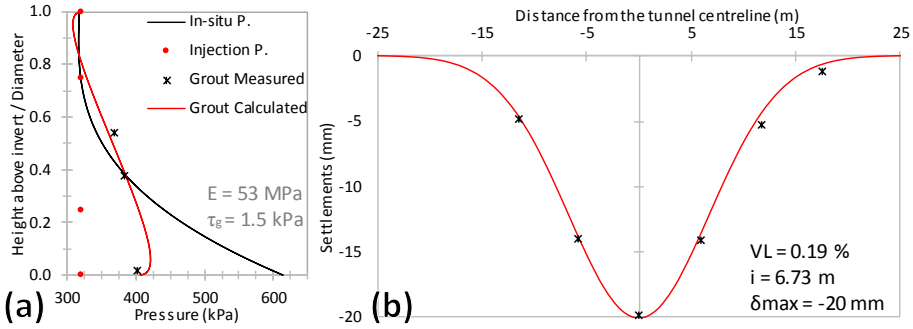

Figure 4.42. Analytical calculation of grout pressures (a) and Empirical Gaussian curve of surface settlements (b).

For a direct estimate of the surface settlements, a finite element calculation is required. The values of grout yield stress and injection pressure used in the analytical calculation are kept constant through all analyses to highlight the way each model reacts to the injection strategy. The aim here is not to calibrate the models to fit the surface settlements, but to determine if it possible to make accurate predictions of displacements from a known set of grout properties and injection pressures. The surface settlements from four numerical calculations are compared with the measured values, fitted with a Gaussian curve, in Figure 4.43.

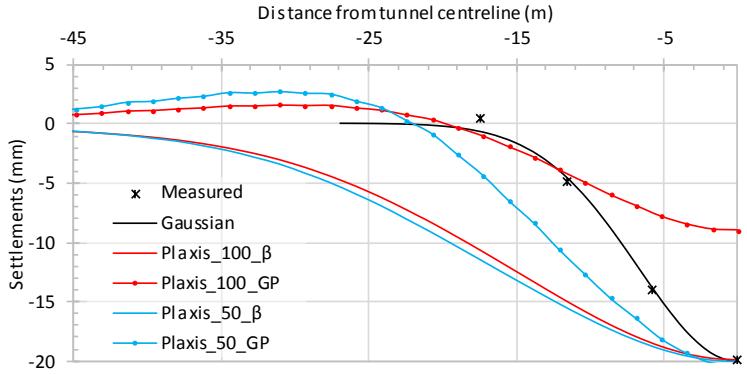

Figure 4.43. Calculated surface settlements against measured values at the moment of injection.

Initially, the ground parameters are defined at the lower bound of the range presented in Table 4.3. The first Plaxis calculation is performed with the traditional stress-release method (Plaxis_100_β). The fit for the maximum settlement was achieved with a stress release factor of 12%. The resultant trough was much wider than the measured settlements, which is typical of standard numerical calculations. The second model considered the iteratively calculated grout pressures (Plaxis_100_GP), which resulted in a maximum settlement of just 9 mm.

A better fit was achieved by reducing the rigidity parameters of all layers by 50%. The calibrated curve for the stress release model (Plaxis_50_β, β=7.2%) is still very wide, but the results with the grout pressures were much closer to the measured values (Plaxis_50_GP). The maximum angular distortion from this settlement trough, 1/765, is still smaller than the Gaussian distortion of 1/560. Nevertheless, it represents a significant improvement over the stress release model (Plaxis_50_β, 1/1420).

The resultant deformations can also be evaluated through the final soil-lining gap (Figure 4.44a). The numerical models predicted higher values for the convergence around the tunnel roof and the expansion around the tunnel springline, and smaller values for uplift around the invert. The average deformation around the tunnel perimeter was 7.25 mm for the analytical model, 2.16 mm for Plaxis_100 and 5.09 mm for Plaxis_50, all in contraction.

These deformations are connected, through the methodology described before, with the grout pressures, which can be seen in Figure 4.44b against the measured values. All the profiles were quite similar, and match the measured pressures relatively well. However, the gradients are a bit higher than what was measured.

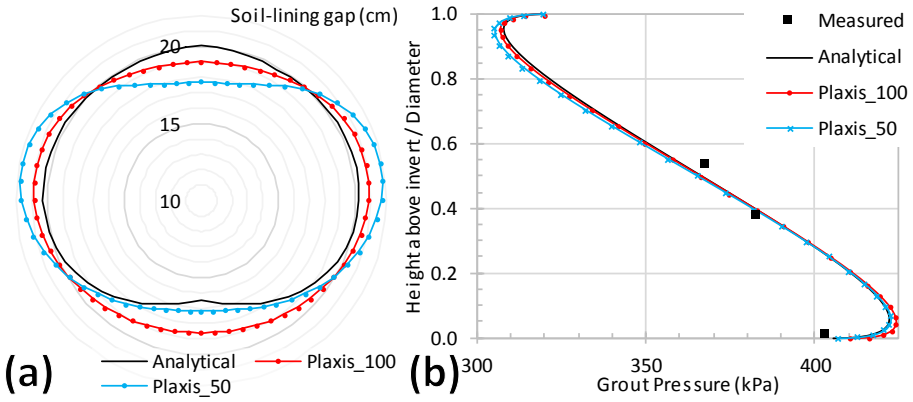

Figure 4.44. Calculated profiles of grout pressure against measured values

4.5.3. Grout consolidation

In this section, the mathematical models will focus on reproducing the evolution of grout pressures with time presented in Figure 4.41a. The calculations are performed with the same parameters from the previous section. The porosity of the liquid and filtered grout are assumed n_i = 0.4 and n_f = 0.3, respectively. Two permeability values were considered for the filtered grout: 1.10^{-8} and 6.10^{-8} m/s. The results of the analytical calculation are presented in Figure 4.45.

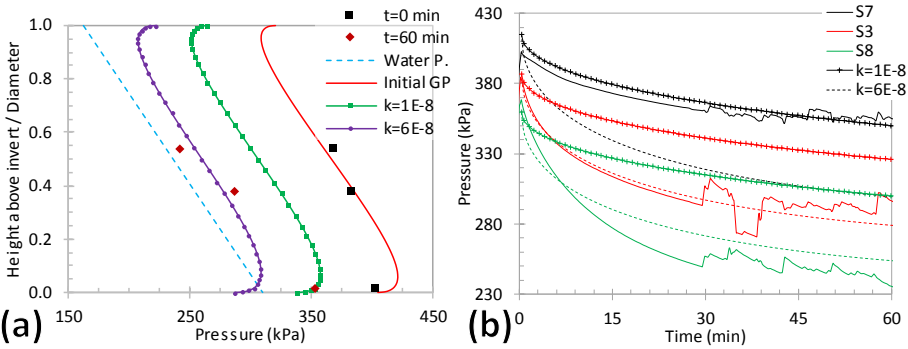

Figure 4.45. Analytical calculation of grout consolidation during the first hour after injection. Profiles of pressure along the tunnel height (a) and pressure dissipation with time (b).

The smaller permeability resulted in grout pressures that were generally higher than the measured values, even though the results around the tunnel invert were very accurate, for both the final pressure (Figure 4.45a) and the pressure dissipation with time (Figure 4.45b). The pressure dissipation was too small to match the pressures around sensors S3 and S8, close to the tunnel springline. For the higher permeability, the resultant distribution was closer to the values around S3 and S8, and the dissipation with time was very accurate around S3. However, the pressure dissipation around the tunnel invert was higher than the field response.

From an initial volume loss of 0.20%, the calculated profiles of grout pressure caused an average contraction equivalent to 0.48% and 0.69% volume loss for the permeability values of 1.10^{-8} and 6.10^{-8} m/s, respectively. If these values are used in the empirical Gaussian curve to calculate the surface settlements, the maximum settlements above the tunnel centreline would be 50 and 71 mm, respectively. However, during the first hour after injection, the measured settlements increased by less than 1 mm, as can be seen in Figure 4.39.

The numerical calculation with Plaxis exposed the different ground reactions along the tunnel perimeter (Figure 4.46). For the smaller permeability, the

contraction induced by consolidation caused a very small dissipation of pressure. For the higher permeability, the response was quite accurate around the tunnel invert, even though the initial pressure was about 15 kPa higher than the measured value. However, the pressures around the tunnel springline were much higher than measured. The final profiles of pressure along the tunnel height were very close around the tunnel roof, and differed in about 20 kPa through the rest of the perimeter.

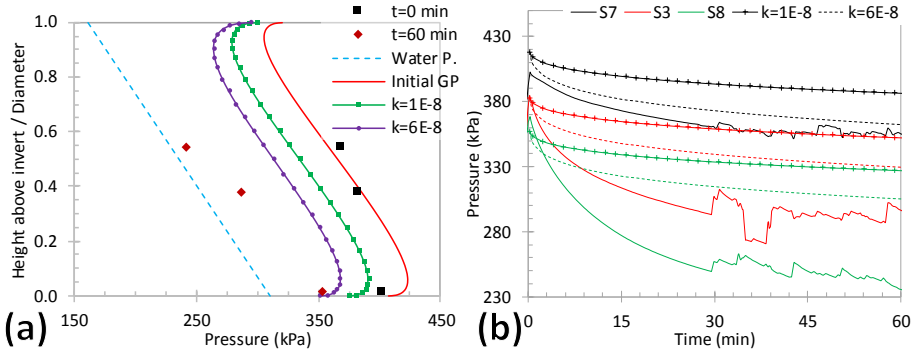

Figure 4.46. Numerical calculation of grout consolidation during the first hour after injection. Profiles of pressure along the tunnel height (a) and pressure dissipation with time (b).

The resultant displacements are presented in Figure 4.47.

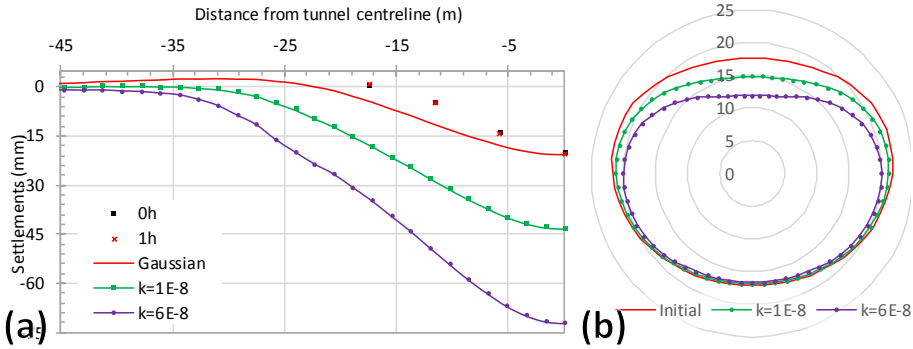

Figure 4.47. Numerical calculation of grout consolidation during the first hour after injection. Profiles of pressure along the tunnel height (a) and pressure dissipation with time (b).

During consolidation, the initial average contraction of 5.2 mm (*VI* = 0.14%) increased to about 16 mm (*VI* = 0.43%) and 29.4 mm (*VI* = 0.79%) for the permeability values of 1.10^{-8} and 6.10^{-8} m/s, respectively. This contraction happened mostly around the tunnel roof, which had a much more flexible

response than the tunnel invert. At the surface, the maximum settlements were 43 and 72 mm. Again these were much higher values than the 20 mm measured in the field.

4.5.4. Overview

The validation of the calculation methods presented in this chapter highlights the failures and successes of the second part of the methodology outlined in Section 2.5, which was supposed to develop a model to predict the ground movements during tunnelling. The chapter was focused on tunnels excavated with closed-face tunnel boring machines, and mathematical models based on the numerical solution of static equilibrium equations. All new developments proposed were based on a simple idea, to predict the forces acting around a TBM and to use them directly as boundary conditions in the mathematical models. This led to a study of the different physical processes that have been identified around TBMs through the results of field measurements and physical models. Simple mathematical models to represent the processes involved in tail void grouting were then incorporated into numerical calculations to compute the forces and displacements at equilibrium.

The first model tried to simulate the excavation stage when grout is being injected at the back of a TBM. The model was able to reproduce the distribution of grout pressures around the excavation perimeter quite well. For the surface settlements, the model made better predictions than the traditional stress-release method. The settlement trough was more or less in-between the results of the traditional calculation and the real measured values. Although it is an improvement, it is still not an accurate model to represent a real mechanized tunnel excavation.

There are several possible reasons for the differences between calculated and measured values, the most likely is the geometrical domain of the problem. The starting point of any zone where grout is being injected in a TBM is not a geostatic 2D domain, it is a three-dimensional region, which has been pressurized and then excavated by the face of the TBM, and then supported by the pressures around the shield until it reaches the tail of the TBM. Nonetheless, a 3D mathematical model relies on the same principles, it is still a boundary value problem that requires adequate boundary conditions. In other words, the forces acting on the excavation perimeter of the tunnel must also be known in a 3D model. However, the model used here to calculate the grout pressures is most likely too simple to predict the pressure distribution for a cylindrical domain. A more complex model, able to solve the velocity field, would be required. Therefore, further

research is needed to devise suitable calculation models to compute the pressure distributions around a cylindrical domain.

The second model attempted to describe how these grout pressures evolve with time as water flows from the liquid grout into the ground. Locally, the pressure dissipation could be matched quite well. However, the calculated distribution of pressures around the tunnel perimeter didn't correspond to the measured values. The calculated vertical pressure gradient, around 8 kPa/m at the moment of injection, decreased during consolidation, as the perimeter contraction intensified the grout friction in the soil-lining gap. On the other hand, the measured values show an increase in the pressure gradient during consolidation, reaching close to 14 kPa/m.

These differences suggest that either the lining is moving inside the grout mixture, or that the grout shear stress is not fully mobilized during consolidation. The first theory affects the soil-lining gap, while the second changes the rate in which the grout dissipates from the tunnel roof to the invert. To properly simulate these assumptions, a more complex rheological model for the grout would also be required, where both the velocity field during flow and the partially-mobilized shear stress during static equilibrium can be determined, taking into account the movements of the lining. At the point where a cylindrical domain can be used, the equilibrium state will have to consider the relation between the lining movements, the grout forces and the dead weight of the tunnel.

Another point of concern are the differences in ground displacements. While they are certainly connected to the distribution of grout pressures, and would most likely improve if the measured values could be reproduced more accurately, the scale of the error suggests that there are other processes involved. Looking directly at the measured values, one can perceive a considerable change in ground stiffness from the moment of injection to the first hour of consolidation. The drop from the initial ground stress to the injection grout pressures caused a maximum surface settlement of 20 mm. From a theoretical geostatic distribution, and the average from the three measurement points, this drop is in the range of 20 kPa. During consolidation, the pressure drop is more than four times higher, while the increment of surface settlement is about 1 mm. This roughly represents an increase of two orders of magnitude in the ground rigidity.

At the same time, the pressure dissipation around the tunnel can be calculated accurately, even though only locally, with the same rigidity used to calibrate the surface settlements at the moment of injection. If the ground around the tunnel was actually 100x more rigid, the final grout pressures would be reached much

faster, as the consolidation contractions would cause higher pressure drops, or the grout permeability in the field would have to be much smaller than what was measured in the lab. These considerations would lead to the unlikely explanation that the grout injection around the tunnel caused a significant increase in the ground stiffness close to the surface, but not in the immediate surrounding of the excavation. In this way the ground could be flexible enough for the slow pressure dissipation to take place around the tunnel, while minimal increments of displacement would be measured at the much stiffer surface. This interpretation is probably wrong, as there is no direct evidence to support it. At the moment this can only be used to justify the need for more field cases with direct instrumentation to record the grout pressures and ground displacements.

5. A Design Tool for Pile Tunnel Interaction

This chapter closes the proposed methodology to compute the consequences of pile tunnel interaction. The framework for pile analysis, discussed in Chapter 3, and the numerical techniques to estimate the settlements around a tunnel, discussed in Chapter 4, are combined in a general design tool for pile tunnel interaction. Considering that not all cases of PTI will involve mechanized tunnels, and the debatable accuracy of the proposed methods, the design tool will also be programmed with an analytical solution for the ground displacements.

Unfortunately, there are no instrumented field tests to this day where the pile settlements and axial forces were recorded concurrently to the grout pressures around a tunnel boring machine working underground. Therefore, the final validation of this methodology resides on its ability to reproduce the fundamental mechanisms identified in Chapter 2.

5.1. Pile equilibrium under ground displacements

In the framework of the modified load-transfer method, ground displacements (GD) act with the pile settlements to define the variable of relative displacements. The balance between the two displacements sets the mobilization of the shaft and toe forces for equilibrium. This relation is quite similar to what was presented in Section 2.6: At a certain depth, if the ground settlements are higher than the pile settlement, negative friction develops, increasing the axial force on the pile. If the ground settlements are smaller than the pile settlement, positive friction develops, reducing the axial force on the pile.

However, at this point the linear model from Equation 1 can be replaced by the tri-linear mobilization model for the shaft friction, and the power law for the toe reaction, both of which have failure limits and distinct paths for loading and unloading. It is also not necessary anymore to impose the pile settlements, and calculate the resultant axial force. Now, they can be directly obtained through a new search for equilibrium.

With these improvements, the pile response due to ground displacements will always depend on the initial mobilization of the pile capacity and the associated settlements. For example, consider a 20 m long, 1 m in diameter, weightless pile supported only by friction. Consider a maximum shaft capacity of 1 MN obtained with a constant shear resistance along depth, and a perfectly plastic mobilization model ($S1$ = $S3$ = 0.1; S2 = 0; τ_{ep} = 1). With a pile modulus of 10 GPa, the settlement at the pile head is 5 mm for a load of 500 kN (WL/UBC = 50%). From this loading state, a profile of ground displacements can be imposed on the pile. For this section, a linear distribution of settlements is considered with 10 mm settlement at the pile head to 0 at the pile toe. The results can be seen in Figure 5.1.

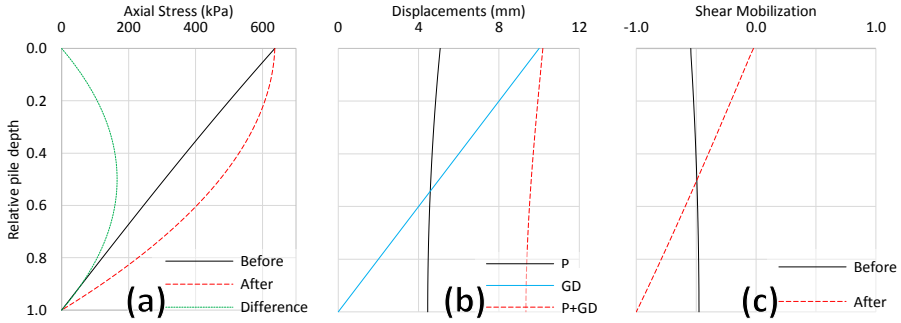

Figure 5.1. Example of friction pile in equilibrium under ground displacements: profiles of axial stress (a), displacements (b) and shear mobilization (c).

The profile of axial stresses shows how the effects of a certain profile of ground displacements can be calculated without violating the boundary conditions of the problem (fixed head load) or the vertical equilibrium (σ^n = 0). The increment of axial stress forms a sort of parabola with the vertex around half of the pile depth. This can be understood through the profiles of settlements and shear mobilization. Before the ground displacements (GD), the pile settlements were almost uniform with depth. In relation to null ground displacements, this caused an almost uniform shear mobilization with depth. The imposition of the GD causes an additional 5 mm of settlement to the pile head. In relation to the linear profile of the GD, the pile settles the same as the ground at the surface, but the

difference increases with depth. The new profile of shear mobilization is in direct relation to that difference, setting zero mobilization at the surface and practically full mobilization at the pile toe. When compared to the original profile of shear mobilization, this represents unloading in the top part of the pile and loading in the bottom part. This causes the axial stresses to increase until half of the pile depth, and decrease from there on, leading to a parabola of axial stress increments.

This example demonstrates how a simple case of a pile under ground displacements requires the simultaneous consideration of several variables. It also shows that the mobilization models have to be able to account for both loading and unloading to find the new state of equilibrium. The proposed framework can bring all these elements into the analysis, and compute the consequences of any profile of ground displacements.

The problem is even more complex when the pile is also supported by a toe reaction. The previous example can be adapted, reducing the shaft capacity by 50% together with a toe capacity of 500 kN. The maximum toe mobilization is reached at 50 mm trough a linear model (λ = 1). For these conditions, the settlement at the pile head is 8.4 mm for a load of 50% the UBC. At this state about 15% of the pile resistance comes from the toe. The results before and after the linear distribution of ground displacements can be seen in Figure 5.2.

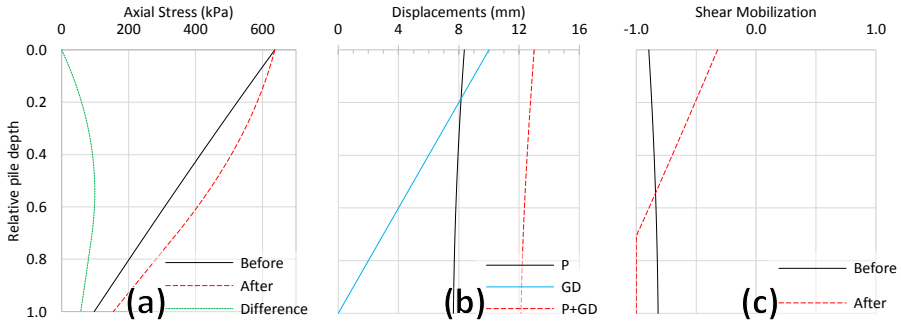

Figure 5.2. Example of pile in equilibrium under ground displacements: profiles of axial stress (a), displacements (b) and shear mobilization (c).

In this case, the new state of equilibrium depends on the balance between the reactions from the shaft and the toe. The GD cause the toe reaction to increase to about 24% of the head load, shifting the lower part of the increment of axial stresses, and the settlements at the pile head to increase to 13 mm. The difference between the pile and the ground settlements also increases along depth, but it is not null at the pile head. The initial shear mobilization was higher than in the previous example. After the GD were imposed, the mobilization

reduced along the top 60% of the pile, and increased from there on, reaching the maximum mobilization for the last 30% of the pile.

It might also be the case that the pile head is somehow constrained by the superstructure it supports. The imminence of movement in one pile might cause a redistribution of loads through the other bearing elements of the building, such as other piles or the pile cap acting as a raft, so that global equilibrium is resolved with a different load boundary condition. Just recently, a method has been proposed to link the pile settlements with the building rigidity, calculating new loading conditions for each increment of pile settlements (Franza et al., 2016; Franza and Marshall, 2016). The framework proposed in this thesis can also consider the effects of ground displacements under these restrictions. The previous example can be recalculated assuming that the superstructure finds a new state of equilibrium with an incremental settlement at the pile head of only 2 mm (Figure 5.3). In this case, the imposed boundary conditions are the head displacement (10.4 mm), and the linear profile of ground displacements (10 mm at the surface, 0 mm at the toe level). The load at the pile head reduces from 500 kN to about 362 kN, and most of the pile shaft is de-mobilized. The toe reaction increases by 25% due to the additional settlement.

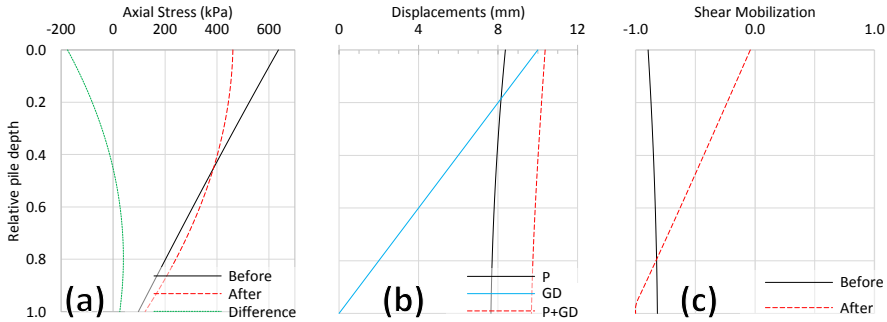

Figure 5.3. Example of pile in equilibrium under ground displacements and restrictions of the superstructure: profiles of axial stress (a), displacements (b) and shear mobilization (c).

The next sections will explore how a pile reacts to the ground displacements related to a tunnel excavation, simulating the process of pile tunnel interaction.

5.2. Ground displacements due to tunnelling

The methodology described in Chapter 4 can be used to compute the ground displacements around mechanized tunnels, especially at the moment when grout is injected around the tunnel lining. To use the displacement field in the framework of pile analysis, it is necessary to determine the vertical displacements

at each pile node. An algorithm to automatically import these values from Plaxis was programmed in a Python script, described in Annex E. However, these mathematical models depend on parameters from the grout and the machine that are not always available, or cannot be estimated, during the design stage. On top of that, several cases of pile tunnel interaction will happen around conventional tunnels. Therefore, a commonly used analytical solution is also employed in this section to estimate the ground displacements around a tunnel.

The analytical solution of Loganathan and Poulos (1998) was derived for a homogeneous undrained clay layer, and assumes that the lining is in contact with the tunnel invert, where there are no ground deformations. This is represented through an equivalent undrained ground loss that models the non-uniform radial convergence of the soil into the oval-shaped soil-lining gap, which sets the displacement field around the tunnel. The ground displacement at any point (x, z) can be calculated with:

$$\delta(x,z) = VL.R^2.\exp\left[\frac{-1.38x^2}{(Z_t+R)^2} - \frac{0.69z^2}{Z_t^{\,2}}\right]. \left\{\frac{(Z_t-z)}{(z-Z_t)^2+x^2} + \frac{(Z_t+z)(3-4\nu)}{(z+Z_t)^2+x^2} + \frac{\left[(z+Z_t)^2-x^2\right]2z}{\left[(z+Z_t)^2+x^2\right]^2}\right\} \quad (41)$$

where *VL* is the volume loss, *R* is the tunnel radius, *x* is the horizontal coordinate, *Zt* is the depth of the tunnel centre, *z* is the vertical coordinate, and ν is the Poisson's ratio.

The following discussions consider a tunnel with a diameter of 10 m, centred at a depth of 30 m. For the analytical analysis, a Poisson ratio of 0.5 was considered, and the displacements were calculated for three stages of volume loss: 0.5, 1.0, and 2.0 %. The numerical calculation considered the model described in Section 4.4.3, with two injection pressures for the grout: 374 and 343 kPa, both set at the tunnel roof, which caused a contraction at the tunnel boundary of 0.5 and 1.0 %, respectively. The resultant surface settlement troughs can be seen in Figure 5.4a.

Five pile positions around the tunnel will be evaluated. Figure 5.4b presents their relative location within the diagram for the analysis of pile tunnel interaction described in Section 2.3. The profiles of vertical displacements must be determined along the three vertical sections at 0, 7.5 and 15 m from the tunnel centreline. These curves are presented in Figure 5.5 for the analytical (a) and numerical (b) methods.

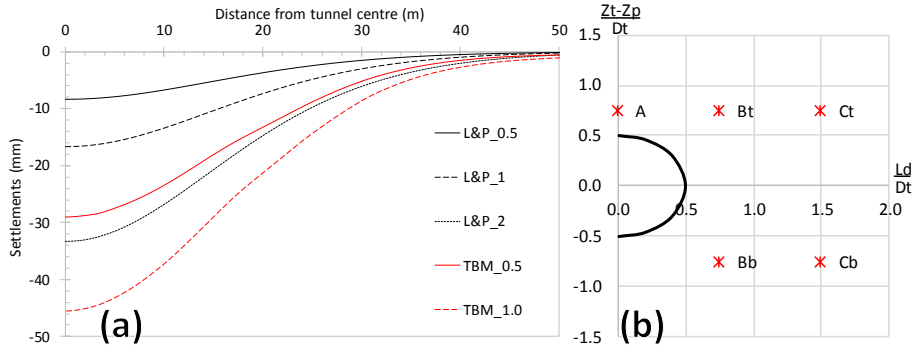

Figure 5.4. Resultant settlement troughs for the analytical and numerical calculations (a), and different pile positions to be assessed around the tunnel (b).

The settlements from the analytical calculation are linearly dependent on the volume loss, as determined in Equation 41. On top of the tunnel (A), the settlements increase continually with depth, so the settlements at the pile toe are about 70% higher than on the pile head. At Ld/Dt = 0.75 (B), the settlements increase until half the tunnel depth (15 m), and decrease from there on. Heave was calculated for depths below the tunnel invert. For the pile above the tunnel (Bt) the settlement at the pile toe was 10% higher than at the pile head, while for the pile below the tunnel (Bb), the toe was under heave of about 20% the magnitude of settlements around the pile head. At 15 m by the side of the tunnel centreline (C), the settlements increase until the depth of only 7.5 m. From there on, the settlements decreased but didn't turned into heave. Above the tunnel (Ct) the settlement at the pile toe was around 70% of the value around the pile head. This reduced to about 1% below the tunnel (Cb).

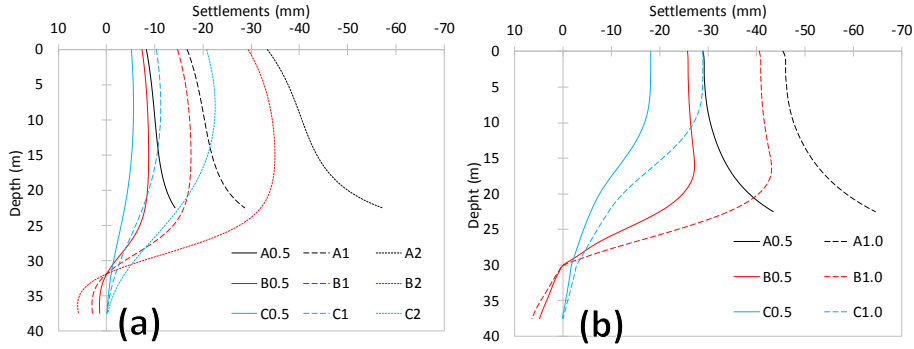

Figure 5.5. Profiles of settlements along depth for the analytical (a) and numerical method (b). The legend refers to the lateral position (A, B, C) and tunnel volume loss (0.5, 1, 2%).

The results of the numerical calculation were quite similar, but the relation between settlement and volume loss is not linear. It is worth noting how the settlement directly above the tunnel (A) is almost constant along the first meters, and then increases more intensely closer to the tunnel. The ratio between the settlements at the pile toe and head was 1.5 and 1.42 for the contractions of 0.5 and 1.0%, respectively. At 7.5 m to the side of the tunnel (B), the settlements were practically constant through the first 15 m, with a slight increase, from where they decreased, turning into heave below the tunnel depth. The settlement ratios were 0.78 and 0.84 above the tunnel (Bt), -0.19 and -0.16 below the tunnel (Bb), for 0.5 and 1.0% contraction, respectively. At Ld/Dt = 1.50 (C), the settlements were also constant through the first 8 m. However, from there on, the settlements decreased faster than in the analytical model. The settlements ratios were 0.32 above the tunnel (Ct), and practically zero below the tunnel (Cb), for both levels of contraction.

5.3. Pile tunnel interaction

Four piles were considered to simulate their reaction to the profiles of ground displacements discussed in the previous section. The piles located above the tunnel (A, Bt, Ct) were 22.5 m long, and the piles below the tunnel (Bb, Cb) were 37.5 m long. All piles were 1 m in diameter, with a material characterized by a Young's modulus of 10 GPa and a volumetric weight of 25 kN/m^3, which resulted in a total weight of 442 kN. The maximum shaft friction of all piles was considered to increase linearly with depth, while the mobilization slopes remained constant through the entire pile: $S1$=$S3$=0.3, $S2$=0, τ_{ep}=1. The total compressive capacity of the piles was fixed at 1.5 MN and 2.6 MN, for the shorter and the longer piles, respectively. This capacity was distributed in two ways, solely to the shaft (T0), and 50% to the shaft and 50% to the toe (T50). When the toe reaction was considered, full mobilization was set at 10% the pile diameter ($\Delta\sigma_T$=100 mm), the mobilization exponent was 0.3 and the rebound factor was 0.1. The ground displacements were imposed from a loading of 50% the ultimate bearing capacity, representing a factor of safety of 2. The stresses and displacement in the pile at this initial state are presented in Figure 5.6.

The settlements at the pile head in the shorter pile were 4.3 mm for the friction pile, and 5.7 mm when the toe reaction was considered. In the longer pile, the head settlement was 6.3 and 8.7 mm, without and with the toe reaction, respectively. At this loading state, about 47% of the load is carried by the toe. This represented 450 kPa for the shorter pile and 750 kPa for the longer one. The longer piles have the higher difference between the settlements at the pile head and at the pile toe, due to the compressibility of the pile body under the

higher load. In the following discussions, the settlements induced by loading is already subtracted to isolate the response due to the ground displacements. The piles are discussed in the order 22.5_T0, 22.5_T50, 37.5_T0, and 37.5_T50. To clear the text, the term pile settlement will be replaced by its symbol: δp.

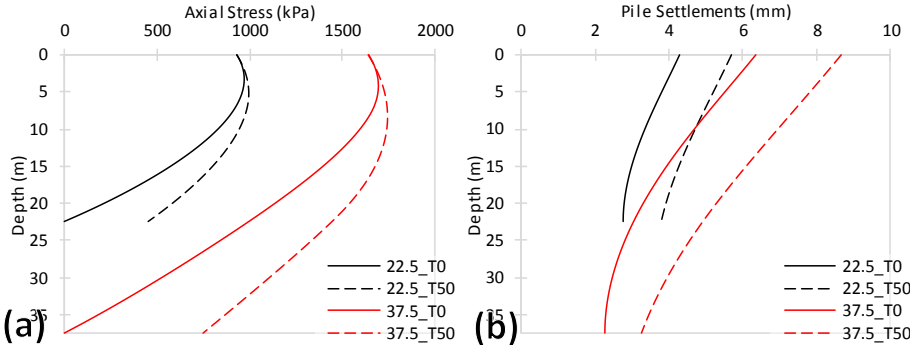

Figure 5.6. Piles at WL=0.5 UBC, axial stresses (a) and displacements (b).

The first pile (22.5_T0) is supported solely by friction and it rests above the tunnel level. The resultant settlements at the pile head due to the tunnelling induced displacements are presented in Figure 5.7 with the values normalized by the surface settlement at each pile position. The results from the soil displacement calculated with the analytical model are marked L, and with the numerical model are marked N, both followed by the contraction level around the tunnel.

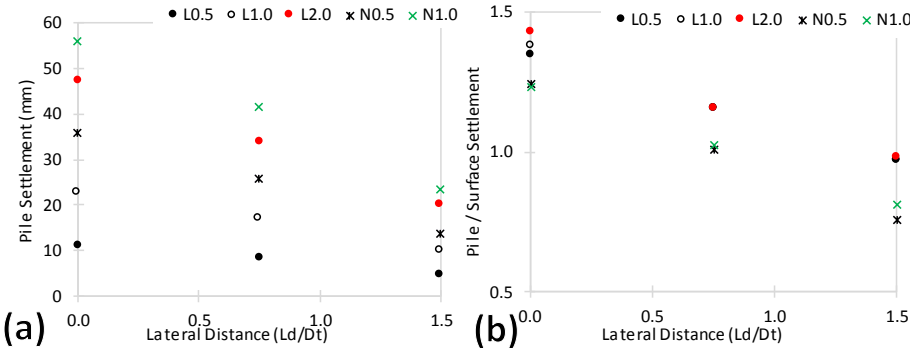

Figure 5.7. Pile 22.5_T0 – Resultant pile settlements (a) and the ratio between the pile settlements at the surface settlements at the pile position (b).

The results show that at the same position, δp can change significantly depending on the ground displacements. For all models, δp decreases with an increase in the lateral distance between the pile and the tunnel (Ld), while δp increases with the tunnel volume loss. The ratios between the pile and the surface settlements

also decreased with *Ld*, and increased with *VL*. However, the variation range was much smaller than for the absolute pile settlement. Even for the analytical model, where the ground displacements were linearly related to *VL*, the relation between the pile and the surface settlements was not constant. Only the numerical model resulted in δp smaller than the surface settlement.

The second point of analysis are the changes in the shear mobilization with depth (Figure 5.8). As a reminder, negative shear is the consequence of a pile settling more than the ground and is directed upwards in the pile, reducing the axial stress. On the other hand, positive shear happens when the ground settles more than the pile, acts downwards in the pile body and is also called negative friction. Directly above the tunnel (A), the ground displacements caused the negative shear to increase, reaching full mobilization from the pile head until the depths of 8, 13 and 17 m for the analytical models with volume losses of 0.5, 1.0 and 2.0%, respectively.

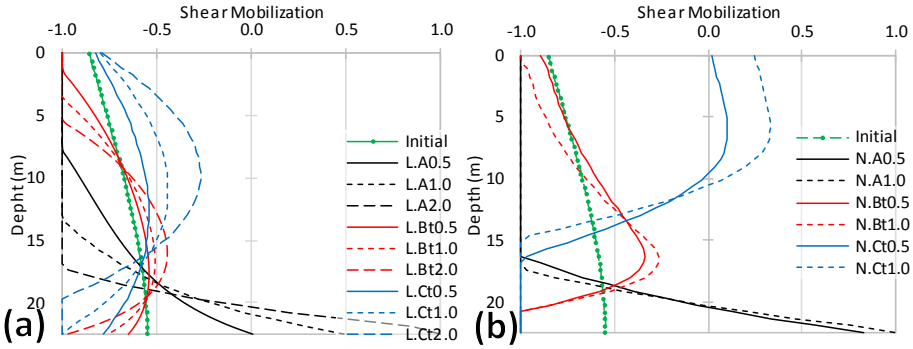

Figure 5.8. Pile 22.5_T0 – Shear mobilization due to the tunnelling induced displacements obtained with the analytical (a) and numerical (b) methods.

This is directly connected to the fact that the pile head settled more than the ground at the surface, as shown in Figure 5.7. As the load boundary conditions are kept constant, an increase in the upwards shear at the top must be compensated by a decrease in the bottom part of the pile. This was also captured by the model, and for *VL* = 1 and 2%, the shear mobilization turned downwards, reaching full positive mobilization for *VL* = 2%. This shows that the ground settlements close to the pile toe were larger than the pile settlements, this is a reasonable conclusion as the ratio of ground settlements between the surface and the level of the pile toe was 1.7 (Figure 5.5), while the ratio between the pile and the surface settlements was always smaller than 1.5. For the numerical model (Figure 5.8b), the pattern was similar, but the differences between the two levels of contraction were very small. This is connected to the fact that both settlement

profiles were very similar in shape (derivative with depth), and just differed in magnitude. As the shaft mobilization is linear, this leads to different magnitudes of pile settlement to achieve the same relative displacement, which leads to similar profiles of shear mobilization.

At Ld/Dt = 0.75 (Bt), the settlements from the analytical model changed slightly from the head to the toe and caused the pile to settle more than the ground at the surface ($\delta p/\delta s > 1$). From the initial state of mobilization, negative shear increased close to the pile head and toe and decreased between the depths of 10 and 20 m. The shaft friction was fully mobilized close to the pile head, and never turned downwards. With the settlements from the numerical model, the pile settled similarly to the ground at the surface ($\delta p/\delta s \approx 1$), which can be seen by the minimal changes in shear mobilization close to the pile head (Figure 5.8b). As the shaft didn't reach full mobilization and the shaft mobilization is linear, the profile of shear mobilization is a scaled version of the profile of settlements from Figure 5.5. The negative shear mobilization decreased between 10 and 19 m depth, followed by a sharp increase as the ground settlements diminished close to the tunnel depth.

The most significant difference between the numerical and analytical models were at 15 m by the side of the tunnel centreline (Ct). For the analytical solution, the piles followed the surface settlements ($\delta p/\delta s \approx 1$), from where there was a decrease in shear mobilization. This was followed by a sharp increase below the depth of 15 m, again due to a drop in the ground settlements close to the tunnel depth. The results of the numerical model were quite different, as the interaction caused the pile to settle less than the ground at the surface ($\delta p/\delta s < 1$), which led to a reversal of the shear direction from the pile head to about 10 m deep. This was compensated by an increase in negative mobilization from a depth of 15 m until the pile toe, as the ground settlements got smaller with depth.

These changes in the shear mobilization along the pile body resulted in increments of axial stress in the pile section, as can be seen in Figure 5.9. Referring to the previous discussion, whenever the shear increased upwards (negative values, left of initial line), the axial stress in the pile was reduced. On the other hand, when the shear decreased or turned downwards (right of initial line), it caused an increase in the axial stress. Here, the mobilization levels are combined with the magnitude of the maximum shear resistance at each point. All profiles converge at the pile head, due the constant load boundary condition, and at the pile toe to guarantee equilibrium.

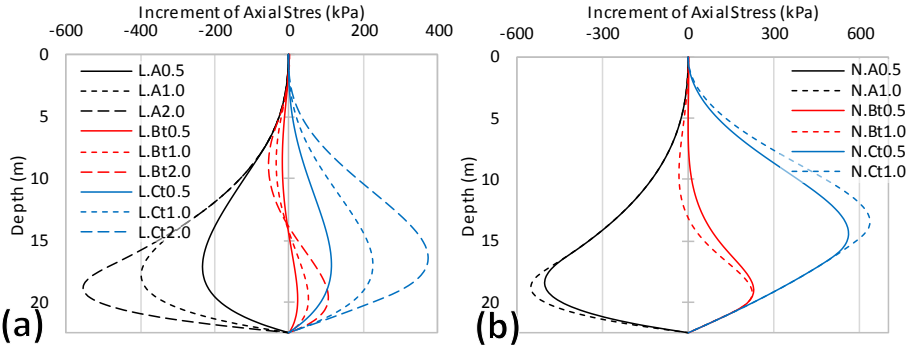

Figure 5.9. Pile 22.5_T0 – Increments of axial stress in the pile due to the tunnelling induced displacements obtained with the analytical (a) and numerical (b) methods.

Overall, the average axial stress in the pile decreased when the pile was just above the tunnel, but increased when the pile was to the side of the tunnel alignment. The maximum increments in the analytical model were calculated between the depths of 17 and 19 m. For the numerical model these were located at a depth of 18 m for the positions A and Bt, but at 14 m for position Ct. For this analysis, the levels of volume loss influenced mostly the magnitude of the increment, without much effect in the shape of the curves, and were more pronounced in the analytical method.

The second pile (22.5_T50) is also 22.5 m long, and has the same compressive capacity of the first one. However, both the toe and the shaft contribute to the pile resistance at this point, as both elements have the same magnitude when fully mobilized. The resultant settlements at the pile head, in absolute terms and normalized by the surface settlements are presented in Figure 5.10.

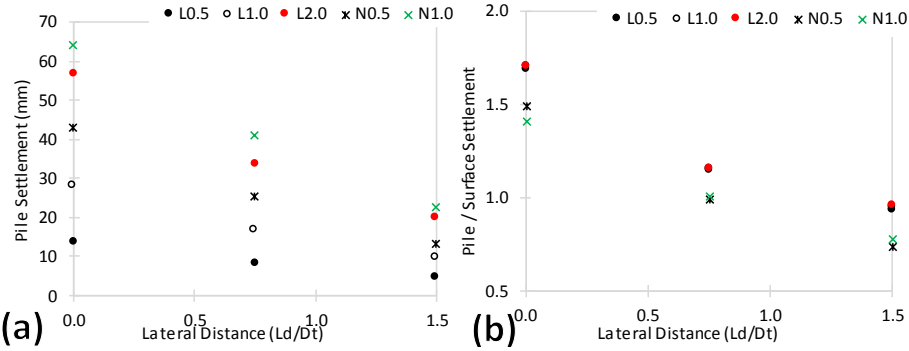

Figure 5.10. Pile 22.5_T50 – Resultant pile settlements (a) and the ratio between the pile settlements at the surface settlements at the pile position (b).

The pile settlements were generally higher than in the previous pile, but that was also the case without ground displacements. As the shaft capacity was smaller, higher settlements were required to mobilize the pile toe. Nevertheless, the general trend persisted, the settlements were inversely proportional to *Ld*, but directly proportional to *VL*. As a consequence of the larger δp, the ratio between the pile and the surface settlements was also higher, particularly above the tunnel.

The changes in the shear mobilization with depth are presented in Figure 5.11. The first point to be noted is that the initial profile presents full mobilization along the top 7 m of the pile. Until the pile toe, the higher settlements required to mobilize the toe reaction induced a higher shear mobilization than on the previous pile (note that the horizontal scale of the graphs is different). From this loading state, whenever the pile settled more than the ground around the region of full mobilization, the forces didn't change, as the interface couldn't reach a higher shear force. However, any variation of the shear mobilization does not necessarily have to be balanced out by opposite changes in another part of the shaft, as now it is possible to transfer part of the load to the pile toe.

The high relative pile settlements on top of the tunnel (A) led to practically full shaft mobilization along the whole pile, for both the analytical and the numerical model. Only very close to the pile toe, where the ground settlements increased significantly (Figure 5.5), did the shear mobilization decrease. Using the analytical model at the lateral position Bt (Ld/Dt = 0.75) - where in the first pile the mobilization increased, decreased and increased again along depth - the top part already started at full mobilization, so there were only changes from depths higher than 7 m. In the numerical model, on the other hand, with the contraction of 0.5%, the shear mobilization decreased through most of the pile ($\delta p/\delta s$ < 1). Only below the depth of 20 m there was an increase in mobilization as the ground settlements diminished close to the tunnel depth.

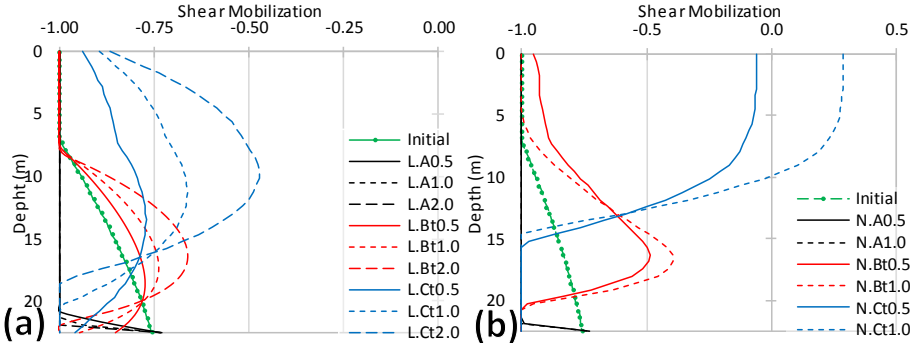

Figure 5.11. Pile 22.5_T50 – Shear mobilization due to the tunnelling induced displacements obtained with the analytical (a) and numerical (b) methods.

Finally, at position Ct (*Ld*/*Dt* = 1.50), where the pile head settled less than the ground at the surface, the ground displacements caused a decrease in the negative shear mobilization from the top of the pile until about 15 m deep. Only with the numerical results at 1.0% contraction, did this result in a reversal in the shear direction (from upwards to downwards), along the top 10 m of the pile. Again, the sharp decrease in the ground settlements close to the tunnel depth caused an increase in the negative shear mobilization close to the pile toe.

The increments of axial stress in the pile, as a consequence of the changes in the shear mobilization, are presented in Figure 5.12. The general trend was the same, the average axial stress decreased when the pile was just above the tunnel, but increased when the pile was to the side of the tunnel alignment.

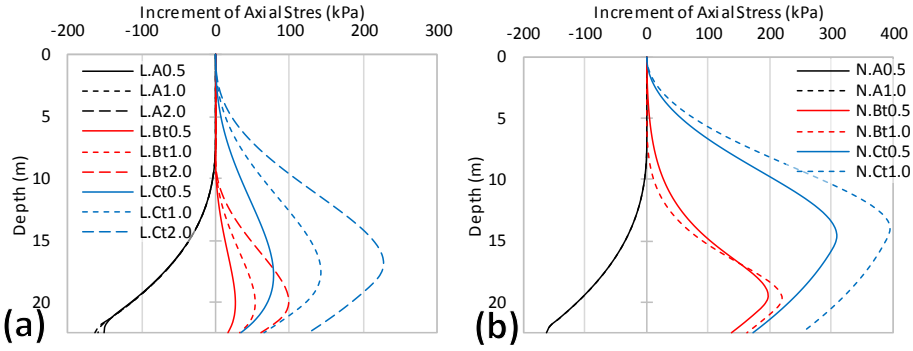

Figure 5.12. Pile 22.5_T50 – Increments of axial stress due to the tunnelling displacements obtained with the analytical (a) and numerical (b) methods.

To the side of the tunnel, the reductions in the shaft mobilization cause the axial stress in the pile to increase. This is partially balanced close to the pile toe, as the ground settlements significantly reduce, increasing the shaft mobilization. The axial load surplus at the end of the shaft is counteracted by the pile toe. The depths where the increments of axial stress were at their maximum were quite similar to the first pile, as they derive from the curvature of the ground displacements, as long as the shear in the region is not fully mobilized.

The regions where the shear remained fully mobilized along the top of the pile can be seen in these graphs with no changes in the axial stress. The increase in the negative shaft mobilization induced in the pile above the tunnel (A) causes a reduction of the axial stresses in the pile body and consequently, at the pile toe. As the final mobilization levels were quite similar among the different stages of volume loss, the final axial stresses are also very close. The pile settlements, on the other hand, are different, as they have to compensate the ground displacements to reach the same relative displacements.

The third pile that was simulated (37.5_T0) is 37.5 m long and is supported solely by the shaft. The settlements at the pile head, in absolute terms and normalized by the surface settlements, are presented in Figure 5.13. The pile toe was deeper than the tunnel, so it only tested at the two positions to the side of the tunnel alignment (Bb and Cb).

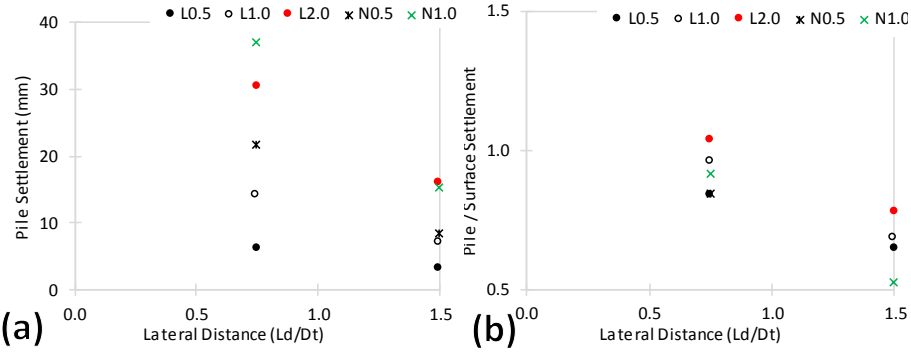

Figure 5.13. Pile 37.5_T0 – Resultant pile settlements (a) and the ratio between the pile settlements at the surface settlements at the pile position (b).

The settlements were generally smaller than the first pile, which also led to smaller ratios to the surface settlements. The parameters for the shaft mobilization were the same, but this longer pile was subjected to the ground settlements at deeper levels, which were quite small, and even turned into heave in some points. The way δp decreases with the lateral distance and increases with the volume loss remains unaltered. The ratios between the pile and the surface settlements were not as close as in the shorter pile, especially among the results from the analytical ground settlements, and were mostly smaller than 1.

The changes in the shear mobilization with depth are presented in Figure 5.14. Here, the initial profile presents full mobilization along the top 8 m of the pile, even though there is no toe reaction. This is simply the result of the loading settlements at the pile head, which were higher than the ones in the second pile, where there was also full shaft mobilization (Figure 5.6).

As the ground settlements at the surface were higher than the pile settlements, there was an overall decrease in the negative shear mobilization, reaching a direction reversal at some points. Similarly to the first pile, this was more pronounced with the settlements from the numerical calculations. Again, as the pile is only supporter through the shaft, any decrease in the shear mobilization at the top must be compensated by an increase at the bottom, and vice versa. The small ground settlements close to the pile toe caused an increase in the

shear mobilization in the bottom part of the pile. All cases, with the exception of L.Cb0.5, reached full negative mobilization along, at least, the last 8 m.

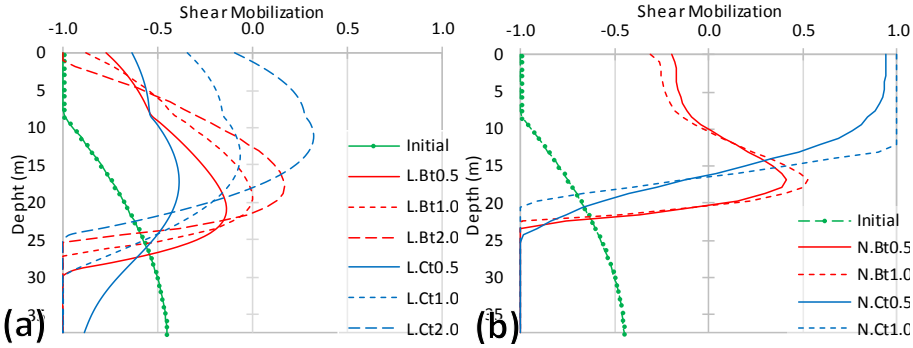

Figure 5.14. Pile 37.5_T0 – Shear mobilization due to the tunnelling induced displacements obtained with the analytical (a) and numerical (b) methods.

The increments of axial stress in the pile are presented in Figure 5.15. As expected, all profiles converge at the pile head and at the pile toe, and the interaction with the tunnel displacements to the side of the tunnel alignment caused positive axial stress increments. However, the magnitude was much higher in this longer pile, reaching up to 1.5 MPa at 20 m depth. In this longer pile, the difference between positions B and C was much smaller than for the shorter one. Probably because the ground settlements at these locations is much more similar closer to the tunnel depth and beyond.

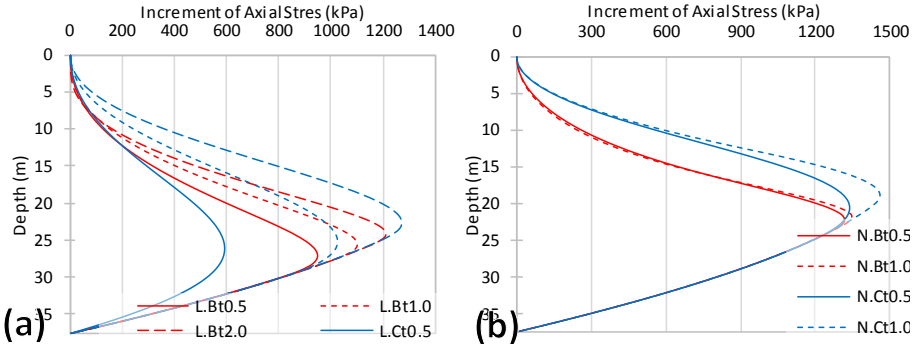

Figure 5.15. Pile 37.5_T0 – Increments of axial stress in the pile obtained with settlements from the analytical (a) and numerical (b) methods.

The regions of full shaft mobilization can be seen where all the lines come together, as they all have the same forces causing the stress increments, and end up in the same point. The maximum stress increments were located between 22 and 26 m for the analytical results, and 19 and 22 m for the numerical ones.

These are roughly the depths at which the shear mobilization changed from smaller to higher than the initial shear profile and it is also the depth where ground settlements at position B start to decrease.

The fourth pile that was simulated (37.5_T50) was also based beneath the tunnel depth and had the same compressive capacity of the third one. The pile is supported by the shaft and the toe, which have the same magnitude when fully mobilized. The resultant settlements at the pile head, in absolute terms and normalized by the surface settlements, are presented in Figure 5.16.

Again, the settlements were smaller than the equivalent shorter pile, due the smaller ground settlements at deeper levels. However, the settlements were also slightly smaller than the third pile, only supported by friction, even though the relation was the opposite without ground displacements. This is an interesting example of how many elements come into play in this mechanism. Even though the settlements necessary to mobilize the toe reaction were higher than to mobilize the shaft, this was overcome by the compression of the pile body. The resultant average axial stress along the pile was higher in the friction pile, which in settlement at the pile head that were larger than in the T50 pile. Nevertheless, the δp continued to decrease with the lateral distance and increase with the volume loss. Now all the pile settled less than the ground at the surface.

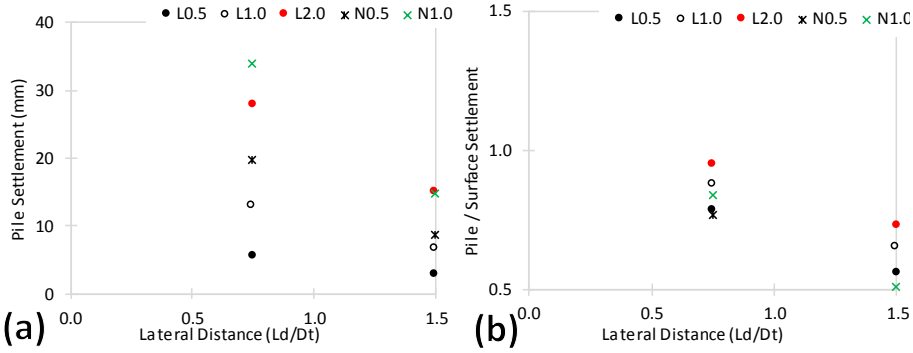

Figure 5.16. Pile 37.5_T50 – Resultant pile settlements (a) and the ratio between the pile settlements at the surface settlements at the pile position (b).

The changes in the shear mobilization with depth are presented in Figure 5.17. The higher initial settlements are in evidence in the full negative shear mobilization along the top 23 m of the pile. Again, as the ground settled more than the pile, there was an overall decrease in the negative shear mobilization, reaching a direction reversal at some points. In all the models, around the depth of 20 m the profiles crossed the line of initial mobilization, and from there on the shaft was fully mobilized upwards.

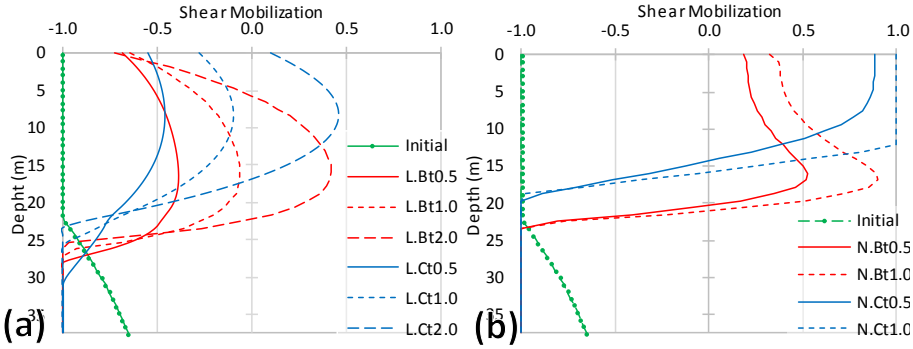

Figure 5.17. Pile 37.5_T50 – Shear mobilization due to the tunnelling induced displacements obtained with the analytical (a) and numerical (b) methods.

The increments of axial stress in the pile are presented in Figure 5.18. As discussed in the analysis of settlements, the stress magnitude was not as a high as in the previous pile, reaching a maximum value of 1.1 MPa. Similarly to the previous pile, the difference between positions B and C was not so significant. As the load in the pile toe is not the same between these models, the regions of full shaft mobilization can only be seen through the inclination of the lines. Again, the position of the maximum stress increments agrees with the position where the shear mobilization curves cross the line of initial mobilization.

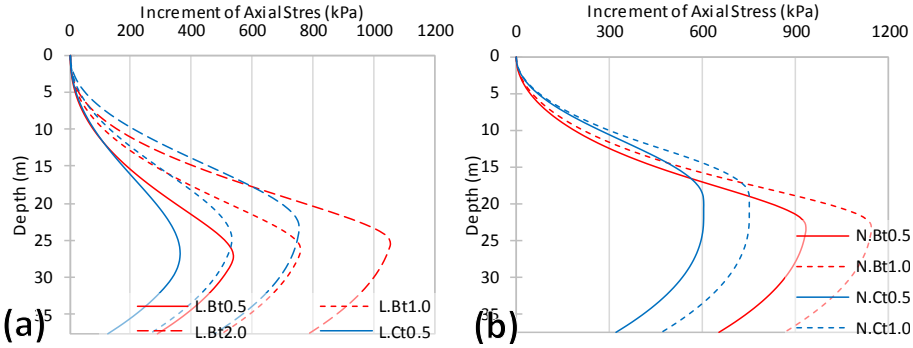

Figure 5.18. Pile 37.5_T50 – Increments of axial stress in the pile obtained with settlements from the analytical (a) and numerical (b) methods.

The response from the pile validation test presented in Chapter 3 requires the definition of a distinct unloading path for the shaft mobilization model (S3). The literature review and the examples of this section show that in some cases of pile tunnel interaction, unloading is induced along the top part of a pile, when the ground settlements are higher than the pile settlements. However, the new state of equilibrium is dictated by the settlements required to mobilize an upwards reaction. In this region the shaft mobilization increases from the loading state.

Therefore, the effect of the unloading slope is quite limited for this process, and an initial estimate can be obtained considering S1 = S3.

It is not possible, at this point, to directly validate this calculation method. Most studies presented in Chapter 2 did not report the ground settlements with depth, or a pile load test with strain measurements. However, some parallels can be traced. This framework offers a rational explanation for the zones of relative pile/soil surface settlements presented in Figure 2.3. The examples at position B show the pattern expected from these models. The pile above the tunnel level (Bt) settled more than the ground at the surface, while at a deeper layer (Bb) it settled less. Here, it is clear that this is a direct consequence of the smaller ground settlements at deeper layers (Figure 5.5).

However, as the data analysis from Section 2.3 made it clear, the relative pile location is insufficient to determine its reaction to a tunnel. Even though their results are correct for some cases, these fixed zones of relative displacement can only indirectly consider the real cause of pile tunnel interaction, the ground displacements. The proposed framework can directly account for that and simulate different profiles for the same relative position. The calculated settlements are within the range of measurements presented in Figure 2.11, even though they are higher than the curves from Figure 2.9 for 1% volume loss.

The results from these examples can also be compared with the empirical assumptions that the pile head settlements are equal to the soil settlements at 2/3 (0.66) of the pile depth or at the pile toe (see Chapter 2). The average results, considering the settlements from the analytical model can be seen in Figure 5.19 for all piles.

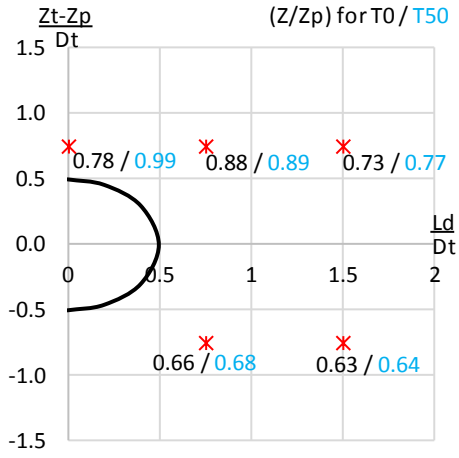

Figure 5.19. Relative depths at which the pile head settlement equals the grout settlement for different pile positions.

It is quite clear that these empirical rules cannot be used to predict the pile settlements accurately. The pile settled similarly to the ground around the pile toe for just one case right above the tunnel (A_T50), while it settled similarly to the ground at 2/3 the pile depth for the piles below the tunnel depth (Bb, Cb). In general, the relative depth where the settlements were equal was higher for piles supported by both toe and shaft resistances (T50) when compared with friction piles (T0) at the same relative position.

Regarding the increments of stress, the basic mechanism is represented: The average axial force of loaded piles is reduced when the piles are right above the tunnel, but increased when the piles were farther away (*Ld* > *Rt*). The results cannot be directly compared with Figure 2.15, as the measured profiles are quite irregular. However, one example offers the possibility for a partial validation. The results from the centrifuge tests of Lee and Chiang (2007) also include a pile load test with the curves for the load-settlement and load transfer with depth. These tests were conducted at 100g, and the model piles were instrumented with full-bridge strain gauges placed at 7 positions along the pile, protected by a thin layer of epoxy, and calibrated before the test. The pile loads were applied through an actuator driven with compressed air.

These results can be used to calibrate the pile model, as in Figure 5.20. The parameters of the pile are reported in the paper as: Zp = 27 m, Dp = 1.06 m, E_p = 19.7 GPa. The volumetric weight of the pile is considered γ_p = 25 kN/m^3. The shaft mobilization model is assumed constant through the whole pile, with the parameters: τ_{max} = 65 kPa, τ_{ep} = 0.6, $S1$ = $S3$ = 0.014, $S2$ = 0.004. The maximum measured toe resistance was $q_{b\ max}$ = 3.9 MPa, and the mobilization model was calibrated with: $\Delta\delta^T$ = 175 mm, Rb = 0.1, and χ = 0.7.

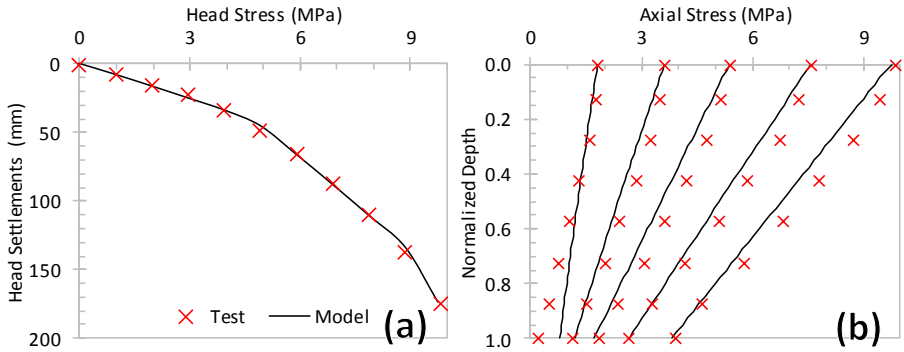

Figure 5.20. Pile calibration from the centrifuge tests of Lee and Chiang (2007).

The geometrical details of the pile tunnel interaction layout are presented in Table 2.1. All piles were positioned at a lateral distance of 4.5 m to the side of

the tunnel (*Dt* = 6 m), which was placed at 4 different depths: *Zt* = 9, 15, 21 or 27 m. There are no available data on the ground settlements, just the estimated contraction of the model tunnel. For a partial validation, it is possible to assume that the ground displacements can be estimated with the analytical model of (Loganathan and Poulos, 1998). The estimated profiles of settlement along the pile, for the different tunnel depths, can be seen in Figure 5.21a. The increments of axial stress are discussed for 10 piles, 4 non-loaded piles (LE1, 3, 6, 8), 4 loaded to 25% the UBC (LE2, 4, 7, 9), and 2 loaded to 50% the UBC (LE5, 10). Their relative position can be seen in Figure 5.21b.

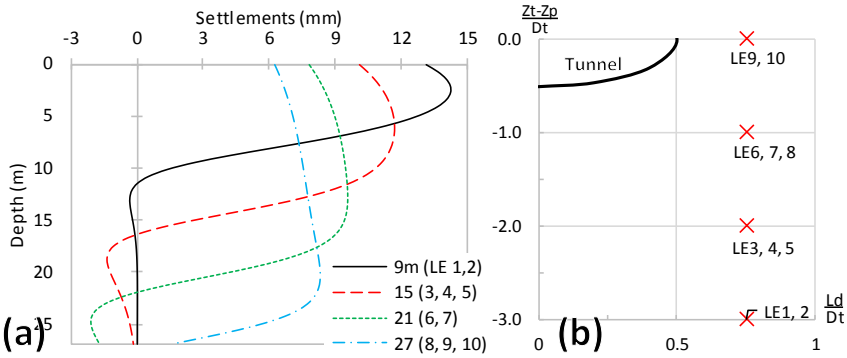

Figure 5.21. Estimated ground settlements (a) and relative pile positions (b).

The calculated increments of axial stress can then be compared with the measured values (Figure 5.22), keeping in mind that the ground settlements were not obtained from the centrifuge test, but estimated for this partial validation. Even so, the results agree with the experiment for most piles.

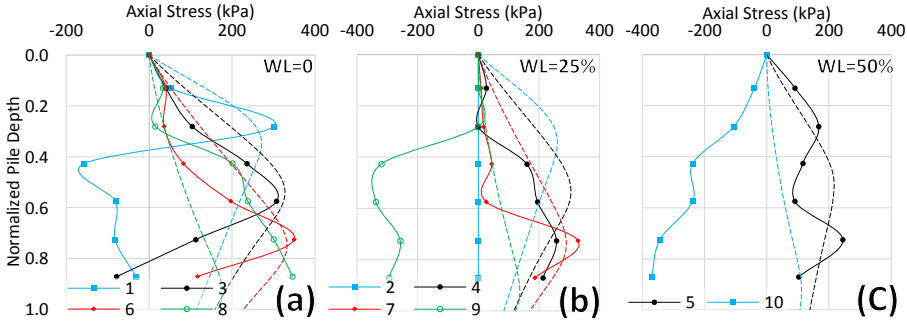

Figure 5.22. Results of the partial validation for the piles with an initial working load of 0 (a), 25 (b) and 50% the ultimate bearing capacity (c). Lines with markers represent the measured values, while the dashed lines represent the results from the model. The numbers indicate the pile number LEx.

For the non-loaded piles (Figure 5.22a) the model predicted both the position and magnitude of the maximum stress increment quite well. For pile LE1,e the measured profile suggests that the actual displacement field included significant heave below the tunnel, instead of the small displacements obtained with the analytical model. For pile LE8 the measured increments were higher than the predicted values.

When the piles were loaded, the model results agree with the measurements for the cases where the tunnel was 15 or 21 m deep (LE4, 5 and 7). The model predicted positive increments for piles LE2, 10 and 5, but no variations were measured at pile LE2, and negative increments were detected at LE9 and LE10. The first deviation (for LE2) seems to be an observational error. The opposite response (LE9, 10) is probably related to the fact that the real displacements in the experiment differ from the analytical solution used in these calculations. The toes from piles LE9 and 10 are located very close to the tunnel, where the displacements are highly dependent on the modelling techniques.

5.4. Overview

Overall, this general two-stage mathematical model achieves the final objective of the thesis to recommend a methodology to calculate the consequences of pile tunnel interaction for engineering design. The methodology is able to reproduce the fundamental mechanisms identified in Chapter 2, in terms of the absolute settlements, their ratio to the ground surface settlements, and the increments of axial stress in the pile.

The basic features of how ground displacements act within the framework of the modified load-transfer method, proposed in Chapter 3, have been discussed. Some example showed how the framework can realistically model friction and end-bearing piles, with any arbitrary profile of ground displacements. The model automatically considers the possibility of loading, unloading or full-mobilization, and their consequences for the load transfer mechanism and pile settlements.

Different examples of displacement fields around a tunnel excavation have been considered in the analysis. A commonly employed analytical solution has been compared with the results from the methodology described in Chapter 4 for the phase of grout injection around a tunnel boring machine. Both methods have been assessed at different stages of volume loss. This also highlights how the methodology suggested in this chapter can work with different sources of input. In this logic, the framework can also be used to estimate the pile reaction to tunnels built with conventional excavation methods, as long as the profiles of ground settlement can be predicted or measured.

These two elements were combined for a thorough analysis, considering five different geometrical layouts, of how a new tunnel affects an existing pile. When the pile is positioned right above the tunnel, the induced ground settlements cause the pile to settle much more than when the pile is to the side of the tunnel alignment. The maximum calculated settlements were 6.4, 4.2 and 2.3% of the pile diameter (1000 mm), for the lateral distances of 0, 0.75 and 1.50 tunnel diameters from the centreline, respectively.

The relation between the profile of ground settlements and the induced pile settlements, dictated the induced axial stresses in the pile. As the pile settled a lot when it was directly above the tunnel, this caused a higher mobilization of the shaft friction upwards, which reduced the axial stress and the load at the pile toe. To the side of the tunnel, where the pile settled less, negative friction was induced in the top part of the pile, increasing the axial stress and the load at the pile toe. However, the examples show how several elements dictate the final response of the pile, making it very difficult to predict the overall response based on simple mechanisms outside a framework where they can all interact together. A partial validation was presented for a centrifuge test in sand. Even though the ground settlements had to be estimated, as the real settlements were not available, the model was able to predict the magnitude of the axial stress increments for most conditions.

6. Conclusion

This thesis presents a new take on the problem of determining how a new tunnel affects an existing pile. Their interaction is mainly related to the fact that the construction of a tunnel results in ground movements, and that these ground movements can influence how a pile transfers its load to the ground. Around 100 studies on pile tunnel interaction have been analysed to expose the current state of knowledge, and to search for methods and concepts that could be used to create a more realistic model of the pile tunnel interaction mechanism.

The case studies revealed that most pile supported structures that were monitored during a tunnel construction were not significantly affected by it. However, there were also cases where interventions were necessary to prevent structural damage. Overall, the literature describes the process of pile tunnel interaction in two ways: (1) The tunnel degrades the toe capacity, which mobilizes the shaft resistance for equilibrium. (2) Negative friction is induced along the pile shaft, which also increases the loading at the pile toe. In both cases, once the shaft is fully mobilized, the pile settles significantly to re-mobilize the pile toe.

Quantitative results were collected from case studies, full-scale tests and centrifuge models. The results were compiled in a framework where they could be compared and contrasted, exposing patterns that were not distinguishable in the individual studies. One of the main points of analysis is how much a pile settles due to its interaction with a tunnel. The measurements indicate that the settlements are always inversely proportional to the horizontal distance between the pile and the tunnel alignment. When considering the axial forces, it was established that, when the piles are not carrying any load, the interaction always causes compressive forces in the pile. In other words, negative friction is induced in non-loaded piles. Along the pile, this variation increases until the depth of the

tunnel centre, and then decreased at deeper levels. However, when piles are carrying a certain load, the results are different. When a pile is right above the tunnel, there is a reduction of forces in the pile section, which can also be seen as a higher shaft mobilization. But when a pile is to the side of the tunnel alignment, the axial forces increase due to negative friction. The quantitative data also provided the basis to study the magnitude of the pile reaction. In terms of pile settlements, most piles do not reach failure (10%·Dp) and for lateral distances larger than two tunnel diameters (Ld > 2·Dt) the pile settlements are generally smaller than 1% of their diameter and 50% of the equivalent surface settlements.

The mathematical models used in the literature to compute the consequences of pile tunnel interaction have also been studied. One of the main deficiencies of these models is that they do not consider a limit on the pile resistance, as they are either based on elastic solutions or unable to solve the large deformations involved in pile failure. Another prevalent problem is reproducibility. Most numerical studies omit important details of the modelling procedures, so the methodology is not adaptable to different conditions. There were also studies proposing explicit equations to calculate the pile reaction, but most of them require a specific solution algorithm for the numerical analysis, which was normally recorded in a software (e.g. PALLAS, PIES, GEPAN, PGROUPN, PRAB, PPRL, LPPR, etc.). However, these codes have either been discontinued or are practically inaccessible for the large majority of the engineering public.

Considering these points, a methodology was proposed to calculate the consequences of pile tunnel interaction. The idea was to design a system for pile analysis that could cope with ground settlements and be implemented in a simple spreadsheet. This was based on the assumption that the ground settlements are the main factor inducing the pile to react to a tunnel excavation. Therefore, the methodology also includes the development of a model to predict the ground movements during tunnelling. These two elements are then used to create a general two-stage mathematical model for the analysis of pile tunnel interaction. These ideas were tested in a pilot methodology, where the pile settlements are imposed to calculate the resultant axial forces based on a simple linear model. The results were promising and supported the next stages of the project.

The system for pile analysis was designed based on an adapted version of the load transfer method, and implemented within a regular spreadsheet. The method is based on the equations for vertical equilibrium, the continuity of displacements, and the models defining the reactions from the pile shaft and toe as functions of displacements. With these elements, the pile settlements and load transfer can be calculated for any loading condition. The effects of ground

displacements are considered by turning the variable of pile settlement into a relative pile-soil settlement in the load mobilization functions. Two mobilization models were proposed considering loading and unloading paths for the pile shaft and toe.

There is a systematic problem with this approach, as most of these functions have only been calibrated for pile loading, even though there are important mechanisms taking place through the unloading stage. The effects of ground displacements can only be assessed if the mobilization models consider the possibility of unloading. Even though unloading is normally understood as the consequence of a load reduction, it can also be the consequence of ground displacements. In a framework based on relative displacements, the pile body moving up is equivalent to the ground moving down. The related literature and the details of the methodology were discussed, and the results were validated for an instrumented pile load test. The method is able to reproduce the field measurements of the load-settlement curve and axial loads along the pile body, during the loading and the unloading stages. Overall the system designed for pile analysis is considered suitable for the methodology proposed to calculate the consequences of pile tunnel interaction.

In order to develop a model to predict the ground movements during tunnelling, a new approach was considered, specifically for tunnels excavated with pressurized tunnel boring machines (TBMs). The study looked for an answer to the following question: What are the forces acting on the excavation perimeter of a tunnel? This led to a thorough review of the processes around a TBM, the physical mechanisms involved, and the numerical techniques used to model them. The literature review shows how the mathematical models used to simulate a TBM tunnel have evolved from a basic stress release to direct accounts of the boundary pressures connected to different elements of a TBM. An intrinsic feature of mechanized tunnelling is that every step of the excavation cycle is performed through mechanical or hydraulic systems. The interaction mechanisms between the TBM and the surrounding ground result from the operation of these systems to excavate and support the ground around the tunnel. It is self-evident that for each of these actions there will be a reaction from the ground to achieve equilibrium. However, these mechanisms are often interpreted within idealized frameworks that do not account for important features of the ground reaction that have been observed in the field. Therefore, these frameworks needed to be adapted to better represent the interaction between the TBM and the ground.

Two methodologies were proposed to evaluate the stages of grout injection and grout consolidation around the tunnel lining at the back of a TBM. During grout

injection, the first methodology calculates the distribution of grout pressures around the tunnel considering how the pressure dissipates from the injection points to the rest of the tunnel perimeter. A model for the grout flow was proposed, where the dissipation is related to the gap between the ground and the tunnel lining. A spreadsheet was used to calculate the grout pressures and a finite element code, where these pressures are used as boundary conditions, was used to calculate the soil displacements. These displacements are then imported back to the spreadsheet, where the results of the two models can interact until numerical equilibrium is achieved. During grout consolidation, the second methodology calculates the relation between the water outflow, from the slurry grout into the ground, and the stress release at the tunnel boundary due to the variation of the grout volume. A Python routine was programmed to incrementally calculate the water outflow, the associate pressure reduction, and the new profile of grout pressures, based on the output of the finite element calculation. Both methodologies were programmed for two different finite element software packages: FlexPDE and Plaxis. The first has a free evaluation license, and so that it can be tested by anyone interested in the process, and was programmed to simulate the ground with a linear elastic model. The second requires a commercial license, but it consider other constitutive models to represent the ground. Theoretical examples were calculated with the two programs and the results discussed.

The methodology was then validated for an instrumented case study of a tunnel in The Netherlands. During the injection phase the model is able to reproduce the grout pressures around the excavation perimeter, and estimate the surface settlements better than the traditional stress-release method. During the consolidation phase, the pressure dissipation can be matched quite well at some locations. However, the calculated distribution of pressures around the tunnel perimeter does not correspond to the measured values. Some reasons for the differences between calculated and measured values were discussed.

Finally, these two separate studies were combined into a design tool to compute the consequences of pile tunnel interaction. The pilot methodology was enhanced with more realistic models for the pile reaction. At this point, the load mobilization functions can account for pile failure and have distinct paths for loading and unloading. The pile settlements can be directly obtained through a root search for equilibrium, and don't have to be imposed anymore. Unfortunately, there are no instrumented field tests to validate both methodologies together, where the pile settlements and axial forces have been recorded concurrently to the grout pressures around a tunnel boring machine. However, the methodology can simulate the fundamental mechanisms of pile

tunnel interaction identified in the literature review. Overall, the designed methodology achieves the final objective of the thesis, and it is recommended to calculate the consequences of pile tunnel interaction for engineering design.

6.1. Recommendations for further research

Based on the successes and failures of this research project, and the knowledge accumulated through the process, six points for future research are recommended:

1. 3D urban management: Cities will continue to grow and densify, and any new project will inevitably interact with the existing infrastructure. The administration of these cities will have to consider a very complex infrastructure grid to assess the impacts of these new projects. This thesis presented a very small aspect of this problem, where the construction of a tunnel might jeopardize the stability of a surface construction with a deep foundation. However, even at this scale, a fundamental problem becomes evident: the inventories of infrastructure do not contain essential information to support a reasonable assessment of their resilience to new developments. This is especially critical underground. Research is needed to develop geospatial tools that can be associated with building information modelling to create inventories of the urban infrastructure. These tools must also be able to include the underground space, with tunnels, piles, anchors, etc. The regulatory agencies have to be informed about the type of information that needs to be collected. It is possible to imagine a requirement for new designs to include the elements to simulate foreseeable interaction processes. Following the example of this thesis, it is possible that a pile foundation will be subjected to ground displacements during its lifecycle. Therefore, it could be required that the design considers that possibility, and calibrates the parameters for a framework where the consequences can be computed.

2. Pile tests during unloading: A fundamental problem faced in this project was that, while most pile load tests are unloaded, the instrumentation records are only reported for the loading stage. This thesis has shown that there are important mechanisms that take place through unloading, such as pile tunnel interaction and residual loads. Therefore, more research is needed to calibrate the unloading branches of the mobilization models. That can be done with centrifuge tests and full-scale pile load tests. The results can support more reliable prediction of a pile response to ground displacements.

3. Characterization of TBM fluids: Following the processes that occur around a TBM during tunnelling, it is clear that many of these processes depend on the properties of the excavation fluids, such as the supporting mixture, and the grout. These properties influence the pore pressures in front of a TBM, mixture in the pressure chamber, screw conveyor operation, flow around the TBM and tail void grouting. Large deviations between theoretical calculations and the real situation can be expected if these fluids are not properly characterized. Research is needed to develop a comprehensive methodology to test these fluids in the field, during the construction. While there have been significant developments in terms of qualitative characterization, which might be a reasonable approach for quality control, it certainly isn't suitable for physically based design calculations.

4. Modelling Bingham fluids at 3D: Another problem in this thesis was that the method used to calculate the grout pressures was only based on the pressure difference, and was not able to solve the velocity field. It was also not possible to determine the static shear in the grout, which was set equal to the yield stress through the assumption of flow imminence. More research is needed to devise suitable calculation models for the flow of Bingham fluids around a TBM. These models have to be stable for deformable domains, as the ground deforms significantly under variations of the grout pressure. Once tested at 2D, these models should also be expanded to a cylindrical domain, to simulate the real geometry of a tunnel problem.

5. Grout consolidation: From all the validations presented in this thesis, the one for the grout consolidation was the least accurate. There was no reasonable explanation for why the incremental settlements during consolidation were insignificant, even though there was a considerable dissipation of the grout pressures supporting the tunnel. The scale of the error suggests that there are other processes involved. More research is needed to understand this process, especially with direct instrumentation in the lining during construction.

6. Combined field-test: Finally, it was not possible to validate the whole methodology as there were no instrumented field tests where the pile settlements and axial forces were recorded concurrently to the grout pressures around a tunnel boring machine. Research is needed to design the layout and instrumentation of such a test, which would support more reliable predictions of a pile response to mechanized tunnels. This can also offer the possibility to check whether the tunnel excavation affects the ultimate bearing capacity of the pile, or if the load is redistributed due to the ground displacements, as considered in this thesis.

Annex A. Data on Pile Tunnel Interaction

Table A.1. Settlement data

I.D.	*Dt* (m)	Zt (m)	*Dp* (cm)	*Zp* (m)	*Ld* (m)	*WL*/ UBC	VI (%)	δp (mm)	δs (mm)
BH1	7.00	18.00	40	18.00	5.10	0.75	1.00	37.90	13.93
BH2	7.00	18.00	40	18.00	6.70	0.75	1.00	1.84	10.73
BH3	7.00	18.00	40	18.00	9.90	0.75	1.00	1.15	5.17
BH4	7.00	18.00	40	18.00	16.30	0.75	1.00	0.00	-
BH5	7.00	23.00	40	18.00	5.10	0.75	1.00	38.45	8.00
BH6	7.00	23.00	40	18.00	6.70	0.75	1.00	18.97	6.21
BH7	7.00	23.00	40	18.00	9.90	0.75	1.00	1.68	3.70
BH8	7.00	23.00	40	18.00	16.30	0.75	1.00	0.00	-
HE1	7.00	14.50	40	18.00	5.10	0.75	0.52	0.67	-
HE1	7.00	14.50	40	18.00	5.10	0.75	1.03	4.17	-
HE1	7.00	14.50	40	18.00	5.10	0.75	1.55	10.53	-
HE1	7.00	14.50	40	18.00	5.10	0.75	2.07	21.02	-
HE1	7.00	14.50	40	18.00	5.10	0.75	2.93	45.82	-
HE1	7.00	14.50	40	18.00	5.10	0.75	3.97	76.42	-
HE1	7.00	14.50	40	18.00	5.10	0.75	5.00	103.14	-
HE2	7.00	14.50	40	18.00	6.70	0.75	0.52	0.53	-
HE2	7.00	14.50	40	18.00	6.70	0.75	1.03	1.27	-
HE2	7.00	14.50	40	18.00	6.70	0.75	1.55	2.01	-
HE2	7.00	14.50	40	18.00	6.70	0.75	2.07	3.67	-
HE2	7.00	14.50	40	18.00	6.70	0.75	2.93	6.90	-
HE2	7.00	14.50	40	18.00	6.70	0.75	3.97	10.68	-
HE2	7.00	14.50	40	18.00	6.70	0.75	5.00	14.37	-
HE3	7.00	14.50	40	18.00	9.90	0.75	0.52	0.00	-
HE3	7.00	14.50	40	18.00	9.90	0.75	1.03	0.00	-
HE3	7.00	14.50	40	18.00	9.90	0.75	1.55	0.09	-
HE3	7.00	14.50	40	18.00	9.90	0.75	2.07	0.64	-
HE3	7.00	14.50	40	18.00	9.90	0.75	2.93	2.01	-
HE3	7.00	14.50	40	18.00	9.90	0.75	3.97	4.33	-
HE3	7.00	14.50	40	18.00	9.90	0.75	5.00	6.82	-
JA1	4.50	21.45	90	15.00	0.00	0.65	0.50	2.30	3.78
JA1	4.50	21.45	90	15.00	0.00	0.65	1.00	9.00	9.18
JA1	4.50	21.45	90	15.00	0.00	0.65	1.50	18.00	16.50

JA1	4.50	21.45	90	15.00	0.00	0.65	2.00	41.00	18.53
JA2	4.50	21.45	90	15.00	3.75	0.82	0.50	2.54	2.49
JA2	4.50	21.45	90	15.00	3.75	0.82	1.00	11.49	8.79
JA2	4.50	21.45	90	15.00	3.75	0.82	1.50	38.60	13.50
JA2	4.50	21.45	90	15.00	3.75	0.82	2.00	163.40	-
JA3	4.50	21.45	90	15.00	7.50	0.50	0.50	0.00	-
JA3	4.50	21.45	90	15.00	7.50	0.50	1.00	4.51	6.77
JA3	4.50	21.45	90	15.00	7.50	0.50	1.50	9.40	8.30
JA3	4.50	21.45	90	15.00	7.50	0.50	2.00	12.47	12.53
JA3	4.50	21.45	90	15.00	7.50	0.50	3.00	16.41	17.92
JA3	4.50	21.45	90	15.00	7.50	0.50	4.00	17.81	21.34
JA3	4.50	21.45	90	15.00	7.50	0.50	5.00	19.28	24.76
JA4	4.50	21.45	90	15.00	11.25	0.42	0.50	0.00	-
JA4	4.50	21.45	90	15.00	11.25	0.42	1.00	0.90	5.49
JA4	4.50	21.45	90	15.00	11.25	0.42	1.50	2.00	6.60
JA4	4.50	21.45	90	15.00	11.25	0.42	2.00	2.22	9.99
JA4	4.50	21.45	90	15.00	11.25	0.42	3.00	3.36	13.76
JA4	4.50	21.45	90	15.00	11.25	0.42	4.00	4.10	16.10
JA4	4.50	21.45	90	15.00	11.25	0.42	5.00	4.51	18.62
JA5	4.50	21.45	90	15.00	15.00	0.60	0.50	0.00	-
JA5	4.50	21.45	90	15.00	15.00	0.60	1.00	0.00	-
JA5	4.50	21.45	90	15.00	15.00	0.60	1.50	0.00	-
JA5	4.50	21.45	90	15.00	15.00	0.60	2.00	0.00	-
JA5	4.50	21.45	90	15.00	15.00	0.60	3.00	0.50	9.77
JA5	4.50	21.45	90	15.00	15.00	0.60	4.00	0.57	10.85
JA5	4.50	21.45	90	15.00	15.00	0.60	5.00	0.82	12.29
JA6	4.50	21.45	90	15.00	18.75	0.50	0.50	0.00	-
JA6	4.50	21.45	90	15.00	18.75	0.50	1.00	0.00	-
JA6	4.50	21.45	90	15.00	18.75	0.50	1.50	1.00	5.60
JA6	4.50	21.45	90	15.00	18.75	0.50	2.00	0.00	-
JA6	4.50	21.45	90	15.00	18.75	0.50	3.00	0.90	6.87
JA6	4.50	21.45	90	15.00	18.75	0.50	4.00	1.31	7.23
JA6	4.50	21.45	90	15.00	18.75	0.50	5.00	1.72	8.31
JA7	4.50	21.45	90	18.75	3.75	0.53	0.50	2.30	2.49
JA7	4.50	21.45	90	18.75	3.75	0.53	1.00	5.30	8.79
JA7	4.50	21.45	90	18.75	3.75	0.53	1.50	18.30	12.20
JA7	4.50	21.45	90	18.75	3.75	0.53	2.00	31.10	16.34
JA8	4.50	21.45	90	18.75	7.50	0.50	0.50	0.00	-
JA8	4.50	21.45	90	18.75	7.50	0.50	1.00	1.48	6.77
JA8	4.50	21.45	90	18.75	7.50	0.50	1.50	1.80	10.70
JA8	4.50	21.45	90	18.75	7.50	0.50	2.00	4.00	12.53
JA8	4.50	21.45	90	18.75	7.50	0.50	3.00	6.40	17.92
JA8	4.50	21.45	90	18.75	7.50	0.50	4.00	7.80	21.34
JA8	4.50	21.45	90	18.75	7.50	0.50	5.00	8.86	24.76
JA9	4.50	21.45	90	18.75	11.25	0.47	0.50	0.00	-
JA9	4.50	21.45	90	18.75	11.25	0.47	1.00	1.15	5.49
JA9	4.50	21.45	90	18.75	11.25	0.47	1.50	2.20	9.50
JA9	4.50	21.45	90	18.75	11.25	0.47	2.00	3.28	9.99
JA9	4.50	21.45	90	18.75	11.25	0.47	3.00	4.27	13.76
JA9	4.50	21.45	90	18.75	11.25	0.47	4.00	4.76	16.10
JA9	4.50	21.45	90	18.75	11.25	0.47	5.00	5.66	18.62
JA10	4.50	21.45	90	18.75	15.00	0.50	0.50	0.00	-
JA10	4.50	21.45	90	18.75	15.00	0.50	1.00	0.00	-
JA10	4.50	21.45	90	18.75	15.00	0.50	1.50	0.00	-
JA10	4.50	21.45	90	18.75	15.00	0.50	2.00	0.00	-
JA10	4.50	21.45	90	18.75	15.00	0.50	3.00	1.39	9.77
JA10	4.50	21.45	90	18.75	15.00	0.50	4.00	1.64	10.85

JA10	4.50	21.45	90	18.75	15.00	0.50	5.00	1.89	12.29
JA11	4.50	21.45	90	18.75	22.50	0.63	0.50	0.00	-
JA11	4.50	21.45	90	18.75	22.50	0.63	1.00	0.00	-
JA11	4.50	21.45	90	18.75	22.50	0.63	1.50	0.00	-
JA11	4.50	21.45	90	18.75	22.50	0.63	2.00	0.00	-
JA11	4.50	21.45	90	18.75	22.50	0.63	3.00	1.56	4.68
JA11	4.50	21.45	90	18.75	22.50	0.63	4.00	2.05	5.04
JA11	4.50	21.45	90	18.75	22.50	0.63	5.00	2.71	5.40
JA12	4.50	21.45	90	16.88	0.00	0.50	0.50	4.00	3.78
JA12	4.50	21.45	90	16.88	0.00	0.50	1.00	91.80	-
JA12	4.50	21.45	90	16.88	0.00	0.50	1.50	165.00	-
JA12	4.50	21.45	90	16.88	0.00	0.50	2.00	185.30	-
LO1	6.00	15.00	80	18.00	5.50	0.50	1.00	10.50	10.40
LO1 Gr.	6.00	15.00	80	18.00	5.50	0.50	1.00	6.60	10.40
LO2	6.00	18.00	80	18.00	5.50	0.50	1.00	11.80	8.50
LO2 Gr.	6.00	18.00	80	18.00	5.50	0.50	1.00	12.20	8.50
LO3	6.00	21.00	80	18.00	5.50	0.50	1.00	11.60	7.70
LO3 Gr.	6.00	21.00	80	18.00	5.50	0.50	1.00	7.60	7.70
MA1	4.65	13.65	90	7.20	0.00	0.63	0.48	0.00	-
MA1	4.65	13.65	90	7.20	0.00	0.63	0.90	0.03	0.14
MA1	4.65	13.65	90	7.20	0.00	0.63	0.97	0.20	-
MA1	4.65	13.65	90	7.20	0.00	0.63	1.52	4.98	-
MA1	4.65	13.65	90	7.20	0.00	0.63	2.00	14.62	-
MA2	4.65	13.65	90	6.83	9.75	0.63	0.90	0.00	-
MA3	4.65	13.65	90	6.90	4.58	0.63	0.48	0.01	-
MA3	4.65	13.65	90	6.90	4.58	0.63	0.90	0.01	0.13
MA3	4.65	13.65	90	6.90	4.58	0.63	0.97	0.25	-
MA3	4.65	13.65	90	6.90	4.58	0.63	1.52	2.19	-
MA3	4.65	13.65	90	6.90	4.58	0.63	2.00	5.94	-
MA4	4.65	13.65	90	6.30	4.88	0.63	0.90	0.01	0.12
NG1	6.08	19.60	80	19.60	4.56	0.67	1.00	15.92	13.70
NG2 T1	6.08	19.60	80	19.60	4.56	0.67	1.00	15.27	12.40
NG2 T2	6.08	19.60	80	19.60	4.56	0.67	1.00	15.92	12.10
NG3 T1	6.08	12.00	80	19.60	4.56	0.67	1.00	9.70	19.64
NG3 T2	6.08	12.00	80	19.60	4.56	0.67	1.00	4.21	18.16
ON1	6.00	15.00	[a]126	20.50	6.00	0.00	3.30	2.90	32.00
RA1	6.00	15.00	[a]126	23.50	6.00	0.00	2.00	6.00	21.30
RA2	6.00	15.00	[a]126	23.50	9.00	0.00	2.00	4.63	14.60
RA3	6.00	15.00	[a]126	23.50	12.00	0.00	2.00	0.73	8.82
RA4	6.00	15.00	[a]126	15.00	6.00	0.00	2.00	23.20	21.30
RA5	6.00	15.00	[a]126	10.00	0.00	0.00	2.00	17.06	30.70
RA6	6.00	15.00	[a]126	10.00	5.00	0.00	2.00	20.32	24.33
RA7	6.00	15.00	[a]126	23.50	17.00	0.00	2.00	1.52	2.40
SE1 T1	8.00	18.90	48	13.00	0.00	0.50	0.20	8.90	6.80
SE2 T1	8.00	18.90	48	13.00	9.00	0.50	0.20	3.80	3.80
SE3 T1	8.00	18.90	48	8.50	0.00	0.50	0.20	11.10	7.70
SE4 T1	8.00	18.90	48	8.50	9.00	0.50	0.20	4.20	4.20
SE1 T2	8.00	18.90	48	13.00	16.00	0.50	0.50	1.80	3.40
SE2 T2	8.00	18.90	48	13.00	7.00	0.50	0.50	9.20	9.20
SE3 T2	8.00	18.90	48	8.50	16.00	0.50	0.50	3.00	4.50
SE4 T2	8.00	18.90	48	8.50	7.00	0.50	0.50	10.60	10.60

*BH - (Bezuijen and van der Schrier 1994) / (Hergarden et al. 1996); HE - (Hergarden et al. 1996); JA - (Jacobsz 2002); LO - (Loganathan et al. 2000); MA - (Marshall 2009); NG - (Ng et al. 2013); ON - (Ong et al. 2005); RA - (Ran 2004); SE - (Selemetas 2005) (Selemetas et al. 2005). [a]Dp values represent the sizes of the cross section edge.

Annex B. Codes for Pile Analysis

The methodology described in Chapter 3 is implemented in an Excel (2016) spreadsheet with subroutines in VBA. The general layout of the application, with R1C1 reference style, can be seen in Figure B.1 for a set-up with 40 calculation nodes along the pile. The code can be accessed through the permanent link: https://doi.org/10.13140/RG.2.2.33263.23202.

The formulas implemented in the spreadsheet, and the VBA codes are given here in text form with the syntax highlights of the Visual Basic language, created through the application Notepad++ v6.9.2.

```
'########## Formulas R1C1 in the Spreadsheet ##########
Cells(11,2) = R8C2*R5C2*R6C2    'Weight = γp * Zp * Ap
Cells(12,2) = (SUM(R3C5:R41C5)+((R2C5+R42C5)/2)) *R7C2*R3C4*R5C2
'Shaft  = SUM(τmax)*Pp*dl
Cells(13,2) = R17C2*R6C2    'Toe = qb*Ap
Cells(14,2) = R12C2+R13C2-R11C2 'UBC = Shaft + Toe - Weight
Cells(15,2) = -R12C2-R11C2  'UTC = -Shaft - Weight
Cells(22,2) = MIN( _     'Toe Mob =
                1; _     'sets the maximum mobilization to 1
                IF(R42C15>0; 'if relative toe displacement is
positive, reaction is null
                    0; _
                    IF(R42C15<=R21C2;   'check if smaller than
saved maximum toe displacement
                        (-R42C15/R18C2)^R19C2; _ 'if so, use
exponential model directly
                        IF(R42C15>R21C2*(1-R20C2); _ 'if not,
check if it is higher than max rebound
                            0; _     'if so, reaction is null
```

	1	2	4	5	6	7	8	9	10	11	12	13	14	15	16	17	18
1	WI/UBC	0	Z/Zp	τ max	S1	τ ep	S2	S3	S1/3	Δδ r	τ r	δs (mm)	δp (mm)	Δδ (mm)	τ/τmáx	τ (kN/m²)	σ (kN/m²)
2			0.00	0.00	0.20	0.50	0.05	0.40	1.00	-93.23	1.00	0.00	93.23	-93.23	1.00	0.00	0
3	Divisions	40	0.03	2.89	0.20	0.50	0.05	0.40	1.00	-93.23	0.99	0.00	93.23	-93.23	0.99	2.86	15
4			0.05	5.77	0.20	0.50	0.05	0.40	1.00	-93.23	0.97	0.00	93.23	-93.23	0.97	5.61	36
5	Zp (m)	20	0.08	8.66	0.20	0.50	0.05	0.40	1.00	-93.23	0.95	0.00	93.23	-93.23	0.95	8.25	63
6	Ap (m²)	0.79	0.10	11.55	0.20	0.50	0.05	0.40	1.00	-93.23	0.93	0.00	93.23	-93.23	0.93	10.77	94
7	Pp (m)	3.14	0.13	14.43	0.20	0.50	0.05	0.40	1.00	-93.22	0.91	0.00	93.22	-93.22	0.91	13.19	131
8	γp (kN/m³)	25	0.15	17.32	0.20	0.50	0.05	0.40	1.00	-93.21	0.89	0.00	93.21	-93.21	0.89	15.49	172
9	Ep (kN/m²)	1E+07	0.18	20.21	0.20	0.50	0.05	0.40	1.00	-93.20	0.87	0.00	93.20	-93.20	0.87	17.68	218
10			0.20	23.09	0.20	0.50	0.05	0.40	1.00	-93.19	0.86	0.00	93.19	-93.19	0.86	19.76	267
11	Weight (kN)	393	0.23	25.98	0.20	0.50	0.05	0.40	1.00	-93.18	0.84	0.00	93.18	-93.18	0.84	21.73	321
12	Shaft (kN)	3628	0.25	28.87	0.20	0.50	0.05	0.40	1.00	-93.16	0.82	0.00	93.16	-93.16	0.82	23.60	379
13	Toe (kN)	3235	0.28	31.75	0.20	0.50	0.05	0.40	1.00	-93.14	0.80	0.00	93.14	-93.14	0.80	25.36	441
14	UBC (kN)	6470	0.30	34.64	0.20	0.50	0.05	0.40	1.00	-93.11	0.78	0.00	93.11	-93.11	0.78	27.03	506
15	UTC (kN)	-4020	0.33	37.53	0.20	0.50	0.05	0.40	1.00	-93.09	0.76	0.00	93.09	-93.09	0.76	28.60	574
16			0.35	40.41	0.20	0.50	0.05	0.40	1.00	-93.06	0.74	0.00	93.06	-93.06	0.74	30.08	645
17	qb (kN/m²)	4119	0.38	43.30	0.20	0.50	0.05	0.40	1.00	-93.02	0.73	0.00	93.02	-93.02	0.73	31.47	719
18	Δδt (mm)	100	0.40	46.19	0.20	0.50	0.05	0.40	1.00	-92.99	0.71	0.00	92.99	-92.99	0.71	32.77	796
19	λtoe	0.30	0.43	49.07	0.20	0.50	0.05	0.40	1.00	-92.94	0.69	0.00	92.94	-92.94	0.69	33.99	875
20	Rb	0.10	0.45	51.96	0.20	0.50	0.05	0.40	1.00	-92.90	0.68	0.00	92.90	-92.90	0.68	35.14	957
21	Δδmax (mm)	-94	0.48	54.85	0.20	0.50	0.05	0.40	1.00	-92.85	0.66	0.00	92.85	-92.85	0.66	36.22	1040
22	Toe Mob	0.69	0.50	57.74	0.20	0.50	0.05	0.40	1.00	-92.79	0.64	0.00	92.79	-92.79	0.64	37.23	1126
23			0.53	60.62	0.20	0.50	0.05	0.40	1.00	-92.74	0.63	0.00	92.74	-92.74	0.63	38.18	1214
24	Error	0.0	0.55	63.51	0.20	0.50	0.05	0.40	1.00	-92.67	0.62	0.00	92.67	-92.67	0.62	39.07	1304
25			0.58	66.40	0.20	0.50	0.05	0.40	1.00	-92.60	0.60	0.00	92.60	-92.60	0.60	39.90	1396
26	Basic Input		0.60	69.28	0.20	0.50	0.05	0.40	1.00	-92.53	0.59	0.00	92.53	-92.53	0.59	40.67	1489
27			0.63	72.17	0.20	0.50	0.05	0.40	1.00	-92.46	0.57	0.00	92.46	-92.46	0.57	41.43	1583
28	Depth and		0.65	75.06	0.20	0.50	0.05	0.40	1.00	-92.37	0.56	0.00	92.37	-92.37	0.56	42.16	1679
29	Maximum Shaft		0.68	77.94	0.20	0.50	0.05	0.40	1.00	-92.29	0.55	0.00	92.29	-92.29	0.55	42.86	1777
30			0.70	80.83	0.20	0.50	0.05	0.40	1.00	-92.20	0.54	0.00	92.20	-92.20	0.54	43.53	1876
31	Shaft		0.73	83.72	0.20	0.50	0.05	0.40	1.00	-92.10	0.53	0.00	92.10	-92.10	0.53	44.19	1976
32	Mobilization Model		0.75	86.60	0.20	0.50	0.05	0.40	1.00	-92.00	0.52	0.00	92.00	-92.00	0.52	44.83	2077
33	Reference		0.78	89.49	0.20	0.50	0.05	0.40	1.00	-91.89	0.51	0.00	91.89	-91.89	0.51	45.47	2180
34	Shaft Values		0.80	92.38	0.20	0.50	0.05	0.40	-1.00	-91.78	0.49	0.00	91.78	-91.78	0.49	45.63	2284
35			0.83	95.26	0.20	0.50	0.05	0.40	-1.00	-91.66	0.43	0.00	91.66	-91.66	0.43	40.94	2383
36	Displacements		0.85	98.15	0.20	0.50	0.05	0.40	-1.00	-91.54	0.37	0.00	91.54	-91.54	0.37	36.37	2473
37			0.88	101.04	0.20	0.50	0.05	0.40	-1.00	-91.42	0.32	0.00	91.42	-91.42	0.32	31.96	2554
38	Mobilized		0.90	103.92	0.20	0.50	0.05	0.40	-1.00	-91.29	0.27	0.00	91.29	-91.29	0.27	27.75	2626
39	Shaft & Axial Loads		0.93	106.81	0.20	0.50	0.05	0.40	-1.00	-91.16	0.22	0.00	91.15	-91.15	0.22	23.77	2690
40			0.95	109.70	0.20	0.50	0.05	0.40	-1.00	-91.02	0.18	0.00	91.02	-91.02	0.18	20.06	2746
41	Cell of		0.98	112.58	0.20	0.50	0.05	0.40	-1.00	-90.88	0.15	0.00	90.88	-90.88	0.15	16.64	2795
42	Root Search		1.00	115.47	0.20	0.50	0.05	0.40	-1.00	-90.74	0.12	0.00	90.74	-90.74	0.12	13.67	2838

Figure B.1. Layout of the PILE.27.TL spreadsheet

```
                                ' if not, calculate the linear
unloading reaction
                                ((R42C15-R21C2*(1-
R20C2))/(R21C2*R20C2))*((-R21C2/R18C2)^R19C2)))) _
                )
Cells(24,2) = R42C18-(R22C2*R17C2)  'Error = σ[n+2] - (Toe Mob *
qb)
''Calculations along the whole vertical domain
For i = 2 to Cells(3,2).Value + 2
    Cells(i,5) = RC[-1]*R5C2*20*0.29 'τmax = (Z/Zp)*Zp*γsoil*β
(effective method)
    Cells(i,14) = IF( _ 'δp =
                    R9C2=0; R[1]C; _     'if Ep=0, calculate a
rigid pile

R[1]C+(1000*((RC[4]+R[1]C[4])*R3C4*R5C2/(2*R9C2))) _
'δp(i+1)+((σ[i]+σ[i+1])*dl/(2*Ep))
                    )
    Cells(i,15) =RC[-2]-RC[-1]  'Δδ = δs-δp
    Cells(i,16) = IF(   'τ/τmáx =
                    RC[-1]=RC[-5]; _     'check if Δδ=Δδref
                    RC[-4]; _            'if so, set τ=τref
                    IF(RC[-1]>RC[-5]; _ 'if not, check if Δδ>Δδref
                        MIN(1; _     'if so, set max mobilization
to 1
                            IF(RC[-4]>=RC[-9]; _     'check if
τref>τep
                                RC[-4]+(RC[-1]-RC[-5])*RC[-8]; _
'if so, τref+(Δδ-Δδref)*S2
```

```
                                    IF(RC[-4]+(RC[-1]-RC[-5])*IF(RC[-
6]=1;RC[-10];RC[-7])>RC[-9];   'check if τref+(Δδ-Δδref)*(S1 or
S3)>τep
                                        RC[-9]+(RC[-1]-RC[-5]-(RC[-9]-
RC[-4])/IF(RC[-6]=1;RC[-10];RC[-7]))*RC[-8]; _    'if so, τep+(Δδ-
Δδref-(τep-τref)/(S1 or S3)
                                        RC[-4]+(RC[-1]-RC[-5])*IF(RC[-
6]=1;RC[-10];RC[-7]))))) _ 'if not, τref+(Δδ-Δδref)*(S1 or S3)
                            ;MAX(-1; _   'if not, set min mobilization
to -1
                                IF(RC[-4]<=-RC[-9]; _   'check if
τref<-τep
                                    RC[-4]+(RC[-1]-RC[-5])*RC[-8]; _
'if so, τref+(Δδ-Δδref)*S2
                                    IF(RC[-4]+(RC[-1]-RC[-5])*IF(RC[-
6]=1;RC[-10];RC[-7])<-RC[-9]; _    'check if τref+(Δδ-Δδref)*(S1
or S3)<-τep
                                        -RC[-9]+(RC[-1]-RC[-5]-(-RC[-
9]-RC[-4])/IF(RC[-6]=1;RC[-10];RC[-7]))*RC[-8]; _  'if so, -
τep+(Δδ-Δδref-(-τep-τref)/(S1 or S3)
                                        RC[-4]+(RC[-1]-RC[-5])*IF(RC[-
6]=1;RC[-10];RC[-7])))))) _    'if not, τref+(Δδ-Δδref)*(S1 or S3)
                        )
    Cells(i,17) = RC[-1]*RC[-12]    'τ = (τ/τmáx)*τ max
    Cells(i,18) = R[-1]C+(R8C2*R3C4*R5C2)+(R7C2*R3C4*R5C2*(R[-
1]C[-1]+RC[-1])/(2*R6C2))
'σ[i]=σ[i+1]+(γp*dl)+(Pp*dl*(τ[i]+τ[i+1])/(2*Ap))
Next i
Cells(2,18) =
IF(R1C2>0;R1C2*R14C2/(100*R6C2);R1C2*R15C2/(100*R6C2)) 'σ[0] =
(WL/UBC)*(UBC or UTC)/(Ap)
Cells(n+2,14) = RC[-1]-RC[1]    'δp = δs - Δδ
Cells(n+2,15) = 'root value
```

```
'########## Interaction Routine ##########
Sub INTERACT()
    Application.ScreenUpdating = False
    Dim n As Long
    Dim x1 As Double
    Dim y1 As Double
    Dim x2 As Double
    Dim y2 As Double
    Dim x3 As Double
    Dim y3 As Double
    n = Cells(3, 2).Value   'number of equidistant nodes along the
pile
    For i = 1 To 2000   'maximum number of iterations
        If i = 1 Then   'first iteration assumes maximum toe
mobilization
            x1 = -Cells(18, 2)  'cell whith max toe displacement
            Cells(n + 2, 15) = x1   'set relative displacement at
last node
            y1 = Cells(24, 2).Value 'residual load (negative
value)
            If (y1 < 0.05 And y1 > -0.05) Then  'check if error is
smaller than tolerance
                Exit For
            End If
            x2 = +Cells(18, 2)  'cell whith max toe displacement
```

```
            Cells(n + 2, 15) = x2   'set relative displacement at
last node
            y2 = Cells(24, 2).Value 'residual load (positive
value)
            If (y2 < 0.05 And y2 > -0.05) Then  'check if error is
smaller than tolerance
                Exit For
            End If
        End If
        ''false position method to find the relative toe
displacement at equilibrium
        x3 = x2 - (y2 * (x2 - x1) / (y2 - y1))
        Cells(n + 2, 15) = x3   'set relative displacement at last
node
        y3 = Cells(24, 2).Value 'residual load
        If (y3 < 0.05 And y3 > -0.05) Then  'check if error is
smaller than tolerance
            Exit For
        End If
        ''update values of depending on the signal
        If y3 > 0 Then
            x2 = x3
            y2 = y3
        Else
            x1 = x3
            y1 = y3
        End If
    Next i
    ''mesage if more iteractions are needed
    If i = 2001 Then
        MsgBox ("Residual Tip Force: " & Round(y3, 1) & " kPa")
    End If
End Sub
```

```
'########## Update Limits Routine ##########
Sub UPDATE()
    Application.ScreenUpdating = False
    Dim n As Long
    n = Cells(3, 2).Value   'number of equidistant nodes along the
pile
    ''update mobilization limits for shaft model
    For i = (n + 2) To 2 Step -1 'Update the nodes from the toe up
        k = 0
        ''check if S1 needs to be changed to S3 and vice-versa
        If _
            'τref > -τep AND τ < -τep AND S3 is being used
            'cross the negative EP limit, from an EP state
            ((Cells(i, 12).Value > -Cells(i, 7).Value) And
(Cells(i, 16).Value < -Cells(i, 7).Value) And (Cells(i, 10).Value
= -1)) _
            Or _
            'τref < τep AND τ > τep AND S3 is being used
            'cross the positive EP limit, from an EP state
            ((Cells(i, 12).Value < Cells(i, 7).Value) And
(Cells(i, 16).Value > Cells(i, 7).Value) And (Cells(i, 10).Value =
-1)) _
            Or _
            'τref < τep AND absolute value of τ > τep AND S1 is
being used
            'cross any EP limit, from an elastic state
```

```
            ((Abs(Cells(i, 12).Value) < Cells(i, 7).Value) And
(Abs(Cells(i, 16).Value) > Cells(i, 7).Value) And (Cells(i,
10).Value = 1)) _
            Then
            k = 1
        End If
        'the reference values are updated before the switch
        Cells(i, 12).Value = Cells(i, 16).Value 'τref = τ
        Cells(i, 11).Value = Cells(i, 15).Value 'Δδref = Δδ
        If k = 1 Then   'k defined in the previous if switches
between S1(1) and S3(-1)
           Cells(i, 10).Value = Cells(i, 10).Value * -1
        End If
    Next i
    ''update mobilization limits for toe model
    If Cells((n + 2), 15).Value < Cells(21, 2).Value Then   'check
if toe disp < saved max toe displacement
        Cells(21, 2).Value = Cells((n + 2), 15).Value
    End If
End Sub
```

```
'########## Reset Values Routine ##########
Sub RESET()
    Application.ScreenUpdating = False
    Dim k As Double
    Dim n As Long
    n = Cells(3, 2).Value   'number of equidistant nodes along the
pile
    Range(Cells(2, 21), Cells(200, 200)).ClearContents 'clear data
previous load cycles
    k = Cells(20, 2).Value  'save value of toe rebound
    Cells(21, 2).Value = 0   'set max toe displacement to 0
    For i = 2 To (n + 2)    'reset parameters of shaft model
        Cells(i, 10).Value = 1  'use S1
        Cells(i, 11).Value = 0  'dSref = 0
        Cells(i, 12).Value = 0  'Tref = 0
    Next i
    Cells(20, 2).Value = 1   'set toe rebound to 1
    Cells(1, 2).Value = 0  'set load to 0
    DoEvents    'let the automatic call interact for solution and
update values
    Cells(20, 2).Value = k  'reinstate toe rebound
    Application.Run ("INTERACT")
    Application.Run ("UPDATE")
End Sub
```

```
'########## Load-Settlement Cycle Routine ##########
Sub LOADSETL()
    Application.ScreenUpdating = False
    Dim LR As Long
    Dim k As Long
    Dim n As Long
    Application.Run ("RESET")   'reset everything
    ActiveSheet.ChartObjects("Chart 7").Activate    'delete the
axial load curves
    For i = ActiveChart.SeriesCollection.Count To 2 Step -1
        ActiveChart.SeriesCollection(i).Delete
    Next i
```

```
    n = Cells(3, 2).Value   'number of equidistant nodes along the
pile
    LR = ActiveSheet.Cells(Rows.Count, 20).End(xlUp).Row    'read
the number of staged set-up
    k = 24  'define column to save the axial load data
    For i = 2 To LR 'for each state of the load-settlement cycle
        Cells(1, 2).Value = Cells(i, 20).Value  'set head load
        DoEvents    'let the automatic call interact for solution
and update values
        Cells(i, 21).Value = Cells(2, 18).Value 'Write load
        Cells(i, 22).Value = Cells(2, 14).Value 'Write settlements
        For j = 2 To n + 2
            Cells(j, k).Value = Cells(j, 18).Value  'write axial
force profile
        Next j
        ActiveSheet.ChartObjects("Chart 7").Activate    'create
new series in the graph
        ActiveChart.SeriesCollection.NewSeries
        ActiveChart.FullSeriesCollection(k - 23).XValues =
"=P25!R2C" & k & ":R" & n + 2 & "C" & k & ""
        ActiveChart.FullSeriesCollection(k - 23).Values =
"=P25!R2C4:R" & n + 2 & "C4"
        k = k + 1   'move to the next column
    Next i
End Sub
```

```
'########## Automatic Call of Sub-Routines ##########
Private Sub Worksheet_Change(ByVal Target As Range)
    Application.ScreenUpdating = False
    ''if cell with the head load (WL/UBC), find new solution and
update limits of mobilization
    If Not Intersect(Target, Range("B1")) Is Nothing Then
        Application.Run ("INTERACT")
        Application.Run ("UPDATE")
        Application.Run ("INTERACT")
        Application.Run ("UPDATE")
    End If
    ''if cells with ground displacements change, find new solution
    If Not Intersect(Target, Range("M2:M42")) Is Nothing Then
        Application.Run ("INTERACT")
    End If
End Sub
```

Annex C. Codes for Tunnel Analysis on FlexPDE

The methodology described in Section 4.3 is implemented in an Excel (2016) spreadsheet with subroutines in VBA. The general layout of the application, with R1C1 reference style, can be seen in Figure C.1 for a set-up with 13 calculation nodes along the half-section of the tunnel. The code can be accessed through the permanent link: https://doi.org/10.13140/RG.2.2.29907.78888.

The formulas implemented in the spreadsheet, and the VBA codes are given here in text form with the syntax highlights of the Visual Basic language, created through the application Notepad++ v6.9.2.

```
'########## Formulas R1C1 in the Spreadsheet ##########
For i = 2 to 13
    Cells(i,9) = R9C2*(1+SIN(RADIANS(RC[-1])))  'H = Rt*(1+sin(θ))
    Cells(i,10) = RC[-1]/R2C9   'H/D = H/H[0]
    Cells(i,11) = ((90-RC[-3])/180)*PI()*R9C2   'L = ((90-
θ)/180)*π*Rt
    Cells(i,12) = (R8C2+R9C2-RC[-3]+R2C2)*10    'uw=(Zt+Rt-
H[i]+GWL)*10 (Hydrostatic)
    Cells(i,15) = MAX(AGGREGATE(4;6;RC[1]:RC[13]);0) 'GP=max from
the results of each node
    For j = 16 to 28
        If i=j-14 Then  'diagonal nodes are injection points
            Cells(i,j) =
IF(ISNUMBER(INDEX(R2C14:R14C14;MATCH(R1C;R2C7:R14C7;0)));_
'check if there is a pressure assigned to the noozle

INDEX(R2C14:R14C14;MATCH(R1C;R2C7:R14C7;0));_   'if so, assume
that pressure
                            "-")
            Else
```

	1	2	3	4	5	6	7	8	9	10	11	12	13
1	γw (kN/m³)	10		x (m)	v (mm)		Point	θ	H (m)	H/D	L (m)	uw (kPa)	Gap (cm)
2	GWL (m)	0		-90.00	1.08		1	90	10.00	1.00	0.00	250	12.79
3	E (MPa)	45		-88.87	1.08		2	75	9.83	0.98	1.31	252	13.01
4	v (effective)	0.3		-87.74	1.08		3	60	9.33	0.93	2.62	257	13.61
5	v (undrained)	0.3		-86.61	1.09		4	45	8.54	0.85	3.93	265	14.46
6	k0	0.5		-85.47	1.09		5	30	7.50	0.75	5.24	275	15.34
7	γ ground (kN/m³)	20		-84.34	1.10		6	15	6.29	0.63	6.54	287	16.00
8	Zt (m)	30		-83.21	1.10		7	0	5.00	0.50	7.85	300	16.20
9	Rt (m)	5.00		-82.08	1.11		8	-15	3.71	0.37	9.16	313	15.88
10	Rlin (m)	4.85		-80.95	1.12		9	-30	2.50	0.25	10.47	325	15.06
11	τ_Y (kPa)	0.5		-79.82	1.14		10	-45	1.46	0.15	11.78	335	13.96
12	γ grout (kN/m³)	20		-78.68	1.15		11	-60	0.67	0.07	13.09	343	12.84
13	Net Force (kN)	-1193		-77.55	1.17		12	-75	0.17	0.02	14.40	348	12.00
14	Volume Loss	0.37%		-76.42	1.18		13	-90	0.00	0.00	15.71	350	11.70
15	Avg. Grad (kN/m³)	15.48		-75.29	1.20								

	14	15	16	17	18	19	20	21	22	23	24	25	26	27	28	29	30
1	Inj. (kPa)	GP (kPa)	1	2	3	4	5	6	7	8	9	10	11	12	13	F (kN)	P0 (kPa)
2	400	400	400	--	--	--	331	--	--	--	214	--	--	--	144	254	500
3	-	398	398	-	--	--	339	--	--	--	223	--	--	--	153	489	495
4	-	403	403	--	-	--	354	--	--	--	238	--	--	--	168	444	481
5	-	415	415	--	--	-	375	--	--	--	258	--	--	--	188	372	463
6	400	431	431	--	--	--	400	--	--	--	283	--	--	--	213	274	447
7	-	451	451	--	--	--	420	-	--	--	312	--	--	--	242	148	440
8	-	473	473	--	--	--	442	--	-	--	342	--	--	--	271	0	450
9	-	495	495	--	--	--	464	--	--	-	372	--	--	--	301	-163	480
10	400	514	514	--	--	--	483	--	--	--	400	--	--	--	330	-327	528
11	-	531	531	--	--	--	500	--	--	--	416	-	--	--	355	-476	587
12	-	542	542	--	--	--	511	--	--	--	427	--	-	--	376	-596	644
13	-	546	546	--	--	--	515	--	--	--	432	--	--	-	391	-670	685
14	400	544	544	--	--	--	513	--	--	--	430	--	--	--	400	-345	700
15																	

Figure C.1. Layout of the TBM.GP.19.Flex spreadsheet

```
            If i>j-14 Then 'check if the node is below the
injection point
                Cells(i,j) = IFERROR(_  'GP[i-1] - (τy*abs(L[i]-
L[i-1])/avg(gap[i]:gap[i-1])) + ((H[i-1]-H[i])*γgrout)
                                        R[-1]C-(R11C2*ABS(RC11-R[-
1]C11)/(0.01*AVERAGE(R[-1]C13:RC13)))+((R[-1]C9-RC9)*R12C2);_
                                        "--")
                Else    'if not, then the node is above
                Cells(i,j) = IFERROR(_  'GP[i+1] - (τy*abs(L[i]-
L[i+1])/avg(gap[i]:gap[i+1])) - ((H[i]-H[i+1])*γgrout)
                                        R[1]C-(R11C2*ABS(R[1]C11-
RC11)/(0.01*AVERAGE(RC13:R[1]C13)))-((RC9-R[1]C9)*R12C2);_
                                        "--")
            End if
        End if
    Next j
    If i=2 or i=13 Then
        Cells(i,29) = RC[-14]*RADIANS(15/2)*R10C2*SIN(RADIANS(RC[-
21])) 'F = GP*dθ*Rlin*sin(θ)
        Else
        Cells(i,29) = RC[-14]*RADIANS(15)*R10C2*SIN(RADIANS(RC[-
21]))
    End if
    ''Geostatic Normal Pressure Around the Tunnel
    Cells(i,30) = ((R7C2*(R8C2+R9C2-
RC9))*SIN(RADIANS(RC8))*SIN(RADIANS(RC8)))+(((((R7C2*(R8C2+R9C2-
RC9))-IF((R1C2*(R8C2+R2C2+R9C2-RC9))>0,(R1C2*(R8C2+R2C2+R9C2-
```

```
RC9)),0))*R6C2)+IF((R1C2*(R8C2+R2C2+R9C2-
RC9))>0,(R1C2*(R8C2+R2C2+R9C2-
RC9)),0))*COS(RADIANS(RC8))*COS(RADIANS(RC8)))
    ''This expression can be taken in steps as follows:
    'Original stresses
    Sytot=γground*(Zt+Rt-H)
    Sxtot=(((γground*(Zt+Rt-H))-IF((γw*(Zt+GWL+Rt-
H))>0;(γw*(Zt+GWL+Rt-H));0))*k0)+IF((γw*(Zt+GWL+Rt-
H))>0;(γw*(Zt+GWL+Rt-H));0)
    'Transform coordinate system from XY to Rθ, with Sxy=0
    Sr = Sxtot*cos(θ)² + Sytot*sin(θ)²
Next i
Cells(13,2) = 2*SUM(R[-11]C[27]:R[1]C[27])  'NetForce = 2*Sum(F)
Cells(14,2) = ((R9C2^2)-
((0.01*AVERAGE(R2C13:R14C13)+R10C2)^2))/(R9C2^2)    'VL = (Rt²-
(Rlin+avg(gap))²)/Rt²
Cells(15,2) = -SLOPE(R2C15:R14C15;R2C9:R14C9)   'Average Gradient
```

```
'########## Define ShellExecute Function ##########
Const SW_SHOW = 1
Const SW_SHOWMAXIMIZED = 3
Option Explicit
Private Declare Function ShellExecute Lib "shell32.dll" Alias
"ShellExecuteA" ( _
ByVal hWnd As Long, _
ByVal Operation As String, _
ByVal fileName As String,
Optional ByVal Parameters As String, _
Optional ByVal Directory As String, _
'vbMinimizedNoFocus or vbNormalNoFocus
Optional ByVal WindowStyle As Long = vbMinimizedNoFocus) As Long
```

```
'########## Example FlexPDE Script ##########
Sub EXAMPLE()
    TITLE 'Stress Analysis'
    SELECT
    errlim = 1e-10

    VARIABLES
    u
    v

    DEFINITIONS
    E = 45000
    nie = 0.3
    niu = 0.3
    k0 = 0.5
    fy = 20
    zt = 30
    rte = 5
    rti = 4.85
    gw = 10
    gwl = 0
    '!elastic constants
    G = E / (2 * (1 + nie))
    Ke = E / (3 * (1 - nie - nie))
    Ku = 2 * G * (1 + niu) / (3 - (6 * niu))
    Kw = Ku - Ke
```

```
    A = Ku + 4 * G / 3
    B = Ku - 2 * G / 3
    C = G
    '!strain definition
    ex = -dx(u)
    ey = -dy(v)
    exy = -dx(v) - dy(u)
    ev = ex+ey
    '!initial total stresses and pwp
    uw0 = IF (y<gwl) THEN (y-gwl)*gw*(-1) ELSE 0
    sy0 = -y*fy
    sx0 = (k0 * (sy0 - uw0)) + uw0
    sz0 = (k0 * (sy0 - uw0)) + uw0
    sxy0 = 0
    '!constitutive relation
    sx = sx0 + A*ex + B*ey
    sy = sy0 + B*ex + A*ey
    sxy = sxy0 + C*exy
    sz = sz0 + niu*(sx + sy)
    uw = uw0 + (Kw * ev)
    '!effective stresses
    sxe = sx - uw
    sye = sy - uw
    sze = sz - uw
    'the code takes a sequence of x,y points around the perimeter
and_
    'calculates the tunnel-lining gap, angle of the deformed
boundary and_
    'angle of the original boundary
    gap=sqrt((x+u-3*zt)^2+(y+v+zt)^2)-rti   'radius of deformed
boundary in relation to tunnel centre, minus the lining radius
    defang=IF (x+u-3*zt)=0 OR (y+v+zt)=0 THEN IF (x+u-3*zt) = 0
THEN IF (y+v+zt)>0 THEN PI/2 ELSE 3*PI/2 ELSE  IF (x+u-3*zt)>0
THEN 0 ELSE PI ELSE IF(x+u-3*zt)<0 THEN ARCTAN((y+v+zt)/(x+u-
3*zt))+PI ELSE IF(y+v+zt)<0 THEN ARCTAN((y+v+zt)/(x+u-3*zt))+2*PI
ELSE ARCTAN((y+v+zt)/(x+u-3*zt))
    defangd=180*defang/pi   'transform radians into degrees
    ang=IF (x-3*zt)=0 OR (y+zt)=0 THEN IF (x-3*zt) = 0 THEN IF
(y+zt)>0 THEN PI/2 ELSE 3*PI/2 ELSE  IF (x-3*zt)>0 THEN 0 ELSE PI
ELSE IF(x-3*zt)<0 THEN ARCTAN((y+zt)/(x-3*zt))+PI ELSE IF(y+zt)<0
THEN ARCTAN((y+zt)/(x-3*zt))+2*PI ELSE ARCTAN((y+zt)/(x-3*zt))
    angd=180*ang/pi     'transform radians into degrees
    'these angle calculations can be expanded to:
    'consider θ=0 at (1,0) of a unit circle
    =IF (((x-3*zt)=0 OR (y+zt)=0);  'check if x or y are zero, so
the point is in one of the axes
        IF((x-3*zt) = 0;    'if so, check if x=0
            IF((y+zt)>0;    'if so, see if y is positive
                PI/2;       'if so, then θ=90
                3*PI/2);    'if not, then θ=270
            IF((x-3*zt)>0   'if x≠0, then check if x is positive
                0;      'if so, then θ=0
                PI))    'if not, then θ=180
        IF((x-3*zt)<0 ; 'if neither x nor y are null, check if x<0
            ARCTAN((y+zt)/(x-3*zt))+PI ;    'if so, calculate the
θ=arctan+180
            IF((y+zt)<0;    'if not, check if y<0
                ARCTAN((y+zt)/(x-3*zt))+2*PI;   'if so, then
θ=arctan+360
                ARCTAN((y+zt)/(x-3*zt)))))
    '!transition and grout pressures
```

```
    gp1=399.167409696981
    gp2=400.871119213497
    gp3=409.021450156271
    gp4=422.794245969645
    gp5=440.923329768661
    gp6=461.801993119229
    gp7=483.611327654373
    gp8=504.456193919129
    gp9=522.500110690465
    gp10=536.103740673367
    gp11=543.966767974577
    gp12=545.267435351343
    '!boundary conditions
    Nu1 =  normal(vector(gp1,0))
    Nv1 =  normal(vector(0,gp1))
    Nu2 =  normal(vector(gp2,0))
    Nv2 =  normal(vector(0,gp2))
    Nu3 =  normal(vector(gp3,0))
    Nv3 =  normal(vector(0,gp3))
    Nu4 =  normal(vector(gp4,0))
    Nv4 =  normal(vector(0,gp4))
    Nu5 =  normal(vector(gp5,0))
    Nv5 =  normal(vector(0,gp5))
    Nu6 =  normal(vector(gp6,0))
    Nv6 =  normal(vector(0,gp6))
    Nu7 =  normal(vector(gp7,0))
    Nv7 =  normal(vector(0,gp7))
    Nu8 =  normal(vector(gp8,0))
    Nv8 =  normal(vector(0,gp8))
    Nu9 =  normal(vector(gp9,0))
    Nv9 =  normal(vector(0,gp9))
    Nu10 =  normal(vector(gp10,0))
    Nv10 =  normal(vector(0,gp10))
    Nu11 =  normal(vector(gp11,0))
    Nv11 =  normal(vector(0,gp11))
    Nu12 =  normal(vector(gp12,0))
    Nv12 =  normal(vector(0,gp12))

    EQUATIONS
    u: dx(sx)+ dy(sxy)=0          {equilibrium in the u-direction
}
    v: dx(sxy)+ dy(sy)+fy=0   {equilibrium in the v-direction }
    RESOLVE (sxy), (uw), (ex), (ey)

    BOUNDARIES
    region 1
    start 'outer' (0,0)
    load(u)=0 load(v)=0 line to (6*zt,0)
    value(u)=0 load(v)=0 line to (6*zt,-4*zt)
    value(u)=0 value(v)=0 line to (0,-4*zt)
    value(u)=0 load(v)=0 line to close
    start 'inner' (3*zt+rte,-zt)
    load(u)= Nu6 load(v)= Nv6 arc(center=3*zt,-zt) angle=15
    load(u)= Nu5 load(v)= Nv5 arc(center=3*zt,-zt) angle=15
    load(u)= Nu4 load(v)= Nv4 arc(center=3*zt,-zt) angle=15
    load(u)= Nu3 load(v)= Nv3 arc(center=3*zt,-zt) angle=15
    load(u)= Nu2 load(v)= Nv2 arc(center=3*zt,-zt) angle=15
    load(u)= Nu1 load(v)= Nv1 arc(center=3*zt,-zt) angle=15
    load(u)= Nu1 load(v)= Nv1 arc(center=3*zt,-zt) angle=15
    load(u)= Nu2 load(v)= Nv2 arc(center=3*zt,-zt) angle=15
    load(u)= Nu3 load(v)= Nv3 arc(center=3*zt,-zt) angle=15
```

```
    load(u)= Nu4 load(v)= Nv4 arc(center=3*zt,-zt) angle=15
    load(u)= Nu5 load(v)= Nv5 arc(center=3*zt,-zt) angle=15
    load(u)= Nu6 load(v)= Nv6 arc(center=3*zt,-zt) angle=15
    load(u)= Nu7 load(v)= Nv7 arc(center=3*zt,-zt) angle=15
    load(u)= Nu8 load(v)= Nv8 arc(center=3*zt,-zt) angle=15
    load(u)= Nu9 load(v)= Nv9 arc(center=3*zt,-zt) angle=15
    load(u)= Nu10 load(v)= Nv10 arc(center=3*zt,-zt) angle=15
    load(u)= Nu11 load(v)= Nv11 arc(center=3*zt,-zt) angle=15
    load(u)= Nu12 load(v)= Nv12 arc(center=3*zt,-zt) angle=15
    load(u)= Nu12 load(v)= Nv12 arc(center=3*zt,-zt) angle=15
    load(u)= Nu11 load(v)= Nv11 arc(center=3*zt,-zt) angle=15
    load(u)= Nu10 load(v)= Nv10 arc(center=3*zt,-zt) angle=15
    load(u)= Nu9 load(v)= Nv9 arc(center=3*zt,-zt) angle=15
    load(u)= Nu8 load(v)= Nv8 arc(center=3*zt,-zt) angle=15
    load(u)= Nu7 load(v)= Nv7 arc(center=3*zt,-zt) angle=15
    to close

    PLOTS
    elevation(gap,defangd) on "inner" export format "#1#b#2"
file="rst.txt" merge points=200
    elevation(x-3*zt, 1000*v) from (0,0) to (6*zt,0) export format
"#1#b#2" file="surface.txt" merge points=200
    vector(U,V) as "Displacement Field"
    END
End Sub
```

```
'########## Create .PDE file Routine ##########
Sub TCreate()
    Dim swpath As String
    swpath = ThisWorkbook.path
    Set fs = CreateObject("Scripting.FileSystemObject")
    Set a = fs.CreateTextFile(swpath & "\tbm10.pde", True)
    ''From here on the command a.Writeline ("") is used for every
line of the script, only the ones with input are shown here
    a.Writeline ("TITLE 'Stress Analysis'")
    '.............
    a.Writeline ("!input")
    a.Writeline ("E = " & 1000 * Range("B3"))
    a.Writeline ("nie = " & Range("B4"))
    a.Writeline ("niu = " & Range("B5"))
    a.Writeline ("k0 = " & Range("B6"))
    a.Writeline ("fy = " & Range("B7"))
    a.Writeline ("zt = " & Range("B8"))
    a.Writeline ("rte = " & Range("B9"))
    a.Writeline ("rti = " & Range("B10"))
    a.Writeline ("gw = " & Range("B1"))
    a.Writeline ("gwl = " & Range("B2"))
    '.............
    a.Writeline ("!transition and grout pressures")
    For i = 1 To 12
        a.Writeline ("gp" & i & "=" & ((Cells(i + 1, 15).Value +
Cells(i + 2, 15).Value) / 2))
    Next i
    '.............
    a.Writeline ("END")
    a.Close
End Sub
```

```
'########## Run the FlexPDE Calculation Routine ##########
Sub TRun()
    Application.ScreenUpdating = False
    Dim RetVal As Long
    Dim swpath As String
    swpath = ThisWorkbook.path
    RetVal = ShellExecute(0, "run", swpath & "\tbm10.pde")
End Sub
```

```
'########## Import FlexPDE Output Routine ##########
Sub TImport()
    Dim path As String
    Dim list() As String
    Dim spt() As String
    Dim gap() As String
    Dim ang() As String
    Dim rgap() As String
    Dim rang() As String
    Dim i As Integer, j As Integer
    Dim counter As Long, gapsum As Variant
    Dim Data As Variant
    Dim sett As Double
    path = ThisWorkbook.path & "\rst.txt"
    i = 1
    ''import data from the .txt output file
    Open path For Input As #1
    Do While Not EOF(1) '
        Line Input #1, Data
        If i > 7 Then   'read the results starting at line 7
            ReDim Preserve list(i - 8) As String
            list(i - 8) = Data  'write the results in the list
string
        End If
        i = i + 1
    Loop
    Close #1
    ''split the data into gap and angle results
    ReDim gap(UBound(list)) As String   'scale the vectors gap and
ang to the size of list
    ReDim ang(UBound(list)) As String
    For i = 0 To UBound(list)
        spt() = Split(RTrim(LTrim(list(i))), "  ")  'split each
line
        gap(i) = RTrim(LTrim(spt(0)))   'the first value will be
the gap
        ang(i) = RTrim(LTrim(spt(1)))   'the second value will be
the angle
    Next i
    ''find the points where the angles are close to the angles in
the spreadsheet
    For i = 0 To 12
        ReDim Preserve rang(i) As String
        ReDim Preserve rgap(i) As String
        rang(i) = Worksheets("TBM_GP").Cells(i + 2, 8)  'read the
reference angle in the spreadsheet
        counter = 0
        gapsum = 0
        For j = 0 To UBound(gap)
```

```
            If rang(i) > 0 Then     'check for values in a [+2; -
2] degrees range
                If ((ang(j) > rang(i) - 2) And (ang(j) < rang(i) +
2)) Then
                    counter = counter + 1
                    gapsum = gapsum + gap(j)
                End If
            Else    'adjust the negative angles to 0-360
                If (ang(j) > rang(i) + 360 - 2 And ang(j) <
rang(i) + 360 + 2) Then
                    counter = counter + 1
                    gapsum = gapsum + gap(j)
                End If
            End If
        Next j
        rgap(i) = gapsum / counter  'average of results in that
range
    Next i
    ''write the gap results in the spreadsheet
    For i = 0 To UBound(rgap)
    Cells(i + 2, 13) = (100 * rgap(i))
    Next i
    ''import the data on surface settlements
    Range("D2:E1000").ClearContents
    path = ThisWorkbook.path & "\surface.txt"
    With ActiveSheet.QueryTables.Add(Connection:="TEXT;" + path,
Destination:=Range("$D$2"))
        .RefreshStyle = xlOverwriteCells
        .TextFileStartRow = 9
        .TextFileTabDelimiter = True
        .Refresh BackgroundQuery:=False
    End With
    ''close the FlexPDE software and erase the files
    Application.Wait (Now + TimeValue("0:00:01"))
    Shell "TASKKILL /F /IM FlexPDE6s.exe", vbHide
    Application.Wait (Now + TimeValue("0:00:02"))
    Kill ThisWorkbook.path & "\tbm10.pde"
    Kill ThisWorkbook.path & "\tbm10.pg6"
    Kill ThisWorkbook.path & "\tbm10.log"
    Kill ThisWorkbook.path & "\tbm10.dbg"
    Kill ThisWorkbook.path & "\rst.txt"
    Kill ThisWorkbook.path & "\surface.txt"
End Sub
```

```
'########## Calculation Cycle Routine ##########
Sub TCycle()
    'the times depend on the processing speed of the computer
    'VBA has no control over the FlexPDE execution to wait for it
to finish
    Application.ScreenUpdating = False
    Application.Run ("TCreate") 'create the .PDE
    Application.Wait (Now + TimeValue("0:00:01"))
    Application.Run ("TRun")    'run the calculation
    Application.Wait (Now + TimeValue("0:00:02"))
    Application.Run ("TImport") 'import the results
End Sub
```

Annex D. Codes for Tunnel Analysis on Python

```
########## Analytical Grout Consolidation ##########
import math
#Parameters
gw = 10
gwl = 0
E= 45
pr = 0.3
k0 = 0.5
soilG = 20
Zt= 30
Rext = 5
Rlin = 4.85
grT = 0.5
grG = 20
kg= 0.00000001
ni= 0.4
nf= 0.3
Gp0= 500
dt= 100
tmax= 10000
refa= 5 #Angle interval
#Basic values
n = int(180/refa)
ang=[]
H=[]
L=[]
pwp = []
P0 = []
gap = (n+1)*[100*(Rext-Rlin)]
GP = (n+1)*[Gp0]
for i in range(n+1):
    ang.append(refa*i)
    H.append((1+math.cos(ang[i]*math.pi/180))*Rext) #Height along
tunnel
    L.append((ang[i]*math.pi/180)*Rext) #Lenght along perimeter
    pwp.append(max(0,gw*(Zt+Rext-H[i]+gwl)))    #Hydrostatic water
pressure
```

```
    P0.append((soilG*(Zt+Rext-H[i])*(math.sin((90-
ang[i])*math.pi/180)**2)) + (((((soilG*(Zt+Rext-H[i]))-
pwp[i])*k0)+pwp[i])*(math.cos((90-ang[i])*math.pi/180)**2)))
#Geostatic radial normal stress
for j in range (10):    #10 iteractions between gap and pressure
    for i in range(1, n+1): #Calculate initial gap and grout-
pressure
        gap[i-1]=100*(Rext-Rlin)+(100*(GP[i-1]-P0[i-
1])*Rext/(2*1000*(E/(2*(1+pr)))))
        GP[i] = GP[i-1]-(grT*(100/((gap[i-1]+gap[i])/2))*abs(L[i-
1]-L[i]))+(grG*(H[i-1]-H[i]))
        gap[i]=100*(Rext-Rlin)+(100*(GP[i]-
P0[i])*Rext/(2*1000*(E/(2*(1+pr)))))
gap0 = gap  #save initial gap
#vectors(L) of time, grout pressure, gap, average dr, filtered
grout
TL = [0]
GPL = [GP]
gapL = [gap]
drAvgL=[0]
XL=[[0]*len(GP)]
##calculation cycles##
T = 0
counter = 0
while T<tmax:
    xG=[]   #clear variables at each cycle
    GP1=[]
    GP2=[]
    gapG=[]
    xG += XL[len(XL)-1] #thickness of filtered grout from previous
stage
    GP1 += GPL[len(GPL)-1]  #grout pressure from previous stage
    GP2 += GP1  #grout pressure updated during iteractions
    gapG += gapL[len(gapL)-1]   #gap from previous stage
    #False position method
        #X variable = Grout pressure at tunnel roof
        #Y variable = Difference in average contraction due to
consolidation and due to grout pressure reduction
    #X1 - first point, equals the previous or initial stage
    #Y1 - negative value
    x1=Gp0-GP1[0]
    dx=[0]*len(GP1) #clear variable
    for i in range(len(GP1)):   #calculate average incremental
contraction due to grout consolidation
        if counter ==0: #for the first stage, assume analytical
equation for total grout thickness (dx)
            dx[i] = 100*math.sqrt(0.2*kg*(1-
ni)*(((GP1[i]+GP2[i])/2)-pwp[i])*dt/(ni-nf))
        else:   #for the following stages, calculate incremental
thickness (dx) with forward time, averaging with new values
            for j in range(15): #interactions to account for dx as
part of the dissipation length
                dx[i] = 1000*kg*(1-ni)*(((GP1[i]+GP2[i])/2)-
pwp[i])*dt/((xG[i]+(dx[i]/2))*(ni-nf))
    drAvg = (sum(dx)/len(dx))*((ni-nf)/(1-ni))  #average
incremental contraction = average dx * (ni-nf)/(1-ni)
    y1=-drAvg   #as first point equals the previous stage, dgap=0
    #X2 - second point, has to generate Y2>0
    x2 = x1 + 5
    GP = (n+1)*[Gp0-x2]
    gap = []    #clear variable
```

```
    gap = (n + 1) * [100*(Rext-Rlin)]
    for j in range (10):
        for i in range(1, n+1): #calculate new gap and grout
pressure
            gap[i-1]=100*(Rext-Rlin)+(100*(GP[i-1]-P0[i-
1])*Rext/(2*1000*(E/(2*(1+pr)))))
            GP[i] = GP[i-1]-(grT*(100/((gap[i-
1]+gap[i])/2))*abs(L[i-1]-L[i]))+(grG*(H[i-1]-H[i]))
            if pwp[i]>GP[i]:
                GP[i] = pwp[i]  #if GP<PWP, then force causing
consolidation stops
            gap[i]=100*(Rext-Rlin)+(100*(GP[i]-
P0[i])*Rext/(2*1000*(E/(2*(1+pr)))))
    GP2 = []    #clear variable
    GP2 += GP   #grout pressure updated during iteractions
    dgap = [abs(gapG[i]-gap[i]) for i in range(len(gap))]
#calculate incremental difference in gap from the previous stage
    dgap = sum(dgap)/len(dgap)  #average incremental gap variation
    dx=[0]*len(GP1) #clear variable
    for i in range(len(GP1)):
        if counter ==0: #calculate average incremental contraction
due to grout consolidation
            dx[i] = 100*math.sqrt(0.2*kg*(1-
ni)*(((GP1[i]+GP2[i])/2)-pwp[i])*dt/(ni-nf))
        else:
            for j in range(15):
                dx[i] = 1000*kg*(1-ni)*(((GP1[i]+GP2[i])/2)-
pwp[i])*dt/((xG[i]+(dx[i]/2))*(ni-nf))
    drAvg = (sum(dx)/len(dx))*((ni-nf)/(1-ni))
    y2 = dgap-drAvg
    while y2<0: #loop to guarantee that Y2 is positive
        x2 = 2*x2   #double the value of x2
        GP = (n+1)*[Gp0-x2]
        for j in range (10):
            for i in range(1, n+1):
                gap[i-1]=100*(Rext-Rlin)+(100*(GP[i-1]-P0[i-
1])*Rext/(2*1000*(E/(2*(1+pr)))))
                GP[i] = GP[i-1]-(grT*(100/((gap[i-
1]+gap[i])/2))*abs(L[i-1]-L[i]))+(grG*(H[i-1]-H[i]))
                if pwp[i]>GP[i]:
                    GP[i] = pwp[i]
                gap[i]=100*(Rext-Rlin)+(100*(GP[i]-
P0[i])*Rext/(2*1000*(E/(2*(1+pr)))))
        GP2 = []
        GP2 += GP
        dgap = [abs(gapG[i]-gap[i]) for i in range(len(gap))]
        dgap = sum(dgap)/len(dgap)
        dx=[0]*len(GP1)
        for i in range(len(GP1)):
            if counter ==0:
                dx[i] = 100*math.sqrt(0.2*kg*(1-
ni)*(((GP1[i]+GP2[i])/2)-pwp[i])*dt/(ni-nf))
            else:
                for j in range(15):
                    dx[i] = 1000*kg*(1-ni)*(((GP1[i]+GP2[i])/2)-
pwp[i])*dt/((xG[i]+(dx[i]/2))*(ni-nf))
        drAvg = (sum(dx)/len(dx))*((ni-nf)/(1-ni))
        y2 = dgap-drAvg
    #X3 - third point, find the root considering a line between X1
and X2
```

```
        #Because the model is linear, this will always find the
root in the first iteration
    x3 = x1-(y1*(x2-x1)/(y2-y1))
    GP = (n+1)*[Gp0-x3]
    for j in range (10):
        for i in range(1, n+1):
            gap[i-1]=100*(Rext-Rlin)+(100*(GP[i-1]-P0[i-
1])*Rext/(2*1000*(E/(2*(1+pr)))))
            GP[i] = GP[i-1]-(grT*(100/((gap[i-
1]+gap[i])/2))*abs(L[i-1]-L[i]))+(grG*(H[i-1]-H[i]))
            if pwp[i]>GP[i]:
                GP[i] = pwp[i]
            gap[i]=100*(Rext-Rlin)+(100*(GP[i]-
P0[i])*Rext/(2*1000*(E/(2*(1+pr)))))
    GP2 = []
    GP2 += GP
    dgap = [abs(gapG[i]-gap[i]) for i in range(len(gap))]
    dgap = sum(dgap)/len(dgap)
    dx=[0]*len(GP1)
    for i in range(len(GP1)):
        if counter ==0:
            dx[i] = 100*math.sqrt(0.2*kg*(1-
ni)*(((GP1[i]+GP2[i])/2)-pwp[i])*dt/(ni-nf))
        else:
            for j in range(15):
                dx[i] = 1000*kg*(1-ni)*(((GP1[i]+GP2[i])/2)-
pwp[i])*dt/((xG[i]+(dx[i]/2))*(ni-nf))
    drAvg = (sum(dx)/len(dx))*((ni-nf)/(1-ni))
    y3 = dgap-drAvg
    #Save Values
    for i in range(len(dx)):
        dx[i]=dx[i]+xG[i]
        if dx[i]>gap[i]:    #if thickness of filtered grout is
larger than gap, the process stops
            T=tmax+1000
            break
    TL.append(TL[len(TL)-1]+dt)
    GPL.append(GP2)
    gapL.append(gap)
    drAvgL.append(drAvgL[len(drAvgL)-1]+drAvg)
    XL.append(dx)
    T = T+dt
    counter = counter+1
##Save Output
g = open("...\\output.py", "w")
g.write("TL = "+str(TL))
g.write("\n")
g.write("GPL = "+str(GPL))
g.write("\n")
g.write("gapL = "+str(gapL))
g.write("\n")
g.write("drAvgL = "+str(drAvgL))
g.write("\n")
g.write("XL = "+str(XL))
g.write("\n")
g.write("T = "+str(T))
g.write("\n")
g.write("counter = "+str(counter))
g.write("\n")
g.write("pwp = "+str(pwp))
g.close()
```

Annex E. Codes for Tunnel Analysis on Plaxis

```
########## CREATE BASE FILE ##########
#Parameters
xt = 100
Zt = 30
Rext = 5.00
refa = 6
n = (360/refa)-1
#Connect to Plaxis Server
localhostport = 10000
plaxis_path = r'C:\Program Files (x86)\Plaxis\PLAXIS 2D'
save_path = r'F:'
import imp
import math
found_module = imp.find_module('plxscripting', [plaxis_path])
plxscripting = imp.load_module('plxscripting', *found_module)
from plxscripting.easy import *
localhostport_input = 10000
localhostport_output = 10001
s_i, g_i = new_server('localhost', localhostport_input )
s_o, g_o = new_server('localhost', localhostport_output )
#Start new file
s_i.new()
g_i.setproperties("WaterWeight", 10)
g_i.Soilcontour.initializerectangular(0,-120,200,0) #set model
dimensions
g_i.borehole(0)
g_i.borehole_1.Head=0   # set groundwater level
#stops the script so that the user can define the ground models
input("Insert the materials, then press enter to continue")
g_i.gotostructures()
exec('g_i.tunnel('+ str(xt) +','+ str(-Zt+Rext) +')')
for i in range (0,n): #define tunnel segments
    g_i.Tunnel_1.CrossSection.add()
        if n=0:

g_i.Tunnel_1.CrossSection.Segments[0].LineProperties.RelativeStart
Angle1 = 180
```

```
    exec('g_i.Tunnel_1.CrossSection.Segments['+ str(i)
+'].SegmentType = "Arc"')
    exec('g_i.Tunnel_1.CrossSection.Segments['+ str(i)
+'].ArcProperties.Radius = '+ str(Rext))
    exec('g_i.Tunnel_1.CrossSection.Segments['+ str(i)
+'].ArcProperties.CentralAngle = '+ str(refa))
for i in range (0,n): #define a perpendicular load and a negative
interface at each segment
    exec('g_i.lineload(g_i.Tunnel_1.SlicePolycurves['+ str(i)
+'])')
    exec('g_i.Tunnel_1.SlicePolycurves['+ str(i)
+'].LineLoad.Distribution = "Perpendicular"')
    exec('g_i.Tunnel_1.SlicePolycurves['+ str(i)
+'].LineLoad.qn_ref = 0')
    exec('g_i.neginterface(g_i.Tunnel_1.SlicePolycurves['+ str(i)
+'])')
    #the interface elemens are not really used in the calculation,
they are defines so that it is easier to import the results at the
nodes created around it.
g_i.generatetunnel(g_i.Tunnel_1)
g_i.gotomesh()
g_i.mesh(0.03)  #fine mesh
g_i.gotoflow()
g_i.gotostages()
g_i.phase(g_i.InitialPhase) #create new Phase_1
#set the tunnel clusters dry and deactivated
g_i.WaterConditions_1_2.Conditions[g_i.Phase_1] = "Dry"
g_i.WaterConditions_2_1.Conditions[g_i.Phase_1] = "Dry"
g_i.BoreholePolygon_1_2.deactivate(g_i.Phase_1)
g_i.BoreholePolygon_2_1.deactivate(g_i.Phase_1)
for i in range (1,n+1): #activate tunnel loads at Phase_1
    exec('g_i.Polycurve_'+ str(i) +'_1.activate(g_i.Phase_1)')
g_i.gotosoil()
g_i.gotostages()
g_i.save(".....Name.p2dx")
```

```
########## CALIBRATION STAGE ##########
#Parameters
Gp0 = 450
xt = 100
Zt = 30
Rext = 5.00
Rlin = 4.85
grT = 0.5
grG = 20
refa = 6
import winsound
import cycle
import math
n = int(360/refa)
gap = (n+1)*[20]
#run a calculation cycle for Gp0 at the tunnel roof
cycle.cycle(Gp0,gap, 1, xt, Rext, Rlin, Zt, grT, grG, refa)
GP = [] #clear variables
gap = []
GP += cycle.GP  #save the results from the calculation cycle
gap += cycle.gap
pwp = cycle.pwp
```

```
########## CONSOLIDATION STAGE ##########
#Parameters
Gp0 = 450
xt = 100
Zt = 30
Rext = 5.00
Rlin = 4.85
grT = 0.5
grG = 20
refa = 6
kg= 0.00000002
ni= 0.4
nf= 0.3
dt= 50
tmax= 1800
n = int(360/refa)
gap = []
GP = []
gap0 = []
import cycle
import math
print("Initial Cycle - Gp0 = "+str(Gp0))
gap = (n+1)*[20]    #run first calculation cycle = calibration
stage
cycle.cycle(Gp0,gap, 1, xt, Rext, Rlin, Zt, grT, grG, refa)
GP += cycle.GP
gap = []
gap += cycle.gap
gap0 += cycle.gap
pwp = cycle.pwp
print("Gap0: "+str(gap[1]))
#vectors(L) where the results of each time step are saved
TL = [0]
GPL = [GP]
gapL = [gap]
drAvgL=[0]
XL=[[0]*len(GP)]
#Start calculation cycles
T = 0
counter = 0
while T<tmax:
    print("")
    print("")
    print("Step: "+str(counter+1))
    xG=[]   #clear variables at each cycle
    GP1=[]
    GP2=[]
    gapG=[]
    xG += XL[len(XL)-1] #thickness of filtered grout from previous
stage
    GP1 += GPL[len(GPL)-1]  #grout pressure from previous stage
    GP2 += GP1  #grout pressure updated during iterations
    gapG += gapL[len(gapL)-1]   #gap from previous stage
    #False position method
        #X variable = Grout pressure at tunnel roof
        #Y variable = Difference in average contraction due to
consolidation and due to grout pressure reduction
    #X1 - first point, equals the previous or initial stage
    #Y1 - negative value
    x1=Gp0-GP1[0]
```

```
    dx=[0]*len(GP1) #clear variable
    for i in range(len(GP1)):   #calculate average incremental
contraction due to grout consolidation
        if counter ==0: #for the first stage, assume analytical
equation for total grout thickness (dx)
            dx[i] = 100*math.sqrt(0.2*kg*(1-
ni)*(((GP1[i]+GP2[i])/2)-pwp[i])*dt/(ni-nf))
        else:   #for the following stages, calculate incremental
thickness (dx) with forward time, averaging with new values
            for j in range(15): #interactions to account for dx as
part of the dissipation length
                dx[i] = 1000*kg*(1-ni)*(((GP1[i]+GP2[i])/2)-
pwp[i])*dt/((xG[i]+(dx[i]/2))*(ni-nf))
    drAvg = (sum(dx)/len(dx))*((ni-nf)/(1-ni))  #average
incremental contraction = average dx * (ni-nf)/(1-ni)
    y1=-drAvg   #as first point equals the previous stage, dgap=0
    print("   X1: "+str(x1))
    print("   DrAVG X1: "+str(drAvg))
    print("   Error Y1: "+str(y1))
    #X2 - second point, has to generate Y2>0
    x2 = x1 + 5
    gap = []    #clear variable
    gap += gapG
    cycle.cycle(Gp0-x2,gap, counter+2, xt, Rext, Rlin, Zt, grT,
grG, refa)  #calculate new gap and grout pressure
    GP2 = []
    GP2 += cycle.GP
    dgap = [abs(gapG[i]-gap[i]) for i in range(len(gap))]
#calculate incremental difference in gap from the previous stage
    dgap = sum(dgap)/len(dgap)  #average incremental gap variation
    dx=[0]*len(GP1) #clear variable
    for i in range(len(GP1)):
        if counter ==0: #calculate average incremental contraction
due to grout consolidation
            dx[i] = 100*math.sqrt(0.2*kg*(1-
ni)*(((GP1[i]+GP2[i])/2)-pwp[i])*dt/(ni-nf))
        else:
            for j in range(15):
                dx[i] = 1000*kg*(1-ni)*(((GP1[i]+GP2[i])/2)-
pwp[i])*dt/((xG[i]+(dx[i]/2))*(ni-nf))
    drAvg = (sum(dx)/len(dx))*((ni-nf)/(1-ni))
    y2 = dgap-drAvg
    print("")
    print("   X2: "+str(x2))
    print("   DrGap X2: "+str(dgap))
    print("   DrAVG X2: "+str(drAvg))
    print("   Error Y2: "+str(y2))
    while y2<0: #loop to guarantee that Y2 is positive
        x2 = x2 + 5 #increase the value of x2
        gap = []
        gap += gapG
        cycle.cycle(Gp0-x2,gap, counter+2, xt, Rext, Rlin, Zt,
grT, grG, refa)
        GP2 = []
        GP2 += cycle.GP
        dgap = [abs(gapG[i]-gap[i]) for i in range(len(gap))]
        dgap = sum(dgap)/len(dgap)
        dx=[0]*len(GP1)
        for i in range(len(GP1)):
            if counter ==0:
```

```
                dx[i] = 100*math.sqrt(0.2*kg*(1-
ni)*(((GP1[i]+GP2[i])/2)-pwp[i])*dt/(ni-nf))
            else:
                for j in range(15):
                    dx[i] = 1000*kg*(1-ni)*(((GP1[i]+GP2[i])/2)-
pwp[i])*dt/((xG[i]+(dx[i]/2))*(ni-nf))
        drAvg = (sum(dx)/len(dx))*((ni-nf)/(1-ni))
        y2 = dgap-drAvg
        print("")
        print("   X2: "+str(x2))
        print("   DrGap X2: "+str(dgap))
        print("   DrAVG X2: "+str(drAvg))
        print("   Error Y2: "+str(y2))
    if abs(y2)>(drAvg*0.05):    #if y2 is not a solution, error is
bigger than 5% the average contraction, then calculate X3
    #X3 - third point, find the root considering a line between X1
and X2
        y3 = 10000  #set a large error, to enter the while loop
        while abs(y3)>(drAvg*0.05): #repeat the calculation while
the error is larger than 5% the average contraction.
            x3 = x1-(y1*(x2-x1)/(y2-y1))
            gap = []
            gap += gapG
            cycle.cycle(Gp0-x3,gap, counter+2, xt, Rext, Rlin, Zt,
grT, grG, refa)
            GP2 = []
            GP2 += cycle.GP
            dgap = [abs(gapG[i]-gap[i]) for i in range(len(gap))]
            dgap = sum(dgap)/len(dgap)
            dx=[0]*len(GP1)
            for i in range(len(GP1)):
                if counter ==0:
                    dx[i] = 100*math.sqrt(0.2*kg*(1-
ni)*(((GP1[i]+GP2[i])/2)-pwp[i])*dt/(ni-nf))
                else:
                    for j in range(15):
                        dx[i] = 1000*kg*(1-
ni)*(((GP1[i]+GP2[i])/2)-pwp[i])*dt/((xG[i]+(dx[i]/2))*(ni-nf))
            drAvg = (sum(dx)/len(dx))*((ni-nf)/(1-ni))
            y3 = dgap-drAvg
            if y3>0:    #update the values of X1 or X2 depending
on the signal
                x2 = x3
                y2 = y3
            else:
                x1 = x3
                y1 = y3
            print("")
            print("   X3: "+str(x3))
            print("   DrGap X3: "+str(dgap))
            print("   DrAVG X3: "+str(drAvg))
            print("   Error Y3: "+str(y3))
    #Add to vectors at the end of each time step
    for i in range(len(dx)):
        dx[i]=dx[i]+xG[i]
    TL.append(TL[len(TL)-1]+dt)
    GPL.append(GP2)
    gapL.append(gap)
    drAvgL.append(drAvgL[len(drAvgL)-1]+drAvg)
    XL.append(dx)
    T = T+dt
```

```
    counter = counter+1
    ##Save Output at the end of each time step.
    g = open('consolidation_results.py', 'w')
    g.write("TL = "+str(TL))
    g.write("\n")
    g.write("GPL = "+str(GPL))
    g.write("\n")
    g.write("gapL = "+str(gapL))
    g.write("\n")
    g.write("drAvgL = "+str(drAvgL))
    g.write("\n")
    g.write("XL = "+str(XL))
    g.write("\n")
    g.write("T = "+str(T))
    g.write("\n")
    g.write("counter = "+str(counter))
    g.write("\n")
    g.write("pwp = "+str(pwp))
    g.close()
```

```
########## CYCLE SUB-ROUTINE ##########
def cycle(Gp0,gpp0,NPhase,xt,Rext,Rlin,Zt,grT,grG,refa):
    #Parameters are defined when the sub-routine is called.
    import math
    import fea
    global gap
    global GP
    global pwp
    n = int(360/refa)
    ang=[]
    H=[]
    L=[]
    GP = (n+1)*[Gp0]
    gap=[]
    gap = gpp0
    for i in range(n+1):
        ang.append(refa*i)
        H.append((1+math.cos(ang[i]*math.pi/180))*Rext) #Height
along tunnel
        L.append((ang[i]*math.pi/180)*Rext) #Lenght along
perimeter
    err = 100   #set a large error, to enter the while loop
    while (err>0.05):   #repeat the calculation while the maximum
difference at any node between the gaps calculated at two
consecutive iterations is larger than 0.5mm.
        for i in range(1, n+1): #Calculate profile of grout-
pressures from roof to invert (0 to 180°)
            GP[i] = GP[i-1]-(grT*(100/((gap[i-
1]+gap[i])/2))*abs(L[i-1]-L[i]))+(grG*(H[i-1]-H[i]))
        GP[n] = GP[0]
        for i in range(n-1, int(n/2), -1): #Calculate profile of
grout-pressures from invert to roof (180° to 360°)
            GP[i] = GP[i+1]-
(grT*(100/((gap[i+1]+gap[i])/2))*abs(L[i]-L[i+1]))-(grG*(H[i]-
H[i+1]))
        fea.fea(GP, NPhase, xt, -Zt, Rext, Rlin, refa) #call a
Plaxis calculation with this profile of grout pressures
        gap1 = fea.gap  #import back the gap and pwp
        pwp = fea.pwp
        err = abs(gap1[0]-gap[0])   #calculate error
```

```
        for i in range(len(gap)):
            if abs(gap1[i]-gap[i])>err:
               err = abs(gap1[i]-gap[i])
            gap[i]=gap1[i]
        print("       GPxGap Error: "+str(err))
    #Save output
    a = open('results_boundary.txt', 'w')
    for i in range(len(GP)):
        a.write(str(gap[i]))
        a.write("\t")
        a.write(str(pwp[i]))
        a.write("\t")
        a.write(str(GP[i]))
        a.write("\n")
    a.close()
```

```
########## FEA SUB-ROUTINE ##########
def fea(GP, NPhase, xt, yt, rte, rti, refa):
    #Connect to Plaxis Server
    #The commands to import the script are different between the
script and a sub-routine
    localhostport = 10000
    plaxis_path = r'C:\Program Files (x86)\Plaxis\PLAXIS 2D'
    save_path = r'F:'
    import imp
    import math
    found_module = imp.find_module('plxscripting', [plaxis_path])
    plxscripting = imp.load_module('plxscripting', *found_module)
    from plxscripting.server import Server, InputProcessor
    from plxscripting.connection import HTTPConnection
    from plxscripting.plxproxyfactory import PlxProxyFactory
    from plxscripting.plxproxy import PlxProxyObject
    from plxscripting.image import TYPE_NAME_IMAGE, create_image
    def new_server(address, port, timeout=5.0):
        ip = InputProcessor()
        conn = HTTPConnection(address, port, timeout)
        pf = PlxProxyFactory(conn)
        s = Server(conn, pf, ip)

s.result_handler.register_json_constructor(TYPE_NAME_IMAGE,
create_image)
        return s, s.plx_global
    localhostport_input = 10000
    localhostport_output = 10001
    s_i, g_i = new_server('localhost', localhostport_input )
    s_o, g_o = new_server('localhost', localhostport_output )
    global gap
    global pwp
    n = int(360/refa)
    z = g_i.Phases.count()  #Create the new phase if necessary
    z = [int(s) for s in z.split() if s.isdigit()]
    z = int(z[0])
    if NPhase+1 > z:
        exec('g_i.phase(g_i.Phase_' + str(NPhase-1)+')')
        exec('g_i.Phase_' +
str(NPhase)+'.Deform.UseDefaultIterationParams = False')
        exec('g_i.Phase_' +
str(NPhase)+'.Deform.MaxLoadFractionPerStep = 0.9')
    else:
```

```
        exec('g_i.Phase_1.Deform.UseDefaultIterationParams =
False')
        exec('g_i.Phase_1.Deform.MaxLoadFractionPerStep = 0.9')

    for i in range (0, n):      ##New Grout Pressures
        # The way Plaxis defines the indexes for the line loads is
different from the indexes of the segments, so a mathematical
formula is used here to correctly position the loads
        if (i % 2) == 0:
            exec('g_i.LineLoad_'+ str(i+1)
+'_1.qn_ref[g_i.Phase_'+ str(int(NPhase)) +'] = (GP[' + str(n-
((i+1)//2)-1) +']+GP[' + str(n-((i+1)//2)) +'])/2')
        else:
            exec('g_i.LineLoad_'+ str(i+1)
+' 1.qn ref[g i.Phase '+ str(int(NPhase)) +'] = (GP[' +
str(((i+1)//2)-1) +']+GP[' + str(((i+1)//2)) +'])/2')
    exec('g_i.Phase_'+ str(int(NPhase)) +'.ShouldCalculate =
True')
    g_i.calculate() #Run calculation
    g_i.save("....Name.p2dx")   #Save file
    exec('g_i.view(g_i.Phase_'+ str(int(NPhase)) +')')  ## Import
Values
    #Coordinates and displacements along the interface
    x = str('g_o.getresults(g_o.Phase_'+ str(int(NPhase)) +',
g_o.Interface.X, "node")')
    y = str('g_o.getresults(g_o.Phase_'+ str(int(NPhase)) +',
g_o.Interface.Y, "node")')
    u = str('g_o.getresults(g_o.Phase_'+ str(int(NPhase)) +',
g_o.Interface.Ux, "node")')
    v = str('g_o.getresults(g_o.Phase_'+ str(int(NPhase)) +',
g_o.Interface.Uy, "node")')
    pwp0 = str('g_o.getresults(g_o.Phase_'+ str(int(NPhase)) +',
g_o.Interface.PWater, "node")')
    x = eval(x)
    y = eval(y)
    u = eval(u)
    v = eval(v)
    pwp0 = eval(pwp0)
    x=list(x)   #list the values
    y=list(y)
    u=list(u)
    v=list(v)
    pwp0=list(pwp0)
    g o.close() #close the output program
    ang0=[]
    gap0=[]
    for i in range(0, len(x)):  #calculate the angles based on the
coordinates
        pwp0[i]=-1*pwp0[i]
        gap0.append(100*(math.sqrt(((x[i]+u[i]-
xt)**2)+((y[i]+v[i]-yt)**2))-rti))   #calculate the soil lining
gap
        if (x[i]-xt==0) or (y[i]-yt==0):
            if (x[i]-xt==0):
                if (y[i]-yt>0):
                    ang0.append(0)
                else:
                    ang0.append(180)
            else:
                if (x[i]-xt>0):
                    ang0.append(90)
```

```
                else:
                    ang0.append(270)
        else:
            if (x[i]-xt>0):
                ang0.append(90-(math.atan((y[i]-yt)/(x[i]-
xt))*180/math.pi))
            else:
                ang0.append(270-(math.atan((y[i]-yt)/(x[i]-
xt))*180/math.pi))
    ang1=[]     #remove angle duplicates
    joint=[]
    for i in range(0,len(gap0)):
        if ang0[i] not in ang1:
            ang1.append(ang0[i])
            joint.append([ang0[i],gap0[i],pwp0[i]])
    joint.sort(key=lambda x: x[0])  #order values in terms of the
angle
    ang2, gap2, pwp2 = zip(*joint)
    ang2 = list(ang2)
    gap2 = list(gap2)
    pwp2 = list(pwp2)
    angref=[]   #interpolate to reference angles
    gap=[]
    pwp=[]
    angref.append(0)
    gap.append(gap2[len(ang2)-1]+(((360-ang2[len(ang2)-
1])*(gap2[0]-gap2[len(ang2)-1]))/((ang2[0]+360)-ang2[len(ang2)-
1])))
    pwp.append(pwp2[len(ang2)-1]+(((360-ang2[len(ang2)-
1])*(pwp2[0]-pwp2[len(ang2)-1]))/((ang2[0]+360)-ang2[len(ang2)-
1])))
    for i in range(1,n):
        angref.append(i*refa)
        a = ang2.index(min([element for element in ang2 if element
> angref[i]]))
        gap.append(gap2[a-1] + (((angref[i]-ang2[a-1])*(gap2[a]-
gap2[a-1]))/(ang2[a]-ang2[a-1])))
        pwp.append(pwp2[a-1] + (((angref[i]-ang2[a-1])*(pwp2[a]-
pwp2[a-1]))/(ang2[a]-ang2[a-1])))
    angref.append(360)
    gap.append(gap[0])
    pwp.append(pwp[0])
```

```
########## SETTLEMENTS ROUTINE ##########
#Save the surface settlements, after all the calculations are done
#Connect to Plaxis
localhostport = 10000
plaxis_path = r'C:\Program Files (x86)\Plaxis\PLAXIS 2D'
save_path = r'F:'
import imp
import math
found_module = imp.find_module('plxscripting', [plaxis_path])
plxscripting = imp.load_module('plxscripting', *found_module)
from plxscripting.easy import *
localhostport_input = 10000
localhostport_output = 10001
s_i, g_i = new_server('localhost', localhostport_input )
s_o, g_o = new_server('localhost', localhostport_output )
k=0
while k==0:
```

```
    NPhase = input("Type in the Phase Number:  ")   #ask for the
Phase to be imported
    eval("g_i.view(g_i.Phase_"+ NPhase +")")
    g_i.view(g_i.Phase_1)
    xS = eval('g_o.getresults(g_o.Phase_'+ NPhase +', g_o.Soil.X,
"node")')
    yS = eval('g_o.getresults(g_o.Phase_'+ NPhase +', g_o.Soil.Y,
"node")')
    vS = eval('g_o.getresults(g_o.Phase_'+ NPhase +', g_o.Soil.Uy,
"node")')
    xS=list(xS)
    yS=list(yS)
    vS=list(vS)
    g_o.close()
    xvjoint=[]
    xS2=[]
    for i in range(0, len(xS)): #remove duplicates
        if yS[i]==0 and (xS[i] not in xS2):
            xS2.append(xS[i])
            xvjoint.append([xS[i],vS[i]])
    xvjoint.sort(key=lambda x: x[0])    #order values based on
horizontal coordinate
    xS, vS = zip(*xvjoint)
    #Save output
    g = eval(str(r'open("results_surface'+ NPhase +'.txt", "w")'))
    for i in range(0, len(xS)):
        g.write(str(xS[i]))
        g.write("\t")
        g.write(str(1000*vS[i]))
        g.write("\n")
    g.close()
```

```
########## IMPORT SETTLEMENTS AT LD ROUTINE ##########
localhostport = 10000
plaxis_path = r'C:\Program Files (x86)\Plaxis\PLAXIS 2D'
save_path = r'C:'
import imp
import math
found_module = imp.find_module('plxscripting', [plaxis_path])
plxscripting = imp.load_module('plxscripting', *found_module)
from plxscripting.easy import *
localhostport_input = 10000
localhostport_output = 10001
s_i, g_i = new_server('localhost', localhostport_input )
s_o, g_o = new_server('localhost', localhostport_output )
g_i.view(g_i.Phase_1)
n = 40
Xt = 100
Zp = [22.5, 22.5, 22.5, 37.5, 37.5]
Ld = [0, 7.5, 15, 7.5, 15]
for j in range(len(Zp)):
    y = []
    v = []
    for i in range(n+1):
        y.append(i*(Zp[j]/n))
        pv = eval("g_o.getsingleresult(g_o.Phase_1,
g_o.Soil.Uy,(Xt+"+str(Ld[j])+", -i*("+str(Zp[j])+"/n)))")
        pv=1000*eval(pv)
        v.append(pv)
    f = eval(str(r'open("settlements'+ str(j) +'.txt", "w")'))
```

```
    for i in range(len(y)):
        f.write(str(y[i]/Zp[j]))
        f.write("\t")
        f.write(str(v[i]))
        f.write("\n")
    f.close()
g_o.close()
```

References

ABNT, 2010. NBR 6122: Design and construction of foundations. Rio de Janeiro, Brazil.

Abu-Farsakh, M.Y., Voyiadjis, G.Z., 1999. Computational model for the simulation of the shield tunneling process in cohesive soils. International Journal of Numerical and Analytical Methods in Geomechanics 23, 23–44.

Ali, H., Reiffsteck, P., Baguelin, F., van de Graaf, H., Bacconnet, C., Gourves, R., 2010. Settlement of pile using cone loading test: Load settlement curve approach. CPT'10 - 2nd International Symp. Cone Penetration Test.

Altaee, A., Evgin, E., Fellenius, B.H., 1992. Axial load transfer for piles in sand II. Numerical analysis. Canadian Geotechnical Journal 29, 21–30. doi:10.1139/t92-003

Bairoch, P., Goertz, G., 1986. Factors of Urbanisation in the Nineteenth Century Developed Countries: A Descriptive and Econometric Analysis. Urban Studies 23, 285–305. doi:10.1080/00420988620080351

Basile, F., 2014. Effects of tunnelling on pile foundations. Soils and Foundations 54, 280–295. doi:10.1016/j.sandf.2014.04.004

Basile, F.B.J., 2011. Pile-group response due to tunnelling, in: Viggiani, G. (Ed.), Geotechnical Aspects of Underground Construction in Soft Ground - 7th International Symposium (IS-Rome). CRC Press/Balkema, Leiden, Rome, Italy.

Benton, L.J., Phillips, A., 1991. The behaviour of two tunnels beneath a building on piled foundations, in: 10th European Conference on Soil Mechanics and Foundation Engineering. Florence, Italy, pp. 665–668.

Bernat, S., Cambou, B., Dubois, P., 1999. Assessing a soft soil tunnelling numerical model using field data. Géotechnique 49, 427–452.

Bezuijen, A., 2013. Modelling of Foam-Sand-TBM Interaction, in: Meschke, G., Eberhardsteiner, J., Schanz, T., Soga, K., Thewes, M. (Eds.), EURO:TUN 2013 - 3rd International Conference on Computational Methods in Tunnelling and Subsurface Engineering. Bochum, Germany.

Bezuijen, A., 2009. The influence of grout and bentonite slurry on the process of TBM tunnelling. Geomechanics and Tunnelling 2, 294–303. doi:10.1002/geot.200900025

Bezuijen, A., 2007. Bentonite and grout flow around a TBM, in: Barták, Hrdina, Romancov, Zlámal (Eds.), ITA World Tunnel Congress 2007 - Underground

Space – The 4th Dimension of Metropolises. Prague, Czech Republic, pp. 383–388.

Bezuijen, A., 2002. The influence of soil permeability on the properties of a foam mixture in a TBM, in: Geotechnical Aspects of Underground Construction in Soft Ground - 4th International Symposium (IS-Toulouse). Toulouse, France, pp. 221–226.

Bezuijen, A., Pruiksma, J.P., van Meerten, H.H., 2001. Pore pressures in front of tunnel, measurements, calculations and consequences for stability of tunnel face, in: Adachi, T., Kimura, M., Tateyama, K. (Eds.), International Symposium on Modern Tunneling Science and Technology. Kyoto, Japan.

Bezuijen, A., Schaminee, P.E.L., Kleinjan, J.A., 1999. Additive testing for earth pressure balance shields, in: 12th European Conference on Soil Mechanics and Geotechnical Engineering. Amsterdam, the Netherlands.

Bezuijen, A., Talmon, A.M., 2008. Processes around a TBM, in: Ng, C.W.W., Huang, H.W., Liu, G.B. (Eds.), Geotechnical Aspects of Underground Construction in Soft Ground - 6th International Symposium (IS-Shanghai). CRC Press/Balkema, Leiden, Shanghai, China, pp. 3–13.

Bezuijen, A., Talmon, A.M., 2003. Grout, the foundation of a bored tunnel, in: BGA International Conference on Foundations. Dundee, Scotland.

Bezuijen, A., Talmon, A.M., Kaalberg, F.J., Plugge, R., 2004. Field measurements of grout pressures during tunnelling of the Sophia Rail Tunnel. Soils and Foundations 44, 39–48.

Bezuijen, A., van der Schrier, J.S., 1994. The influence of a bored tunnel on pile foundations, in: Lee, F.H., Leung, C.F., Tan, T.S. (Eds.), Centrifuge 94. Taylor & Francis, Rotterdam, The Netherlands, pp. 127–132.

Bezuijen, A., van der Zon, W.H., 2005. Laboratory testing of grout properties and their influence on backfill grouting, in: ITA World Tunnel Congress 2005 - Underground Space Use. Analysis of the Past and Lessons for the Future. Istanbul, Turkey.

Bica, A.V.D., Prezzi, M., Seo, H., Salgado, R., Kim, D., 2014. Instrumentation and axial load testing of displacement piles. Proceedings ICE - Geotechnical Engineering 167, 238–252. doi:10.1680/geng.12.00080

Boonsiri, I., Takemura, J., 2015. Observation of Ground Movement with Existing Pile Groups Due to Tunneling in Sand Using Centrifuge Modelling. Geotechnical and Geological Engineering 621–640. doi:10.1007/s10706-015-9845-0

Boonsiri, I., Takemura, J., 2014. Behavior of pile group response to adjacent tunneling in sand using centrifuge modeling, in: Gaudin, White (Eds.), 8th International Conference on Physical Modelling in Geotechnics. Perth, Australia, pp. 697–703.

Borghi, X., White, D.J., Bolton, M.D., Springman, S., 2001. Empirical pile design based on cone penetrometer data : an explanation for the reduction of unit base resistance between CPTs and piles, in: 5th International Conference on Deep Foundation Practice. Singapore, pp. 125–132.

Briaud, J.L., Tucker, L., 1984. Piles in Sand: A Method Including Residual Stresses. Journal of Geotechnical Engineering doi:10.1061/(ASCE)0733-9410(1984)110:11(1666)

Brinkgreve, R.B.J., Engin, E., Engin, H.K., 2010. Validation of empirical formulas to derive model parameters for sands, in: Benz, Nordal (Eds.), 7th European Conference on Numerical Methods in Geotechnical Engineering. Trondheim, Norway, pp. 137–142.

Brinkgreve, R.B.J., Engin, E., Swolfs, W.M., 2013. Plaxis 2D 2012 Material Models Manual.

Broere, W., Dijkstra, J., 2008. Investigating the influence of tunnel volume loss on piles using photoelastic techniques, in: Ng, C.W.W., Huang, H.W., Liu, G.B. (Eds.), Geotechnical Aspects of Underground Construction in Soft Ground - 6th International Symposium (IS-Shanghai). CRC Press/Balkema, Leiden, Shanghai, China, pp. 621–626.

Burland, J.B., Wroth, C.P., 1974. Settlements of Buildings and Associated Damage, in: Conference on Settlement of Structures. Cambridge, UK.

Chen, L.T., Poulos, H.G., Loganathan, N., 1999. Pile responses caused by tunneling. Journal of Geotechnical and Geoenvironmental Engineering 125, 207–215.

Cheng, C.Y., 2003. Finite element study of tunnel-soil-pile interaction. MEng thesis, National University of Singapore.

Cheng, C.Y., Dasari, G.R., Chow, Y.K., Leung, C.F., 2007. Finite element analysis of tunnel–soil–pile interaction using displacement controlled model. Tunnelling and Underground Space Technology 22, 450–466. doi:10.1016/j.tust.2006.08.002

Cheng, C.Y., Dasari, G.R., Leung, C.F., Chow, Y.K., Rosser, H.B., 2004. 3D Numerical Study of Tunnel-Soil-Pile Interaction, in: ITA World Tunnel Congress 2004 - Underground Space for Sustainable Urban Development. Singapore.

Chin, F.K., 1970. Estimation of the ultimate load of piles not carried to failure, in: SEAGC - 2nd Southeast Asia Conference on Soil Engineering. pp. 81–90.

Chung, K.H., Mair, R.J., Choy, C.K., 2006. Centrifuge modelling of pile-tunnel interaction, in: Ng, C.. W.. W.., Wang, Y.. H.., Zhang, L.. M.. (Eds.), 6th International Conference on Physical Modelling in Geotechnics. Hong Kong, pp. 1151–1156.

Comodromos, E.M., Anagnostopoulos, C.T., Georgiadis, M.K., 2003. Numerical assessment of axial pile group response based on load test. Computers and Geotechnics 30, 505–515. doi:10.1016/S0266-352X(03)00017-X

Coutts, D.R., Wang, J., 2000. Monitoring of reinforced concrete piles under horizontal and vertical loads due to tunnelling, in: Zhao, J., Shirlaw, J.N., Krishnan, R. (Eds.), International Conference on Tunnels and Underground Structures. Singapore, pp. 541–546.

Coyle, H.M., Reese, L.C., 1966. Load Transfer for Axially Loaded Piles in Clay. Journal of the Soil Mechanics and Foundations Engineering Division. - ASCE 92, 1–26.

Cultural Heritage Agency of the Netherlands, 2016. Funderingstechniek. [WWW Document]. URL http://cultureelerfgoed.adlibsoft.com /harvest/bot/vademecum_16.xml (accessed 23.12.16)

Devriendt, M., Williamson, M., 2011. Validation of methods for assessing tunnelling-induced settlements on piles. Ground Engineering March 2011.

Dias, D., Kastner, R., Maghazi, M., 1999. Three dimensional simulation of slurry shield tunnelling, in: Kusakabe, O., Fujita, K., Miyazaki, Y. (Eds.), Geotechnical Aspects of Underground Construction in Soft Ground - 3rd International Symposium (IS-Tokyo). Tokyo, Japan, pp. 351–356.

Dias, T.G.S., Bezuijen, A., 2016. A Different View on TBM Face Equilibrium in Permeable Ground, in: ITA World Tunnel Congress 2016 - Uniting an Industry. Society for Mining, Metallurgy, and Exploration (SME), San Francisco, USA. doi:10.13140/RG.2.1.2223.6561

Dias, T.G.S., Bezuijen, A., 2015a. Data Analysis of Pile Tunnel Interaction. Journal of Geotechnical and Geoenvironmental Engineering 141. doi:10.1061/(ASCE)GT.1943-5606.0001350

Dias, T.G.S., Bezuijen, A., 2015b. A New Teaching Concept for Axially Loaded Piles, in: Manzanal, D., Sfriso, A.O. (Eds.), 15th Pan-American Conference on Soil Mechanics and Geotechnical Engineering - From Fundamentals to Applications in Geotechnics. IOS Press, Buenos Aires, Argentina, pp. 1774–1781. doi:10.3233/978-1-61499-603-3-1774

Dias, T.G.S., Bezuijen, A., 2015c. TBM Pressure Models - Observations, Theory and Practice, in: Sfriso, A.O., Manzanal, D., Rocca, R.J. (Eds.), 15th Pan-American Conference on Soil Mechanics and Geotechnical Engineering - Geotechnical Synergy in Buenos Aires 2015 - Invited Lectures. IOS Press, Buenos Aires, Argentina, pp. 347–374. doi:10.3233/978-1-61499-599-9-347

Dias, T.G.S., Bezuijen, A., 2015d. TBM Pressure models: Calculation tools, in: Kolíc, D. (Ed.), ITA World Tunnel Congress 2015 - SEE Tunnel - Promoting Tunnelling in SEE Region. Dubrovnik, Croatia. doi:10.13140/RG.2.1.1780.4962

Dias, T.G.S., Bezuijen, A., 2014a. Pile Tunnel Interaction: Literature review and data analysis, in: Negro, A., Cecílio Jr., M.O., Bilfinger, W. (Eds.), ITA World Tunnel Congress 2014 - Tunnels for a Better Life. Foz do Iguaçu, Brazil. doi:10.13140/2.1.4372.7040

Dias, T.G.S., Bezuijen, A., 2014b. Pile-Tunnel Interaction: A conceptual analysis, in: Yoo, C., Park, S., Kim, B., Ban, H. (Eds.), Geotechnical Aspects of Underground Construction in Soft Ground - 8th International Symposium (IS-Seoul). CRC Press/Balkema, Leiden, Seoul, South Korea, pp. 251–255. doi:10.1201/b17240-47

Dias, T.G.S., Bezuijen, A., 2014c. Tunnel modelling: Stress release and constitutive aspects, in: Yoo, C., Park, S.-W., Kim, B., Ban, H. (Eds.), Geotechnical Aspects of Underground Construction in Soft Ground - 8th International Symposium (IS-Seoul). CRC Press/Balkema, Leiden, Seoul, South Korea, pp. 197–202. doi:10.1201/b17240-37

Dias, T.G.S., Farias, M.M., Assis, A.P., 2015. Large diameter shafts for underground infrastructure. Tunnelling and Underground Space Technology 45, 181–189. doi:10.1016/j.tust.2014.09.010

Dijk, B.F.J., Kaalberg, F.J., 1998. 3-D Geotechnical Model for the North/Southline in Amsterdam, in: Proceedings of the 4th European Conference on Numerical Methods in Geotechnical Engineering (NUMGE '98). Udine, Italy, pp. 739-749. doi:10.1007/978-3-7091-2512-0_71

Dijkstra, J., Broere, W., Heeres, O.M., 2011. Numerical simulation of pile installation. Computers and Geotechnics 38, 612–622. doi:10.1016/j.compgeo.2011.04.004

Ding, W.Q., Yue, Z.Q., Tham, L.G., Zhu, H.H., Lee, C.F., Hashimoto, T., 2004. Analysis of shield tunnel. International Journal for Numerical and Analytical Methods in Geomechanics 28, 57–91. doi:10.1002/nag.327

Elshafie, M., Choy, C.K., Mair, R.J., 2013. Centrifuge Modeling of Deep Excavations and Their Interaction With Adjacent Buildings. Geotechnical Testing Journal 36.

Engin, H.K., Brinkgreve, R.B.J., van Tol, A.F., 2011. Numerical analysis of installation effects of pile jacking in sand, in: Pietruszczak, S., Pande, G. (Eds.), 2nd International Symposium on Computational Geomechanics. Cavtat-Dubrovnik, Croatia, pp. 744–755.

Farrell, R.P., Mair, R.J., 2011. Centrifuge modelling of the response of buildings to tunnelling, in: Viggiani, G. (Ed.), Geotechnical Aspects of Underground Construction in Soft Ground - 7th International Symposium (IS-Rome). CRC Press/Balkema, Leiden, Rome, Italy, pp. 343–351.

Fellenius, B.H., 2002a. Determining the Resistance Distribution in Piles Part 1. Notes on Shift of No-Load Reading and Residual Load. Geotechnical News Magazine 20, 35–38.

Fellenius, B.H., 2002b. Determining the Resistance Distribution in Piles Part 2. Method for Determining the Residual Load. Geotechnical News Magazine 20, 25–29.

Fellenius, B.H., 1999. Bearing capacity of footings and piles—A delusion ?, in: Deep Foundation Institute. Dearborn, USA.

Feng, S., 2004. Centrifuge modelling of tunnel-pile interaction. MEng thesis, National University of Singapore.

Feng, S.H., Leung, C.F., Chow, Y.K., Dasari, G.R., 2002. Centrifuge modeling of pile responses due to tunneling, in: 15th Symposium on Civil Engineering. Singapore.

Finno, R.J., Clough, G.W., 1985. Evaluation of soil response to EPB shield tunneling. Journal of Geotechnical Engineering 111, 155–173.

Fioravante, V., 2002. On the shaft friction modelling of non-displacement piles in sand. Soils and Foundations 42, 23–33.

Fischer, K.A., Sheng, D., Abbo, A.J., 2007. Modeling of pile installation using contact mechanics and quadratic elements. Computers and Geotechnics 34, 449–461. doi:10.1016/j.compgeo.2007.01.003

Fleming, K., Weltman, A., Randolph, M.F., Elson, K., 2008. Piling engineering, 2nd ed. Blackie and Son, Glasgow, UK.

Fleming, W.G.K., 1992. A new method for single pile settlement prediction and analysis. Géotechnique 42, 411–425.

Forth, R.A., Thorley, C.B.B., 1996. Hong Kong Island Line - Predictions and performance, in: Mair, R.J., Taylor, R.N. (Eds.), Geotechnical Aspects of Underground Construction in Soft Ground - 2nd International Symposium (IS-London). A.A. Balkema, Rotterdam, London, UK.

Frank, R., Kalteziotis, N., Bustamante, M., Christoulas, S., Zervogiannis, H., 1991. Evaluation of performance of two piles using pressuremeter method. Journal of Geotechnical Engineering 117, 695–713.

Franza, A., Idinyang, S., Heron, C.M., Marshall, A.M., 2016. Development of a coupled centrifuge-numerical model to study soil-structure interaction problems, in: Proceedings of the 3rd European Conference on Physical Modelling in Geotechnics (Eurofuge 2016). pp. 135–140.

Franza, A., Marshall, A.M., 2016. Centrifuge modelling of piled structure response to tunnelling, in: Proceedings of the 3rd European Conference on Physical Modelling in Geotechnics (Eurofuge 2016).

Gens, A., Potts, D.M., 1988. Critical state models in computational geomechanics. Engineering with Computers 5, 178–197. doi:10.1108/eb023736

Ghahremannejad, B., Surjadinata, J., Poon, B., Carter, J.P., 2006. Effects of tunneling on model pile foundations, in: Ng, C.. W.. W.., Wang, Y.. H.., Zhang, L.. M.. (Eds.), 6th International Conference on Physical Modelling in Geotechnics. pp. 1157–1162. doi:10.1201/NOE0415415866.ch170

Ghazavi, M., 2001. Influence of Tunnelling in Soft Soils on Axial Response of Piles, in: 5th Iranian Tunnelling Conference. Tehran, Iran.

Gitirana Jr, G., Fredlund, D.G., 2003. Analysis of Transient Embankment Stability Using the Dynamic Programming Method, in: 56th Canadian Geotechnical Conference.

Glisic, B., Inaudi, D., Nan, C., 2002. Pile Monitoring with Fiber Optic Sensors During Axial Compression, Pullout, and Flexure Tests. Transportation Research Record 1808, 11–20. doi:10.3141/1808-02

Guglielmetti, V., Grasso, P., Mahtab, A., Xu, S. (Eds.), 2007. Mechanized tunnelling in urban areas: design methodology and construction control. Taylor & Francis, Leiden.

Guo, W.D., Randolph, M.F., 1998. Rationality of load transfer approach for pile analysis. Computers and Geotechnics 23, 85–112. doi:10.1016/S0266-352X(98)00010-X

Guo, W.D., Randolph, M.F., 1997. Vertically loaded piles in non-homogeneous media. International Journal for Numerical and Analytical Methods in Geomechanics 21, 507–532.

Hartono, E., Leung, C.F., Shen, R.F., Chow, Y.K., Ng, Y.S., Tan, H.T., Hua, C.J., 2014. Behaviour of pile above tunnel in clay, in: Gaudin, White (Eds.), 8th International Conference on Physical Modelling in Geotechnics. Perth, Australia, pp. 833–838.

Henke, S., 2010. Influence of pile installation on adjacent structures. International Journal for Numerical and Analytical Methods in Geomechanics 34, 1191–1210. doi:10.1002/nag

Hergarden, H.J.A.M., van der Poel, J.T., van der Schrier, J.S., 1996. Ground movements due to tunnelling: Influence on pile foundations, in: Mair, R.J., Taylor, R.N. (Eds.), Geotechnical Aspects of Underground Construction in Soft Ground - 2nd International Symposium (IS-London). A.A. Balkema, Rotterdam, London, UK, pp. 519–524.

Higgins, K.G., St. John, H.D., Chudleigh, I.L.J., Potts, D.M., 1999. An example of a pile-tunnel interaction problem, in: Kusakabe, O., Fujita, K., Miyazaki, Y. (Eds.), Geotechnical Aspects of Underground Construction in Soft Ground - 3rd International Symposium (IS-Tokyo). Tokyo, Japan, pp. 99–103.

Hirayama, H., 1990. Load-settlement analysis for bored piles using hyperbolic transfer functions. Soils and Foundations 30, 55–64. doi:10.3208/sandf1972.30.55

Hoek, E., 2004. Numerical Modelling for Shallow Tunnels in Weak Rock, Roscience.

Hoek, E., Carranza-Torres, C., Diederichs, M.S., Corkum, B., 2008. The 2008 Kersten Lecture Integration of geotechnical and structural design in tunneling, in: Proceedings of the University of Minnesota 56th Annual Geotechnical Engineering Conference. Minneapolis, USA.

Huang, M., Mu, L., 2012. Vertical response of pile raft foundations subjected to tunneling-induced ground movements in layered soil. International Journal for Numerical and Analytical Methods in Geomechanics 36, 977–1001. doi:10.1002/nag

Huang, M., Zhang, C., Li, Z., 2009. A simplified analysis method for the influence of tunneling on grouped piles. Tunnelling and Underground Space Technology 24, 410–422. doi:10.1016/j.tust.2008.11.005

ITA, 2016. History of the tunnelling construction.

ixtract GmbH, 2014. Drilling through the city. [WWW Document]. URL https://www.behance.net/gallery/20377183/ixtract-tunnel-boring-machine-TBM (accessed 23.12.16)

Jacobsz, S.W., 2002. The effects of tunnelling on piled foundations. PhD thesis, University of Cambridge.

Jacobsz, S.W., Bowers, K.H., Moss, N.A., Zanardo, G., 2005. The effects of tunnelling on piled structures on the CTRL, in: Bakker, K.J., Bezuijen, A., Broere, W., Kwast, E.A. (Eds.), Geotechnical Aspects of Underground Construction in Soft Ground - 5th International Symposium (IS-Amsterdam). Taylor & Francis/Balkema, Leiden, Amsterdam, the Netherlands, pp. 115–121. doi:10.1201/NOE0415391245.ch12

Jacobsz, S.W., Standing, J.R., Mair, R.J., Hagiwara, T., Sugiyama, T., 2002. Centrifuge modelling of tunnelling near driven piles, in: Kastner, R., Emeriault, F., Dias, D., Guilloux, A. (Eds.), Geotechnical Aspects of Underground Construction in Soft Ground - 4th International Symposium (IS-Toulouse). Specifique, Lyon, Toulouse, France, pp. 687–692.

Jacobsz, S.W., Standing, J.R., Mair, R.J., Soga, K., Hagiwara, T., Sugiyama, T., 2004. Centrifuge modelling of tunnelling near driven piles. Soils and Foundations 44, 51–58.

Jacobsz, S.W., Standing, J.R., Mair, R.J., Soga, K., Hagiwara, T., Sugiyama, T., 2001. Tunnelling effects on driven piles, in: Jardine, F.M. (Ed.), International Conference on the Response of Buildings to Excavation-Induced Ground Movements. London, UK, pp. 337–348.

Jardine, R.J., Chow, F.C., Standing, J.R., Overy, R.F., Saldivar-Moguel, E., van Linschoten, C.S., Ridgway, A., 2005. An updated assessment of the ICP pile capacity procedures, in: Cassidy, M., Gourvenec, S. (Eds.), International Symposium on Frontiers in Offshore Geotechnics. Taylor & Francis, Perth, Australia, pp. 691–696. doi:10.1201/NOE0415390637.ch77

Kaalberg, F.J., Teunissen, E.A.H., van Tol, A.F., Bosch, J.W., 2005. Dutch research on the impact of shield tunnelling on pile foundations, in: Bakker, K.J., Bezuijen, A., Broere, W., Kwast, E.A. (Eds.), Geotechnical Aspects of

Underground Construction in Soft Ground - 5th International Symposium (IS-Amsterdam). Taylor & Francis/Balkema, Leiden, Amsterdam, the Netherlands, pp. 123–131.

Karlsrud, K., 2014. Ultimate Shaft Friction and Load-Displacement Response of Axially Loaded Piles in Clay Based on Instrumented Pile Tests. Journal of Geotechnical and Geoenvironmental Engineering 140, 4014074. doi:10.1061/(ASCE)GT.1943-5606.0001170

Kasper, T., Meschke, G., 2004. A 3D finite element simulation model for TBM tunnelling in soft ground. International Journal for Numerical and Analytical Methods in Geomechanics 28, 1441-1460. doi:10.1002/nag.395

Kavvadas, M., 2005. Numerical Analysis in the Design of Urban Tunnels, in: 11th International Association for Computer Methods and Advances in Geomechanics Conference. Torino, Italy.

Kitiyodom, P., Masumoto, T., Kawaguchi, K., 2005a. Analyses of pile foundations subjected to ground movements induced by tunnelling, in: Bakker, K.J., Bezuijen, A., Broere, W., Kwast, E.A. (Eds.), Geotechnical Aspects of Underground Construction in Soft Ground - 5th International Symposium (IS-Amsterdam). Taylor & Francis/Balkema, Leiden, Amsterdam, the Netherlands, pp. 551–557.

Kitiyodom, P., Matsumoto, T., 2003. A simplified analysis method for piled raft foundations in non-homogeneous soils. International Journal for Numerical and Analytical Methods in Geomechanics 27, 85–109. doi:10.1002/nag.264

Kitiyodom, P., Matsumoto, T., 2002. A simplified analysis method for piled raft and pile group foundations with batter piles. International Journal for Numerical and Analytical Methods in Geomechanics 26, 1349–1369. doi:10.1002/nag.248

Kitiyodom, P., Matsumoto, T., Kawaguchi, K., 2005b. A simplified analysis method for piled raft foundations subjected to ground movements induced by tunnelling. International Journal for Numerical and Analytical Methods in Geomechanics 29, 1485–1507. doi:10.1002/nag.469

Klar, A., Soga, K., 2005. The effect of ground settlements on the axial response of piles: some closed form solutions. Cambridge University Engineering Department Technical Report (CUED TR) 341

Konda, T., Nagaya, J., Hashimoto, T., Shahin, H.M., Nakai, T., 2013. In-situ Measurement and Numerical Analysis on Tunnel Lining and Ground Behaviour due to Shield Excavation, in: Meschke, G., Eberhardsteiner, J., Schanz, T., Soga, K., Thewes, M. (Eds.), EURO:TUN 2013 - 3rd International Conference on Computational Methods in Tunnelling and Subsurface Engineering. Bochum, Germany, pp. 17–19.

Korff, M., 2012. Response of piled buildings to the construction of deep excavations. PhD thesis, University of Cambridge.

Korff, M., Mair, R.J., Van Tol, F.A.F., 2016. Pile-Soil Interaction and Settlement Effects Induced by Deep Excavations. Journal of Geotechnical and Geoenvironmental Engineering 138, 4016034. doi:10.1061/(ASCE)GT.1943-5606.0001434

Kraft, L.M., Ray, R.P., Kagawa, T., 1981. Theoretical t-z Curves. Journal of Geotechnical Engineering 107, 1543–1561.

Leca, E., New, B., 2007. Settlements induced by tunneling in Soft Ground. Tunnelling and Underground Space Technology 22, 119–149. doi:10.1016/j.tust.2006.11.001

Lee, C.J., 2012a. Three-dimensional numerical analyses of the response of a single pile and pile groups to tunnelling in weak weathered rock. Tunnelling and Underground Space Technology 32, 132–142. doi:10.1016/j.tust.2012.06.005

Lee, C.J., 2012b. Numerical analysis of the interface shear transfer mechanism of a single pile to tunnelling in weathered residual soil. Computers and Geotechnics 42, 193–203. doi:10.1016/j.compgeo.2012.01.009

Lee, C.J., Chiang, K.H., 2007. Responses of single piles to tunneling-induced soil movements in sandy ground. Canadian Geotechnical Journal 44, 1224–1241. doi:10.1139/T07-050

Lee, C.J., Jacobsz, S.W., 2006. The influence of tunnelling on adjacent piled foundations. Tunnelling and Underground Space Technology 21, 430. doi:10.1016/j.tust.2005.12.072

Lee, C.J., Jun, S.H., Yoo, N.J., Kim, G.W., 2007. The effects of tunnelling on an adjacent single pile, in: Barták, J., Hrdina, I., Romancov, G., Zlámal, J. (Eds.), ITA World Tunnel Congress 2007 - Underground Space -The 4th Dimension of Metropolises. Prague, Czech Republic, pp. 527–532.

Lee, C.J., Kao, C.M., Chiang, K.H., 2003. Pile response due to nearby tunneling, in: BGA International Conference on Foundations: Innovations, observations, design and practice, Dundee, Scotland.

Lee, G.T.K., Ng, C.W.W., 2005a. Three-dimensional numerical simulation of tunnelling effects on an existing pile, in: Bakker, K.J., Bezuijen, A., Broere, W., Kwast, E.A. (Eds.), Geotechnical Aspects of Underground Construction in Soft Ground - 5th International Symposium (IS-Amsterdam). Taylor & Francis/Balkema, Leiden, Amsterdam, the Netherlands, pp. 139–144.

Lee, G.T.K., Ng, C.W.W., 2005b. Effects of advancing open face tunneling on an existing loaded pile. Journal of Geotechnical and Geoenvironmental Engineering 131, 193–201. doi:10.1061/(ASCE)1090-0241(2005)131

Lee, J.H., Salgado, R., 1999. Determination of pile base resistance in sands. Journal of Geotechnical and Geoenvironmental Engineering 125, 673–683.

Lee, R.G., Turner, A.J., Whitworth, L.J., 1994. Deformations caused by tunnelling beneath a piled structure, in: 3th International Conference on Soil Mechanics and Foundation Engineering. New Delhi, India, pp. 873–878.

Lee, S., Cheang, W., Swolfs, W., Brinkgreve, R.B.J., 2009. Plaxis-GiD Modelling of Tunnel-Pile Interaction, in: 2nd International Conference on Computational Methods in Tunnelling. Bochum, Germany.

Lee, S.W., Choy, C.K.M., Tse, S.C., van Gool, F.R., Cheang, W.W.L., Brinkgreve, R.B.J., 2011. 3D Numerical Modelling of Tunnelling Intersecting Piles, in: Viggiani, G. (Ed.), Geotechnical Aspects of Underground Construction in Soft Ground - 7th International Symposium (IS-Rome). CRC Press/Balkema, Leiden, Rome, Italy.

Lee, Y., Yoo, C., 2008. Two distinctive shear strain modes for pile-soil-tunnelling interaction in a granular mass, in: Ng, C.W.W., Huang, H.W., Liu, G.B. (Eds.), Geotechnical Aspects of Underground Construction in Soft Ground - 6th International Symposium (IS-Shanghai). CRC Press/Balkema, Leiden, Shanghai, China, pp. 683–688.

Lee, Y.J., Bassett, R.H., 2007. Influence zones for 2D pile–soil-tunnelling interaction based on model test and numerical analysis. Tunnelling and Underground Space Technology 22, 325–342. doi:10.1016/j.tust.2006.07.001

Lee, Y.J., Yoo, C.S., 2006. Behaviour of a bored tunnel adjacent to a line of loaded piles, in: ITA World Tunnel Congress 2006 - Safety in the Underground Space. Seoul, Korea. doi:10.1016/j.tust.2005.12.185

Liu, J., Xiao, H.B., Tang, J., Li, Q.S., 2004. Analysis of load-transfer of single pile in layered soil. Computers and Geotechnics 31, 127–135. doi:10.1016/j.compgeo.2004.01.001

Lobo-Guerrero, S., Vallejo, L.E., 2005. DEM analysis of crushing around driven piles in granular materials. Géotechnique 55, 617–623.

Loganathan, N., Poulos, H.G., 1998. Analytical prediction for tunneling-induced ground movements in clays. Journal of Geotechnical and Geoenvironmental Engineering 124, 846–856.

Loganathan, N., Poulos, H.G., Stewart, D.P., 2000. Centrifuge model testing of tunnelling-induced ground and pile deformations. Géotechnique 50(3), 283-294.

Loganathan, N., Poulos, H.G., Xu, K.J., 2001. Ground and pile-group responses due to tunnelling. Soils and Foundations 41, 57–67.

Mahmood, K., Kim, W.B., Yang, H.S., 2011. A Parametrical Study of Tunnel-Pile Interaction using Numerical Analysis. Geosystem Engineering 14, 169–174.

Mair, R.J., 2011. Tunnelling and deep excavations - Ground movements and their effects, in: Anagnostopoulos, A., Pachakis, M., Tsatsanifos, C. (Eds.), 15th European Conference on Soil Mechanics and Geotechnical Engineering. Athens, Greece, pp. 39–70.

Mair, R.J., Taylor, R.N., Bracegirdle, A., 1993. Subsurface settlement profiles above tunnels in clays. Géotechnique 43, 315–320.

Mair, R.J., Williamson, M.G., 2014. The influence of tunnelling and deep excavation on piled foundations. in: Yoo, C., Park, S., Kim, B., Ban, H. (Eds.), Geotechnical Aspects of Underground Construction in Soft Ground - 8th International Symposium (IS-Seoul). CRC Press/Balkema, Leiden, Seoul, South Korea, pp. 21–30

Marshall, A.M., 2012. Tunnel-pile interaction analysis using cavity expansion methods. Journal of Geotechnical and Geoenvironmental Engineering 138, 1237–1246. doi:10.1061/(ASCE)GT.1943-5606.0000709.

Marshall, A.M., 2009. Tunnelling in sand and its effect on pipelines and piles. PhD thesis, University of Cambridge.

Marshall, A.M., Haji, T., 2015. An analytical study of tunnel–pile interaction. Tunnelling and Underground Space Technology 45, 43–51. doi:10.1016/j.tust.2014.09.001

Marshall, A.M., Mair, R.J., 2011. Tunneling beneath driven or jacked end-bearing piles in sand. Canadian Geotechnical Journal 48, 1757–1771. doi:10.1139/T11-067

Masini, L., Rampello, S., Soga, K., 2014. An Approach to Evaluate the Efficiency of Compensation Grouting. Journal of Geotechnical and Geoenvironmental Engineering doi:10.1061/(ASCE)GT.1943-5606.0001180.

Massad, F., 2014. Theoretical and Experimental Studies on the Resilience of Driven Piles. Soils and Rocks 37, 113–132.

Massad, F., 1995. The analysis of piles considering soil stiffness and residual stresses, in: 10th Pan-American Conference on Soil Mechanics and Foundation Engineering. Guadalajara, Mexico, pp. 1199–1210.

Masumoto, T., Kitiyodom, P., Kawaguchi, K., 2005. Three-dimensional analyses of piled raft foundations subjected to ground movements induced by tunnelling, in: Bakker, K.J., Bezuijen, A., Broere, W., Kwast, E.A. (Eds.), Geotechnical Aspects of Underground Construction in Soft Ground - 5th International Symposium (IS-Amsterdam). Taylor & Francis/Balkema, Leiden, Amsterdam, the Netherlands, pp. 601–607.

Mayne, P.W., Coop, M.R., Springman, S.M., Huang, A.B., Zornberg, J.G., 2009. State of the art report: Geomaterial behavior and testing, in: Hamza, M., Shahien, M., El-Mossallamy, Y. (Eds.), 17th International Conference on Soil Mechanics and Geotechnical Engineering. Alexandria, Egypt, pp. 2777–2872.

Mcnamara, A.M., Taylor, R.N., Stallebrass, S.E., Romano, M.C., 2003. Influence of tunnelling on the behaviour of existing piled foundations, in: BGA International Conference on Foundations.

Meguid, M.A., Mattar, J., 2009. Investigation of Tunnel-Soil-Pile Interaction in Cohesive Soils. Journal of Geotechnical and Geoenvironmental Engineering 135, 973–979. doi:10.1061/(ASCE)GT.1943-5606.0000004

Melis, M., Medina, L., Rodríguez, J.M., 2002. Prediction and analysis of subsidence induced by shield tunnelling in the Madrid Metro extension. Canadian Geotechnical Journal 39, 1273-1287. doi:10.1139/t02-073

Meschke, G., Ninić, J., Stascheit, J., Alsahly, A., 2013. Parallelized computational modeling of pile–soil interactions in mechanized tunneling. Engineering Structures 47, 35–44. doi:10.1016/j.engstruct.2012.07.001

Mindlin, R.D., 1936. Force at a point in the interior of a semi-infinite solid. Journal of Applied Physics 7, 195–202.

Mohammed, M.H., Pusch, R., Knutsson, S., Hellström, G., 2014. Rheological Properties of Cement-Based Grouts Determined by Different Techniques. Engineering 6, 217–229. doi:10.4236/eng.2014.65026

Morton, J.D., King, K.H., 1979. Effects of tunneling on the bearing capacity and settlement of piled foundations, in: Jones, M.J. (Ed.), Tunnelling 79 - 2nd International Symposium of the Institution of Mining and Metallurgy. London, UK, pp. 57–68.

Mroueh, H., Shahrour, I., 2002. Three-dimensional finite element analysis of the interaction between tunneling and pile foundations. International Journal for Numerical and Analytical Methods in Geomechanics 26, 217–230. doi:10.1002/nag.194

Mu, L., Huang, M., Finno, R.J., 2012. Tunnelling effects on lateral behavior of pile rafts in layered soil. Tunnelling and Underground Space Technology 28, 192–201. doi:10.1016/j.tust.2011.10.010

Nakai, T., 2004. Constitutive Modeling of Geomaterials: Principles and Applications, CRC Press.

Namazi, E., Hajihassani, M., Marto, A., Mohamad, H., 2011a. Influence of existing loaded piles on tunnels, in: Tunnels and Underground Structures in South-East Europe - 1st International Congress. Dubrovnik, Croatia.

Namazi, E., Mohamad, H., Jorat, M.E., Hajihassani, M., 2011b. Investigation on the Effects of Twin Tunnel Excavations Beneath a Road Underpass. The Electronic Journal of Geotechnical Engineering 16, 441–450.

Ng, C.W.W., Lu, H., Peng, S.Y., 2013. Three-dimensional centrifuge modelling of the effects of twin tunnelling on an existing pile. Tunnelling and Underground Space Technology 35, 189–199. doi:10.1016/j.tust.2012.07.008

Ninić, J., 2015. Computational strategies for predictions of the soil-structure interaction during mechanized tunneling. PhD thesis, Ruhr Universitat Bochum.

Ninić, J., Stascheit, J., Meschke, G., 2011. Numerical simulation of interactions between TBM-driven tunnel construction and pile foundations, in: 13th International Conference of the International Association for Computer Methods and Advances in Geomechanics. Melbourne, Australia, pp. 9–11.

Ong, C.W., Leung, C.F., Yong, K.Y., Chow, Y.K., 2006. Pile responses due to tunnelling in clay, in: Ng, C.. W.. W.., Wang, Y.. H.., Zhang, L.. M.. (Eds.), 6th International Conference on Physical Modelling in Geotechnics. Hong Kong, pp. 1177–1182. doi:10.1201/NOE0415415866.ch173

Ong, C.W., Leung, C.F., Yong, K.Y., Chow, Y.K., 2005. Centrifuge modelling of pile responses due to tunnelling in clay, in: Underground Singapore.

Pang, C.H., 2006. The effects of tunnel construction on nearby pile foundation. PhD thesis, National University of Singapore.

Pang, C.H., Yong, K.Y., Chow, Y.K., 2005a. Three-dimensional numerical simulation of tunnel advancement on adjacent pile foundation, in: Solak, Y., Erdem, T. (Eds.), ITA World Tunnel Congress 2005 - Underground Space Use. Analysis of the Past and Lessons for the Future. Istanbul, Turkey, pp. 1141–1148.

Pang, C.H., Yong, K.Y., Chow, Y.K., Wang, J., 2005b. The response of pile foundations subjected to shield tunnelling, in: Bakker, K.J., Bezuijen, A., Broere, W., Kwast, E.A. (Eds.), Geotechnical Aspects of Underground Construction in Soft Ground - 5th International Symposium (IS-Amsterdam). Taylor & Francis/Balkema, Leiden, Amsterdam, the Netherlands, pp. 737–743.

PDE Solutions Inc., 2012. FlexPDE Student Version 6.32s User Guide. Washington, United States of America.

Peck, R.B., 1969. Deep Excavations and Tunneling in Soft Ground, in: 7th International Conference on Soil Mechanics and Foundation Engineering. Mexico City, Mexico, pp. 225–290.

Poulos, H.G., 2002. Prediction of behaviour of piled building foundations due to tunnelling operations, in: Kastner, R., Emeriault, F., Dias, D., Guilloux, A. (Eds.), Geotechnical Aspects of Underground Construction in Soft Ground - 4th International Symposium (IS-Toulouse). Specifique, Lyon, Toulouse, France.

Poulos, H.G., 1989. Pile behaviour - theory and application. Géotechnique 39, 365–415.

Poulos, H.G., Davis, E.H., 1980. Pile foundation analysis and design.

Poulos, H.G., Davis, E.H., 1968. The Settlement Behaviour of Single Axially Loaded Incompressible Piles and Piers. Géotechnique 18, 351–371. doi:10.1680/geot.1968.18.3.351

Press, W.H., Teukolsky, S.A., Vetterling, W.T., Flannery, B.P., 2007. Numerical Recipes: The art of scientific computing, 3rd ed.

Rabcewicz, L. V, 1964. The New Austrian Tunnelling Method. Water Power.

Ran, X., 2004. Tunnel pile interaction in clay. MEng thesis, National University of Singapore.

Randolph, M.F., 2003. Science and empiricism in pile foundation design. Géotechnique 53, 847–875. doi:10.1680/geot.2003.53.10.847

Randolph, M.F., Wroth, C.P., 1979. An analysis of the vertical deformation of pile groups. Géotechnique 29, 423–439.

Randolph, M.F., Wroth, C.P., 1978. Analysis of deformation of vertically loaded piles. Journal of Geotechnical Engineering Division - ASCE 104, 1465–1488.

Robbins, D., 2013. A Tradition of Innovation - The Next Push For Machine Tunnelling. ITA Muir Wood Lecture.

Rowe, R.K., Lo, K.Y., Kack, G.J., 1983. A method of estimating surface settlement above tunnels constructed in soft ground. Canadian Geotechnical Journal 20, 11–22. doi:10.1139/t83-002

Sagaseta, C., 1987. Analysis of undrained soil deformation due to ground loss. Géotechnique 37, 301–320. doi:10.1680/geot.1988.38.4.647

Schanz, T., Vermeer, A., Bonnier, P.G., 1999. The hardening soil model: formulation and verification, in: Symposium Beyond 2000 in Computational Geotechnics.

Scheffer, M., Rahm, T., König, M., 2014. Simulation-Based Analysis of Surface Jobsite Logistics in Mechanized Tunneling, in: Computing in Civil and Building Engineering - International Conference. American Society of Civil Engineers, Reston, VA, pp. 705–712. doi:10.1061/9780784413616.088

Schroeder, F.C., 2002. The influence of bored piles on existing tunnels. PhD thesis, Imperial College, University of London.

Selemetas, D., 2005. The response of full-scale piles and piled structures to tunnelling. PhD thesis, University of Cambridge.

Selemetas, D., Standing, J.R., Mair, R.J., 2005. The response of full-scale piles to tunnelling, in: Bakker, K.J., Bezuijen, A., Broere, W., Kwast, E.A. (Eds.), Geotechnical Aspects of Underground Construction in Soft Ground - 5th International Symposium (IS-Amsterdam). Taylor & Francis/Balkema, Leiden, Amsterdam, the Netherlands, pp. 763–769.

Selemetas, D., Standing, J.R., Mair, R.J., Sharrocks, D.M., Parker, F., Allen, R., 2002. The response of a piled structure to tunnelling and jacking, in: Kastner, R., Emeriault, F., Dias, D., Guilloux, A. (Eds.), Geotechnical Aspects of Underground Construction in Soft Ground - 4th International Symposium (IS-Toulouse). Specifique, Lyon, Toulouse, France, pp. 367–372.

Shahin, H.M., Nakahara, E., Nagata, M., 2009. Behaviors of ground and existing structures due to circular tunneling, in: Hamza, M., Shahien, M., El-Mossallamy, Y. (Eds.), 17th International Conference on Soil Mechanics and Geotechnical Engineering. Alexandria, Egypt, pp. 1786–1789. doi:10.3233/978-1-60750-031-5-1786

Shahin, H.M., Nakai, T., Zhang, F., Kikumoto, M., Nakahara, E., 2011. Behavior of ground and response of existing foundation due to tunneling. Soils and Foundations 51, 395–409.

Shirlaw, J.N., 1999. Discussion: Can settlements over tunnels be accurately predicted using advanced numerical methods?, in: Kusakabe, O., Fujita, K., Miyazaki, Y. (Eds.), Geotechnical Aspects of Underground Construction in Soft Ground - 3rd International Symposium (IS-Tokyo). Tokyo, Japan, pp. 471–472.

Shirlaw, J.N., Richards, D.P., Ramond, P., Longchamp, P., 2004. Recent experience in automatic tail void grouting with soft ground tunnel boring machines, in: ITA World Tunnel Congress 2004 - Underground Space for Sustainable Urban Development. Singapore, pp. 1–8.

Son, M., Cording, E.J., 2005. Estimation of building damage due to excavation-induced ground movements. Journal of Geotechnical and Geoenvironmental Engineering 131, 162–177.

Standing, J., Leung, W., 2005. Investigating stresses around tunnels and piles using photo-elasticity techniques, in: Bakker, K.J., Bezuijen, A., Broere, W., Kwast, E.A. (Eds.), Geotechnical Aspects of Underground Construction in Soft Ground - 5th International Symposium (IS-Amsterdam). Taylor & Francis/Balkema, Leiden, Amsterdam, the Netherlands, pp. 171–177.

Surjadinata, J., Carter, J.P., Hull, T.S., Poulos, H.G., 2005. Analysis of effects of tunnelling on single piles, in: Bakker, K.J., Bezuijen, A., Broere, W., Kwast, E.A. (Eds.), Geotechnical Aspects of Underground Construction in Soft Ground - 5th International Symposium (IS-Amsterdam). Taylor & Francis/Balkema, Leiden, Amsterdam, the Netherlands, pp. 665–671.

Surjadinata, J., Hull, T.S., Carter, J.P., Poulos, H.G., 2006. Combined finite- and boundary-element analysis of the effects of tunneling on single piles. International Journal of Geomechanics 6, 374–377.

Surjadinata, J.Q., Hull, T.S., Carter, J.P., 2011. Effects of Tunnelling on a Single Pile : Three-Dimensional Design Tool, in: Viggiani, G. (Ed.), Geotechnical Aspects of Underground Construction in Soft Ground - 7th International Symposium (IS-Rome). CRC Press/Balkema, Leiden, Rome, Italy.

Swoboda, G., Abu-Krisha, A., 1999. Three-dimensional numerical modelling for TBM tunnelling in consolidated clay. Tunnelling and Underground Space Technology 14, 327-333. doi:10.1016/S0886-7798(99)00047-4

Takahashi, K., Fukazawa, N., Hagiwara, T., Hosoda, M., 2004. Observational control of slurry shield tunnels with super close spacing under the nearby bridge abutments loads, in: ITA World Tunnel Congress 2004 - Underground Space for Sustainable Urban Development. Singapore, pp. 1–6.

Talmon, A.M., Aanen, L., Bezuijen, A., van der Zon, W.H., 2001. Grout pressures around a tunnel lining, in: Adachi, T., Kimura, M., Tateyama, K. (Eds.), International Symposium on Modern Tunneling Science and Technology. Kyoto, Japan, pp. 817–822.

Talmon, A.M., Bezuijen, A., 2013. Analytical model for the beam action of a tunnel lining during construction. International Journal for Numerical and Analytical Methods in Geomechanics 37, 181–200. doi:10.1002/nag.1092

Talmon, A.M., Bezuijen, A., 2008. Backfill grouting research at Groene Hart Tunnel, in: Geotechnical Aspects of Underground Construction in Soft Ground - 6th International Symposium (IS-Shanghai). Shanghai, China, pp. 349–355.

TEC, 2014. Tunnels & Tunnelling - Experience Record - Bored Tunnels.

Thewes, M., Budach, C., Bezuijen, A., 2011. Foam conditioning in EPB tunnelling, in: Geotechnical Aspects of Underground Construction in Soft Ground - 7th International Symposium (IS-Rome). Rome, Italy, pp. 127–135.

tunnelbuilder.com, 2004. NFM Technologies TBM Breaks Through Green Heart Tunnel in the Netherlands [WWW Document]. URL http://tunnelbuilder.com/News/NFM-Technologies-TBM-Breaks-Through-Green-Heart-Tunnel-in-the-Netherlands.aspx (accessed 10.11.16).

UITP, 2015. Statistics brief: World metro figures.

Ulitskii, V.M., 1995. History of pile foundation engineering. Soil Mechanics and Foundation Engineering32, 110.

UN (Ed.), 2012. United Nations Demographic Yearbook.

UNESCO, 2011. UNESCO World Heritage Candidature - Prehistoric Pile Dwellings around the Alps.

Vermeer, P.A., Bonnier, P.G., 1991. Pile settlements due to tunnelling, in: 10th European Conference on Soil Mechanics and Foundation Engineering. Florence, Italy, pp. 869–872.

Vermeer, P.A., Möller, S.C., Ruse, N., 2003. On the application of numerical analysis in tunnelling, in: 12th Asian Regional Conference on Soil Mechanics and Geotechnical Engineering.

Verruijt, A., 1993. Soil Dynamics. Delft University of Technology.

Verruijt, A., Booker, J.R., 1996. Surface settlements due to deformation of a tunnel in an elastic half plane. Géotechnique 46, 753–756.

Viana da Fonseca, A., Santos, J.A., Esteves, E.C., Massad, F., 2007. Analysis of Piles in Residual Soil from Granite Considering Residual Loads. Soils and Rocks 30, 63–80.

Viggiani, G., Atkinson, J.H., 1995. Stiffness of fine-grained soil at very small strains. Géotechnique 45, 249–265. doi:10.1680/geot.1995.45.2.249

Wang, W., Wu, J., Li, Y., 2013. Super-long bored pile foundation for super high-rise buildings in China', in: 18th International Conference on Soil Mechanics and Geotechnical Engineering - Challenges and Innovations in Geotechnics. Paris, France, pp. 2897–2900.

Whitworth, L.J., Turner, A.J., Lee, R.G., 1993. Bitumen slip coated trial piles and prototype underreamed trial pile at Angel Square, Islington. Ground Engineering. Jan/Feb, 28–33.

Williamson, M., 2014. Tunnelling Effects on Bored Piles in Clay. PhD thesis, University of Cambridge.

Wood, D.M., 2004. Geotechnical Modelling. Taylor & Francis, Abingdon, UK. doi:10.4324/9780203477977

Wood, D.M., 1990. Soil behaviour and critical state soil mechanics. Cambridge University Press.

Xu, K.J., Poulos, H.G., 2001. 3-D elastic analysis of vertical piles subjected to "passive" loadings. Computers and Geotechnics 28, 349–375.

Xu, K.J., Poulos, H.G., 2000. General elastic analysis of piles and pile groups. International Journal for Numerical and Analytical Methods in Geomechanics 24, 1109–1138.

Yang, J.S., Wang, M.C., 2002. Evaluation of tunneling-induced downdrag on end-bearing piles. Electronic Journal of Geotechnical Engineering

Yang, M., Sun, Q., Li, W., Ma, K., 2011. Three-dimensional finite element analysis on effects of tunnel construction on nearby pile foundation. Journal of Central South University of Technology 18, 909–916. doi:10.1007/s11771−011−0780−9

Yang, X.J., Deng, F.H., Wu, J.J., Liu, J., Wang, F.Q., 2009. Response of carrying capacity of piles induced by adjacent Metro tunneling. International Journal of Mining Science and Technology 19, 176–181. doi:10.1016/S1674-5264(09)60033-8

Yao, J., Taylor, R.N., Mcnamara, A.M., 2008. The effects of loaded bored piles on existing tunnels, in: Ng, C.W.W., Huang, H.W., Liu, G.B. (Eds.), Geotechnical Aspects of Underground Construction in Soft Ground - 6th International Symposium (IS-Shanghai). CRC Press/Balkema, Leiden, Shanghai, China, pp. 735–741.

Yoo, C., Kim, S.B., 2008. Three-dimensional numerical investigation of multifaced tunneling in water-bearing soft ground. Canadian Geotechnical Journal 45, 1467–1486. doi:10.1139/T08-071

Yoo, C., Wu, S.J., 2011. Interaction between tunnelling and bridge foundation - 3D numerical investigation, in: Viggiani, G. (Ed.), Geotechnical Aspects of Underground Construction in Soft Ground - 7th International Symposium (IS-Rome). CRC Press/Balkema, Leiden, Rome, Italy.

Zanardo, G., Jacobsz, S.W., Woods, E., Coughlan, D., 2004. Assessment of the tunneling-induced effects on continuous bridges, in: Bridge Maintenance, Safety and Management - 2nd International Conference. Kyoto, Japan.

Zhang, R., Zheng, J., Pu, H., Zhang, L., 2011. Analysis of excavation-induced responses of loaded pile foundations considering unloading effect. Tunnelling and Underground Space Technology 26, 320–335. doi:10.1016/j.tust.2010.11.003

Zhang, Z., Zhang, Q., Yu, F., 2011. A destructive field study on the behavior of piles under tension and compression. Journal of Zhejiang University - Science A: Applied Physics & Engineering 12, 291–300. doi:10.1631/jzus.A1000253

Zhao, M., Yang, M., Zou, X., 2005. Vertical bearing capacity of pile based on load transfer model. Journal of Central South University of Technology 12, 488–493. doi:10.1007/s11771-005-0188-5

Zizka, Z., Thewes, M., Popovic, I., 2015. Analysis of Slurry Pressure Transfer on the Tunnel Face during Excavation, in: Kolíc, D. (Ed.), ITA World Tunnel Congress 2015 - SEE Tunnel - Promoting Tunnelling in SEE Region. Dubrovnik, Croatia.

Zou, J., 2003. Analysis of pile-soil-tunnel interaction. National University of Singapore.

Zou, J., Chow, Y.K., Dasari, G.R., Leung, C.F., Ng, C.S., 2003. Pile-soil-tunnel interaction in some layered soil profiles, in: 12th Asian Regional Conference on Soil Mechanics and Geotechnical Engineering. Singapore.